Freie Universität Berlin

ODTLES: Turbulence Modeling Using a One-Dimensional Turbulence Closed Extended Large Eddy Simulation Approach

Inauguraldissertation
zur Erlangung des akademischen Grades eines
Doktors der Naturwissenschaften

vorgelegt beim Fachbereich Mathematik und Informatik
der Freien Universität Berlin

von

Diplom-Physiker Christoph Glawe

Berlin
August 2015

Christoph Glawe: *ODTLES: Turbulence Modeling Using a One-Dimensional Turbulence Closed Extended Large Eddy Simulation Approach,* © August 2015

BETREUER:

Prof. Dr.-Ing. Rupert Klein
Freie Universität Berlin
Fachbereich Mathematik und Informatik
Institut für Mathematik
Arnimallee 2-6
14195 Berlin, Deutschland

TAG DER DISPUTATION:

25.02.2016

PUBLICATIONS

Some ideas and figures have appeared previously in the following publications:

[1] C. Glawe, F.T. Schulz, E.D. Gonzalez-Juez, H. Schmidt, and A.R. Kerstein. ODTLES simulations of turbulent flows through heated channels and ducts. In *Proceedings of TSFP-8*, Poitiers, France, 2013.

[2] C. Glawe, H. Schmidt, A.R. Kerstein, and R. Klein. XLES part I: Introduction to extended large eddy simulation. *submitted to J. Comput. Phys.*, 2015.

[3] C. Glawe, H. Schmidt, A.R. Kerstein, and R. Klein. XLES part II: From extended large eddy simulation to ODTLES. *submitted to J. Comput. Phys.*, 2015.

ABSTRACT

Standard turbulence models, like Reynolds averaged Navier-Stokes (*RaNS*) and large eddy simulation (*LES*), are applied to flows e. g. in engineering and geophysics, but they miss small scale effects, which are frequently of importance, e. g. in reactive flows, flows with apparent Prandtl or Schmidt number effects, or even wall bounded flows. A recent alternative to these standard approaches is the one-dimensional turbulence (*ODT*) model, which is limited to 1D subdomains.

In this thesis we provide a generalized, innovative filter strategy for highly turbulent flows, called extended *LES* (*XLES*), including a formal theory and one special approach in the *XLES* family of models, called *ODT* closed *XLES* (*ODTLES*).

ODTLES combines the *ODT* ability to describe all turbulent scales including molecular diffusion within a 1D sub-domain, with the ability of *XLES* to represent a 3D domain with a 3D resolution at most weakly depending on the turbulent intensity.

XLES and especially *ODTLES* are shown to be consistently derived from the governing equations and numerically sufficiently approximated, which includes the convergence towards direct numerical simulations (*DNS*).

Comparative and predictive numerical studies for turbulent channels, ducts and Rayleigh-Bénard flows show the potential of *ODTLES*.

ZUSAMMENFASSUNG

Turbulenzmodelle wie Reynolds averaged Navier-Stokes (*RaNS*) und Large Eddy Simulationen (*LES*) werden unter anderem in ingenieurwissenschaftlichen, aber auch geophysikalischen Strömungen eingesetzt, vernachlässigen dabei allerdings kleinskalige Effekte, die oftmals von großer Wichtigkeit sind, wie zum Beispiel bei Verbrennungen oder in Strömungen die abhängig von Prandtl- oder Schmidt-Zahlen sind. Ein alternativer Modellierungsansatz wird in one-dimensional turbulence (*ODT*) Modellen verfolgt, die zwar auf einen 1D-Unterraum beschränkt sind, darin allerdings alle turbulenten Skalen beschreiben können.

In dieser Dissertation wird eine Verallgemeinerung bekannter *LES*-Verfahren, genannt extended *LES* (*XLES*), vorgestellt und eine Schließung der *XLES*-Gleichungen mit dem *ODT*-Modell sowohl hergeleitet als auch umgesetzt.

Das *ODT* closed *XLES* (*ODTLES*) Modell kombiniert die Vorteile des *ODT*-Modells mit der Möglichkeit komplexe 3D-Gebiete in Simulationen zu beschrieben. Dabei wird gezeigt dass *XLES* und insbesondere *ODTLES* wohl definierte und konsistente Gleichungssysteme beschreiben, deren numerische Lösung gegen direkte numerische Simulationen (*DNS*) konvergiert.

In numerischen Studien werden Kanal-,Duct-,und Rayleigh-Bénard Strömungen untersucht, die sehr gut mit vorhandenen *DNS*-Ergebnissen übereinstimmen.

Phantasie ist wichtiger als Wissen, denn Wissen ist begrenzt.

— Albert Einstein

ACKNOWLEDGMENTS

The author would like to thank all colleagues at BTU Cottbus-Senftenberg and FU Berlin for fruitful discussions, especially emphasizing Eckhard Dietze, Martin Götze, Zoltan Jozefik, Thomas von Larcher (who provided results for an implicit LES analysis), and Falko Meiselbach and the supervisors Prof. Heiko Schmidt and Prof. Rupert Klein. Special thanks are directed to Alan Kerstein who was incredible patient and a person full of ideas.

Also the author would like to thank H. Kawamura and colleagues, R. Moser and colleagues, and M. Uhlmann and colleagues for providing DNS results online ([48], [63], and [106]), as well as Philipp Schlatter and colleagues [87] for providing τ_W statistics, Klaus Petschel ([79], [80]) for providing Rayleigh-Bénard DNS results for comparison, and R.J.A.M. Stevens and colleagues for providing Nusselt scaling plots ([101]).

This work was supported by the Brandenburg University of Technology Cottbus-Senftenberg, the Freie Universität Berlin, the Helmholtz graduate research school GeoSim, the International Graduate School (IGS) at the BTU Cottbus-Senftenberg, and the Deutsche Forschungsgemeinschaft (DFG) within the SPP 1276 MetStröm. The latter also provided financial support for several stays of Alan Kerstein at BTU Cottbus-Senftenberg.

CONTENTS

LIST OF FIGURES

LIST OF TABLES

ACRONYMS

AME	autonomous microstructure evolution
AMG	algebraic multigrid method
aODT	adaptive *ODT*
aODTLES	*aODT* closed *XLES*
CDM	central difference method
CFD	computational fluid dynamics
CFL-number	Courant-Friedrichs-Lewy number
CN	2nd order Crank-Nicolson scheme
CN-CDM	*CN* scheme in time and spatial *CDM*
CN-RK3-CDM	coupled scheme with *CN* and *RK3* in time and spatial *CDM*

CN-RK3-RK3-CDM	coupled scheme with *CN* and two times *RK3* in time and spatial *CDM*
CPU	central processing unit
CRCP	Cloud Resolving Convection Parameterization
DES	detached eddy simulation
DGM	discontinuous Galerkin method
DNS	direct numerical simulation
#DoFs	number of degrees of freedom
EE1	first order forward Euler scheme
EE1-CDM	*EE1* scheme in time and spatial *CDM*
EMC	ensemble mean closure
ENO	essentially non-oscillatory
FDM	finite difference method
FEM	finite element method
FVM	finite volume method
GCM	global circulation model
IE1	first order backward Euler scheme
IMEX	implicit/explicit time scheme
LBMS	lattice-based multiscale simulation
LEM	linear-eddy model
LES	large eddy simulation
LES-U	unclosed *LES*
LES-wm	wall-modeled *LES*
LES-wr	wall-resolved *LES*
LSC	large scale circulation
MPI	message passing interface
ODT	one-dimensional turbulence
ODTLES	*ODT* closed *XLES*
ODTLES#1	first *ODTLES* version
PDE	partial differential equation
PDF	probability density function
Q3D	quasi-3D multi-scale modeling
RaNS	Reynolds averaged Navier-Stokes
RK3	3 stage 3rd order *TVD* Runge-Kutta scheme
RK3-CDM	*RK3* scheme in time and spatial *CDM*
RK3-RK3-CDM	coupled scheme with *RK3* and *RK3* in time and spatial *CDM*

RSS	resolved small scale
SGM	sub-grid model
SGS	sub-grid scale
URaNS	unsteady Reynolds averaged Navier-Stokes
XLES	extended *LES*
XLES-grid	grid representing *XLES* equations
XLES-U	unclosed *XLES*
XLES vector	vector representing *XLES* variables

NOMENCLATURE

DIMENSIONLESS PARAMETERS

Kn	Knudsen number. $Kn = \frac{\lambda}{L}$
Ma	Mach number. $Ma = \frac{u}{c}$
Nu	Nusselt number. $Nu = \frac{\alpha L}{\kappa}$
Pr	Prandtl number. $Pr = \frac{\nu}{\kappa}$
Ra	Rayleigh number. $Ra = \frac{g(\Delta\theta)}{\nu\kappa} L^3$
Ra_c	critical Rayleigh number. (transition to convective transport)
Ra_u	critical Rayleigh number. (transition to the ‘ultimate regime’)
Re_t	turbulent Reynolds number. $Re_t = \frac{u' L_t}{\nu}$
Re_B	bulk Reynolds number. $Re_B = \frac{u_B h}{\nu}$
Re_τ	friction Reynolds number. $Re_\tau = \frac{u_\tau h}{\nu}$
$Re_{\tau_{ave}}$	spanwise averaged friction Reynolds number. $Re_{\tau_{ave}} = \frac{1}{\lvert\partial\Omega\rvert} \int_{\partial\Omega} \frac{u_\tau(x)\, h}{\nu}\, dx_1\ dx_{2\lvert 3}$

LATIN CHARACTERS

c	local speed of sound. $\left[\frac{m}{s}\right]$
C	*ODT* parameter influencing the overall eddy rate
$\underline{\underline{l}}^{\dagger}$	convolution and deconvolution matrix

V	specific potential energy. $\left[\frac{m^2}{s^2}\right]$
k	specific turbulent kinetic energy. $\left[\frac{m^2}{s^2}\right]$
F_i	specific external forcing in Cartesian x_i-direction. $\left[\frac{m}{s^2}\right]$
g_2	gravity acceleration in the x_2-direction. $\left[\frac{m}{s^2}\right]$
h	half channel height, half duct height, or Rayleigh-cell height. $[m]$
K_N	*XLES* resolution ratio. $K_N = N_{RSS}/N_{LES}$
L	representative physical length scale. $[m]$
l_{max}	maximum eddy size. $[m]$
l_{max_k}	maximum eddy size in x_k-direction. $[m]$
N_{DNS}	number of *DNS* cells
n_I	counter for iterations
N_{LES}	number of *LES* cells
n_r	counter for recursive steps
N_{RSS}	number of RSS cells
N_s	number of Runge-Kutta stages
C_{Nu}	Nusselt scaling prefactor
p	pressure. $\left[\frac{kg}{m\,s^2}\right]$
Q	numerical sub-filter parameter
C_S	Smagorinsky constant
T	temperature. $[K]$
T_0	mean temperature. $[K]$
t_{ave}	non-dimensional averaging time
L_t	representative turbulent length scale. $[m]$
u_B	bulk velocity. $u_B = \frac{1}{\lvert\Omega\rvert}\int_{\Omega} u_1 \, dx_1 \, dx_2 \, dx_3$, $\left[\frac{m}{s}\right]$
u	velocity. $\left[\frac{m}{s}\right]$
u_i	velocity in x_i-direction. $\left[\frac{m}{s}\right]$
$\mathbb{1}$	unity operator
Z	*ODT* parameter scaling the viscous damping of eddies

GREEK CHARACTERS

α	coefficient of volume expansion. $\left[\frac{1}{K}\right]$
Ψ	ansatz function
$\mathcal{F}_A$	ansatz function space

Γ	aspect ratio
$\underline{\sigma}_{\dagger}^{\mathrm{spatial}}$	deconvolution algorithm error term
$\underline{\sigma}_{\theta}^{\mathrm{spatial}}$	spatial scalar error term
$\underline{\sigma}_{\mathrm{SGS}_{ij}}^{\mathrm{spatial}}$	*SGS* momentum error term
$\underline{\sigma}_{\mathrm{XLES-U}_{\theta j}}^{\mathrm{spatial}}$	*XLES-U* spatial scalar error term
$\underline{\sigma}_{\mathrm{XLES-U}_{ij}}^{\mathrm{spatial}}$	*XLES-U* spatial momentum error term
γ_{eff}	effective Nusselt scaling exponent
κ	thermal diffusivity. $\left[\frac{m^2}{s}\right]$
λ	mean free path. $[m]$
η_K	Kolmogorov length scale. $[m]$
ν	kinematic viscosity. $\left[\frac{m^2}{s}\right]$
Ω	computational domain
Ω_n	individual computational 3D grid cell
ϕ_i	solution field. $\phi_i = \{u_i, \theta\}$
$\phi_{k,i}$	*XLES* solution field. $\phi_{k,i} = \{u_{k,i}, \theta_k\}$
ν_r	residual viscosity. $\left[\frac{m^2}{s}\right]$
ρ	density. $\left[\frac{kg}{m^3}\right]$
ρ_0	constant mean density. $\left[\frac{kg}{m^3}\right]$
ρ'	density variation. $\left[\frac{kg}{m^3}\right]$
τ	integral time scale. $[s]$
$\underline{\tau}_{ij}^{\mathrm{XLES}}$	*XLES* residual stress tensor
$\underline{\tau}_{\theta j}^{\mathrm{XLES}}$	*XLES* residual scalar flux
τ_W	wall shear stress. $\tau_W = \rho\nu\partial_{x_2}u_1\vert_{x_2=0}$, $\left[\frac{kg\,m}{s^2}\right]$
φ	test function
$\mathcal{F}_T$	test function space
θ	scalar field. $\theta = \frac{\rho'}{\rho_0} = \alpha(T - T_0)$
ϵ	turbulent dissipation. $\left[\frac{m^2}{s^3}\right]$
ν_T	turbulent viscosity. $\left[\frac{m^2}{s}\right]$
u_τ	friction velocity. $\left[\frac{m}{s}\right]$

CALLIGRAPHIC SYMBOLS

$\underline{\mathcal{X}}_{ij}^{\mathrm{XLES}}$	*XLES* coupling tensor term
$\underline{\mathcal{X}}_{\theta j}^{\mathrm{XLES}}$	*XLES* scalar coupling term

$\underline{\mathcal{C}}_{ij}^{XLES}$	*XLES* cross-stress term
$\underline{\mathcal{C}}_{\theta j}^{XLES}$	*XLES* scalar cross-stress-type term
$\underline{\mathcal{L}}_{ij}^{2D}$	*XLES* Leonard stress
$\underline{\mathcal{L}}_{\theta j}^{2D}$	*XLES* scalar Leonard stress-type term
$\underline{\mathcal{M}}_{ij}$	*XLES* momentum microscale term
$\underline{\mathcal{M}}_{ODT}$	*ODTLES* microscale term
$\underline{\mathcal{M}}_{ODT}^{\delta_i}$	reduced *ODTLES* microscale term
$\underline{\mathcal{M}}_{\theta j}$	*XLES* scalar microscale term
$\underline{\mathcal{D}}_{ODT}$	*ODT* diffusion terms
$\underline{\mathcal{R}}_{ij}^{XLES}$	2D *SGS* Reynolds stress term
$\underline{\mathcal{R}}_{j\theta}^{XLES}$	2D scalar *SGS* Reynolds stress-type term
$\underline{\mathcal{D}}_{XLES}$	*XLES* diffusion terms

MATHEMATICAL SYMBOLS

$\underline{\underline{l}}^{1D}$	1D filter matrix. $\underline{\underline{l}}^{1D} = \begin{pmatrix} [l_1] & 0 & 0 \\ 0 & [l_2] & 0 \\ 0 & 0 & [l_3] \end{pmatrix}$
$\underline{\underline{l}}^{2D}$	2D filter matrix. $\underline{\underline{l}}^{2D} = \begin{pmatrix} [l_2 l_3] & 0 & 0 \\ 0 & [l_1 l_3] & 0 \\ 0 & 0 & [l_1 l_2] \end{pmatrix}$
$\underline{\underline{l}}^{3D}$	3D filter matrix. $\underline{\underline{l}}^{3D} = \begin{pmatrix} [l_1 l_2 l_3] & 0 & 0 \\ 0 & [l_1 l_2 l_3] & 0 \\ 0 & 0 & [l_1 l_2 l_3] \end{pmatrix}$
Δx^{LES}	3D large scale cell size. $[m]$
Δx_k^{LES}	3D large scale cell size in x_k-direction. $[m]$
Δx^{RSS}	*RSS* cell size. $[m]$
$*$	element-wise Hademard multiplication
δ_{ij}	Kronecker delta. $\delta_{ij} = \begin{cases} 1, \text{ if } i = j \\ 0, \text{ else} \end{cases}$
$\underline{\underline{1}}$	matrix of ones
∂_a	partial derivative with respect to a. $\partial_a = \frac{\partial}{\partial a}$
sgn	the sign function

DIACRITICS

a^{+}	wall coordinate
$\hat{a}$	directly resolved *XLES* property
$\check{a}$	resolved small scale *XLES* property
$\underline{\underline{a}}$	*XLES* matrix
$\overline{a}$	directly and indirectly resolved *XLES* property
$\widetilde{a}$	unresolved *XLES* property
$\underline{a}$	*XLES* vector

SUBSCRIPS AND SUPERSCRIPTS

a^{d}	discrete property
$a^{d;m,n,o}$	discrete property with index $\{m, n, o\}$ on a regular grid
a_{i}	vector index $i \in \{1, 2, 3\}$
a_{k}	*XLES* vector element $k \in \{1, 2, 3\}$
$a_{k,i}$	vector index i of *XLES* vector element k
a^{ODT}	*ODT* related property
a^{LES}	*LES* related property
a^{*}	various meanings indicated when occurring
a^{XLES}	*XLES* related property

Part I

THEORY

1

INTRODUCTION AND OVERVIEW

Motions of fluids are part of our everyday life, e. g. if a droplet of blue ink dribbles into a glass of water several physical phenomena effect the flow: Small filaments of ink develop and move (convection) through the water. Additionally the ink seems to fade out (diffuse) and vanishes after some time leaving a glass of very pale blue water. By stirring the fluid this effect is greatly accelerated due to turbulent mixing.

To describe and predict the effects of turbulence is essential to understand this turbulent mixing and more importantly phenomena with major technological and environmental impacts on human society and even human existence. Turbulence influenced the density and associated gravity variations that led to the formation of present-day galaxies, stars, and planets. Without turbulent mixing, planetary atmospheric phenomena such as clouds, storms, and precipitation essential for life on Earth would be unimaginably different. Turbulence in the ocean has innumerable effects on oceanic biota, starting with the commingling of phytoplankton with needed nutrients. Due to its broad influence and baffling complexity, progress in fundamental and practical understanding of turbulent mixing is exceptionally challenging, yet crucial for scientific advancement encompassing a wide class of problems in earth science, astrophysics, and engineering. For such problems, better understanding of turbulence interactions with buoyancy effects and chemical and thermodynamic processes is essential (adapted from [2]).

On a molecular level of fluid motions innumerable molecules are rapidly moving, interacting with each other and with the boundaries (surface of the glass in the example above). Fortunately these molecules are often locally in an equilibrium.

This allows to represent a wide range of molecular movements due to a fluid state (e. g. defined by the density (ρ), pressure (p), temperature (T), ...) and the actual transport of fluid parcels with the velocity in x_i-direction (u_i), $i = \{1, 2, 3\}$ within a continuum interpretation (see section 1.1). The non-dimensional Knudsen number ($Kn = \frac{\lambda}{L}$) corresponds to the ratio of the mean free path (λ) of the fluid molecules and the problem specific representative physical length scale (L). For $Kn \ll 1$, which is valid for all problems considered in this thesis, a continuum representation is accurate. Noteworthy exceptions are e. g. flights in high altitude and flows in micro-machineries. The size of this representative physical length scale (L) depends on the fluid properties and the boundary-and initial conditions (see e. g. [109] and [25] for details). The dynamic of such a continuous fluid is mathematically well described by partial differential equations (*PDE*s): E. g. the compressible Navier-Stokes equations represent the conservation of density (ρ), momentum density (ρu_i) and energy density (ρE), but analytic solutions cannot be derived for real life applications e. g. with complex boundary conditions. For a turbulent flow, even in a very simple domain, a numerical approximation of these *PDE*s is indispensable. Due to growing computational power, an increasing number of scientific and industrial problems are amenable to computer simulations, not least in the field of computational fluid dynamics (*CFD*).

In a direct numerical simulation (*DNS*) all temporal and spatial scales occurring within a flow are numerically represented (see section 2). Thus impacts of numerical errors and simplifying model assumptions are not influencing the investigated physics. *DNS* is limited to moderate turbulent Reynolds numbers (Re_t) and Rayleigh numbers (Ra) due to the high computational effort and thus mostly used in fundamental turbulence research. E. g. many real-world flows have friction Reynolds numbers $\mathrm{Re}_\tau \gtrsim 10^6$ (following [94]), but until now the most turbulent wall-bounded *DNS* (by Lee and Moser [62]) describes a flow with $\mathrm{Re}_\tau \approx 5200$. Note that due to $\mathrm{Kn} \sim \frac{1}{\mathrm{Re}_t}$ even highly turbulent regimes are well described by a continuous fluid.

A wide range of techniques are developed to decrease the computational effort of numerical simulations. The techniques can be separated into numerical techniques (including high-order approximations, adaptive mesh-refinement, multi-grid methods) and model based approaches, e. g. reduced chemical mechanisms and of course turbulence models, see section 3. Realistic turbulent problems, e.g. in engineering and meteorology, require the application of these turbulence models to reduce the computational effort.

The concept of all turbulent models considered here is to decrease the problem size (number of degrees of freedom (*#DoFs*)) by exploiting properties of the investigated turbulent problems. This includes e. g. eddy viscosity assumptions, self-similarity assumptions of turbulent scales, and case specific domain symmetries.

Thus turbulence models can be classified into models exploiting:

1. Self-similarity properties and eddy viscosity:

   Most turbulence models, e. g. Reynolds averaged Navier-Stokes (*RaNS*) and large eddy simulation (*LES*), assume an eddy viscosity or take advantage from self-similarity properties of turbulent scales. Hereby the *#DoFs* (and therefore the computational effort) is reduced mostly by affecting the representation of small scale effects, e. g. small turbulent scales.

   RaNS describes the dynamics of time-averaged fields while the influence of fluctuating terms is modeled (see section 3.1). On the one hand highly turbulent flows (e.g. $\mathrm{Re}_\tau \gtrsim 10^6$) corresponding to realistic flows are computationally feasible. On the other hand *RaNS* generally is not useful for computing time-accurate flow statistics and small scale effects. Unsteady Reynolds averaged Navier-Stokes (*URaNS*) models allow to describe problems which are unsteady on a timescale widely independent of turbulent timescales.

   LES is increasingly used for industrial applied and fundamental turbulent flows in recent years. In *LES* spatially filtered equations are numerically solved while the unresolved sub-grid scale (SGS) terms are modeled to close the equations, e.g. by an eddy viscosity sub-grid model (*SGM*) (see section 3.2). Even in very fundamental turbulent flows *LES* resolves a wide range of scales including at least some portion of the inertial range of the turbulent cascade. On the one hand this limits the achievable Reynolds numbers relative to the achievable Reynolds numbers in *RaNS* simulations. On the other hand the higher level of description allows to apply *LES*, e. g. to aeroacoustics and unsteady turbulent problems.

The parameterization of a certain range of small scales in *RaNS* and *LES* can cause problems especially in multi-physics regimes such as buoyant entrainment phenomena (e. g. investigated by Dietze et al. [22]) and reacting flows because much of the complexity is relegated to the unresolved small scales. In these cases *LES* modeling might include statistical models, e. g. probability density function (*PDF*) methods, to increase the level of representation.

RaNS-LES hybrid schemes, especially to mention the detached eddy simulations (*DES*) (see [97]) try to balance the strengths and weaknesses of *URaNS* (see section 3.1) and *LES*.

2. Domain symmetry properties:

   1D model approaches e.g. the linear-eddy model (*LEM*) (see [74]) and the one-dimensional turbulence (*ODT*) model (see section 3.3) reduce the *#DoFs* by describing the 3D turbulence within a 1D sub-domain. These models appropriately describe the full turbulent cascade and can reproduce self-similarity properties of the turbulent scales, but they are limited to problems with one characteristic and predominant direction. Such a regime is valid inter alia in important problems within the research fields of fundamental combustion, atmospheric science, and fundamental turbulence research. Thereby the numerical representation of molecular diffusive effects and various other small scale effects become computationally feasible also in highly turbulent flows. E. g. Meiselbach [71] recently described wall bounded flows with $\mathrm{Re}_\tau \leqslant 6 \times 10^5$ using adaptive *ODT* (*aODT*) (by Lignell et al. [67]), which is clearly in the range of real-world applications, but limited to cases that are reasonable within a 1D sub-domain.

3. Combination of 1. and 2.

   There are several approaches combining 1D models with a *LES*-related concept to describe turbulent flows including small scale effects in a 3D computation, e.g. LES-ODT (e.g. by [10]), LES-LEM (by [74]), LEM3D (e.g. by [86]), and the *ODTLES* model introduced by Schmidt et al. [89].

   In [2] an extended *LES* (*XLES*) approach (see section 3.4) is introduced leading to 2D filtered equations especially tailored to be closed by 1D models and concurrently preserving consistent large scale properties. *ODTLES* can be interpreted as an *ODT* closed *XLES* approach (see section

3.5). Thus *ODTLES* is one special approach in the *XLES* family of models.

Hereby *ODTLES* benefits from the ability of *ODT* to computationally feasibly represent the full turbulent spectrum of highly turbulent flows. Thus the 3D resolution is not required to resolve a certain portion of the turbulent spectrum (like in *LES*) and therefore is mainly independent of the turbulence intensity. Nevertheless a 3D representation of non-turbulent effects not captured by *ODT* is required, e. g. inherent secondary instabilities as shown for the flow through a square duct in section 4.2.

An equivalent interpretation with identical consequences is that the 1D approach closing the *XLES* equations only requires local symmetry properties which ideally corresponds to the *XLES* 3D resolution.

An as yet unrealized *XLES* model implementation is called *aODT* closed *XLES* (*aODTLES*). *aODTLES* potentially reaches the computational costs of *RaNS* simulations for highly turbulent flows, e. g. over a flat-plate airfoil, as estimated in section 3.5.7.

Additionally an ensemble mean closure (EMC) called *SGM* can be applied, if the *ODT-SGM* within *ODTLES* is not fully resolved (investigated by McDermott [69] and introduced into *ODTLES* by Schmidt et al. [89]). This leads to a three-tiered multi-scale model with *ODT* closing unresolved 3D terms and EMC representing unresolved *ODT* scales. In this thesis an EMC model is not used.

Of course the classification above does not claim to be complete, but illustrates conceptual differences and similarities between individual models.

Related model concepts are the superparameterizations known from meteorology and climatology (see e. g. [34], [46]): E. g. in Cloud Resolving Convection Parameterizations (*CRCP*) a 2D simulation describes the cloud dynamics within a 3D cell of a global circulation model (*GCM*). This *CRCP* model can be interpreted to some extent by a 1D filtered *XLES* approach. These 1D filtered *XLES* equations are not further investigated in this thesis.

Another model concept not further addressed in this thesis is the class of *PDF* models, which describes turbulence properties using a time-dependent probability density function (*PDF*). For an overview we refer to [82].

In table 1 turbulent flows are classified by their turbulence intensity, the complexity of the computational domain, and the ability of the approach to resolve physical small scale effects, including e. g. chemical reactions and scalar properties.

ODTLES is a promising alternative to *RaNS* and *LES* for moderate turbulent Reynolds number flows in domains of moderate complexity, especially for multi-physics problems with inherent small-scale effects. Future implementation might close the *XLES* equations using *aODT*. This *aODTLES* model poten-

Table 1: Suitability of turbulence models in characteristic turbulent flow regimes, classified by the turbulent intensity and the domain complexity. Additionally the superscript * indicates that small scale effects are numerically represented. The expression (a)ODT ((a)ODTLES) encompasses *ODT* and *aODT* (*ODTLES* and *aODTLES*). Here *RaNS* also includes *RaNS*-*LES*-hybrid models.

	simple domain	moderate domain	complex domain
low Re_t	DNS* RaNS LES (a)ODT* (a)ODTLES*	DNS* RaNS LES (a)ODTLES*	DNS* RaNS LES
moderate Re_t	RaNS LES (a)ODT* (a)ODTLES*	RaNS LES (a)ODTLES*	RaNS LES
high Re_t	RaNS aODT* aODTLES*	RaNS aODTLES*	RaNS

tially increases the achievable turbulent Reynolds number significantly without loosing the ability to accurately represent small scale effects.

E. g. the flow around a flying airplane is clearly within the regime of complex domains with high turbulent Reynolds numbers and *RaNS* models (and increasingly *RaNS*-*LES*-hybrid models) are currently applied. To increase the level of description table 1 suggests two model candidates: the turbulent Reynolds number achievable by *LES* can be increased due to progress in modeling and computational resources (Spalart [95] predicts *LES* to be applicable to an airplane in the year 2045), and *aODTLES* can be developed and extended to more complex domains. Thus *aODTLES* can become a worthwhile field of research opening perspectives in computational engineering including highly turbulent flows.

In this work fundamental studies of highly turbulent flows in simple domains are investigated: In chapter 4 shear driven flows through channels and ducts and in chapter 5 buoyancy driven flows are shown. All computed results are in good agreement with existing *DNS* and furthermore *ODTLES* is able to exceed the turbulence intensities achievable by *DNS*.

Some ideas and figures have appeared previously in the author's publications [1, 2, 3], as indicated within the corresponding sections.

In this work we distinguish between the expressions *XLES* to describe the *XLES* approach including an approximation or model for arising microscale terms, *ODTLES* if these terms are in particular described by *ODT* and unclosed *XLES* (*XLES-U*), if microscale terms are neglected.

If not mentioned otherwise the term *XLES* corresponds to the 2D filtered *XLES* approach.

Note that in this work no Einstein summation convention is used.

1.1 CONTINUUM MECHANICS

The compressible Navier-Stokes equations describe flow dynamics using conservation laws (for ρ, ρu_i, ρE). In a (sufficiently smooth) continuum these dynamic variables are well defined and their derivatives are available in each point in space.

Additional assumptions about the inner structure of the fluid are necessary to close the equations: In this thesis an ideal gas (equation of state) and a Newtonian fluid (linear relation between viscous stresses and local strain rate) is presumed (see [109]).

Within these compressible Navier-Stokes equations, non-dimensional numbers correspond to characteristic physical regimes. E. g. the Mach number ($Ma = \frac{u}{c}$) defines the ratio of the velocity (u) to the local speed of sound (c). Note that due to $Kn \sim Ma$ flows with very high Mach number disobey continuity properties and methods of rarefied gas dynamics are required (see e. g. [41]). In this thesis the low-Mach number regime is presumed, which means that acoustic waves have a negligible effect.

Klein [55, 56, 57] introduces an asymptotic analysis of the compressible Navier-Stokes equations amongst others leading to low-mach number flow regimes described by e. g. the Oberbeck-Boussinesq equations for buoyant flows without background stratification. The Oberbeck-Boussinesq approximation, widely used in buoyant engineering problems and fundamental geophysical research, is valid if variations in the density are much smaller than the density itself. By decomposing the density into $\rho = \rho_0 + \rho'$ with a constant mean density (ρ_0) and a density variation (ρ'), the Oberbeck-Boussinesq approximation states $\rho' \ll \rho_0$.

The conservation of mass (Eq. (1)) and momentum (Eq. (2)) are enriched by a equation for a scalar field $\theta = \frac{\rho'}{\rho_0}$ (Eq. (3)):

$$0 = \sum_{j=1}^{3} \partial_{x_j} u_j \tag{1}$$

$$0 = \frac{1}{\rho_0}\partial_{x_i} p + \left[\partial_t - \nu \sum_{j=1}^{3} \partial_{x_j}^2\right] u_i + \sum_{j=1}^{3} \partial_{x_j} u_j \cdot u_i - g_2\theta + F_i \tag{2}$$

$$0 = \left[\partial_t - \kappa \sum_{j=1}^{3} \partial_{x_j}^2\right] \theta + \sum_{j=1}^{3} \partial_{x_j} u_j \cdot \theta \tag{3}$$

with the kinematic viscosity (ν), the thermal diffusivity (κ), the pressure (p), a possible specific external forcing in Cartesian x_i-direction (F_i), and the gravity acceleration in the x_2-direction (g_2) influencing the vertical velocity u_2. Only small temperature differences occur on the Oberbeck-Boussinesq approximation, which leads to an alternative scalar interpretation $\theta = \frac{\rho'}{\rho_0} = \alpha(T - T_0)$ with the mean temperature (T_0) and the coefficient of volume expansion (α). For simplicity we assume in this thesis a constant ν, κ, and the constant mean density (ρ_0) to be $1\frac{kg}{m^3}$. The velocity in x_i-direction (u_i) and the scalar field (θ) are summarized by the solution field $\phi_i = \{u_i, \theta\}$.

In a non-dimensional form, Eq. (2) includes the non-dimensional turbulent Reynolds number ($Re_t = \frac{u' L_t}{\nu}$) which describes the ratio of advective and diffusive effects and corresponds to a turbulent intensity. Hereby a representative turbulent length scale (L_t) and a characteristic velocity (u) are necessary. In a turbulent flow the smallest length scale is estimated by the Kolmogorov length scale $\eta_K = \frac{\nu^3 L_t}{u^3} \sim \frac{L_t}{Re_t^{3/4}}$. There are other non-dimensional numbers, e. g. the Prandtl number ($Pr = \frac{\nu}{\kappa}$), which corresponds to another small length scale (the Batchelor length scale). Also chemical processes, e. g. in atmospheric flows or in combustors lead to important small scale effects (not described by Eqs. 1–3). In buoyancy driven flows the Rayleigh number ($Ra = \frac{g(\Delta\theta)}{\nu\kappa} L^3$) describes the ratio of buoyant and molecular-transport effects. Hereby a representative physical length scale (L) and a characteristic temperature difference ($\Delta\theta$) are necessary. In a *DNS* all these physical effects are numerically represented.

The Eqs. 1–3 are applied to a Rayleigh-Bénard convection in chapter 5 to demonstrate the *ODTLES* ability to describe buoyancy driven flows.

In chapter 4 shear driven turbulent problems are investigated. In the considered cases the gravitational forcing plays a subordinated role and therefore is neglected. Nevertheless the scalar field (θ) can be interpreted as a passive scalar as realized in *ODTLES* results presented in [1]. In this thesis shear driven turbulent flows are computed by solving the so called incompressible Navier-Stokes equations (conservation of mass in Eq. (4) and momentum in Eq. (5)):

$$0 = \sum_{j=1}^{3} \partial_{x_j} u_j \tag{4}$$

$$0 = \partial_{x_i} p + \left[\partial_t - \nu \sum_{j=1}^{3} \partial_{x_j}^2 \right] u_i + \sum_{j=1}^{3} \partial_{x_j} u_j \cdot u_i + F_i. \tag{5}$$

These equations are another (more simplified) asymptotic limit of the compressible Navier-Stokes equations (cf. [54]):

2

NUMERICAL METHODS

There is a wide range of numerical methods appropriate to describe incompressible flows, e. g. finite difference methods (*FDM*), finite volume methods (*FVM*), and finite element methods (*FEM*).

Historically *FDM* (see e. g. [37]) is the oldest numerical method to solve *PDE*s and still successfully used e. g. in state of the art *DNS* solvers (see e. g. [73]).

FEM (see e. g. [114]) is suitable for elliptic and parabolic problems and especially applied to solid body problems but also used in further engineering areas. Many commercial flow and multi-physics solvers are based on *FEM* (e. g. ANSYS® CFX®[1], COMSOL Multiphysics®).

The *FVM* (see e. g. [104]) is very successfully applied to hyperbolic problems, e. g. to describe convective transport problems in compressible and incompressible flows. A number of commercial and non-commercial flow solvers are based on *FVM*, e. g. STAR-CD®, ANSYS® Fluent®, and OPENFOAM®[2].

More recent developments lead to discontinuous Galerkin methods (*DGM*) suitable to solve hyperbolic, elliptic, and parabolic problems. These are applied in the fields of gas dynamics, acoustics, in plasma physics and so on (see e. g. [39]).

The present *ODTLES* implementation uses ideas of *FVM* and *FDM*. The mathematical ansatz of *FEM* and *DGM* allows an alternative and equivalent interpretation of the *XLES* approach, as introduced in appendix A.3.

In the following, variables (e.g. the velocities u_i) and operators are assumed to be continuous. Discretized variables are marked with the superscript d (e.g. the discrete velocity: u_i^d).

2.1 IMPLEMENTED NUMERICAL METHODS

To solve the conservation equations (1) – (3) the derivation operators ∂_{x_i}, $\partial^2_{x_i}$, and ∂_t have to be numerically approximated.

This thesis focuses on turbulence modeling and thus easy to implement and well known numerical schemes are applied. These schemes have to be stable and numerical properties like dissipation or dispersion should not strongly affect the underlying physics to allow a deeper investigation of the turbulence modeling approach (introduced in section 3.4) and its apparent influence on the physics (investigated in chapters 4 and 5).

The full computational domain (Ω) is discretely approximated by computational grid cells. In this thesis only structured (regular) grids are used. In one computational grid cell, the discrete velocity values u_i are face-centered, while the pressure (p) and the scalar field (θ) are cell centered, which is called a staggered grid. Especially the treatment of the mass conservation equation Eq. (1) and the related pressure gradient $\partial_{x_i} p$ within the momentum equation Eq. (2) is more straightforward on a structured grid (see e. g. [24]).

---

[1] CFX is a trademark of Sony Corporation in Japan

[2] released free and open source to the general public

In section 2.1.1 the implemented spatial numerical approximations of the individual conservation terms are introduced. Section 2.1.2 introduces the implemented time discretizations. The individual combinations of the chosen spatial and temporal schemes lead to a numerical approximation with the required numerical properties. The *XLES* approach requires several terms to be spatially approximated by different resolutions simultaneously (see section 3.4.2.2) and thus leads to coupled numerical schemes investigated in sections 3.6.2 and 3.6.3.

2.1.1 *Spatial Schemes*

The numerical schemes applied in the current *ODTLES* implementation are briefly introduced. For an overview of existing numerical discretizations we refer to textbooks (e. g. [24]).

The *ODTLES* implementation introduced in this thesis uses a spatial second order central difference method (*CDM*). As shown in section 3.6.2 a *CDM* potentially leads to a dissipation free advection scheme with low dispersive behavior. Thus the *CDM* is also used in recent *DNS* simulations (see e. g. [78]). Rai and Moin [83] showed that a second-order *FDM* in a *DNS* leads to accurate low-order statistics, while high order statistics require high-order approximations.

For stability and accuracy reasons a *CDM* can require a high order time discretization (see section 2.1.2).

Spatial *FDM* are derived from a Taylor series

$$\phi(x) = \sum_{n=0}^{\infty} \frac{\partial_x^n \phi(a)}{n!} \approx \phi(a) + \partial_x \phi(a)(x-a) + \frac{1}{2}\partial_x^2 \phi(a)(x-a)^2 \tag{6}$$

here aborted after the second order term. Eq. (6) contains the first and second order derivatives $\partial_x \phi(a)$ and $\partial_x^2 \phi(a)$ at a specific point a.

2.1.1.1 *First Order Derivative*

From the Taylor series in Eq. (6) we find the *CDM* approximation of first order derivatives on a regular grid in 1D:

$$\partial_x \phi(x) \approx \left[\phi\left(x + \frac{\Delta x}{2}\right) - \phi\left(x - \frac{\Delta x}{2}\right)\right] / \Delta x. \tag{7}$$

For a staggered grid interpolations are required, especially for the nonlinear advection terms, as summarized in table 2 for the advecting velocity (advected property) A (B).

Table 2: *CDM* first order derivatives approximated on a staggered grid include linear interpolations. By applying a regular grid the computational cells are numbered by the integers $\{m, n, o\}$ corresponding to $\{x_1, x_2, x_3\}$-directions. Here A (B) corresponds to the advecting velocity (advected property). $(AB)\left(x_n + \frac{\Delta x}{2}\right)$ and $(AB)\left(x_n - \frac{\Delta x}{2}\right)$ can be interpreted as fluxes within a *FVM*. The scalar advection term (first row) is illustrated in figure 1. All terms are shown *w.l.o.g.* for $j = 2$ (corresponding to the x_2-direction). According to Eq. (7) all discrete terms are divided by Δx_2 (neglected here for clarity reasons).

CDM: $\partial_{x_2}(AB)(x)$	$(AB)\left(x_n + \frac{\Delta x}{2}\right)$	$(AB)\left(x_n - \frac{\Delta x}{2}\right)$
$A = u_2^d\,(x_n)$ $B = \theta^d\,(x_n)$	$A = u_2^{d;m,n,o}$ $B \approx \frac{1}{2}\left(\theta^{d;m,n+1,o} + \theta^{d;m,n,o}\right)$	$A = u_2^{d;m,n-1,o}$ $B \approx \frac{1}{2}\left(\theta^{d;m,n,o} + \theta^{d;m,n-1,o}\right)$
$A = u_2^d\,(x_n)$ $B = u_1^d\,(x_n)$	$A \approx \frac{1}{2}\left(u_2^{d;m+1,n,o} + u_2^{d;m,n,o}\right)$ $B \approx \frac{1}{2}\left(u_1^{d;m,n+1,o} + u_1^{d;m,n,o}\right)$	$A \approx \frac{1}{2}\left(u_2^{d;m+1,n,o} + u_2^{d;m,n,o}\right)$ $B \approx \frac{1}{2}\left(u_1^{d;m,n,o} + u_1^{d;m,n-1,o}\right)$
$A = u_2^d\,(x_n)$ $B = u_3^d\,(x_n)$	$A \approx \frac{1}{2}\left(u_2^{d;m,n,o+1} + u_2^{d;m,n,o}\right)$ $B \approx \frac{1}{2}\left(u_3^{d;m,n+1,o} + u_3^{d;m,n,o}\right)$	$A \approx \frac{1}{2}\left(u_2^{d;m,n,o+1} + u_2^{d;m,n,o}\right)$ $B \approx \frac{1}{2}\left(u_3^{d;m,n,o} + u_3^{d;m,n-1,o}\right)$
$A = u_2^d\,(x_n)$ $B = u_2^d\,(x_n)$	$A \approx \frac{1}{2}\left(u_2^{d;m,n+1,o} + u_2^{d;m,n,o}\right)$ $B \approx \frac{1}{2}\left(u_2^{d;m,n+1,o} + u_2^{d;m,n,o}\right)$	$A \approx \frac{1}{2}\left(u_2^{d;m,n,o} + u_2^{d;m,n-1,o}\right)$ $B \approx \frac{1}{2}\left(u_2^{d;m,n,o} + u_2^{d;m,n-1,o}\right)$

Within table 2 the terms $\partial_{x_2}(AB)(x_n - \frac{\Delta x}{2})$ and $\partial_{x_2}(AB)(x_n + \frac{\Delta x}{2})$ can be interpreted as fluxes within a *FVM*. Thus the *XLES* implementation introduced within section 3.4 can be interpreted as a *FVM* on several coupled staggered grids. The *CDM* is also applied to derive the pressure gradient (not shown in table 2), e. g. $\partial_{x_2} p \left(x_n + \dfrac{\Delta x}{2}\right) \approx \dfrac{p^{d;m,n+1,o} - p^{d;m,n,o}}{\Delta x}$.

2.1.1.2 *Second Order Derivative*

From the Taylor series in Eq. (6) we find the *CDM* for a spatial second order derivative on a 1D regular grid:

$$\partial_x^2 \phi(x) \approx \frac{\phi\,(x + \Delta x) - 2\phi\,(x) + \phi\,(x - \Delta x)}{(\Delta x)^2} \tag{8}$$

which is for a discrete property $\phi^d = \{u_i^d, \theta^d\}$ *w.l.o.g.* in x_2-direction

$$\partial_x^2 \phi \approx \frac{\phi^{d;m,n+1,o} - 2\phi^{d;m,n,o} + \phi^{d;m,n-1,o}}{(\Delta x)^2} \tag{9}$$

as illustrated in figure 1.

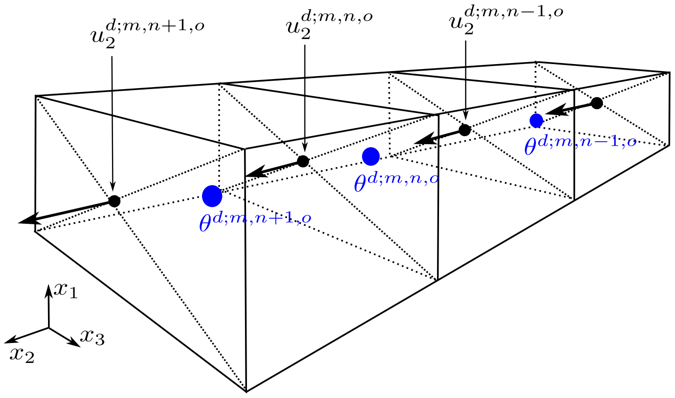

Figure 1: Regular, staggered grid illustration with cell centered discrete scalar values θ^d and pressure (p) and face centered discrete velocities *w.l.o.g.* in x_2-direction u_2^d. An additional index indicates an integer counter n through the grid in x_2-direction with $1 \leqslant n \leqslant N_2$. The computational domain (Ω) is represented by N_2 discrete cells in x_2-direction.

2.1.1.3 *Boundary Conditions*

To treat boundary conditions for the staggered grid in figure 1 the Taylor series in Eq. (6) with derivatives at the first cell $a = x_1$ leads to the discrete approximation $\partial_x \phi^{d;m,1,o}$ and $\partial_x^2 \phi^{d;m,1,o}$. To eliminate one unknown derivative from Eq. (6) two conditions have to be fulfilled (indexes $\{m, o\}$ are skipped):

- Here we are using a Dirichlet boundary condition

$$\phi(x_1 - \frac{1}{2}\Delta x) = \phi^{d;0} = \phi^{d;1} + \partial_x \phi^{d;1} \left(-\frac{1}{2}\Delta x\right) + \frac{1}{2}\partial_x^2 \phi^{d;1} \left(-\frac{1}{2}\Delta x\right)^2 \tag{10}$$

- and a condition for the second cell $\phi(x_2) = \phi^{d;2}$

$$\phi(x_1 + \Delta x) = \phi^{d;2} = \phi^{d;1} + \partial_x \phi^{d;1}(\Delta x) + \frac{1}{2}\partial_x^2 \phi^{d;1} (\Delta x)^2 \tag{11}$$

For the first order derivative the Dirichlet boundary condition determines the corresponding flux, while the second flux stays unchanged.

For the second order derivative at the first cell we find the ansatz $2\phi(x_1 - \frac{1}{2}\Delta x) + \phi(x_1 + \Delta x)$ solves the system of Eqs. (10) and (11), leading to

$$\partial_x^2 \phi^{d;1} = \frac{-4\phi^{d;1} + 4/3\phi^{d;2} + 8/3\phi^{d;0}}{\Delta x^2}. \tag{12}$$

The equivalent derivations for the last cell $a = x_N$ are skipped here.

2.1.2 *Time Schemes*

The transport equation

$$0 = \partial_t \phi + f(\phi) \tag{13}$$

has to be integrated in time from timestep n (at t_n) to timestep $n+1$ (at t_{n+1}):

$$0 = \int_{t_n}^{t_{n+1}} \partial_t \phi \, dt + \int_{t_n}^{t_{n+1}} f(\phi) \, dt = \phi(t_{n+1}) - \phi(t_n) + \int_{t_n}^{t_{n+1}} f(\phi) \, dt. \tag{14}$$

The function $f(\phi)$ is approximated by one of the spatial discretizations introduced in section 2.1.1.

The approximation $\int_{t_n}^{t_{n+1}} f(\phi) \, dt \approx f(\phi(t_n))\Delta t$ leads to the first order forward Euler scheme (*EE1*):

$$\phi(t_{n+1}) = \phi(t_n) + \Delta t \, f(\phi(t_n)) \tag{15}$$

with the time step size Δt. The time step size of explicit schemes is restricted by a (global) Courant-Friedrichs-Lewy condition, e. g. for the advective terms:

$$\Delta t \leqslant \mathrm{CFL} \min_{i,m,n,o} \left(\frac{\Delta x_i^{d;m,n,o}}{u_i^{d;m,n,o}} \right) \tag{16}$$

with the spatial cell size in x_i-direction Δx_i and a Courant-Friedrichs-Lewy number (*CFL*-number), which is a constant for each specific numerical time scheme (see e. g. [104]).

In local time stepping schemes the time step size is restricted locally, e. g. for each individual computational cell (see e. g. [30]). The additional level of approximation and implementation effort is justified especially for very inhomogeneous spatial resolutions within (oftentimes unstructured) grids.

Using the approximation $\int_{t_n}^{t_{n+1}} f(\phi) \, dt \approx f(\phi(t_{n+1}))\Delta t$ leads to the first order backward Euler scheme (*IE1*):

$$\phi(t_{n+1}) = \phi(t_n) + \Delta t f(\phi(t_{n+1})) \tag{17}$$

which is implicit and stable without any time step restriction. This time scheme requires the solution of a system of linear equations.

The 2nd order Crank-Nicolson scheme (*CN*) is in between the *EE1* and *IE1* using the approximation $\int_{t_n}^{t_{n+1}} f(\phi) \, dt \approx \frac{1}{2}(f(\phi(t_n)) + f(\phi(t_{n+1})))\Delta t$ leading to

$$\phi(t_{n+1}) = \phi(t_n) + \Delta t \frac{1}{2} \left(f(\phi(t_n)) + f(\phi(t_{n+1})) \right) \tag{18}$$

Table 3: Coefficients for *RK3* by Spiteri and Ruuth [98] are required to solve Eq. (19).

N_s	α_{ls}	β_{ls}
3	1 $\frac{3}{4}\ \ \frac{1}{4}$ $\frac{1}{3}\ \ 0\ \ \frac{2}{3}$	1 $0\ \ \frac{1}{4}$ $0\ \ 0\ \ \frac{2}{3}$

and also requires a system of equations solver. For both the *IE1* and the *CN* with a spatial *CDM* the system of equation can be written as a tridiagonal matrix which is efficiently solved by the Thomas algorithm (see e. g. [72]).

Higher order approximations of the integral $\int_{t_n}^{t_{n+1}} f(\phi)\,dt$ are given e. g. by Runge-Kutta schemes (see e. g. [98]).

In this thesis next to the *CN*, a 3 stage 3rd order *TVD* Runge-Kutta scheme (*RK3*) is used for advection terms. For details on *XLES* specific time integration, see sections 3.6.2 and 3.6.3.

Most explicit Runge-Kutta schemes can be written as a recursive multi-stage approach with $N_s l + 1$ number of Runge-Kutta stages:

$$\int_{t_n}^{t_{n+1}} f(\phi)\,dt \approx \sum_{s=0}^{i-1} \left(\alpha_{ls}\phi(t'_s) + \beta_{ls}\Delta t f(\phi(t'_s))\right) \text{ with } i = 1, \dots, l+1 \qquad (19)$$

with $t'_0 = t_n$ and $t'_{l+1} = t_{n+1}$. Numerous Runge-Kutta schemes are possible, where e. g. the representation order, the memory requirements, and possible *CFL*-numbers restrictions depend on the coefficients α_{ls} and β_{ls}, and N_s.

In this thesis a 3 stage 3rd order *TVD* Runge-Kutta scheme (*RK3*) by Spiteri and Ruuth [98] with the coefficients α_{ls} and β_{ls} in table 3 is used.

2.1.2.1 *1D Advection Schemes*

The 3D advection scheme in the current *XLES* implementation is connected to *XLES* and *ODT* specific modeling ideas and thus investigated in detail in section 3.4. Even the 1D advection scheme contains coupled numerical schemes (investigated e. g. in section 3.6.2), which are briefly investigated here.

The *XLES* specific 2D filtering leads to highly resolved and coarsely resolved properties, which are treated numerically differently:

- Highly resolved properties are discretized using a standard 2nd order Crank-Nicolson scheme (*CN*) in time (see [19]). We will refer to this fully discrete scheme as *CN* scheme in time and spatial *CDM* (*CN-CDM*).
- The coarse grained resolved properties are discretized using a 3 stage 3rd order *TVD* Runge-Kutta scheme (*RK3*) (see [98]). We will refer to this fully discrete scheme as *RK3* scheme in time and spatial *CDM* (*RK3-CDM*).

The numerical properties of the (uncoupled) numerical schemes are:

- The advection scheme *CN-CDM* is stable, dissipation free and has low dispersion.
- The *RK3-CDM* scheme is found to be stable and produces little dispersion and dissipation.

These properties transfer to the coupled advection schemes, as demonstrated in sections 3.6.2 and 3.6.3.

2.1.3 *Poisson Problem*

The pressure gradient in Eq. (5) can be used to enforce mass conservation in Eq. (4), here shown for the incompressible Navier-Stokes equations. Therefore a predictor-corrector idea is often applied (see also section 3.5.5), where the predictor generates an interim velocity field u_i^* by solving

$$u_i^* = u_i(t_n) + \int_{t_n}^{t_{n+1}} \left(-\nu \sum_{j=1}^{3} \partial_{x_j}^2 u_i(t_n) + \sum_{j=1}^{3} \partial_{x_j} u_j(t_n) \cdot u_i(t_n) + F_i(t_n) \right) dt, \tag{20}$$

$$u_i(t_{n+1}) = u_i^* + \int_{t_n}^{t_{n+1}} \partial_{x_i} p \, dt. \tag{21}$$

where discrete approximations introduced in section 2.1.1 can be applied. The time integrals in Eqs. (20) and (21) can either be approximated by an *EE1* scheme or the full predictor-corrector cycle can easily be solved in each stage of an explicit Runge-Kutta scheme.

The interim velocity u_i^* is not necessarily divergence free (violating Eq. (4)), even if the velocity field $u_i(t_n)$ is divergence free.

Inserting Eq. (21) into the mass equation (4) and discretizing the time integral in Eq. (21) using e. g. an *EE1* scheme leads to a Poisson equation, an elliptic problem:

$$\frac{1}{\Delta t} \sum_{i=3}^{3} \partial_{x_i} u_i^* = - \sum_{i=3}^{3} \partial_{x_i} \partial_{x_i} p \tag{22}$$

where a discrete approximation of $\frac{1}{\Delta t} \sum_{i=3}^{3} \partial_{x_i} u_i^*$ is known from the predictor step (Eqs. (20)). Note that within the Laplace operator $\sum_{i=3}^{3} \partial_{x_i} \partial_{x_i}$ the partial derivatives ∂_{x_i} are coming both, from the momentum equation (4) and the mass equation (5), which should be considered for the discretization of this Laplace operator (see e. g. [24] for details).

The Poisson equation (22) can be solved using an iterative equation solver e. g. provided by the HYPRE library (e. g. [23]).

In the *ODTLES* implementation an algebraic multigrid method (*AMG*), provided by the HYPRE library, is applied.

3

TURBULENCE MODELING

Turbulence is a multi-scale process involving all scales from an integral length scale (e. g. the size of the domain) down to the Kolmogorov length scale (η_K). The most widely used turbulence models in *CFD* are based on eddy viscosity assumptions or self-similarity properties of the turbulent scales. In particular the governing equations are averaged in time (*RaNS*) or space (*LES*) to significantly decrease the computational effort compared to *DNS*. The influence of non-represented scales on the spatial or temporal averaged flow state needs to be modeled.

Physical small scale effects are not necessarily describable by viscosity or obeying self-similarity properties and thus are hard to describe within commonly applied models.

In consequence the resolved state misses small scale effects, which are frequently of importance, see e.g. in the whole area of reactive flows, flows with apparent Prandtl or Schmidt number effects, or even wall bounded flows.

Near-wall flows locally disobey eddy viscosity properties of turbulent scales and thus require an additional treatment in many *RaNS* and *LES* models either by highly resolved near-wall regions or wall-specific model assumptions.

Some ideas of *RaNS* and especially *LES* are used in the *XLES* derivation and thus these models are briefly introduced.

3.1 REYNOLDS AVERAGED NAVIER-STOKES EQUATIONS

Reynolds averaged Navier-Stokes equations describe the dynamic of mean flow variables. Therefore the governing incompressible Navier-Stokes equations (Eq. (4) and Eq. (5)) are averaged, indicated by $\langle \, \rangle$.

Additionally the corresponding scales of the flow variables are decomposed for modeling purpose into:

$$u_j = \langle u_j \rangle + u_j' \tag{23}$$

with the mean velocity field

$$\langle u_i \rangle = \lim_{\tau \to \infty} \frac{1}{\tau} \int_t^{t+\tau} u_i \, dt' \tag{24}$$

and the fluctuating terms $u_i' = u_i - \langle u_i \rangle$.

Note that the mean field in Eq. (23) is correctly defined as an integral over the velocity *PDF*, but following the ergodic hypothesis for a statistically stationary flow this mean can be replaced by the time integral in Eq. (24). An ensemble average is another approach estimating the mean for flows that can be replicated.

In unsteady Reynolds averaged Navier-Stokes (*URaNS*) equations all occurring turbulent time scales, which are required to define the mean fields in Eq. (24), are assumed to be finite and smaller than some time evolution of the mean field itself. This assumption has to be validated carefully for each individual problem and allows in principle time dependent *RaNS* simulations (see [95] and authors cited therein for details).

Using the identity

$$\left\langle u_i' \right\rangle = 0, \tag{25}$$

which is valid for time averaging (see [82]), the *RaNS* equations (here shown for the incompressible Navier-Stokes equations (4) and (5)) are:

$$0 = \sum_{j=1}^{3} \partial_{x_j} \langle u_i \rangle \tag{26}$$

$$0 = \partial_{x_i} \langle p \rangle + \left[\partial_t - \nu \sum_{j=1}^{3} \partial_{x_j}^2 \right] \langle u_i \rangle + \sum_{j=1}^{3} \partial_{x_j} \left\langle u_j \right\rangle \cdot \langle u_i \rangle + \langle F_i \rangle + \tau_{ij}^{\mathrm{RaNS}} \tag{27}$$

with the Reynolds stresses

$$\tau_{ij}^{\mathrm{RaNS}} = \partial_{x_j} \left\langle u_j' \cdot u_i' \right\rangle \tag{28}$$

which has to be modeled.

A wide range of *RaNS* models are known (see e. g. [112] and [82] for an overview) and can be classified into two categories:

1. Models based on an eddy viscosity hypothesis:

   The Reynolds stress terms $\tau_{ij}^{\mathrm{RaNS}}$ are described by a turbulent viscosity (ν_T):

   $$\left\langle u_j' \cdot u_i' \right\rangle - \frac{2}{3} k \delta_{ij} \approx -\nu_T \left(\partial_{x_j} \langle u_i \rangle + \partial_{x_i} \left\langle u_j \right\rangle \right) = -2\nu_T \left\langle S_{ij} \right\rangle \tag{29}$$

   with the mean rate-of strain tensor $\left\langle S_{ij} \right\rangle$, the Kronecker delta ($\delta_{ij}$) and the specific turbulent kinetic energy (k). The most simple models are algebraic models: The mixing-length model describes ν_T by a characteristic length scale $l^* = l_m$ and a characteristic velocity change $u^* = l_m |\partial_x \langle u \rangle|$ (using e. g. the wall-normal gradient of the mean velocity $|\partial_x \langle u \rangle|$. This characteristic velocity change is related to the specific turbulent kinetic energy by $k \sim (u^*)^2$. The resulting turbulent viscosity is:

   $$\nu_T = l^* u^* \approx (l_m)(l_m |\partial_x \langle u \rangle|) \tag{30}$$

   where the flow specific length scale l_m has to be prescribed and an effective viscosity can be defined $\nu_{eff} = \nu + \nu_T$. The mixing-length model is incomplete, because l_m need to be specified.

   The Spallart-Allmaras model (see [96]) solves a model transport equation for ν_T and is complete (independent of l_m), but requires 8 closure coefficients and 3 closure functions and is restricted mainly to aerodynamics.

The most frequently applied model is the $k-\epsilon$-model (see e. g. [44]).

The characteristic velocity is described by $u^* \sim k^{1/2}$. The turbulent dissipation (ϵ) behaves like $\epsilon \sim k^{3/2}/l_m$ which leads to a turbulent viscosity described by $\nu_T \sim \frac{k^2}{\epsilon}$. Two model transport equations for k and ϵ are solved, leading to a complete model which requires 5 model parameters (see e. g. [60] for details).

Further two equation models are e. g. described by Wilcox [112].

Eddy viscosity models require additional treatment in the near-wall region, e. g. damping functions, to improve the results.

2. Reynolds-stress models:

   Reynolds-stress models solve an model transport equation directly for τ_{ij}^{RaNS}, which requires a model description of dissipation effects, a pressure-rate of strain, and Reynolds-stress fluxes. There are simple algebraic models (not complete) and models using up to 7 additional model transport equations, which increases the computational effort by a factor of ≈ 2 compared to standard $k-\epsilon$-models. Contrary to eddy viscosity models, some Reynolds-stress models can e. g. describe the secondary flow in a duct.

3.2 LARGE EDDY SIMULATION

Early large eddy simulation was originally motivated by meteorological applications (e. g. [93]). Nowadays *LES* is still used for meteorological flows, but also applied to complex geometries occurring in engineering applications (see e. g. [28]).

In *LES* the governing equations (here shown for the incompressible Navier-Stokes equations (4) and (5)) are spatially filtered. Commonly applied 3D filter functions $[l_1 l_2 l_3]$ are usually defined as tensor products of 1D filter functions $[l_k]$ ($k = \{1, 2, 3\}$). Here an operator notation for the filter in x_k-direction is used.

If these operations are applied to continuous fields the filter corresponds to a convolution and the filtered field is continuous too.

Another concept, applied in this thesis, is the idea of implicit filtering, which is often presupposed in *LES*: The numerical grid (cf. figure 2b) with the large scale cell size Δx_k^{LES} implicitly defines the filter. Thus the implicit filtered fields are strongly connected to the discretization. Figure 2 shows illustrative discrete grids for *DNS* and *LES*. The effective filter length $[l_k^{eff}]$ depends mainly on the properties of the implemented numerical scheme:

$$[l_k^{eff}] = Q \Delta x_k^{LES} \tag{31}$$

with a numerical sub-filter parameter $Q = \mathcal{O}(1)$ depending on the numerical scheme which is investigated for *XLES* in section 4.1.3.

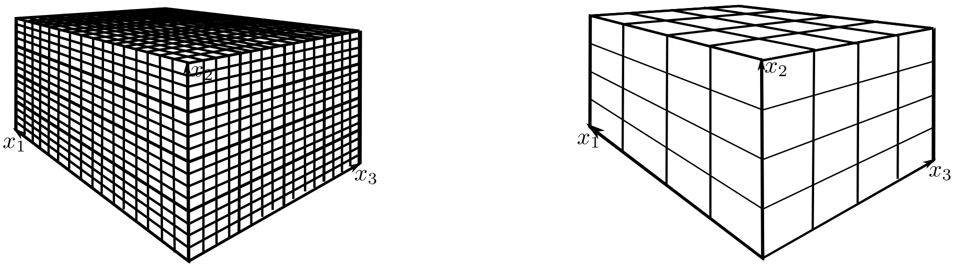

(a) *DNS* grid: $u_i^d \approx u_i$. (b) *LES* grid: $\overline{u}_i^{d,\text{LES}} \approx [l_1 l_2 l_3] u_i$.

Figure 2: In *DNS* all present spatial scales of the velocity field u_i are numerically represented by a discrete grid (illustrative with $N_{\text{DNS}} = 16$ cells per direction). In *LES* 3D filtered velocity fields $\overline{u}_i^{d,\text{LES}} = [l_1^d l_2^d l_3^d] u_i$ (l_k^d defined in Eq. (32)) are numerically represented (illustrated with $N_{\text{LES}} = 4$ cells per direction). The spatial *#DoFs* is decreased from 16^3 to 4^3 in this example.

The acronym LES is used to differentiate between standard *LES* properties and those defined in *XLES* in section 3.4.

Here a discrete 1D box filter

$$[l_k^d] u_i = \frac{1}{\Delta x_k^{\text{LES}}} \int_{-\frac{\Delta x_k^{\text{LES}}}{2}}^{\frac{\Delta x_k^{\text{LES}}}{2}} u_i \, dx_k' \tag{32}$$

is applied to the continuous velocity field and corresponds to the discrete *LES* grid.

Because of this box filter, the cell-averaged variables are used during the computation and a numerical interpretation in terms of the *FVM* is more intuitive as a point value based *FDM* for both the considered *LES* and introduced *XLES* schemes. The idea of implicit filtering and the consequences to a *FVM* are studied e. g. by Denaro [20].

In *LES* the filtered velocities correspond to the 3D large scale field $\overline{u}_i^{\text{LES}} = [l_1 l_2 l_3] u_i$ while the sub-grid scale (*SGS*) terms correspond to the small scale field $\widetilde{u}_i^{\text{LES}} = [\mathbb{1} - l_1 l_2 l_3] u_i$. Here $[l_k]$ can be interpreted as the effective implicit filter in Eq. (31). The numerical sub-filter parameter (Q) and the characteristic filter form is not required to derive the filtered equations, but influence the *SGM*.

Note that some *SGM*s require the simultaneous application of multiple 3D filtered fields with different filter sizes.

To derive the 3D filtered equation (to be simulated) and the sub-grid scale (*SGS*) terms (to be modeled) the spatial scales are separated for modeling purpose using these 1D filter operators:

$$u_i = [l_1 l_2 l_3 + (\mathbb{1} - l_1 l_2 l_3)] \, u_i = \overline{u}_i^{\text{LES}} + \widetilde{u}_i^{\text{LES}} \tag{33}$$

with the unity operator $[\mathbb{1}]$ and the resolved *LES* scales $\overline{u}_i^{\text{LES}}$ and unresolved *LES* scales $\widetilde{u}_i^{\text{LES}}$.

The 3D filtered *LES* equations are:

$$0 = \sum_{j=1}^{3} \partial_{x_j} \overline{u}_i^{\mathrm{LES}} \tag{34}$$

$$0 = \partial_{x_i} \overline{p}^{\mathrm{LES}} + \left[\partial_t - \nu \sum_{j=1}^{3} \partial_{x_j}^2 \right] \overline{u}_i^{\mathrm{LES}} + \sum_{j=1}^{3} \partial_{x_j} \overline{u}_j^{\mathrm{LES}} \cdot \overline{u}_i^{\mathrm{LES}} + \overline{F}_i^{\mathrm{LES}} + \tau_{ij}^{\mathrm{LES}} \tag{35}$$

with the residual stress tensor representing the *SGS* terms

$$\tau_{ij}^{\mathrm{LES}} = \partial_{x_j} \left(\overline{u_j \cdot u_i}^{\mathrm{LES}} - \overline{u}_j^{\mathrm{LES}} \cdot \overline{u}_i^{\mathrm{LES}} \right) \tag{36}$$

which describes the unresolved scales influencing the large scale field. In particular for homogeneous turbulence the turbulent small scales are acceptably represented by simple models, e. g. by eddy viscosity models. The Smagorinsky model was the first eddy viscosity based *LES* model introduced by Smagorinsky [93] (see also [68]).

The eddy viscosity assumption (cf. Eqs. (28) and (29)) is

$$\tau_{ij}^{\mathrm{LES}} = -2 \partial_{x_j} \nu_r \overline{S}_{ij}^{\mathrm{LES}} \tag{37}$$

with the filtered rate-of-strain

$$\overline{S}_{ij}^{\mathrm{LES}} = \frac{1}{2} \left(\partial_{x_j} \overline{u}_i^{\mathrm{LES}} + \partial_{x_i} \overline{u}_j^{\mathrm{LES}} \right) \tag{38}$$

and the residual viscosity (ν_r). For an incompressible Newtonian fluid the derivative of this strain rate is of a similar form as diffusion terms. Thus an effective viscosity $\nu + \nu_r$ can be applied. In analogy to the mixing-length hypothesis (see section 3.1) the residual viscosity is

$$\nu_r \sim l_m^2 \overline{S}_{ij}^{\mathrm{LES}} \quad \rightarrow \quad \nu_r = (C_S \Delta x)^2 \overline{S}_{ij}^{\mathrm{LES}} \tag{39}$$

with the filter length Δx. Here the filter length is assumed to match the grid size Δx^{LES}, corresponding to Q= 1. Nevertheless other Q-values can be used to shift the Smagorinsky constant (C_S). The filter length scale corresponds to a typical length scale (cf. Eq. (30)). In standard *LES* the filter length is within the inertial range of the turbulent cascade.

For every eddy viscosity model with $\nu_r > 0$ the energy transfer is from the filtered motions to the residual ones (no backscatter effect). This is only realistic for flows with a downward turbulent cascade. For homogeneous turbulence the turbulent cascade is downwards and the Smagorinsky constant $C_S \approx 17$ can be estimated for a sharp spectral filter (see e. g. [82],[68]). Unfortunately a Smagorinsky *LES* with constant C_S leads to wrong behavior for laminar flows occurring e. g. in the near-wall region of wall-bounded flows and the required *LES* resolution strongly depends on the local flow properties.

Several modifications were proposed to overcome this limitation: Moin and Kim [75] introduced a damping function leading to a non-constant C_S. Near-wall models have been introduced leading to wall-modeled *LES* (*LES-wm*) contrary to wall-resolved *LES* (*LES-wr*).

Additionally the standard Smagorinsky model is shown to be too dissipative in applications (following [111]). Therefore Germano et al. [32] proposed a dynamical Smagorinsky model using multiple 3D filter functions, which became a very successful *LES* model.

Each numerical scheme that approximates the *LES* equations leads to various numerical effects on the filtered field. To exploit this fact, e. g. the spatial-truncation errors can replace the eddy viscosity model and act like a *SGM*. This approach is called implicit *LES* (see e. g. [7]) and requires a profound understanding of the numerical properties and effects of the implemented schemes.

Note that contrary to *RaNS* an *LES* identity of the form $\overline{\overline{u}_i^{\mathrm{LES}}}^{\mathrm{LES}} = \overline{u}_i^{\mathrm{LES}}$ does not hold in general (cf. Eq. (25)).

Thus a more detailed investigation of small-scale effects requires a decomposition of the *SGS* terms (introduced by Leonard [64]):

$$\tau_{ij}^{\mathrm{LES}} = \mathcal{L}_{ij}^{3D} + \mathcal{C}_{ij}^{3D} + \mathcal{R}_{ij}^{3D} \tag{40}$$

with

- 3D Leonard stresses

  $$\mathcal{L}_{ij}^{3D} = \partial_{x_j}\left(\overline{\overline{u}_j^{\mathrm{LES}} \cdot \overline{u}_i^{\mathrm{LES}}}^{\mathrm{LES}} - \overline{u}_j^{\mathrm{LES}} \cdot \overline{u}_i^{\mathrm{LES}}\right) \tag{41}$$

  describe the influence of the 3D test-filter on the resolved advection terms.

- *LES* cross-stress terms

  $$\mathcal{C}_{ij}^{3D} = \partial_{x_j}\left(\overline{\overline{u}_j^{\mathrm{LES}} \cdot \tilde{u}_i^{\mathrm{LES}} + \tilde{u}_j^{\mathrm{LES}} \cdot \overline{u}_i^{\mathrm{LES}}}^{\mathrm{LES}}\right) \tag{42}$$

  describe the interaction of resolved and unresolved terms.

- 3D SGS Reynolds stresses

  $$\mathcal{R}_{ij}^{3D} = \partial_{x_j}\left(\overline{\tilde{u}_j^{\mathrm{LES}} \cdot \tilde{u}_i^{\mathrm{LES}}}^{\mathrm{LES}}\right) \tag{43}$$

  describe the interaction of unresolved terms.

Here the outer filter is often called test-filter revealing notational similarities to functional formulations (cf. appendix A.3). A more recent decomposition introduced by Germano [31] provides advantageous properties e. g. Galilean invariant individual stress terms, but in preparation for section 3.4 the decomposition by Leonard [64] is sufficient.

Jiménez and Moser [42] have shown that "the good a posteriori performance of dynamic Smagorinsky sub-grid models in *LES* [...] appears to be only weakly related to their ability to correctly represent the subgrid physics". Thus in multi-physics computations modeling of physical small-scale effects is especially hard and requires serious caution not least concerning any resolution decisions (see e. g. [21]).

3.3 ONE-DIMENSIONAL TURBULENCE (ODT)

Note that this section introduces *ODT* in a buoyant extension. Parts of this section are adapted from the incompressible Navier-Stokes interpretation of *ODT* introduced by the author in [3, section 2].

The *ODT* model describes the dynamics of a three dimensional turbulent flow within a one-dimensional sub-domain, including fully resolved molecular diffusion. Thus *ODT* exploits problem specific symmetry properties and is e. g. able to describe the turbulent channel flow including high order flow statistics with satisfactory accuracy (see section 4.1.2).

ODT stand-alone is able to compute meaningful results, even with one velocity component (see [50]). Nevertheless to capture anisotropic flow behavior and especially as a closure within a 3D approach, two or three velocity components are advantageous.

In wall-bounded flows (especially in turbulent channel flows) described by *ODT* with three velocity components, the wall-normal and the spanwise velocities are identical, so two-component *ODT* captures similar statistical flow properties. (Note that *ODT* results in section 4.1.2 are computed with 2 velocity components).

Here we introduce *ODT* including 2 velocity components. This *ODT* model is a modification of the *ODT* vector formulation by Kerstein et al. [53], which includes 3 velocity components. A corresponding *ODT* example code is available online (see [51]). Additionally the concept of a variable density formulation of *ODT* by Ashurst and Kerstein [6] is incorporated.

ODT emulates the time evolution of a turbulent fluid in a 1D sub-space, which is oriented in the Cartesian x_k-direction. The 2 *ODT* velocity components $u_{k,i} = u_i(x_k)$ (*w.l.o.g.* $u_{1,2}$ and $u_{1,3}$ for $k = 1$) are oriented orthogonally to the x_k-direction. The time evolution of a velocity field $u_{k,i} = u_i(x_k)$ (cf. Eq. (2)) and a scalar field $\theta_k = \theta(x_k)$ (cf. Eq. (3)) in this 1D sub-space is described by:

$$0 = \partial_t u_{k,i} + \mathcal{D}_{ODT_k}(u_{k,i}) + e_{u_{k,i}}(u_{k,j}, x_0, l) \text{ with } i,j,k = \{1,2,3\} \wedge i \neq k \wedge j \neq k \tag{44}$$

$$0 = \partial_t \theta_k + \mathcal{D}_{ODT_k}(\theta_k) + e_{\theta_k}(x_0, l) \tag{45}$$

with the *ODT* diffusion terms $\mathcal{D}_{\mathrm{ODT}_k}(u_{k,i}) = -\nu\partial^2_{x_k}u_{k,i}$ and $\mathcal{D}_{\mathrm{ODT}_k}(\theta_k) = -\kappa\partial^2_{x_k}\theta_k$ which are numerically approximated by *IE1* in time and a *CDM* in space (see sections 2.1.1 and 2.1.2). An example clarifies the index notation in Eq. (44): for *w.l.o.g.* $k = 1$ the velocities $u_{1,i}$ with $i = \{2,3\}$ are advanced, where *w.l.o.g.* for $i = 2$ the function $e_{u_{1,2}}(u_{1,j}, x_0, l)$ depends on the two velocity components $u_{1,j}$ with $j = \{2,3\}$. The index notation resembles the *XLES* index notation used in the following sections where the velocity $u_{k,i}$ is oriented in the x_i-direction within a grid representing *XLES* equations (*XLES-grid*) highly resolved in the x_k-direction ($i \neq k$).

The terms $e_{u_{k,i}}(u_{k,j}, x_0, l)$ respective $e_{\theta_k}(x_0, l)$ are instantaneous eddy functions affecting $u_{k,i}$ respective θ_k within the eddy range $x_k \in [x_0, x_0 + l]$. A maximum eddy size ($l_{\max}$) is enforced, hence $l \leqslant l_{\max}$. The eddy function $e_{\phi_{k,i}}$ (with the solution field $\phi_{k,i} = \{u_{k,i}, \theta_k\} = \{u_i(x_k), \theta(x_k)\}$) is introduced to represent a stochastic procedure that emulates turbulent advection:

$$e_{\phi_{k,i}} : \begin{pmatrix} u_i(x_k,t) \\ \theta(x_k,t) \end{pmatrix} \to \begin{pmatrix} u_i(f(x_k,x_0,l),t) + c_i(u_{k,j})K(x_k) \\ \theta_k(f(x_k,x_0,l),t) \end{pmatrix}. \tag{46}$$

Note that the advection function $e_{u_{k,i}}(u_{k,j}, x_0, l)$ depends on both velocity components $u_{k,j}$ (with $j \neq k$) due to c_i, defined in Eq. (48). The mapping function $f(x_k, x_0, l)$, representing fluid transport, is measure preserving (the non-local analog of vanishing velocity divergence), continuous, and satisfies the requirement of scale locality (at most order-unity changes in property gradients). These indispensable physical requirements for $f(x_k, x_0, l)$ are satisfied by a triplet map, which places three compressed copies of the original profile ($\{u_{k,i}(x_k), \theta_k(x_k)\}$, $x_k \in [x_0, x_0 + l]$) in the eddy range $x_0 < x_k < x_0 + l$. The middle copy is reversed to preserve continuity, as illustrated in figure 3. The triplet map $x_k \to f(x_k, x_0, l)$ is:

$$f(x_k,x_0,l) = x_0 + \begin{cases} 3(x_k - x_0), & \text{if } x_0 \leqslant x_k \leqslant x_0 + \frac{1}{3}l \\ 2l - 3(x_k - x_0), & \text{if } x_0 + \frac{1}{3}l \leqslant x_k \leqslant x_0 + \frac{2}{3}l \\ 3(x_k - x_0) - 2l, & \text{if } x_0 + \frac{2}{3}l \leqslant x_k \leqslant x_0 + l \\ (x_k - x_0), & \text{else.} \end{cases} \tag{47}$$

In Eq. (46), $K(x_k, x_0, l)$ is a kernel function which in combination with the amplitudes c_i assures momentum and energy conservation and controls the energy redistribution among the velocity components. A possible definition is: $K(x_k, x_0, l) = x_k - f(x_k, x_0, l)$. This energy redistribution is a 1D interpretation of the pressure-fluctuation effect in a 3D flow and therefore is called 'pressure scrambling'.

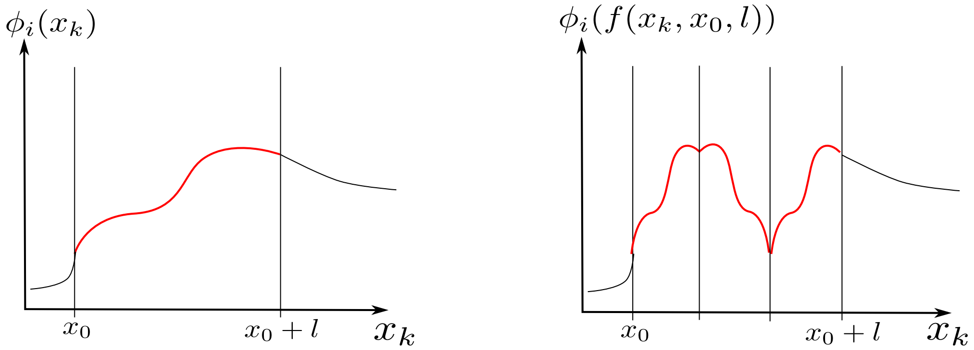

(a) Profile before triplet map.

(b) Profile after triplet map.

Figure 3: Illustration of a continuous triplet map in Eq. (47): The profile within the eddy range $x_0 < x_k < x_0 + l$ is replaced by 3 compressed copies of the original profile, while the middle copy is reversed.

Determination of the amplitudes c_i requires additional modeling. Kerstein et al. [53] derive the amplitudes:

$$c_i = \frac{27}{4l}\left(-u_{K;k,i} + \operatorname{sgn}(u_{K;k,i})\sqrt{u_{K;k,i}^2 + \sum_{j\neq k}\alpha T_{ij} u_{K;k,j}^2}\right) \; ; i \neq k \tag{48}$$

with the definition

$$u_{K;k,i} \equiv \frac{1}{l^2}\int u_{k,i}(f(x_k, x_0, l))K(x_k, x_0, l)\, dx_k \tag{49}$$

and the transfer matrix

$$\alpha T = \alpha\begin{pmatrix} -1 & 1 \\ 1 & -1 \end{pmatrix}. \tag{50}$$

Note that Eq. (50) is valid for 2 velocity components, while the transfer matrix in [53] is 3-dimensional.

The free parameter α ensures the amplitudes c_i in Eq. (48) to be real values for $0 \leqslant \alpha \leqslant 1$. We choose $\alpha = 1/2$ corresponding to the equalization of the two component available energies in the present formulation.

During an eddy event, the transfer matrix T redistributes the turbulent kinetic energy among velocity components.

This 'pressure scrambling' accounts for the tendency for pressure fluctuations to restore isotropy (especially for $\alpha = 1/2$) and is invariant under exchange of indices. By construction the momentum and total energy are not changed by the pressure scrambling.

During the *ODT* time evolution in Eqs. (44) and (45), the eddy size l and the location x_0 are sampled from a probability distribution representing the physics: For a given $\{l, x_0\}$ an eddy turnover time τ_e can be calculated leading to an occurrence frequency $\frac{1}{\tau_e}$. Since the *ODT* triplet map is an instantaneous process, the frequency for the eddy specified by $\{l, x_0\}$ is chosen from an event rate distribution:

$$\lambda(x_0, l) = \frac{C}{l^2 \tau_e(x_0, l)} = \frac{C}{l^3}\sqrt{k - V - \frac{\nu^2}{l^2}Z} \tag{51}$$

involving particular definitions of the available specific turbulent kinetic energy (k) and the created specific potential energy difference (V). The values l_{max}, C, and Z are adjustable model parameters. The latter is introduced to cut off eddies with unphysically small energy and the parameter C is an overall rate coefficient determining the strength of the turbulence. The maximum eddy size (l_{max}) is chosen to characterize the largest (global) scale within the flow, e.g. half channel height, half duct height, or Rayleigh-cell height (h).

Meiselbach [71] found the Z-parameter to be weakly dependent on the turbulent Reynolds number, but the dependency is marginal for $Re_\tau \leqslant 10000$, investigated in this thesis.

3.4 EXTENDED LARGE EDDY SIMULATION (XLES)

Note that this section introduces *XLES* and *ODTLES* in the Oberbeck-Boussinesq approximation. Parts of this section are adapted from the incompressible Navier-Stokes interpretation of *XLES* and *ODTLES* introduced by the author in [2] and [3]. All following sections and chapters contain scientific contribution by the author and their validation.

Extended *LES* (*XLES*) is a new approach and concept to filter the governing equations. Possible modifications of the 3D filtering applied in *LES* are:

- 2D filtering the governing equations: Since *ODT* incurs relatively low computational costs to fully resolve small scale effects (e.g. molecular diffusion) in 1D, it is worthwhile but also fairly non-trivial to include it into an *LES*-like 3D approach. To achieve this, *XLES* solves 2D filtered equations on a structured grid, tailored to include 1D models as *SGM*s, because one highly resolved Cartesian direction is maintained (this e.g. allows resolved molecular diffusion within an ODT sub-grid model). In this sense the term *SGM* is used to describe unresolved terms rather than to describe unresolved spatial scales. To derive a preferably general model, all Cartesian directions are treated equally: Three 2D filters, each corresponding to one highly resolved Cartesian direction, are applied independently to the governing equations. This leads to three coupled sets of 2D filtered equations, derived in detail in section 3.4. This 2D filtered *XLES* is investigated in this work and *XLES* refers to 2D filtered *XLES* if not mentioned otherwise. As considerations in appendix A.3.3 suggest, *XLES* is not restricted to structured grids.

- 1D filtering the governing equations: E. g. the concepts of superparameterizations for meteorological flows is related to 1D filtered equations within the *XLES* framework. Multiple coupled 1D filtered (2D highly resolved) systems of equations are imaginable. The 3D large scale fields are consistent due to coupling terms. The 1D filtered equations are not investigated in detail in this work.

There are conceptual conclusions: On the one hand *XLES* can be interpreted as a superparameterization using 1D models. On the other hand e. g. the concept of the Cloud Resolving Convection Parameterization (*CRCP*) model by Grabowski and Smolarkiewicz [34] and quasi-3D multi-scale modeling (*Q3D*) by Jung and Arakawa [46] can be expressed to some extend by *XLES*-like 1D filtering. Note that superparameterization approaches often contain another level of sub-grid modeling for the highly resolved properties. In *ODTLES* this can be achieved by introducing the ensemble mean closure (EMC), as described by Schmidt et al. [89].

Though primarily intended to explain *ODTLES* to the *LES* community, *XLES* also gives new insights into *ODTLES*. E. g. *XLES* allows the representation of scalar properties by multiple *XLES-grid*s consistently (see section 3.4.2.2) and moreover is a novel autonomous modeling strategy because the ansatz is very general and not limited to one-dimensional models like *ODT*.

In *ODTLES*, in the one hand the *ODT-SGM* is able to represent the full spectrum of the turbulent cascade within a 1D sub-domain, including the large scale effects and on the other hand *XLES* contains 1D small scale terms. Thus the classical term 'scale separation' is misleading for *XLES* and especially *ODTLES*, because it is often associated with 3D large scale terms to be simulated. We will refer to a 'filter separation' between the *XLES* resolved scales and the unresolved scales modeled by *ODT*, where not necessarily 3D large scale terms are treated by *XLES*, but 1D or 2D filtered equations are solved. Especially in *ODTLES* the 'filter separation' can be interpreted to separate rather physical effects than spatial (or temporal) scales. Thereby the *XLES* approach only needs to represent 3D effects not represented by *ODT* (e. g. the domain geometry or secondary instabilities, as investigated in section 4.2.1). This leads to a *XLES* 3D resolution which is rather independent of the turbulence intensity. *ODTLES* can describe highly turbulent flows including small scale effects in domains of moderate complexity, relevant e.g. in the fields of combustion research, atmospheric science, fundamental turbulence research and many more. *ODTLES* results in chapters 4 and 5 demonstrate this ability for shear driven and buoyancy driven turbulent flows.

To derive resolved (to be simulated) and unresolved (to be modeled) terms the spatial 1D scales are separated for modeling purpose using these 1D filter operators:

$$\begin{aligned} u_i &= [\mathbb{1}\mathbb{1}\mathbb{1}]\, u_i \\ &= [(l_1 + (\mathbb{1} - l_1))(l_2 + (\mathbb{1} - l_2))(l_3 + (\mathbb{1} - l_3))]\, u_i \\ &\equiv [(l_1 + s_1)(l_2 + s_2)(l_3 + s_3)]\, u_i \\ &= [l_1l_2l_3 + s_1l_2l_3 + l_1s_2l_3 + l_1l_2s_3 + s_1s_2l_3 + s_1l_2s_3 + l_1s_2s_3 + s_1s_2s_3]\, u_i \end{aligned} \tag{52}$$

with the unity operator ($\mathbb{1}$) and the 1D small scale operator

$$[s_k] = [\mathbb{1} - l_k]. \tag{53}$$

The tensor product ansatz causes combinations of 1D operators to be commutable, e.g. $s_1l_2l_3 = l_3s_1l_2$.

In table 4 the 'filter separations' are compared between *LES*, *DNS* and *XLES* (2D filtered). Additionally the *XLES* (1D filtered) idea is used to introduce a notation for a possible superparameterization related to *CRCP* by Grabowski and Smolarkiewicz [34] (here called *XLES-CRCP*).

Table 4: Comparison of 'filter separation' approaches. *LES* is summarized in section 3.2. $\phi_i = \{u_i, \theta\}$ summarizes the dynamic variables. *XLES-CRCP* is an *XLES*-interpretation of a *CRCP* superparameterization by Grabowski and Smolarkiewicz [34] (here x_2 is the vertical direction).

Model	resolved	unresolved
LES	$\overline{\phi}_i^{LES} = [l_1l_2l_3]\phi_i$	$\widetilde{\phi}_i^{LES} = [s_1l_2l_3 + l_1s_2l_3 + l_1l_2s_3$ $+s_1s_2l_3 + s_1l_2s_3 + l_1s_2s_3 + s_1s_2s_3]\phi_i$
DNS	$[\mathbb{1}\mathbb{1}\mathbb{1}]\phi_i$	0
XLES	$\overline{\phi}_i =$ $[l_1l_2l_3 + s_1l_2l_3 + l_1s_2l_3 + l_1l_2s_3]\phi_i$	$\widetilde{\phi}_i =$ $[s_1s_2l_3 + s_1l_2s_3 + l_1s_2s_3 + s_1s_2s_3]\phi_i$
XLES-CRCP	$\overline{\phi}_i = [l_1l_2l_3 + s_1l_2l_3 + l_1s_2l_3 +$ $l_1l_2s_3 + s_1s_2l_3 + l_1s_2s_3]\phi_i$	$\widetilde{\phi}_i = [s_1l_2s_3 + s_1s_2s_3]\phi_i$

The *LES* '3D scale separation' is a special case of a 'filter separation', but essential differences exists in the capability of the microscale models *ODT* and an *LES* eddy viscosity model (see section 3.2).

In *DNS* all available scales are resolved numerically.

In *XLES* the resolved scales are connected to 2D filtered fields. *W.l.o.g.* we apply $[l_1l_2]$ leading to:

$$[l_1l_2]\phi_i = [l_1l_2l_3 + l_1l_2s_3]\phi_i. \tag{54}$$

To treat all Cartesian directions equally, all possible 2D-filtered terms $[l_2l_3]\phi_i$, $[l_1l_3]\phi_i$, and $[l_1l_2]\phi_i$ are resolved numerically.

The *XLES* resolved approach can be interpreted as the *LES* resolved scales ($[l_1l_2l_3]$) with additionally 1D resolved small scale (*RSS*) terms in all Cartesian directions ($[s_1l_2l_3] + [l_1s_2l_3] + [l_1l_2s_3]$). Both, the *XLES* resolved scales and the unresolved scales (e. g. modeled by *ODT*) impose special requirements on the numerical scheme and modeling, because techniques known from *LES* cannot be applied one-to-one to *XLES*.

The *XLES-CRCP* concept is based on 1D filtered equations for $[l_1]\phi_i = [l_1(l_2 + s_2)(l_3 + s_3)]\phi_i$ and $[l_3]\phi_i = [(l_1 + s_2)(l_2 + s_2)l_3]\phi_i$ leaving 2 highly resolved 2D systems of equations to be simulated (also possible with three 2D systems). These equations can be solved numerically. This concept is a reinterpretation of a *CRCP* approach and shows the relation of *XLES* and meteorological concepts. Further details might be in the scope of future investigations.

3.4.1 *XLES: Spatial 2D-Filtering*

The basic *XLES* concept is to apply 2D filters to the mass, momentum, and scalar equations (1)–(3), maintaining one Cartesian direction highly resolved. Using these filters, three 2D filtered *XLES* solution fields $\phi_{k,i} = \{u_{k,i}, \theta_k\}$, each corresponding to one highly resolved Cartesian direction x_k ($k = \{1, 2, 3\}$), are introduced.

We use a vector notation (called *XLES* vector notation), indicated by an underbar (e.g. $\underline{\phi}_i$). Each vector element contains one of the three 2D filtered solution fields:

$$\begin{pmatrix} [l_2l_3]\phi_i \\ [l_1l_3]\phi_i \\ [l_1l_2]\phi_i \end{pmatrix} = \begin{pmatrix} l_2l_3 & 0 & 0 \\ 0 & l_1l_3 & 0 \\ 0 & 0 & l_1l_2 \end{pmatrix} \begin{pmatrix} \phi_i \\ \phi_i \\ \phi_i \end{pmatrix} \equiv \underline{\underline{l}}^{2D}\, \underline{\phi}_i \equiv \underline{\hat{\phi}}_i \tag{55}$$

with the 2D filter matrix $\underline{\underline{l}}^{2D}$. Here *w.l.o.g.* the 2D filter operator $[l_2l_3]$ (corresponding to *XLES-grid* 1) corresponds to a tensor product of 1D filter operators $[l_2]$ and $[l_3]$. This tensor product is commutable: $[l_2l_3]$=$[l_3l_2]$.

The 2D filtered fields $\underline{\hat{\phi}}_i$ (we refer to $\underline{\hat{\phi}}_i$ as the *XLES* vector) are discretized using three overlapping staggered *XLES-grid*s with face-centered velocities and cell-centered pressure and scalar fields, illustrated in figure 4b–4d, where each *XLES-grid* $k = \{1, 2, 3\}$ discretizes one *XLES* vector element $\hat{\phi}_{k,i}$.

The 2D filtering follows the idea of implicit filtering (cf. section 3.2). The discrete grid contains averaged values corresponding to the discrete 1D box filter definition $[l_k^d]$:

$$[l_k^d]\phi_i = \frac{1}{\Delta x_k^{LES}} \int_{-\frac{\Delta x_k^{LES}}{2}}^{\frac{\Delta x_k^{LES}}{2}} \phi_i \, dx'_k. \tag{56}$$

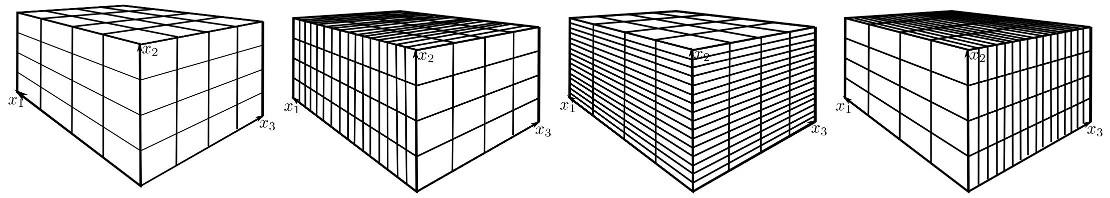

(a) LES grid: $\overline{\phi}_i^{d,LES} \approx [l_1 l_2 l_3]\phi_i$. (b) Grid 1: $\hat{\phi}^d_{1,i} \approx [l_2 l_3]\phi_i$. (c) Grid 2: $\hat{\phi}^d_{2,i} \approx [l_1 l_3]\phi_i$. (d) Grid 3: $\hat{\phi}^d_{3,i} \approx [l_1 l_2]\phi_i$.

Figure 4: In *XLES* the solution field $\phi_i = \{u_i, \theta\}$ is resolved using multiple *XLES-grid*s illustrated in 4b-4d. 3D large scale properties, corresponding to a standard *LES* grid are for illustration represented with $N_{LES} = 4$ cells per direction in 4a (cf. figure 2). In *XLES* the 3D large scale properties are derived by 1D filtering the *XLES* properties: $\overline{\phi}_i^{LES} = [l_k]\hat{\phi}_{k,i}$, $k = \{1, 2, 3\}$. The discrete *XLES* resolved small scale (*RSS*) properties are represented for illustration by $N_{RSS} = 16$ cells in 4b-4d.

The effective implicit filter size in x_k-direction is $[l_k^{eff}] = Q\Delta x_k^{LES}$ with the numerical sub-filter parameter $Q \approx \mathcal{O}(1)$ depending on the numerical scheme. Thus the discrete representation and the filter properties are strongly connected. Again $[l_k]$ can be interpreted as the effective implicit filter. The numerical sub-filter parameter (Q) and the characteristic filter form is not required to derive the 2D filtered equations, but influence especially the choice of the maximum eddy size (l_{max}) within the *ODTLES* model.

By explicitly averaging the flow state in the highly resolved *XLES-grid* direction using Eq. (56) a discrete representation within a 3D large scale grid (see figure 4a) is possible with the equivalent effective large scale filter properties as in the two filtered directions. Thus computations using this 3D large scale grid correspond to an implicitly 3D filtered scheme with an effective filter size $[l_k^{eff}] = \Delta Q x_k^{LES}$ in each direction x_k, $k = \{1, 2, 3\}$.

The *XLES* 'filter separation' (cf. table 4) decomposes the full solution field into three parts (using the *XLES* vector notation):

$$\begin{aligned}
\underline{\phi}_i \equiv \begin{pmatrix} \phi_i \\ \phi_i \\ \phi_i \end{pmatrix} &= \begin{pmatrix} [l_2 l_3]\phi_i \\ [l_1 l_3]\phi_i \\ [l_1 l_2]\phi_i \end{pmatrix} + \begin{pmatrix} [l_1 s_2 l_3 + l_1 l_2 s_3]\phi_i \\ [s_1 l_2 l_3 + l_1 l_2 s_3]\phi_i \\ [s_1 l_2 l_3 + l_1 s_2 l_3]\phi_i \end{pmatrix} + \begin{pmatrix} [\mathcal{S}]\phi_i \\ [\mathcal{S}]\phi_i \\ [\mathcal{S}]\phi_i \end{pmatrix} \\
&\equiv \underline{\underline{l}}^{2D}\,\underline{\phi}_i + \underline{\underline{C}}\,\underline{\underline{s}}^{1D}\underline{\underline{l}}^{2D}\underline{\phi}_i + [\mathcal{S}]\underline{\phi}_i
\end{aligned} \tag{57}$$

with the *XLES-SGS* terms $\mathcal{S} = [l_1 s_2 s_3 + s_1 l_2 s_3 + s_1 s_2 l_3 + s_2 s_2 s_3]$:

1. 'Directly Resolved':

   The 2D filter $\underline{\underline{l}}^{2D}$ applied to the full solution field (ϕ_i) leads to the *XLES* vector: $\underline{\hat{\phi}}_i = \underline{\underline{l}}^{2D}\,\underline{\phi}_i$. Each *XLES-grid* represents its own 'directly resolved' solution field distinct from the other *XLES-grid*s.

2. 'Indirectly Resolved':

There are 'indirectly resolved' small scale terms ('directly resolved' by another *XLES-grid*): $\underline{\underline{C}}\,\underline{\underline{s}}^{1D}\underline{\underline{l}}^{2D}\underline{\phi}_i$. Especially within non-linear advection terms (in Eq. (2)), they determine the coupling between the *XLES-grid*s. The coupling matrix $\underline{\underline{C}}$ and the small scale matrix $\underline{\underline{s}}^{1D}$ in Eq. (57) are:

$$\underline{\underline{C}} = \begin{pmatrix} 0 & \mathbb{1} & \mathbb{1} \\ \mathbb{1} & 0 & \mathbb{1} \\ \mathbb{1} & \mathbb{1} & 0 \end{pmatrix} \quad \text{and} \quad \underline{\underline{s}}^{1D} = \begin{pmatrix} s_1 & 0 & 0 \\ 0 & s_2 & 0 \\ 0 & 0 & s_3 \end{pmatrix}. \tag{58}$$

The matrix $\underline{\underline{s}}^{1D}$ defines the resolved small scale (RSS) properties $\check{\underline{\phi}}_i$ (these are simulated in *XLES*, contrary to *LES*):

$$\underline{\underline{s}}^{1D}\underline{\underline{l}}^{2D}\,\underline{\phi}_i \equiv \check{\underline{\phi}}_i = \hat{\underline{\phi}}_i - \underline{\underline{l}}^{1D}\hat{\underline{\phi}}_i = \hat{\underline{\phi}}_i - \overline{\underline{\phi}}_i^{LES} \tag{59}$$

with the 1D filter matrix

$$\underline{\underline{l}}^{1D} = \begin{pmatrix} l_1 & 0 & 0 \\ 0 & l_2 & 0 \\ 0 & 0 & l_3 \end{pmatrix}. \tag{60}$$

In index notation: The term (*w.l.o.g.*) $[l_1 s_2 l_3]\phi_i = [l_1 l_3]\phi_i - [l_1 l_2 l_3]\phi_i$ can be interpreted numerically, because $\hat{\phi}_{2,i} = [l_1 l_3]\phi_i$ is exclusively available in *XLES-grid* 2 and the 1D filtered *XLES* field $[l_2]\hat{\phi}_{2,i} = [l_1 l_2 l_3]\phi_i$, corresponding to the LES properties $\overline{\phi}_i^{LES}$ (see figure 4), is also available in *XLES-grid* 2.

3. 'Not Resolved':

   The scales $[\mathcal{S}]\phi_i = [s_1 s_2 l_3 + s_1 l_2 s_3 + l_1 s_2 s_3 + s_1 s_2 s_3]\phi_i$ are not resolved in any *XLES-grid* , but their influence could be modeled e. g. by the *ODT* model (see sections 3.3 and 3.5).

We summarize all resolved scales ('directly' and 'indirectly'):

$$\overline{\underline{\phi}}_i = [l_1 l_2 l_3 + s_1 l_2 l_3 + l_1 s_2 l_3 + l_1 l_2 s_3]\underline{\phi}_i = (\underline{\underline{l}}^{2D} + \underline{\underline{C}}\,\underline{\underline{s}}^{1D}\underline{\underline{l}}^{2D})\underline{\phi}_i. \tag{61}$$

A possible interpretation of the *XLES* resolved scales is the numerical approximation of $\overline{\phi}_i$ instead of $\overline{\phi}_i^{LES} = [l_1 l_2 l_3]\phi_i$ in *LES* (cf. table 4). Appendix A.1 shows that expressing $\overline{\underline{\phi}}_i$ in index notation automatically leads to three coupled *XLES-grid*s (corresponding to Eq. (61)).

An equivalent derivation and interpretation of the *XLES* filter idea is described in appendix A.3: Formally this procedure is similar to derivations of variational methods, as *FEM* and *DGM* and thus allows the application of techniques known from these methods also to the *XLES* framework. This can e. g. include unstructured grids. Thereby 2D convolutions are applied as ansatz and test functions (an extension of the implicit filter and a test-filter) to the governing equations.

3.4.2 *XLES: Momentum Conservation*

Similar to *LES*, in *XLES* filtered equations are solved. Contrary to *LES* the *XLES* equations are derived by applying a 2D filter matrix $\underline{\underline{l}}^{2D}$ to the governing equations. For the momentum equations (2) this leads to (using *XLES* vector notation):

$$0 = \partial_{x_i} \underline{\hat{p}} + \left(\partial_t - \nu \sum_{j=1}^{3} \partial_{x_j}^2 \right) \underline{\hat{u}}_i + \sum_{j=1}^{3} \partial_{x_j} \underline{\hat{u}}_j * \underline{\hat{u}}_i + \sum_{j=1}^{3} \underline{\tau}_{ij}^{XLES} + g_2 \underline{\hat{\theta}} + \underline{\hat{F}}_i \tag{62}$$

with the 2D filtered pressure

$$\underline{\hat{p}} = \underline{\underline{l}}^{2D} \underline{p} = \begin{pmatrix} [l_2 l_3] p \\ [l_1 l_3] p \\ [l_1 l_2] p \end{pmatrix}, \tag{63}$$

the 2D filtered gravitational forcing ($g_2 \underline{\hat{\theta}}$, see also section 3.4.3), the *XLES* residual stress tensors $\underline{\tau}_{ij}^{XLES}$, and the Hadamard operator $*$, an entry-wise multiplication between *XLES* vectors and matrices.

The three 2D filtered momentum equations, each describing three velocity components (hence the number of equations is tripled), coexist and are solved simultaneously.

Compared to *LES* advection terms $\partial_{x_j} \overline{u}_j^{LES} \overline{u}_j^{LES}$ the *XLES* advection terms $\partial_{x_j} \underline{\hat{u}}_j * \underline{\hat{u}}_i = \partial_{x_j} (\underline{\overline{u}}_j^{LES} + \underline{\check{u}}_j) * (\underline{\overline{u}}_i^{LES} + \underline{\check{u}}_i)$ contain additional *XLES-grid* specific *RSS* terms.

The contribution associated with the *XLES* residual stress tensors

$$\underline{\tau}_{ij}^{XLES} = \underline{\underline{l}}^{2D} \left(\partial_{x_j} \underline{u}_j * \underline{u}_i \right) - \partial_{x_j} \underline{\hat{u}}_j * \underline{\hat{u}}_i \tag{64}$$

is captured through the use of some form of modeling or approximation.

3.4.2.1 *Decomposition of the XLES Residual Stresses*

To investigate the *XLES* residual stresses in more detail, a 2D decomposition (a modified version of the 3D decomposition by Leonard [64] in section 3.2) is performed , leading to:

$$\underline{\tau}_{ij}^{XLES} = \underline{\mathcal{X}}_{ij}^{XLES} + \underline{\mathcal{L}}_{ij}^{2D} + \underline{\mathcal{C}}_{ij}^{XLES} + \underline{\mathcal{R}}_{ij}^{XLES} \tag{65}$$

where:

- *XLES* coupling tensor terms

$$\underline{\mathcal{X}}_{ij}^{\mathrm{XLES}} = \partial_{x_j} \left(\underline{\hat{u}}_j * \underline{\underline{C}}\,\underline{\underline{s}}^{1D} \underline{\underline{l}}^{2D} \underline{u}_i + \underline{\underline{C}}\,\underline{\underline{s}}^{1D} \underline{\underline{l}}^{2D} \underline{u}_j * \underline{\hat{u}}_i + \underline{\underline{C}}\,\underline{\underline{s}}^{1D} \underline{\underline{l}}^{2D} \underline{u}_j * \underline{\underline{C}}\,\underline{\underline{s}}^{1D} \underline{\underline{l}}^{2D} \underline{u}_i \right) \tag{66}$$

involve 'indirectly resolved' terms. These stress terms couple the momentum equations represented by different *XLES-grid*s. A possible approximation of $\underline{\mathcal{X}}_{ij}^{\mathrm{XLES}}$ is investigated in section 3.4.2.2. In *LES* these terms are not simulated and therefore typically modeled or approximated and contribute to *LES* cross-stress and 3D *SGS* Reynolds stress terms (cf. section 3.2).

- 2D *XLES* Leonard stresses

$$\underline{\mathcal{L}}_{ij}^{2D} = \left(\underline{\underline{l}}^{2D} \partial_{x_j} \left(\underline{\hat{u}}_j * \underline{\hat{u}}_i\right) - \partial_{x_j} \underline{\hat{u}}_j * \underline{\hat{u}}_i\right) + \left(\underline{\underline{l}}^{2D} \underline{\mathcal{X}}_{ij}^{\mathrm{XLES}} - \underline{\mathcal{X}}_{ij}^{\mathrm{XLES}}\right) \tag{67}$$

describe the influence of the 2D test-filter on the ('directly' and 'indirectly') resolved *XLES* advection terms (see section 3.4.2.3 for details and compare to *LES* in section 3.2).

- *XLES* cross-stress terms

$$\underline{\mathcal{C}}_{ij}^{\mathrm{XLES}} = \underline{\underline{l}}^{2D} \partial_{x_j} \left(\underline{\tilde{u}}_j * \underline{\hat{u}}_i + \underline{\hat{u}}_j * \underline{\tilde{u}}_i\right) + \underline{\underline{l}}^{2D} \partial_{x_j} \left(\underline{\tilde{u}}_j * \underline{\underline{C}}\,\underline{\underline{s}}^{1D} \underline{\underline{l}}^{2D} \underline{u}_i + \underline{\underline{C}}\,\underline{\underline{s}}^{1D} \underline{\underline{l}}^{2D} \underline{u}_j * \underline{\tilde{u}}_i \right) \tag{68}$$

describe the interaction of resolved ('directly' and 'indirectly') and unresolved *XLES* terms (see section 3.4.2.3 for details and compare to *LES* in section 3.2).

- 2D *SGS* Reynolds stress terms

$$\underline{\mathcal{R}}_{ij}^{\mathrm{XLES}} = \underline{\underline{l}}^{2D} \partial_{x_j} \left(\underline{\tilde{u}}_j * \underline{\tilde{u}}_i\right) \tag{69}$$

describe the interaction of terms not resolved in *XLES* (see section 3.4.2.3 for details and compare to *LES* in section 3.2).

The *XLES* stress terms $\underline{\mathcal{L}}_{ij}^{2D}$, $\underline{\mathcal{C}}_{ij}^{\mathrm{XLES}}$, and $\underline{\mathcal{R}}_{ij}^{\mathrm{XLES}}$ are investigated in more detail in section 3.4.2.3 and can be interpreted in the context of the *ODT* model, as shown in section 3.5.

As mentioned in section 3.2 an improved decomposition by Germano [31] is possible also for the 2D filtered fields investigated here. Nevertheless the 2D decomposition following [64] is sufficient to introduce *ODT* into the *XLES* framework and therefore used here in preparation for section 3.5.

3.4.2.2 *XLES: Coupling Tensor Terms*

The *XLES* coupling tensor terms ($\underline{\mathcal{X}}_{ij}^{\mathrm{XLES}}$) in Eq. (66) are decomposed into two terms (using $\underline{\check{u}}_i$ from Eq. (59)):

$$\underline{\mathcal{X}}_{ij}^{\mathrm{XLES}} = \underline{\underline{C}}\partial_{x_j}\left(\underline{\hat{u}}_j * \underline{\hat{u}}_i - \underline{\overline{u}}_j^{\mathrm{LES}} * \underline{\overline{u}}_i^{\mathrm{LES}}\right) + \partial_{x_j}\left(\underline{\underline{1}}\,\underline{\check{u}}_j * \underline{\underline{1}}\,\underline{\check{u}}_i - \underline{\underline{1}}(\underline{\check{u}}_j * \underline{\check{u}}_i)\right) \tag{70}$$

(proof by insertion) with the matrix of ones $\underline{\underline{1}}$ and where:

1. The first term in Eq. (70) exclusively contains advection terms with advecting and advected velocities represented within the same *XLES-grid*. This can be interpreted as a linearization affecting the coupling, while the individual advection terms $\partial_{x_j}\hat{u}_{k,j}\hat{u}_{k,i}$ and $\partial_{x_j}\overline{u}_{k,j}^{\mathrm{LES}}\overline{u}_{k,i}^{\mathrm{LES}}$ in each *XLES-grid* k remain non-linear. We investigate *w.l.o.g.* one element of a coupling vector $\left(\underline{\underline{C}}\partial_{x_j}\underline{\hat{u}}_j * \underline{\hat{u}}_i\right)$ in detail: For *XLES* vector element 1 we find e.g.

   $$\partial_{x_j}([l_1 l_3]u_j\,[l_1 l_3]u_i) \tag{71}$$

   with the velocities $[l_1 l_3]u_j = \hat{u}_{2,j}$ ($j = \{1, 2, 3\}$) only discretely represented in *XLES-grid* 2.

   This coupling vector can be reinterpreted:

   $$(\underline{\underline{C}}\,\partial_{x_j}\underline{\hat{u}}_j * \underline{\hat{u}}_i) \approx \underline{\underline{l}}^{\dagger} * \underline{\underline{C}}\,\partial_{x_j}\underline{\hat{u}}_j * \underline{\hat{u}}_i \tag{72}$$

   with the matrix

   $$\underline{\underline{l}}^{\dagger} = \begin{pmatrix} \mathbb{1} & l_1^{-1}l_2 & l_1^{-1}l_3 \\ l_2^{-1}l_1 & \mathbb{1} & l_2^{-1}l_3 \\ l_3^{-1}l_1 & l_3^{-1}l_2 & \mathbb{1} \end{pmatrix}. \tag{73}$$

   Using Eq. (72) the same example in Eq. (71) leads to:

   $$[l_1^{-1}][l_2]\partial_{x_j}([l_1 l_3]u_j\,[l_1 l_3]u_i) \tag{74}$$

   which is computed in *XLES-grid* 2 and then coupled to *XLES-grid* 1. Eq. (73) contains deconvolution operators $[l_k^{-1}]$, which are realizable if only large scale information is present. This is the case in *XLES*: the velocities $[l_1 l_3]u_j$ and $[l_1 l_3]u_i$ in the example in Eq. (74) are large scale in the x_1-direction, which is the direction of the deconvolution.

   A discrete (numerical) approximation $\underline{\underline{l}}^{\dagger_d} \approx \underline{\underline{l}}^{\dagger}$ is provided by Eq. (56) for the averaging and an algorithm is introduced in section 3.6.1 for the reconstruction (deconvolution). Note that the reconstruction algorithm maintains the averaged values.

Using the matrix $\underline{\underline{l}}^{\dagger}$ (including deconvolutions) the linearized *XLES* coupling tensor terms are:

$$\underline{\mathcal{X}}_{ij}^{\mathrm{XLES}} = \underline{\underline{l}}^{\dagger} * \underline{\underline{C}} \partial_{x_j} \left(\underline{\hat{u}}_j * \underline{\hat{u}}_i - \underline{\overline{u}}_j^{\mathrm{LES}} * \underline{\overline{u}}_i^{\mathrm{LES}} \right). \tag{75}$$

The deconvolution within the coupling terms Eq. (75) is fundamentally different in *XLES* than in existing approaches without resolved small scales. The reason is that the deconvolution in *XLES* is not intended to construct small-scale features that are otherwise non-existent, but rather, to modify a small-scale structure that already exists at the resolved small scales, recognizing that this structure also has low-wavenumber content. Indeed, the goal in principle is to modify appropriately that low-wavenumber content while preserving the high-wavenumber content to the greatest possible extent (see the example in sections 3.6.2 and 3.6.3).

2. The second term in Eq. (70) can be expanded as follows:

$$\begin{aligned} &\partial_{x_j} \left(\underline{\underline{1}}\, \underline{\check{u}}_j * \underline{\underline{1}}\, \underline{\check{u}}_i - \underline{\underline{1}} (\underline{\check{u}}_j * \underline{\check{u}}_i) \right) \qquad (76) \\ =&\partial_{x_j} \underline{1} (\check{u}_{1,j} \check{u}_{2,i} + \check{u}_{1,j} \check{u}_{3,i} + \check{u}_{2,j} \check{u}_{1,i} + \check{u}_{2,j} \check{u}_{3,i} + \check{u}_{3,j} \check{u}_{1,i} + \check{u}_{3,j} \check{u}_{2,i}). \end{aligned}$$

   These terms contain interactions of small-scale velocities resolved in different *XLES-grid*s. We neglect these non-linear coupling terms. For an intact energy cascade within the turbulent flow this assumption is reasonable because it implies that the velocities $\check{u}_{k,j} = \hat{u}_{k,j} - \overline{u}_{k,j}^{\mathrm{LES}}$ are smaller than $\hat{u}_{k,j}$.

By neglecting the non-linear coupling terms an *XLES-U* spatial momentum error term can be defined:

$$\underline{\sigma}_{\mathrm{XLES-U}_{ij}}^{\mathrm{spatial}} = \partial_{x_j} \left(\underline{\underline{1}}\, \underline{\check{u}}_j * \underline{\underline{1}}\, \underline{\check{u}}_i - \underline{\underline{1}} (\underline{\check{u}}_j * \underline{\check{u}}_i) \right). \tag{77}$$

In unclosed *LES* (*LES-U*), the *LES*-limit of *XLES*-U (see section 3.4.7), the model error $\underline{\sigma}_{\mathrm{XLES-U}_{ij}}^{\mathrm{spatial}}$ vanishes and thus comparing a convergence study of *XLES-U* and *LES-U* allows to estimate $\underline{\sigma}_{\mathrm{XLES-U}_{ij}}^{\mathrm{spatial}}$ for a specific case (cf. section 4.1.4).

3.4.2.3 *XLES-SGS: Leonard Stress, Cross-Stress and SGS Reynolds Stress Terms*

In this section the (to be modeled) stress tensors containing *XLES* unresolved terms $\underline{\tau}_{ij}^{\mathrm{XLES}} - \underline{\mathcal{X}}_{ij}^{\mathrm{XLES}} = \underline{\mathcal{L}}_{ij}^{\mathrm{2D}} + \underline{\mathcal{C}}_{ij}^{\mathrm{XLES}} + \underline{\mathcal{R}}_{ij}^{\mathrm{XLES}}$ are investigated:

- The Leonard stresses $\underline{\mathcal{L}}_{ij}^{\mathrm{2D}} = \underline{\underline{l}}^{\mathrm{2D}} \partial_{x_j} \left(\underline{\hat{u}}_j * \underline{\hat{u}}_i + \underline{\mathcal{X}}_{ij}^{\mathrm{XLES}} \right) - \partial_{x_j} \left(\underline{\hat{u}}_j * \underline{\hat{u}}_i + \underline{\mathcal{X}}_{ij}^{\mathrm{XLES}} \right)$ can in principle be calculated by explicit filtering the directly and indirectly resolved *XLES* advection terms.

For implicit filtered *LES* and *XLES* the filter shape and effective filter length are not known, but the 2D Leonard stresses are expected to be small within a discrete formulation using implicit filtering, as long as the test-filter also corresponds to the discrete representation.

Ferziger and Peric [24] (and authors therein) report that explicit filtering the *LES* advection terms produces immoderate dissipation and neglecting the 3D Leonard stresses improves the outcome.

According to these arguments we neglect $\underline{\mathcal{L}}_{ij}^{2D}$.

Other attempts to model the 3D Leonard stresses are not transferred to the 2D Leonard stresses in this work.

- The *XLES* cross-stress terms ($\underline{\mathcal{C}}_{ij}^{XLES}$) and 2D *SGS* Reynolds stress terms ($\underline{\mathcal{R}}_{ij}^{XLES}$)

  describe interactions including the *XLES* unresolved scales $\underline{\widetilde{u}}_i = [\mathcal{S}]u_i$ (see table 4). These terms can be modeled (e.g. by *ODT*).

  We decompose these stress terms:

$$\begin{aligned} \underline{\mathcal{C}}_{ij}^{XLES}+\underline{\mathcal{R}}_{ij}^{XLES} =& \partial_{x_j}\left(\underline{\underline{l}}^{2D}+\underline{\underline{l}}^{\dagger} * \underline{\underline{C}}\,\underline{\underline{l}}^{2D}\right)\left(\underline{\widetilde{u}}_j * \underline{\check{u}}_i + \underline{\check{u}}_j * \underline{\widetilde{u}}_i\right) \\ &+\partial_{x_j}\left(\underline{\underline{l}}^{2D} \phantom{+\underline{\underline{l}}^{\dagger} * \underline{\underline{C}}\,\underline{\underline{l}}^{2D}}\right)\left(\underline{\widetilde{u}}_j * \underline{\overline{u}}_i^{LES} + \underline{\overline{u}}_j^{LES} * \underline{\widetilde{u}}_i + \underline{\widetilde{u}}_i * \underline{\widetilde{u}}_j\right) \end{aligned} \tag{78}$$

  into:

  1. The terms $\partial_{x_j}\left(\underline{\underline{l}}^{2D}+\underline{\underline{l}}^{\dagger} * \underline{\underline{C}}\,\underline{\underline{l}}^{2D}\right)\left(\underline{\widetilde{u}}_j * \underline{\check{u}}_i + \underline{\check{u}}_j * \underline{\widetilde{u}}_i\right)$

     depend on the resolved small scale velocities $\underline{\check{u}}_j$ exclusively available in one *XLES-grid*.

  2. The terms $\partial_{x_j}\underline{\underline{l}}^{2D}\left(\underline{\widetilde{u}}_j * \underline{\overline{u}}_i^{LES} + \underline{\overline{u}}_j^{LES} * \underline{\widetilde{u}}_i + \underline{\widetilde{u}}_i * \underline{\widetilde{u}}_j\right)$

     are independent of the *XLES-grid* (equal in all *XLES-grid*s). If a modeling approach is simultaneously applied in different *XLES-grid*s, a *SGS*-coupling is required to guarantee a consistent 3D large scale field. Ad hoc introduction of an additional coupling, e.g.

$$\left(\underline{\underline{l}}^{2D}+\underline{\underline{l}}^{\dagger} * \underline{\underline{C}}\,\underline{\underline{l}}^{2D}\right)\left(\underline{\widetilde{u}}_j * \underline{\overline{u}}_i^{LES} + \underline{\overline{u}}_j^{LES} * \underline{\widetilde{u}}_i + \underline{\widetilde{u}}_i * \underline{\widetilde{u}}_j\right), \tag{79}$$

     would lead to double counting of small scale terms available in all *XLES-grid*s. Nevertheless the exact relation

$$\begin{aligned} &\underline{\underline{l}}^{2D}\left(\underline{\widetilde{u}}_j * \underline{\overline{u}}_i^{LES} + \underline{\overline{u}}_j^{LES} * \underline{\widetilde{u}}_i + \underline{\widetilde{u}}_i * \underline{\widetilde{u}}_j\right) \\ =&\frac{1}{3}\left(\underline{\underline{l}}^{2D}+\underline{\underline{l}}^{\dagger} * \underline{\underline{C}}\,\underline{\underline{l}}^{2D}\right)\left(\underline{\widetilde{u}}_j * \underline{\overline{u}}_i^{LES} + \underline{\overline{u}}_j^{LES} * \underline{\widetilde{u}}_i + \underline{\widetilde{u}}_i * \underline{\widetilde{u}}_j\right). \end{aligned} \tag{80}$$

avoids double counting due to the factor $\frac{1}{3}$ (proof of $\underline{\underline{l}}^{2D}\underline{\mathbb{1}} = \frac{1}{3}\left(\underline{\underline{l}}^{2D}+\underline{\underline{l}}^{\dagger} * \underline{\underline{C}}\,\underline{\underline{l}}^{2D}\right)\underline{\mathbb{1}}$ by insertion).

We reformulate and summarize the *XLES* unresolved terms in Eq. (78):

$$\underline{\mathcal{C}}_{ij}^{\mathrm{XLES}} + \underline{\mathcal{R}}_{ij}^{\mathrm{XLES}} = (\underline{\underline{l}}^{2D} + \underline{\underline{l}}^{\dagger} * \underline{\underline{\underline{C}}}\,\underline{\underline{l}}^{2D})\underline{\mathcal{M}}_{ij} \tag{81}$$

with the *XLES* momentum microscale term

$$\underline{\mathcal{M}}_{ij} = \partial_{x_j}\left(\underline{\widetilde{u}}_j * \underline{\check{u}}_i + \underline{\check{u}}_j * \underline{\widetilde{u}}_i + \frac{1}{3}\left(\underline{\widetilde{u}}_j * \underline{\overline{u}}_i^{\mathrm{LES}} + \underline{\overline{u}}_j^{\mathrm{LES}} * \underline{\widetilde{u}}_i + \underline{\widetilde{u}}_j * \underline{\widetilde{u}}_i\right)\right). \tag{82}$$

Each vector element $\mathcal{M}_{k,ij}$ contains the unresolved terms in *XLES-grid* k. These terms are coupled to the other *XLES-grid*s by the *SGS* coupling terms $\underline{\underline{l}}^{\dagger} * \underline{\underline{\underline{C}}}\,\underline{\underline{l}}^{2D}\underline{\mathcal{M}}_{ij}$.

Additionally to the *XLES-U* spatial momentum error term ($\underline{\sigma}_{\mathrm{XLES-U}_{ij}}^{\mathrm{spatial}}$) in Eq. (77) neglecting the Leonard stresses introduces *SGS* momentum error term:

$$\underline{\sigma}_{\mathrm{SGS}_{ij}}^{\mathrm{spatial}} = \underline{\mathcal{L}}_{ij}^{2D}. \tag{83}$$

Summarizing section 3.4.2.2 and 3.4.2.3 we can write the *XLES* momentum equations:

$$\begin{aligned}0 =&\partial_{x_i}\underline{\hat{p}} + \left(\partial_t - \nu\sum_{j=1}^{3}\partial_{x_j}^2\right)\underline{\hat{u}}_i + \sum_{j=1}^{3}\partial_{x_j}\underline{\hat{u}}_j * \underline{\hat{u}}_i + g_2\underline{\hat{\theta}} + \sum_{j=1}^{3}\left(\underline{\underline{l}}^{2D}\underline{\mathcal{M}}_{ij}\right) + \sum_{j=1}^{3}\underline{\sigma}_{\mathrm{XLES}_{ij}}^{\mathrm{spatial}}\\ &+\sum_{j=1}^{3}\left(\underline{\underline{l}}^{\dagger} * \underline{\underline{\underline{C}}}\,\partial_{x_j}(\underline{\hat{u}}_j * \underline{\hat{u}}_i - \underline{\overline{u}}_j^{\mathrm{LES}} * \underline{\overline{u}}_i^{\mathrm{LES}}) + \underline{\underline{l}}^{\dagger} * \underline{\underline{\underline{C}}}\,\underline{\underline{l}}^{2D}\,\underline{\mathcal{M}}_{ij}\right)\end{aligned} \tag{84}$$

with the spatial momentum error term $\underline{\sigma}_{\mathrm{XLES}_{ij}}^{\mathrm{spatial}} = \underline{\sigma}_{\mathrm{XLES-U}_{ij}}^{\mathrm{spatial}} + \underline{\sigma}_{\mathrm{SGS}_{ij}}^{\mathrm{spatial}}$. The last line in Eq. (84) corresponds to the full coupling, including the *SGS* terms and the 'indirectly resolved' terms.

Please note at this stage no concrete *SGS* model is introduced to model $\underline{\mathcal{M}}_{ij}$.

3.4.3 *XLES: Scalar Conservation*

In the *XLES* momentum equation (84) the gravitational forcing $g_2\underline{\hat{\theta}}$ depends on the scalar field. Thus an *XLES* interpretation of the scalar equation (3) is required:

$$0 = \left[\partial_t - \kappa\sum_{j=1}^{3}\partial_{x_j}^2\right]\underline{\hat{\theta}} + \sum_{j=1}^{3}\partial_{x_j}\underline{\hat{u}}_j * \underline{\hat{\theta}} + \underline{\tau}_{\theta j}^{\mathrm{XLES}} \tag{85}$$

with the *XLES* residual scalar flux

$$\underline{\tau}_{\theta j}^{\mathrm{XLES}} = \underline{\underline{l}}^{2D}\left(\partial_{x_j}\underline{u}_j * \underline{\theta}\right) - \partial_{x_j}\underline{\hat{u}}_j * \underline{\hat{\theta}}. \tag{86}$$

Following considerations for *LES* by Sagaut [85], the *XLES* residual scalar flux can be decomposed similar to the *XLES* residual stress tensor ($\underline{\tau}_{ij}^{\mathrm{XLES}}$) in section 3.4.2.1:

$$\underline{\tau}_{\theta j}^{\mathrm{XLES}} = \underline{\mathcal{X}}_{\theta j}^{\mathrm{XLES}} + \underline{\mathcal{L}}_{\theta j}^{\mathrm{2D}} + \underline{\mathcal{C}}_{\theta j}^{\mathrm{XLES}} + \underline{\mathcal{R}}_{\theta j}^{\mathrm{XLES}} \tag{87}$$

with the *XLES* scalar coupling terms ($\underline{\mathcal{X}}_{\theta j}^{\mathrm{XLES}}$), the *XLES* scalar Leonard stress-type terms ($\underline{\mathcal{L}}_{\theta j}^{\mathrm{2D}}$), the *XLES* scalar cross-stress-type terms ($\underline{\mathcal{C}}_{\theta j}^{\mathrm{XLES}}$), and 2D scalar *SGS* Reynolds stress-type terms ($\underline{\mathcal{R}}_{j\theta}^{\mathrm{XLES}}$).

The decomposed *XLES* residual scalar fluxes in Eq. (87) are defined equally to the *XLES* residual stress tensors in sections 3.4.2.2 and 3.4.2.3. The arguments leading to Eq. (75) also lead to

$$\underline{\mathcal{X}}_{\theta j}^{\mathrm{XLES}} = \underline{\underline{l}}^{\dagger} * \underline{\underline{C}} \partial_{x_j} \left(\underline{\hat{u}}_j * \underline{\hat{\theta}} - \underline{\overline{u}}_j^{\mathrm{LES}} * \underline{\overline{\theta}}^{\mathrm{LES}} \right) \tag{88}$$

and the reasoning leading to Eq. (82) leads to the *XLES* scalar microscale term:

$$\underline{\mathcal{M}}_{\theta j} = \partial_{x_j} \left(\underline{\widetilde{u}}_j * \underline{\check{\theta}} + \underline{\check{u}}_j * \underline{\widetilde{\theta}} + \frac{1}{3} \left(\underline{\widetilde{u}}_j * \underline{\overline{\theta}}^{\mathrm{LES}} + \underline{\overline{u}}_j^{\mathrm{LES}} * \underline{\widetilde{\theta}} + \underline{\widetilde{u}}_j * \underline{\widetilde{\theta}} \right) \right) \tag{89}$$

and its coupling $\underline{\underline{l}}^{\dagger} * \underline{\underline{C}}\, \underline{\underline{l}}^{\mathrm{2D}} \underline{\mathcal{M}}_{\theta j}$. The corresponding spatial scalar error terms are:

$$\underline{\sigma}_{\theta}^{\mathrm{spatial}} = \partial_{x_j} \left(\underline{\underline{1}}\, \underline{\check{u}}_j * \underline{\underline{1}}\, \underline{\check{\theta}} - \underline{\underline{1}} (\underline{\check{u}}_j * \underline{\check{\theta}}) \right) + \underline{\mathcal{L}}_{\theta j}^{\mathrm{2D}}. \tag{90}$$

All arguments concerning the *XLES* Leonard stress in section 3.4.2.3 apply also to the *XLES* scalar Leonard stress-type term.

Note that within the LEM3D model an alternative scalar coupling is introduced (see [86]), bypassing some small scale energy conservation issues. This coupling approach behaves well for mixing applications and in principle can be used within *XLES*. Note that this scalar coupling does not result from the filtered governing equations.

3.4.4 *XLES: Time Scale Separation*

The *XLES* advection terms are represented by three overlapping *XLES-grid*s, including coupling terms between these *XLES-grid*s, and an additional *ODT* advancement for *ODTLES*. This *ODT* advancement involves instantaneous stochastic mappings (cf. section 3.3).

On the one hand, the simplest and physically most convenient way to advance the coupling terms and a dynamical *SGM* (like *ODT*) in time is an *EE1* (see section 2.1.2), which allows a straightforward interpretation of coupling terms and the stochastic turbulent advection within *ODT*. On the other hand, an efficient numerical advection scheme includes high order time integration.

A known compromise is to linearize the advection: The linear advection part is advanced by a high order numerical scheme (here *RK3* and *CN*, see section 2.1.2), while the non-linear part is implemented by an *EE1*. One possible way to interpret such an approach is to integrate the dynamical velocity field over one time step and use this velocity field to advect the dynamical variables within the next time step.

Within this macroscale time step multiple random occurrences of instantaneous *ODT* mappings can change the instantaneous velocity profile. Due to the time integration these mappings are considered within the advecting velocity profile of the next time step.

In section 3.6.4 alternative time schemes are suggested which potentially avoid the linearization of the advection terms.

A time scale separation is not required to derive a well-defined *XLES* approach (see [2]). Nevertheless the time scale separation simplifies the inclusion of *ODT* and thus is invoked here:

$$u_j = \left\langle u_j \right\rangle + u_j' \tag{91}$$

with the large time scale

$$\left\langle u_j \right\rangle = \frac{1}{\tau} \int_t^{t+\tau} u_j \, dt' \tag{92}$$

and the small time scale (fluctuations) $u_j' = u_j - \left\langle u_j \right\rangle$. Note that the time filter and spatial filters in *XLES* are independent of each other: $\left\langle [l_k] u_j \right\rangle = [l_k] \left\langle u_j \right\rangle$.

In contrast to *RaNS* and *URaNS* models, time averaging is not applied to the dynamical variables, but to the advecting velocities. This is especially reasonable because *ODT* is a dynamical model introducing small time scale effects.

The integral time scale (τ) corresponds to the 3D large scale flow while in *URaNS* τ is assumed to correspond to the largest turbulent scale. A natural choice for τ in *XLES* is the discrete time step size of the 3D large scale advancement scheme. Thus the modeling strategy is directly connected to the numerical realization which does not imply that the *XLES* approach is not complete.

As introduced in section 2.1.2 the time step size τ within an explicit time integration scheme is restricted by:

$$\tau = \mathrm{CFL}_{\mathrm{LES}} \min_{k,i,o,m,n} \left(\frac{\Delta x_k^{\mathrm{LES}}}{\hat{u}_{k,i}^{d;o,m,n}} \right) \tag{93}$$

within all *XLES-grid*s $k = \{1, 2, 3\}$ and with all velocity directions x_i ($i = \{1, 2, 3\}$).

The time scale separation within *XLES-U* implies additional error terms caused by the time scale separation:

$$\underline{\sigma}^{\text{temporal}}_{\text{XLES}-\text{U}_{ij}} = \partial_{x_j} \underline{\hat{u}}'_j * \underline{\hat{u}}_i, \tag{94}$$

$$\underline{\sigma}^{\text{temporal}}_{\text{XLES}-\text{U}_{\theta j}} = \partial_{x_j} \underline{\hat{u}}'_j * \underline{\hat{\theta}}. \tag{95}$$

By defining the integral time scale τ based on the resolved small scale cell size Δx_k^{RSS} in *XLES-grid* k, the time scale separation is suppressed, because all *XLES-U* velocities are large scale in time:

$$\tau = \text{CFL}_{\text{RSS}} \min_{k,i,m,n,o} \left(\frac{\Delta x_k^{\text{RSS}}}{\hat{u}_{k,i}^{d;m,n,o}} \right). \tag{96}$$

The *CFL*-number can be used to switch between Eq. (93) and Eq. (96) and thus becomes a model parameter balancing (and controlling) the temporal model errors $\underline{\sigma}^{\text{temporal}}_{\text{XLES}-\text{U}_{ij}}$ and $\underline{\sigma}^{\text{temporal}}_{\text{XLES}-\text{U}_{\theta j}}$ and the model performance. For a regular grid the *CFL*-numbers CFL_{LES} and CFL_{RSS} are directly connected to the *XLES* resolution ratio $K_N = N_{\text{RSS}}/N_{\text{LES}}$ due to $\text{CFL}_{\text{LES}} = K_N \, \text{CFL}_{\text{RSS}}$.

E. g. the *CFL*-number can be increased from $\text{CFL}_{\text{RSS}} = 0.5$ to $\text{CFL}_{\text{LES}} = 0.5$ for performance reasons: On the one hand *ODTLES* is still stable and well defined and e.g. for $N_{\text{RSS}} = 512$ and $N_{\text{LES}} = 16$ this leads to an increased *XLES* time-step size by a factor of $K_N = 32$ (*ODT* advancement only is indirectly influenced). On the other hand this approach tolerates certain model errors (see Eqs. (94) and (95)).

In specific problems, e. g. the Rayleigh-Bénard flow investigated in chapter 5 the *CFL*-number and therefore also the error terms $\underline{\sigma}^{\text{temporal}}_{\text{XLES}-\text{U}_{ij}}$ and $\underline{\sigma}^{\text{temporal}}_{\text{XLES}-\text{U}_{\theta j}}$ only have small effects.

Since *ODTLES* allows a huge number of turbulent *ODT* events within the time scale τ, the averaged velocities are smoothed, which is part of the *ODTLES* modeling strategy. Again the *CFL*-number is controlling this modeling impact, because with τ based on Eq. (96) the number of *ODT* turbulent events per τ is decreased.

ODT describes fluctuations (small time scale terms) in *ODT*-direction x_k corresponding to advection terms of the form $\partial_{x_j} \hat{u}'_{k,k} \hat{u}_{k,i}$ and $\partial_{x_j} \hat{u}'_{k,k} \hat{\theta}_k$. The corresponding time averaged advecting velocity $\langle \hat{u}_{k,k} \rangle$ is specified due to mass conservation, see section 3.4.5. The terms $\partial_{x_j} \hat{u}'_{k,k} \hat{u}_{k,i}$ and $\partial_{x_j} \hat{u}'_{k,k} \hat{\theta}_k$ correspond formally to the temporal *XLES-U* model error in Eqs. (94) and (95), controlled by *CFL*-number, but can be interpreted by *ODT*, which is possible due to the time scale separation.

Additionally to the terms $\underline{\mathcal{M}}_{ij}$ and $\underline{\mathcal{M}}_{\theta j}$, *ODT* 'directly' and 'indirectly' (due to coupling) represents fluctuations across 3D large scale cells:

$$\sum_{j=1}^{3}\left(\partial_{x_j}\underline{\hat{u}}_j'*\underline{\hat{u}}_i+(\underline{\underline{C}}\partial_{x_j}\underline{\hat{u}}_j'*\underline{\hat{u}}_i)^{\mathsf{T}}\right)=\left(\underline{\underline{\mathbb{1}}}+\underline{\underline{l}}^{\dagger}*\underline{\underline{C}}\right)\begin{pmatrix}\partial_{x_1}\hat{u}_{1,1}'\hat{u}_{1,i}\\ \partial_{x_2}\hat{u}_{2,2}'\hat{u}_{2,i}\\ \partial_{x_3}\hat{u}_{3,3}'\hat{u}_{3,i}\end{pmatrix}+\sum_{j=1}^{3}\underline{\sigma}_{\mathrm{ODTLES}_{ij}}^{\mathrm{temporal}}, \tag{97}$$

$$\sum_{j=1}^{3}\left(\partial_{x_j}\underline{\hat{u}}_j'*\hat{\theta}+(\underline{\underline{C}}\partial_{x_j}\underline{\hat{u}}_j'*\underline{\hat{\theta}})^{\mathsf{T}}\right)=\left(\underline{\underline{\mathbb{1}}}+\underline{\underline{l}}^{\dagger}*\underline{\underline{C}}\right)\begin{pmatrix}\partial_{x_1}\hat{u}_{1,1}'\hat{\theta}_1\\ \partial_{x_2}\hat{u}_{2,2}'\hat{\theta}_2\\ \partial_{x_3}\hat{u}_{3,3}'\hat{\theta}_3\end{pmatrix}+\sum_{j=1}^{3}\underline{\sigma}_{\mathrm{ODTLES}_{\theta j}}^{\mathrm{temporal}}. \tag{98}$$

This model assumption leads to a temporal *ODTLES* model error terms replacing Eqs. (94) and (95):

$$\underline{\sigma}_{\mathrm{ODTLES}_{ij}}^{\mathrm{temporal}}=\begin{pmatrix}\partial_{x_2}\check{u}_{1,2}'\check{u}_{1,i}+\partial_{x_3}\check{u}_{1,3}'\check{u}_{1,i}\\ \partial_{x_1}\check{u}_{2,1}'\check{u}_{2,i}+\partial_{x_3}\check{u}_{2,3}'\check{u}_{2,i}\\ \partial_{x_1}\check{u}_{3,1}'\check{u}_{3,i}+\partial_{x_2}\check{u}_{3,2}'\check{u}_{3,i}\end{pmatrix}, \tag{99}$$

$$\underline{\sigma}_{\mathrm{ODTLES}_{\theta j}}^{\mathrm{temporal}}=\begin{pmatrix}\partial_{x_2}\check{u}_{1,2}'\check{\theta}_1+\partial_{x_3}\check{u}_{1,3}'\check{\theta}_1\\ \partial_{x_1}\check{u}_{2,1}'\check{\theta}_2+\partial_{x_3}\check{u}_{2,3}'\check{\theta}_2\\ \partial_{x_1}\check{u}_{3,1}'\check{\theta}_3+\partial_{x_2}\check{u}_{3,2}'\check{\theta}_3\end{pmatrix}. \tag{100}$$

The error term in Eqs. (99) and (100) summarize all fluctuating terms not in *ODT*-direction x_k. Again these error terms are controlled by the *CFL*-number.

Applying the time scale separation to the advecting velocities leads to a modified *XLES* momentum equation (cf. Eq. (101)):

$$\begin{aligned}0=&\partial_{x_i}\left\langle\underline{\hat{p}}\right\rangle+\left(\partial_t-\nu\sum_{j=1}^{3}\partial_{x_j}^2\right)\underline{\hat{u}}_i+\sum_{j=1}^{3}\partial_{x_j}\langle\underline{\hat{u}}_j\rangle*\underline{\hat{u}}_i-g_2\underline{\hat{\theta}}+\underline{\hat{F}}_i\\ &+\underline{\mathcal{M}}_{\mathrm{ODT}}^{i}+\underline{\sigma}_{u_i}^{\mathrm{spatial}}+\underline{\sigma}_{\mathrm{ODTLES}_{u_i}}^{\mathrm{temporal}}\\ &+\sum_{j=1}^{3}\underline{\underline{l}}^{\dagger}*\partial_{x_j}\underline{\underline{C}}\left(\langle\underline{\hat{u}}_j\rangle*\underline{\hat{u}}_i-\langle\underline{\overline{u}}_j\rangle^{\mathrm{LES}}*\underline{\overline{u}}_i^{\mathrm{LES}}\right)+\underline{\underline{l}}^{\dagger}*\underline{\underline{C}}\,\underline{\mathcal{M}}_{\mathrm{ODT}}^{i}\end{aligned} \tag{101}$$

and a modified scalar equation (cf. Eq. (85):

$$0 = \left(\partial_t - \kappa \sum_{j=1}^{3} \partial_{x_j}^2 \right) \underline{\hat{\theta}} + \sum_{j=1}^{3} \partial_{x_j} \langle \underline{\hat{u}}_j \rangle * \underline{\hat{\theta}} + \underline{\mathcal{M}}^{\theta}_{\mathrm{ODT}} + \underline{\sigma}_{\theta}^{\mathrm{spatial}} + \underline{\sigma}^{\mathrm{temporal}}_{\mathrm{ODTLES}_{\theta}} \tag{102}$$

$$+ \sum_{j=1}^{3} \underline{\underline{l}}^{\dagger} * \partial_{x_j} \underline{\underline{C}} \left(\langle \underline{\hat{u}}_j \rangle * \underline{\hat{\theta}} - \langle \underline{\overline{u}}_j \rangle^{\mathrm{LES}} * \underline{\overline{\theta}}^{\mathrm{LES}} \right) + \underline{\underline{l}}^{\dagger} * \underline{\underline{C}}\, \underline{\mathcal{M}}^{\theta}_{\mathrm{ODT}}.$$

The advection terms assumed to be modeled directly by *ODT* (involving 3 velocity components) are:

$$\underline{\mathcal{M}}^{i}_{\mathrm{ODT}} = \sum_{j=1}^{3} \left(\underline{\underline{l}}^{2D} \underline{\mathcal{M}}_{ij} + \partial_{x_i} \underline{\hat{p}}' + \partial_{x_j} \underline{\hat{u}}_j' * \underline{\hat{u}}_i \right) \tag{103}$$

$$\underline{\mathcal{M}}^{\theta}_{\mathrm{ODT}} = \sum_{j=1}^{3} \left(\underline{\underline{l}}^{2D} \underline{\mathcal{M}}_{\theta j} + \partial_{x_j} \underline{\hat{u}}_j' * \underline{\hat{\theta}} \right). \tag{104}$$

The derivation of the *ODTLES* microscale term $\underline{\mathcal{M}}_{\mathrm{ODT}} = \{\underline{\mathcal{M}}^{i}_{\mathrm{ODT}}, \underline{\mathcal{M}}^{\theta}_{\mathrm{ODT}}\}$ in Eqs. (101) and (102) is tailored for *ODT*, which is emphasized by the acronym *ODT*. Additionally the *ODT* advancement is coupled between the *XLES-grid*s due to $\underline{\underline{l}}^{\dagger} * \underline{\underline{C}}\, \underline{\mathcal{M}}_{\mathrm{ODT}}$.

The term $\partial_{x_i} \underline{\hat{p}}' = \underline{\underline{l}}^{2D} \partial_{x_i} \underline{p}'$ describes pressure fluctuations. By construction *ODT* is mass conservative, nevertheless pressure fluctuations are modeled by applying the so called 'pressure scrambling' (see section 3.3).

The full *ODTLES* advancement cycle is summarized in section 3.5.5.

An alternative approach to include the *ODT* advancement cycle into a 3D approach is applied by Cline [18] within the lattice-based multiscale simulation (*LBMS*): Each individual turbulent event within the *ODT* advancement is coupled. This approach introduces small time scale communication within a parallel algorithm, potentially impactful for highly turbulent flows with many *ODT* turbulent events.

3.4.5 *XLES: Mass Conservation*

In the incompressible flow regime, the filtered velocity fields need to be divergence free to ensure mass conservation. Because the *XLES* dynamics take place on the integral time scale (τ), the 2D filtered mass equation Eq. (4) (in *XLES* vector notation)

$$0 = \sum_{i=1}^{3} \partial_{x_i} \underline{\underline{l}}^{2D} \langle \underline{u} \rangle_i = \sum_{i=1}^{3} \partial_{x_i} \langle \underline{\overline{u}}_i \rangle^{\mathrm{LES}} + \sum_{i=1}^{3} \partial_{x_i} \langle \underline{\check{u}}_i \rangle, \tag{105}$$

is decomposed into 3D large scale velocity fields $\langle \underline{\overline{u}}_i \rangle^{\mathrm{LES}}$ and *RSS* velocities $\langle \underline{\check{u}}_i \rangle$. Eq. (105) is enforced on the integral time scale τ by the procedure described in this section, while velocity fluctuations (corresponding to the small time scale), described by the *ODT* advancement, are mass conservative by construction (see section 3.3).

A possible approach to solve Eq. (105) is to ensure mass conservation for both decomposed velocity fields $\langle \underline{\overline{u}}_i \rangle^{\mathrm{LES}}$ and $\langle \underline{\check{u}}_i \rangle = \underline{\underline{s}}^{1D} \langle \underline{u_i} \rangle$:

1. The equation $0 = \sum_{i=1}^{3} \partial_{x_i} \langle \underline{\overline{u}}_i \rangle^{\mathrm{LES}}$

   corresponds to the mass conservation in *LES* schemes. A standard discrete approach applied in *LES* can be used. In our implementation a pressure Poisson equation is solved (see section 2.1.3). This leads to a large scale pressure field $\left\langle \underline{\overline{p}} \right\rangle^{\mathrm{LES}} = \underline{\underline{l}}^{3D} \langle \underline{p} \rangle$, whose gradient enforces a divergence free velocity field $\langle \overline{u}_i \rangle^{\mathrm{LES}}$ by solving $\partial_t \langle \overline{u}_i \rangle^{\mathrm{LES}} + \partial_{x_i} \left\langle \underline{\overline{p}} \right\rangle^{\mathrm{LES}} = 0$ (cf. Eq. (21)).

2. The equation $0 = \sum_{i=1}^{3} \partial_{x_i} \langle \underline{\check{u}}_i \rangle$,

   corresponding to the *RSS* velocity fields, is discretely fulfilled without additional effort under some conditions.

   In appendix (A.2) the *XLES* mass conservation is derived in detail and three conditions are identified to ensure the *RSS* velocities to be divergence free:

   - Consistency condition: $\langle \overline{u}_{k,i} \rangle^{\mathrm{LES}}$ is equal in all *XLES-grid*s k which is valid due to the coupling terms $\left\langle \underline{\mathcal{X}}_{ij}^{\mathrm{XLES}} \right\rangle$ and $\left\langle \underline{\underline{l}}^{\dagger} * \underline{\underline{C}}\, \underline{\mathcal{M}}_{\mathrm{ODT}}^{i} \right\rangle$ (see section 2.1.3).
   - A divergence free 3D large scale velocity field which is valid after the standard pressure projection.
   - A tensor product of discrete 1D box filters (averaging) defined in Eq. (56) is used. Here we use the coarse-grained (large scale) and staggered control volume of the size $\Delta x_k^{\mathrm{LES}}$ (this cell size equals the filter size) shown in figure 4a. Please note this filter definition is only used explicitly to create $\langle \overline{u}_i \rangle^{\mathrm{LES}_d} = [l_k^d] \langle \hat{u}_{k,i} \rangle$ within the coupling terms and the mass conservation.

In summary the discrete mass conservation is assured by a standard 3D approach (large scale) with $\mathcal{O}(N_{\mathrm{LES}}^3)$ cells, if a discrete box filter and a staggered grid are used. Especially the Poisson problem can limit the parallel scalability of *DNS* implementations (it scales with $\mathcal{O}(N_{\mathrm{DNS}}^3)$ per timestep).

In *XLES* the velocity fields, including consistent 3D large scale informations, are discretely interpreted in three *XLES-grid*s simultaneously. Owing to the absence of a 3D small scale velocity field, small scale pressure effects vanish from the equations: $[l_k^{-1^d} l_k^d] \langle \hat{p} \rangle = \langle \hat{p} \rangle$, but *ODT* explicitly models small time scale pressure effects (see section 3.3). For the *XLES* system of equations an existing redundancy of the discrete velocity fields can be exploited by deriving the velocity components $\underline{\hat{u}}^{d}_{k,k}$ within each 3D large scale cell due to a direct solution, *w.l.o.g.* in *XLES-grid* 1:

$$\begin{aligned}\hat{u}^{d}_{1,1}\left(\frac{-\Delta x_1^{\mathrm{LES}}}{2}+x_1\right) &= \overline{u}_1^{d,\,\mathrm{LES}}\left(-\frac{\Delta x_1^{\mathrm{LES}}}{2}\right)\\ &\quad-\int_{-\frac{\Delta x_1^{\mathrm{LES}}}{2}}^{-\frac{\Delta x_1^{\mathrm{LES}}}{2}+x_1}\partial_{x_2}\hat{u}^{d}_{1,2}\,dx_1'-\int_{-\frac{\Delta x_1^{\mathrm{LES}}}{2}}^{-\frac{\Delta x_1^{\mathrm{LES}}}{2}+x_1}\partial_{x_3}\hat{u}^{d}_{1,3}\,dx_1'\end{aligned}\tag{106}$$

for $x_1 \leqslant \Delta x_1^{\mathrm{LES}}$. Eq. (106) is a semi discrete interpretation of Gauss's theorem for a divergence free velocity field, here for velocities in *XLES-grid* 1 (see figure 4b) within one 3D large scale cell (see figure 4a) on a staggered grid (no interpolation necessary).

Since *w.l.o.g.* $\hat{u}_{1,1}$ is specified due to Eq. (106), the momentum equation Eq. (101) in *XLES-grid* 1 only needs to be solved for $i = \{2,3\}$. In consequence 6 momentum equations are dynamically solved (2 velocity components in each of 3 *XLES-grid*s), while 3 velocity components can be derived by Eq. (106).

These reduced momentum equations can be expressed by multiplying a Kronecker delta operator matrix

$$\underline{\underline{\mathbb{1}}}-\underline{\underline{\delta_i}}=\begin{pmatrix}1-\delta_{1i} & 0 & 0\\ 0 & 1-\delta_{2i} & 0\\ 0 & 0 & 1-\delta_{3i}\end{pmatrix},\ \text{with}\,(1-\delta_{ki})=\begin{cases}0,\ \text{if}\,k=i\\ 1,\ \text{else}\end{cases}\tag{107}$$

to the momentum equation (101), leading to

$$\begin{aligned}0 =&(\underline{\underline{\mathbb{1}}}-\underline{\underline{\delta_i}})\left(\partial_{x_i}\left\langle\underline{\overline{p}}\right\rangle^{\mathrm{LES}}+\left(\partial_t-\nu\sum_{j=1}^{3}\partial^2_{x_j}\right)\underline{\hat{u}}_i+\sum_{j=1}^{3}\partial_{x_j}\left\langle\underline{\hat{u}}_j\right\rangle*\underline{\hat{u}}_i\right)\\ &+(\underline{\underline{\mathbb{1}}}-\underline{\underline{\delta_i}})\left(\sum_{j=1}^{3}\left(\underline{\underline{l}}^{\dagger}*\underline{\underline{C}}\partial_{x_j}(\left\langle\underline{\hat{u}}_j\right\rangle*\underline{\hat{u}}_i-\left\langle\underline{\overline{u}}_j\right\rangle^{\mathrm{LES}}*\underline{\overline{u}}_i^{\mathrm{LES}})\right)\right)+(\underline{\underline{\mathbb{1}}}-\underline{\underline{\delta_i}})\sum_{j=1}^{3}(\underline{\sigma}^{\mathrm{spatial}}_{\mathrm{XLES}_{ij}}+\sigma_{\mathrm{ODT}_{ij}})\\ &+(\underline{\underline{\mathbb{1}}}-\underline{\underline{\delta_i}})\sum_{j=1}^{3}\left(\underline{\underline{l}}^{2D}\underline{\mathcal{M}}^{i}_{\mathrm{ODT}}\right)+(\underline{\underline{\mathbb{1}}}-\underline{\underline{\delta_i}})\sum_{j=1}^{3}\left(\underline{\underline{l}}^{\dagger}*\underline{\underline{C}}\,\underline{\underline{l}}^{2D}\underline{\mathcal{M}}^{i}_{\mathrm{ODT}}\right).\end{aligned}\tag{108}$$

Please note the Kronecker delta operator matrix is also applied to the *ODTLES* momentum microscale term ($\underline{\mathcal{M}}^{i}_{\mathrm{ODT}}$) and therefore can be exploited within a model approach, which leads to an *ODT* model with 2 velocity components (see section 3.3). Additionally the factor $\frac{1}{3}$ within Eq. (82) can be replaced by $\frac{1}{2}$. We introduce the reduced *ODTLES* microscale term $\underline{\mathcal{M}}^{\delta_i}_{\mathrm{ODT}} =$

$\{(\underline{\underline{\mathbb{1}}} - \underline{\underline{\delta_i}})\underline{\mathcal{M}}^{i}_{ODT}, \underline{\mathcal{M}}^{\theta}_{ODT}\}$, which contains 2 velocity components per vector element.

Since in *XLES* no 3D small scale velocity field is defined, small scale pressure effects can only be captured by the modeling approach, in *ODT* due to 'pressure scrambling' (see section 3.3).

Note that the Kronecker delta operator matrix is not applied to the scalar equation (102), because for the scalar fields only the 3D large scale field $\overline{\theta}^{LES}$ is redundant, corresponding to the consistency condition which is enforced due to coupling terms (see section 3.4.6).

In the *XLES* and especially *ODTLES* implementation the *XLES* velocity fields calculated due to Eq. (106) are checked in each timestep to be consistent with the boundary condition. The computed inconsistency does not exceed 10^{-12} which lies in the range of the chosen floating point accuracy.

In general an *XLES* approach with 3 velocity components in each *XLES-grid* is possible. Such *XLES* momentum equations are derived similarly to the scalar *XLES* equation introduced in section 3.4.3.

3.4.6 *XLES: Consistency Preservation*

Both, the *XLES* mass conservation in section 3.4.5 and the coupling terms in sections 3.4.2.2 and 3.4.2.3 assume the 3D large scale solution fields $\underline{\overline{\phi}}_i^{LES} = \{\underline{\overline{u}}_i^{LES}, \underline{\overline{\theta}}^{LES}\}$ to be consistent, meaning each *XLES-grid* k contains the identical 3D large scale field: $\overline{\phi}_i^{LES} = \overline{\phi}_{k,i}^{LES} \equiv [l_k]\hat{\phi}_{k,i}$ with $[l_k]$ being defined in Eq. (56) and $\overline{\phi}_{k,i}^{LES} = \{\overline{u}_{k,i}^{LES}, \overline{\theta}_k^{LES}\}$.

In the *XLES* vector notation this condition can be written as:

$$\underline{\underline{l}}^{1D}\underline{\hat{\phi}}_i = \underline{\overline{\phi}}_i^{LES} = \overline{\phi}_i^{LES}\begin{pmatrix}1\\1\\1\end{pmatrix} \tag{109}$$

with the 1D filter matrix defined in Eq. (60). This means consistency preserving terms should be independent of the *XLES-grid* k.

We assume that the initial conditions are consistent (this can easily be achieved) and need to prove a consistency preserving *XLES*-advancement including advective and diffusive terms and the sub-grid modeling.

The 'directly resolved' advection terms themselves ($\partial_{x_j}\underline{\hat{u}}_j * \underline{\hat{\phi}}_j$) are violating the consistency condition, but by including the corresponding coupling ('indirectly resolved' terms):

$$\partial_{x_j}\underline{\hat{u}}_j * \underline{\hat{\phi}}_i + \underline{\underline{l}}^{\dagger} * \partial_{x_j}\underline{\underline{C}}\left(\langle\underline{\hat{u}}_j\rangle * \underline{\hat{\phi}}_i - \langle\underline{\overline{u}}_j\rangle^{LES} * \underline{\overline{\phi}}_i^{LES}\right), \tag{110}$$

the consistency is preserved. The same is valid for unresolved terms and their couplings: $\underline{\underline{l}}^{2D}\underline{\mathcal{M}}_{\phi j} + \underline{\underline{l}}^{\dagger a} * \underline{\underline{C}}\,\underline{\underline{l}}^{2D}\underline{\mathcal{M}}_{\phi j}$ (proof by insertion).

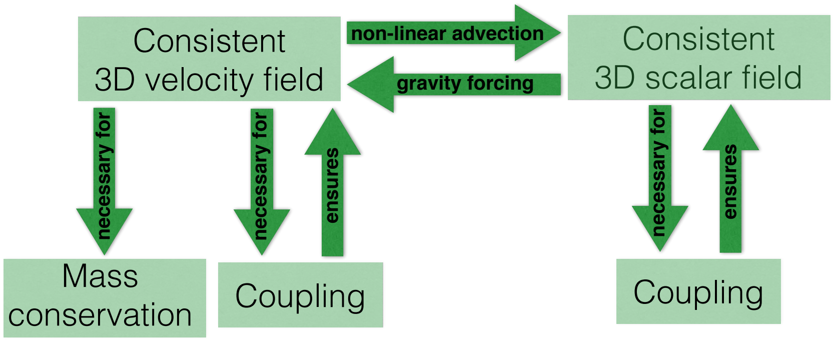

Figure 5: On the one hand the consistency preservation is invoked before the advection step to define the coupling terms. On the other hand the coupling guarantees the consistency to be still preserved after the advection step. The velocity and scalar fields depend on each other due to physical motivated terms, e. g. the gravitational forcing term.

By rearranging the *XLES* advection terms and their corresponding couplings, we find:

$$\underline{\hat{u}}_j * \underline{\hat{\phi}}_i + \underline{\underline{l}}^\dagger * \partial_{x_j} \underline{\underline{C}} \left(\langle \underline{\hat{u}}_j \rangle * \underline{\hat{\phi}}_i - \langle \underline{\overline{u}}_j \rangle^{\mathrm{LES}} * \underline{\overline{\phi}}_i^{\mathrm{LES}} \right) = \underline{\overline{u}}_j * \underline{\overline{\phi}}_i - \underline{\sigma}_{\mathrm{XLES}_{\phi j}} \qquad (111)$$

with $\overline{\phi}_{k,i} = [l_1 l_2 l_3 + s_1 l_2 l_3 + l_1 s_2 l_3 + l_1 l_2 s_3]\phi_i$, which is equal in all *XLES-grid*s k. Note that the term $\underline{\sigma}_{\mathrm{XLES}_{\phi j}}$ is also equal in all *XLES-grid*s (cf. Eqs. (76) and (77)). Thus *XLES* can alternatively be interpreted to advance $\underline{\overline{\phi}}_i$ with the coupled advection terms in Eq. (111). In this interpretation the *XLES* residual stress tensor (Eq. (64)) would only include terms modeled by *ODT*. Since $\underline{\mathcal{X}}_{ij}^{\mathrm{XLES}}$ is approximated by a simplifying linearization, it is reasonable to include $\underline{\mathcal{X}}_{ij}^{\mathrm{XLES}}$ and $\underline{\mathcal{X}}_{\theta j}^{\mathrm{XLES}}$ to the residual stress instead of the advection term.

In the implementation of *XLES-U* and *ODTLES* we check that the 3D large scale velocity and scalar fields are still consistent every 100 timesteps to avoid numerical errors violating consistency preservation. All computations show the consistency to be limited by the floating point accuracy.

3.4.7 *XLES: 'LES-limit' and 'DNS-limit'*

In the limit $N_{\mathrm{RSS}} \rightarrow N_{\mathrm{LES}}$ the 2D filtered *XLES-U* equations collapse to the 3D filtered *LES-U* equations in each *XLES-grid*, because the *RSS* velocities vanish: $\underline{\check{\phi}}_i = \underline{\hat{\phi}}_i - \underline{\overline{\phi}}_i^{\mathrm{LES}} = 0$ and therefore $\underline{\sigma}_{\mathrm{XLES-U}_{ij}}^{\mathrm{spatial}}$ and $\underline{\sigma}_{\mathrm{XLES-U}_{\theta j}}^{\mathrm{spatial}}$ also vanish.

For $N_{\mathrm{LES}} \rightarrow N_{\mathrm{DNS}}$ in each direction, all velocity scales are resolved by the 3D grid and *XLES-U* (and *LES-U*) converges to *DNS*.

Within the *ODT* model, applied as an *SGM* within *ODTLES*, all turbulent events are suppressed in the 'DNS-limit'. Thus *DNS* is also a distinguished limit of *ODTLES*.

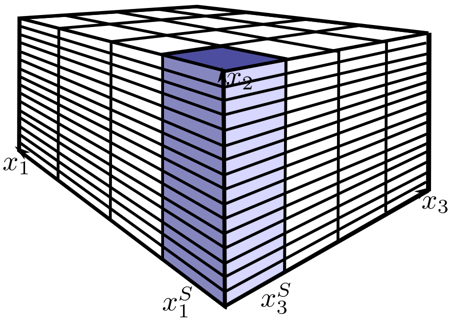

Figure 6: Illustrative 1D stack in *XLES-grid* 2 in x_2-direction at (x_1^S, x_3^S).

The 'LES-limit' and 'DNS-limit' also hold for the scalar equation (102) by assuming a *LES-U* respective *DNS* approximation of the Oberbeck-Boussinesq equations Eqs. (1) – (3).

Results in section 4.1.4 show *XLES-U*, *LES-U*, and *ODTLES* to converge towards *DNS*.

3.5 ODT CLOSED XLES (ODTLES)

In this section *ODT* is interpreted as a microscale model within the *XLES* approach. In *ODT* a stochastic process mimics 3D turbulent advection within a 1D sub-domain. Thus, an interpretation of the *ODT* turbulent advection in terms of the Navier-Stokes advection is not straightforward and *ODTLES* is not directly deducible from filtered Navier-Stokes equations.

Nevertheless *XLES* microscale terms w.l.o.g. in *XLES-grid* 2 ($\mathcal{M}_{2,ODT}^{\delta_i}$ in Eq. (103)) are interpreted by $N_{LES_1} \times N_{LES_3}$ so called stacks, each containing highly resolved 1D information, e.g. defined by one line at (x_1^S, x_2, x_3^S) with constant x_1^S and x_3^S (see figure 6). The unresolved terms $\mathcal{M}_{2,ODT}^{\delta_i}(x_1^S, x_2, x_3^S)$ in each of these stacks S contain 2 velocity components and can be modeled by the *ODT* advancement (Eq. (46)):

$$\mathcal{M}_{2,ODT}^{\delta_i}(x_1^S, x_2, x_3^S) = e_{2,i}(\hat{u}_{2,i}; x_2, l) + \sigma_{k,ODT}\,, \text{ and } l \leqslant l_{max} = \Delta x_k^{LES} \qquad (112)$$

with the *ODT* momentum error term ($\sigma_{ODT_{ij}}$). Note that the *ODT* model introduced in section 3.3 also advances 2 velocity components which are orthogonal to the x_k-direction.

The maximum eddy size (l_{max}) within the *ODT* model corresponds to the largest (global) scale. By using *ODT* as a model within the *XLES* framework, the maximum eddy size l_{max} defines the boundary between turbulent scales described by the 3D advection scheme and by the *ODT* turbulent advection. Since *ODT* should capture turbulent effects not resolved by the 3D advection scheme, the maximum eddy size (l_{max}) mainly depends on the numerical properties of the 3D advection scheme and needs to be determined by numerical tests (see section 4.1.3). We found $l_{max} = \Delta x_k^{LES}$ to be convenient, which corresponds to the ability of the implemented numerical advection scheme to resolve e.g. the Kolmogorov length scale (η_K) with approximately one 3D cell in the 'DNS-limit' of *XLES* (all scales are represented in 3D) as described in section 4.1.4. Additionally the choice $l_{max} = \Delta x_k^{LES}$ corresponds to a numerical sub-filter parameter (Q) in the range of one. *ODTLES* computations in section 4.1.2 and especially the shown spectrum of the streamwise turbulent kinetic energy (in figure 23) confirm $l_{max} = \Delta x_k^{LES}$ to be appropriate.

Closure of *XLES* can involve any form of modeling that specifies the *RSS* time advancement on an entire *XLES-grid* such as *XLES-grid* 2 shown in figure 4c. This is not required to involve a collection of model instantiations on individual stacks, such as the illustrative stack in that figure. Nevertheless, *ODT* advancements within *ODTLES* are formulated in this way. On this basis, the *XLES* 3D advection can be viewed as a form of coupling of the *ODT* stacks within one grid. In this context, the grid-to-grid coupling can be seen as a higher level of coupling. This is mentioned because previous *ODTLES* formulations (cf. section 3.5.6) did not envision the *XLES* closed by *ODT*. Thereby *ODT* is not the only conceivable *RSS* closure strategy within an *XLES-grid*.

3.5.1 *ODTLES: ODT Modeling Effects*

ODT introduces local turbulent events depending on the local flow state. In low Reynolds number channel flows the 3D grid is under-resolved only in the near-wall region (unless the grid is very coarse) and thus *ODT* works as a dynamical and highly accurate near-wall model, as figure 7a illustrates. Thus *ODTLES* overcomes the lower quality of *ODT* stand-alone simulations for low Reynolds number flows. For highly turbulent flows, the 3D resolution in the core region of the channel is under-resolved too: In this case ODT small scale eddy events additionally occur in the core region introducing local turbulent transport effects, as figure 7b illustrates.

In contrast to wall-modeled *LES*, the *ODT* turbulent transport treats all regions consistently without introducing additional assumptions for the near-wall region.

Additionally the *ODT* modeling depends on a fully resolved (1D) flow state and thus allows dominant small scale effects (e.g. local stratification, chemical processes, ...), which are not well captured by commonly applied eddy viscosity models.

Note that *ODT* 'eddies' occur mainly in wall-normal *ODT*-lines, because the *ODT* parameters are adjusted for wall-bounded flow (see *ODT* parameter study in section 4.1.1).

3.5.1.1 *ODTLES Modeling: Connection to Implicit LES*

Von Larcher et al. [110] uses an *FEM-BV-VX* approach by Horenko [40] which "makes use of Finite-Element Method (FEM)-based time series analysis with

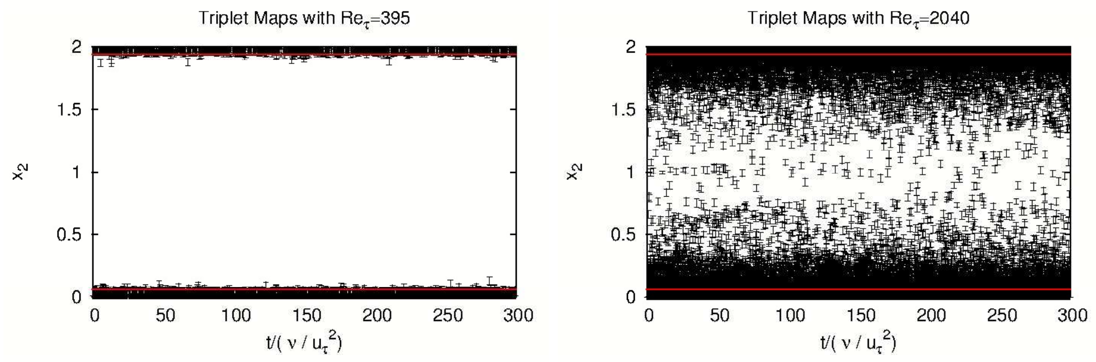

(a) Eddies at $Re_\tau = 395$.

(b) Eddies at $Re_\tau = 2040$.

Figure 7: *ODT* turbulent events ('eddies') illustrated as error bars occurring in *XLES-grid* 2 (superposition of eddies in wall-normal direction x_2). The size of the 3D cell closest to the walls is illustrated by red lines ($N_{LES} = 32$). For low Reynolds numbers, *ODT* primarily acts as a near-wall model (7a); for high Reynolds numbers *ODT* acts as a sub-grid model over a larger extent of the flow domain (7b).

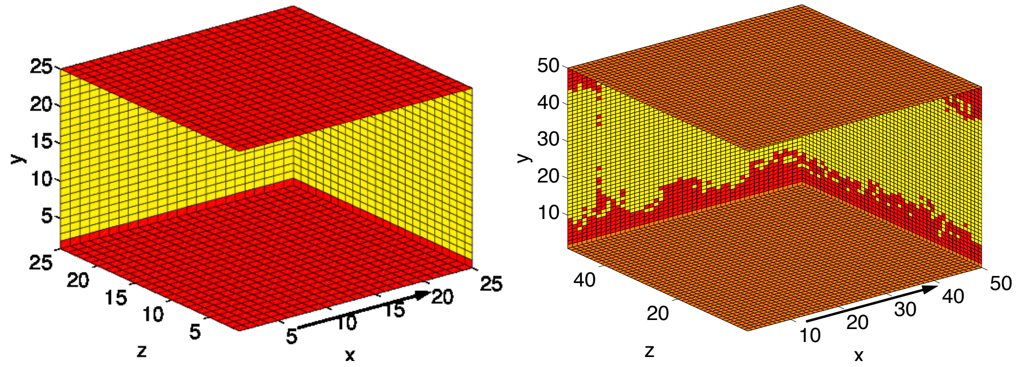

(a) $N_{LES} = 25$: 2 local models: core model (yellow) and wall model (red).

(b) $N_{LES} = 50$: 3 local models: core model (yellow), transition model (red), and wall model (brown).

Figure 8: Implicit *LES* channel flow study by von Larcher et al. for $Re_\tau = 590$ and different resolutions $N_{LES} = \{25, 50\}$. Time series are analyzed by an *FEM-BV-VX* approach. They found 2 respectively 3 local and static models appropriate to reproduce key flow properties. The figures were published by von Larcher et al. [110]:

[Reproduced with permission from T. von Larcher: Towards a Framework for the Stochastic Modelling of Subgrid Scale Fluxes for Large Eddy Simulation, Meteorologische Zeitschrift, 2015. ©2015 Schweizerbart Science Publishers].

bounded variation (BV) of model parameters, and it allows for the simultaneous dimension reduction and identification of dynamical models with external factors"[1] to analyze high order implicit *LES* simulations of a turbulent channel flow with $\mathrm{Re}_\tau = 590$. Hereby the *VX* in *FEM-BV-VX* indicates that a vector model with exogenous variables is used.

For two investigated equidistant resolutions they find:

- $N_{\mathrm{LES}} = 25$ cells per direction:

  The solution is optimally represented by 2 local models where both models are static in time.

- $N_{\mathrm{LES}} = 50$ cells per direction:

  The solution is optimally represented by 3 local models where all models are static in time.

Figure 8 shows the local distribution of the optimal models for $N_{\mathrm{LES}} = 25$ (figure 8a) and $N_{\mathrm{LES}} = 50$ (figure 8b).

The study is compatible with the *ODTLES* 'eddy' distribution in figure 7. The core model by von Larcher et al. [110] corresponds to the *XLES-U* sub-model of *ODTLES* without 'eddies' (cf. figure 8a and 7a), the transitional and the wall models correspond to the full *ODTLES* model (*XLES-U* and *ODT*) indicated by the occurrence of 'eddies' in figure 7. The *ODTLES* interpretation of the transitional model only occurs for the high Reynolds case in figure 7b.

3.5.2 *ODTLES: 'ODT-limit'*

From an algorithmic point of view *ODTLES* includes another distinguished limit that we refer to as the 'ODT-limit': *ODTLES* collapses to the *ODT* stand-alone model if only one 3D large scale cell represents the full computational domain (Ω). In this case there are no fluxes corresponding to *XLES-U*, but *ODT* turbulent effects are simulated.

From an physical point of view in the 'ODT-limit' only property variations in one direction can occur within the control volume. Thus a physically reasonable behavior requires a certain symmetry properties to allow a one-dimensional description.

For such a symmetric case, e. g. a turbulent channel with infinite walls, the 'ODT-limit' can be used to estimate the *ODT* momentum error term ($\sigma_{\mathrm{ODT}_{ij}}$) by comparing *ODT* and *DNS* (see 4.1.2).

The ability of *ODT* to describe the full spectrum of 3D turbulent effects is a required property to get an *ODTLES* 3D resolution largely independent of the turbulent intensity unless Reynolds-number variations trigger a global flow structure transition (see duct flow in section 4.2.1). Indeed, demonstrated model performance in the 'ODT-limit' (i.e. *ODT* stand-alone, see 4.1.2) strongly

---

[1] von Larcher et al. [110]

indicates that *ODT* adequately describes the *XLES-SGS* terms. This is also supported by *ODTLES* results that are shown to be in good agreement with *DNS* in chapters 4 and 5. Unfortunately a detailed theoretical investigation of the 'ODT-limit' requires a convenient *ODT* interpretation in Navier-Stokes terms, which is not derived to a satisfying level yet, but ensemble statistics are formally analogous to corresponding Navier-Stokes terms to a considerable extent (e.g. the interpretation of *ODT* budget terms of the turbulent kinetic energy in 4.1.2).

3.5.3 *ODTLES: ODT Momentum Coupling*

The turbulent *ODT* advection $e_{\phi_{k,i}}$ (in *XLES-grid* k) models the unresolved *XLES* terms $\underline{\mathcal{M}}^{\delta_i}_{\mathrm{ODT}}$. These are coupled across the *XLES-grid*s due to the *SGS* coupling term $\underline{\underline{l}}^{\dagger} * \underline{\underline{C}}\,\underline{\mathcal{M}}^{\delta_i}_{\mathrm{ODT}}$ (see also Eq. (108)). The *ODT* diffusion terms $\mathcal{D}_{\mathrm{ODT}_k} = (-\nu)\partial^2_{x_k}\hat{u}_{k,i}$ (for $k \neq i$) in *XLES-grid* k represent the molecular diffusion as a continuum and are connected to the *XLES* diffusion terms $(\underline{\underline{\mathbb{1}}} - \underline{\underline{\delta}}_i)(-\nu)\sum_{j=1}^{3}\partial^2_{x_j}\underline{\hat{u}}_{k,i}$. The *XLES* diffusion terms *w.l.o.g.* in *XLES-grid* 1:

$$\nu\partial^2_{x_1}\hat{u}_{1,i} + \nu\partial^2_{x_2}\hat{u}_{1,i} + \nu\partial^2_{x_3}\hat{u}_{1,i}\ , \quad \text{with}\, i = \{2,3\} \tag{113}$$

are solved in three ways:

1. Diffusion 'directly resolved' by *ODT*: $\underline{\mathcal{D}}_{\mathrm{ODT}}$

   The terms $-\nu\partial^2_{x_1}\hat{u}_{1,i}$ with $i = \{2,3\}$ in Eq. (113) are interpreted by *ODT* incorporated in *XLES-grid* 1. These terms are resolved by N_{RSS} cells (representing molecular diffusion, similar to *DNS*)

2. Diffusion 'indirectly resolved' by *ODT*: $\underline{\underline{l}}^{\dagger} * \underline{\underline{C}}\,\underline{\mathcal{D}}_{\mathrm{ODT}}$

   The terms $-\nu\partial^2_{x_2}\hat{u}_{1,3}$ and $-\nu\partial^2_{x_3}\hat{u}_{1,2}$ in Eq. (113) are interpreted by *ODT* domains residing in *XLES-grid* 2 respectively *XLES-grid* 3. E. g. , the first term is coupled from *XLES-grid* 2 to *XLES-grid* 1 by $-[l_1^{-1}][l_2]\nu\partial^2_{x_2}\hat{u}_{2,3}$ (index notation for $\underline{\underline{l}}^{\dagger} * \underline{\underline{C}}\,\underline{\mathcal{D}}_{\mathrm{ODT}}$). The diffusion is fully resolved, but additionally averaged (convolved) and reconstructed (deconvolved, cf. section 3.6.1).

3. Diffusion resolved by *XLES*: $\underline{\mathcal{D}}_{\mathrm{XLES}}$

   The terms $-\nu\partial^2_{x_2}\hat{u}_{1,2}$ and $-\nu\partial^2_{x_3}\hat{u}_{1,3}$ in Eq. (113) are not interpreted by *ODT* in any *XLES-grid* (this is caused by $(\underline{\underline{\mathbb{1}}} - \underline{\underline{\delta}}_i)$; see section 3.4.5). A numerical interpretation is possible within *XLES-grid* 1 using N_{LES} cells: $-\nu\partial^2_{x_i}\hat{u}_{1,i}$ with $i = \{2,3\}$. These diffusive terms are not resolved down to the molecular level. The *XLES* resolved diffusion terms are written as $\underline{\mathcal{D}}_{\mathrm{XLES}}$ and numerically represented by an explicit Euler scheme in time and a spatial central difference scheme (see also section 3.5.5).

In summary the *ODT* model is incorporated into *XLES-grid* k by interpreting diffusive effects $\mathcal{D}_{\mathrm{ODT}_k}$ and the unresolved advection terms $\mathcal{M}^{\delta_i}_{\mathrm{ODT}_k}$:

$$\mathcal{M}^{\delta_i}_{\mathrm{ODT}_k} - \nu \partial^2_{x_k} \hat{u}_{k,i} = e_{u_{k,i}} + \mathcal{D}_{\mathrm{ODT}_k}(\hat{u}_{k,i}) + \sigma_{\mathrm{ODT}_{k,ij}}, \text{ for } i \neq k \tag{114}$$

Additionally the (diffusive and advective) *ODT* terms are coupled between the *XLES-grids* by $\underline{\underline{l}}^{\dagger} * \underline{\underline{C}}(\underline{e}_{u_i} + \underline{\mathcal{D}}_{\mathrm{ODT}}(\underline{\hat{u}}_i))$. *XLES* diffusion terms $\underline{\mathcal{D}}_{\mathrm{XLES}}$ are introduced to represent diffusive terms not captured by *ODT*.

The under-resolved diffusion terms $\underline{\mathcal{D}}_{\mathrm{XLES}}$ are generally smaller than the correct local diffusion and might be omitted in typical applications. Nevertheless these terms are conceptually desirable, because they allow the correct behavior in the 'DNS-limit' (and are included in all computations in this thesis). Note that omitting those terms might also enhance the parallel efficiency.

3.5.4 *ODTLES: ODT Scalar Coupling*

The main difference between the treatment of the *XLES* velocity $\hat{u}_{k,i}$ and the *XLES* scalar $\hat{\theta}_k$ in each individual *XLES-grid* k is that due to the mass conservation (in section 3.4.5) a redundancy of the discrete velocity fields $\hat{u}^d_{k,i}$ is exploited and thus only $\hat{u}_{k,i}$ with $k \neq i$ is dynamically treated. For the scalar field $\hat{\theta}_k$ the only redundancy corresponds to the existence of a scalar large scale $\overline{\theta}^{\mathrm{LES}} = [l^d_k]\hat{\theta}_k$ which is consistent with all scalars $\hat{\theta}_k$ in different *XLES-grids* (see section 3.4.6).

Thus the *XLES* diffusion terms *w.l.o.g.* on *XLES-grid* 1

$$\kappa \partial^2_{x_1} \hat{\theta}_1 + \kappa \partial^2_{x_2} \hat{\theta}_1 + \kappa \partial^2_{x_3} \hat{\theta}_1 \tag{115}$$

are resolved in three different *XLES-grids*: The diffusion term represented by *ODT*-lines in *XLES-grid* k is $\mathcal{D}_{\mathrm{ODT}_k} = -\kappa \partial^2_k \hat{\theta}_k$. E. g. *XLES* diffusion terms in *XLES-grid* 1 are fully resolved by N_{RSS} cells (representing molecular diffusion, similar to *DNS*) and additionally averaged (convolved) and reconstructed (deconvolved) for $k \neq 1$ (coupled diffusion terms). Thus the *ODT* model represents θ_k in *XLES-grid* k by interpreting diffusive effects $\underline{\mathcal{D}}_{\mathrm{ODT}}$ and the unresolved advection terms $\mathcal{M}^{\theta}_{\mathrm{ODT}_k}$

$$\mathcal{M}^{\theta}_{\mathrm{ODT}_k} - \kappa \partial^2_{x_k} \hat{\theta}_k = e_{\theta_k} + \mathcal{D}_{\mathrm{ODT}}(\hat{\theta}_k) + \sigma_{\mathrm{ODT}_\theta}, \text{ for } k, i = \{1, 2, 3\} \tag{116}$$

and its coupling $\underline{\underline{l}}^{\dagger} * \underline{\underline{C}}(\underline{e}_{\theta} + \underline{\mathcal{D}}_{\mathrm{ODT}}(\underline{\hat{\theta}}))$.

An additional *XLES* scalar diffusion term (cf. section 3.5.3) is not required.

The scalar treatment can also be used as a basis for an *ODT* closed *XLES* approach with 3 velocity components in each *XLES-grid*.

In section 3.5.5 the *ODTLES* advancement cycle is described, which in some sense also summarizes sections 3.5.3 and 3.5.4.

3.5.5 *ODTLES: Time Advancement and Synopsis*

To advance the *XLES* equations in time a modified predictor-corrector procedure (cf. section 2.1.3) is used: The *XLES* equations including coupling terms and *ODT* advancement are solved, predicting velocity fields in each *XLES-grid*. Simultaneously time averaged velocity fields are computed. A corrector step enforces the time averaged velocity fields to be divergence free (to ensure mass conservation).

Since the predictor-step involves *ODT* advancement and several coupling terms, a fractional time step algorithm is introduced. Table 5 summarizes the numerical discretizations of the individual fractional steps. The multi-scale nature of *ODTLES* is reflected in the advancement algorithm, which involves spatial as well as temporal operator splitting. The mesh geometry is a two-fold spatial decomposition, consisting of three *XLES-grid*s that are each spatially well resolved in one of the coordinate directions, with a further decomposition of each *XLES-grid* into a 2D array of *ODT* instantiations. Hereby all velocities are discretized using a staggered grid while the scalar field and the pressure are cell-centered. The full time advancement cycle includes predictor (p) and corrector (c) steps:

- (p 4) in table 5:

  The most highly disaggregated time-advancement sub-process is the concurrent autonomous advancement of these *ODT* instantiations (cf. section 3.3). The advective mechanism during this advancement represents turbulent eddy motions not resolved on the coarse 3D grid. In each *ODT* instantiation, only the small eddies aligned with the *XLES-grid* orientation are represented. Therefore this advancement does not account for the effects of small eddies aligned in the other coordinate directions. However, these effects are captured in the *ODT* instantiations within the *XLES-grid*s oriented in those directions. The *ODT* advancement within *ODTLES* also contains the *XLES* diffusion terms ($\mathfrak{D}_{\text{XLES}}$) treated as forcing terms for the *ODT* diffusion solver.

- (p 5) in table 5:

  A coupling correction is applied that modifies each *ODT* state after autonomous *ODT* advancement in order to incorporate the effect of small eddies captured by *ODT* advancement on the other two *XLES-grid*s. This is implemented by evaluating the net eddy-induced property fluxes through each face of the coarse 3D grid. Each of these faces is on the boundary between two adjacent *ODT* domains (or on a flow boundary). The associated property fluxes, evaluated as described in section 3.3, determine property transfers between these *ODT* domains through the faces. These fluxes are applied to the corresponding box-filtered *ODT* states, giving an corrected coarse 3D flow field. This correction is communicated back to the *ODT*-resolved level by means of reconstruction, represented symbolically by the operator $[l_k^{-1}]$ within the convolution and deconvolution matrix $(\underline{\underline{l}}^{\dagger})$. This coupling includes *ODT*-resolved diffusive fluxes (see sections 3.5.3 and 3.5.4).

- (p 2) in table 5:

  Unlike autonomous *ODT* advancement, the subsequent advection sub-process is coarse-grained (though in a time filtered rather than spatially filtered sense) and its advancement is fully 3D within each *XLES-grid*. This captures, in some fashion, the 3D-resolved advective fluxes through all control-volume faces within each *XLES-grid*, but because the three *XLES-grid*s contain separately evolving small-scale structure, the resulting coarse 3D flow field is different on each *XLES-grid*.

- (p 3) in table 5:

  These inconsistencies are corrected in a manner somewhat like the coupling correction used to incorporate directional coupling effects following autonomous *ODT* advancement. As in the correction of autonomous *ODT* advancement, the correction that restores consistency of the coarse 3D flow fields on the three *XLES-grid*s after the 3D advection sub-process is communicated back to the *ODT*-resolved level by means of reconstruction, as indicated symbolically by the operator $[l_k^{-1}]$ within convolution and deconvolution matrix $(\underline{\underline{l}}^{\dagger})$. The corresponding coupled numerical approximations are described and validated in sections 3.6.2 and 3.6.3.

- (c 1), (c 2), and (p 1) in table 5:

  Upon the completion of the corrected 3D advection advancement, the coarse 3D flow fields on the three *XLES-grid*s are consistent, but this consistent flow field does not obey the continuity equation. To restore the solenoidal property of this constant-density flow, pressure projection is applied as indicated in (c 2). As in the other correction procedures, the pressure-projection update is communicated back to the *ODT*-resolved level by means of reconstruction, as indicated symbolically by the 1D deconvolution matrix $\underline{\underline{l}}^{-1} = \begin{pmatrix} l_1^{-1} & 0 & 0 \\ 0 & l_2^{-1} & 0 \\ 0 & 0 & l_3^{-1} \end{pmatrix}$ in (p 1).

Table 5: *ODTLES* time advancement (predictor (p) and corrector (c)). *ODT* indicates the *ODT*-advancement. Individual spatial and temporal discretizations are introduced in section 2. Coupled advection schemes are investigated in sections 3.6.2 and 3.6.3. In step (p 1) the pressure gradient enforces the time averaged velocities to be divergence free. Step (p 2) and (p 3) describe the *XLES-U* advection and coupling, while (p 4) and (p 5) contain the *ODT* advancement and corresponding coupling. The corrector steps (c 1) and (c 2) describe the solution of the pressure Poisson problem on the 3D large scale.

step	advanced term	time	spatial
p 1	$\langle \overline{\underline{u}^*}_i \rangle^{LES} = \langle \overline{\underline{u}}_i \rangle^{LES}(t) + \int_t^{t+\tau} \partial_{x_i} \left\langle \overline{\underline{p}} \right\rangle_t^{LES} dt \; ; \quad \langle \hat{\underline{u}}_i \rangle_t = \underline{\underline{l}}^{-1} \langle \overline{\underline{u}^*}_i \rangle^{LES}$	EE1	UP1
	$\overline{\underline{u}^*}_i{}^{LES} = \overline{\underline{u}}_i{}^{LES}(t) + \int_t^{t+\tau} \partial_{x_i} \left\langle \overline{\underline{p}} \right\rangle_t^{LES} dt \quad ; \quad \hat{\underline{u}}_i^* = \underline{\underline{l}}^{-1} \overline{\underline{u}^*}_i^{LES}$	EE1	UP1
p 2	$\hat{\underline{u}}_i^{**} = \hat{\underline{u}}_i^* + \int_t^{t+\tau} \sum_{j=1}^{3} \partial_{x_j} (\langle \hat{\underline{u}}_j \rangle_t * \hat{\underline{u}}_i^*) \, dt'$	CN-RK3, RK3-RK3	CDM
	$\hat{\underline{\theta}}^* = \hat{\underline{\theta}} + \int_t^{t+\tau} \sum_{j=1}^{3} \partial_{x_j} (\langle \hat{\underline{u}}_j \rangle_t * \hat{\underline{\theta}}) \, dt'$	CN-RK3-RK3	CDM
p 3	$\hat{\underline{u}}_i^{***} = \hat{\underline{u}}_i^{**} + \int_t^{t+\tau} \underline{\underline{l}}^\dagger * \sum_{j=1}^{3} \partial_{x_j} \left(\langle \hat{\underline{u}}_j \rangle_t * \hat{\underline{u}}_i^* - \langle \overline{\underline{u}}_j \rangle_t^{LES} * \overline{\underline{u}}_i^{*,LES} \right) \, dt'$	EE1	CDM
	$\hat{\underline{\theta}}^{**} = \hat{\underline{\theta}}^* + \int_t^{t+\tau} \underline{\underline{l}}^\dagger * \sum_{j=1}^{3} \partial_{x_j} \left(\langle \hat{\underline{u}}_j \rangle_t * \hat{\underline{\theta}} - \langle \overline{\underline{u}}_j \rangle_t^{LES} * \overline{\underline{\theta}}^{LES} \right) \, dt'$	EE1	CDM
p 4	$\hat{\underline{u}}_i^{****} = \hat{\underline{u}}_i^{***} + \int_t^{t+\tau} (e_{u_i}(\hat{\underline{u}}_i^{***}) + \underline{\mathcal{D}}_{ODT}) (\hat{\underline{u}}_i^{***}) \, dt' + \int_t^{t+\tau} \underline{\mathcal{D}}_{XLES}(\hat{\underline{u}}_i^{***}) \, dt' - \int_t^{t+\tau} g_2 \hat{\underline{\theta}}^{**} \, dt'$	IE1, *ODT*, EE1	CDM
	$\hat{\underline{\theta}}^{***} = \hat{\underline{\theta}}^{**} + \int_t^{t+\tau} \left(e_\theta(\hat{\underline{\theta}}^{**}) + \underline{\mathcal{D}}_{ODT} \right) (\hat{\underline{\theta}}^{**}) \, dt'$	IE1 *ODT*	CDM
p 5	$\hat{\underline{u}}_i(t+\tau) = \hat{\underline{u}}_i^{****} + \int_t^{t+\tau} \underline{\underline{l}}^\dagger * \underline{\underline{C}} \, (e_{u_i}(\hat{\underline{u}}_i^{***}) + \underline{\mathcal{D}}_{ODT}) (\hat{\underline{u}}_i^{***}) \, dt'$	EE1	CDM
	$\hat{\underline{\theta}}(t+\tau) = \hat{\underline{\theta}}^{***} + \int_t^{t+\tau} \underline{\underline{l}}^\dagger * \underline{\underline{C}} \left(e_\theta(\hat{\underline{\theta}}^{**}) + \underline{\mathcal{D}}_{ODT} \right) (\hat{\underline{\theta}}^{**}) \, dt'$	EE1	CDM
c 1	$\langle \overline{\underline{u}}_i \rangle_{t+\tau}^{LES} = \underline{\underline{l}}^{1D} \langle \hat{\underline{u}}_i \rangle_{t+\tau} \; ; \quad \overline{\underline{u}}_i^{LES}(t+\tau) = \underline{\underline{l}}^{1D} \hat{\underline{u}}_i(t+\tau)$	1D filter	
c 2	$0 = \sum_{i=1}^{3} \partial_{x_i} \langle \overline{\underline{u}}_i \rangle_{t+\tau}^{LES} \rightarrow \partial_{x_i} \left\langle \overline{\underline{p}} \right\rangle_{t+\tau}^{LES}$	AMG (Poisson problem)	

The subscript (e.g. $\langle\,\rangle_t$) introduced in time averaged properties indicates the time t (averaged over the last time step) respective $t+\tau$ (averaged over the actual time step with the time step size τ).

The *ODT* advancement is for highly turbulent flows the most costly subprocess in the *ODTLES* advancement cycle, which leads to a highly parallelizable algorithm (see section 3.5.8).

3.5.6 *ODTLES: Comparison to Previous ODTLES Versions*

The first *ODTLES* model was introduced by Schmidt et al. [89] and further examined in [33] and [1] is called here first *ODTLES* version (*ODTLES#1*) to differentiate it from the *ODT* closed *XLES* (*ODTLES*) introduced and examined in [2], [3], and in this thesis.

ODTLES#1 is not derived as a 2D filter approach of the governing equations, but as an intuitive inclusion of 3D effects into the *ODT* model. Despite the very different conceptual ideas behind *ODTLES* and *ODTLES#1* equations, differences in both the derived equations and the computed results are moderate and the *XLES* notation can be used even to present the conceptual differences. This for an *ODTLES#1* advancement cycle is presented in table 6 (without scalar equation) to be compared with table 5.

Table 6: *ODTLES#1* time advancement (predictor (p) and corrector (c). *ODT* indicates the *ODT*-advancement. The Poisson equation is solved by a Jacobi-preconditioned conjugate gradient method (*CG*).

step	advanced term	time	spatial
p 1	$\left\langle \overline{\underline{u}^{*}}_{i} \right\rangle^{LES} = \langle \overline{\underline{u}}_i \rangle^{LES}(t) + \int_t^{t+\tau} \partial_{x_i} \left\langle \underline{\hat{p}} \right\rangle_t^{LES} dt \; ; \; \langle \underline{\hat{u}}_i \rangle_t = \underline{\underline{l}}^{-1} \left\langle \overline{\underline{u}^{*}}_{i} \right\rangle^{LES}$	EE1	UP1
	$\hat{\underline{u}}^{*}{}_{i} = \underline{\hat{u}}_i(t) + \int_t^{t+\tau} \underline{\underline{l}}^{-1} \partial_{x_i} \left\langle \overline{\underline{p}} \right\rangle_t^{LES} dt$	EE1	UP1
p 2	$\underline{\hat{u}}_i^{**} = \underline{\hat{u}}_i^{*} + \int_t^{t+\tau} \sum_{j=1}^{3} \partial_{x_j} (\langle \underline{\hat{u}}_j \rangle_t * \underline{\hat{u}}_i^{*}) \, dt'$	EE1	CDM
p 4	$\underline{\hat{u}}_i^{***} = \underline{\hat{u}}_i^{**} + \int_t^{t+\tau} (e_i(\underline{\hat{u}}_i^{**}) + \mathcal{D}_{ODT})(\underline{\hat{u}}_i^{**}) \, dt' + \int_t^{t+\tau} \mathcal{D}_{XLES}(\underline{\hat{u}}_i^{**}) \, dt'$	EE1, *ODT*, EE1	CDM
c 1	$\langle \overline{u}_{k,i} \rangle_{t+\tau}^{LES} = \frac{1}{2} \sum_{k=1;k\neq i}^{3} [l_k] \, \langle \hat{u}_{k,i} \rangle_{t+\tau}$	1D filter	
c 2	$0 = \sum_{i=1}^{3} \partial_{x_i} \langle \overline{u}_i \rangle_{t+\tau}^{LES} \rightarrow \partial_{x_i} \langle \overline{p} \rangle_{t+\tau}^{LES}$	Jacobi-precond. CG (Poisson problem)	

The differences between *ODTLES* and *ODTLES#1* are categorized into:

- Differences in the equations are illustrated by the advancement cycles in tables 5 and 6:
  - In *ODTLES#1* the *ODTLES* specific coupling terms (p 3) and (p 5) in table 5 are not considered. Thus the predicted *ODTLES#1* velocity fields $\underline{\hat{u}}_i^{***}$ are not consistent on the 3D large scale. An ad-hoc coupling $\langle \overline{u}_{k,i} \rangle_{t+\tau}^{LES} = \frac{1}{2} \sum_{k=1;k\neq i}^{3} [l_k] \langle \hat{u}_{k,i} \rangle_{t+\tau}$ is performed to define a 3D large scale velocity field, which is required to ensure mass conservation. Thus the *ODTLES#1* fields $\underline{\hat{u}}_i$ are only coupled due to the pressure projection.
  - This also implies that a coupled scalar equation cannot be derived for *ODTLES#1*. Nevertheless in [1] a scalar equation is included, but only represented by *XLES-grid* 2 and thus no scalar coupling is required.
- Differences in the numerical approximation:
  - The applied *ODT* version is slightly different (*ODTLES#1* uses an *ODT* model by Vebjorn Nilsen, e. g. presented in [69]), but both versions lead to similar results and thus differences are not presented in detail.
  - All time integrations in *ODTLES#1* are approximated using *EE1*. Especially the resulting *EE1* scheme in time and spatial *CDM* (*EE1-CDM*) is known to be unstable for advection terms.
  - The Poisson solver in the corrector step (c 2) differs. The conjugate gradient method (*CG*) solver applied in *ODTLES#1* leads to similar solutions compared to *AMG*, but requires considerable larger computation time.
  - In *ODTLES#1* an unlimited reconstruction algorithm (see section 3.6.1) is applied.
  - *ODTLES#1* uses the *ODT* parameter $l_{max} = 4\Delta x^{LES}$ (compared to $l_{max} = 1\Delta x^{LES}$ in *ODTLES*). As declared at the beginning of section 3.5 this parameter mainly depends on the numerical properties of the implemented unclosed approach.

Schmidt et al. [89] provides a homogeneous turbulence examination using *ODTLES#1* especially indicating that the interplay between the 3D advancement and the *ODT* model behaves well and leads to a reasonable turbulent cascade.

Comparing *ODTLES* and *ODTLES#1* shear driven turbulent flows, *ODTLES#1* introduces certain oscillations to the root mean square velocities (reported by [33] and [1]) but no further major qualitative change in results.

The reasons for the similarity in the computed results, even considering the conceptual and numerical differences between *ODTLES#1* and *ODTLES* especially include the higher l_{max}-parameter which increases the *ODT* turbulence effect and thus compensate shortcomings of the *ODTLES#1* 3D advection representation. Section 4.1.3 shows the influence of l_{max} for a turbulent channel flow. In particular the unclosed *ODTLES#1* approach (*ODTLES#1* without *ODT* turbulent advection) would not show a convergence like the *XLES-U* approach (presented in section 4.1.4).

3.5.7 *ODTLES: Efficiency*

Different turbulence models, e.g. *RaNS*, wall-modeled *LES* (*LES-wm*), wall-resolved *LES* (*LES-wr*), and *ODTLES*, differ strongly in both represented physical effects and computational effort. In this section the computational costs of the different model approaches are estimated by developing a relation between the grid-size (used as a measure for the computational effort) and the Reynolds number following Chapman [13] and especially Choi and Moin [17] and references cited therein.

The investigated domain is a box of the size $L_1 \times L_2 \times L_3$. A highly turbulent boundary layer over a flat-plate airfoil of the thickness δ fills the volume $[x_0, L_1] \times \delta(x_1) \times L_3$. The flow is assumed to reach the plate at $x_1 = x_0$ with a turbulent intensity Re_{x_0}. The boundary layer size $\delta(x_1)$ increases until reaching $x_1 = L_1$ with a corresponding Reynolds number Re_{L_1}. The number of grid cells N within the turbulent boundary layer is estimated for *ODTLES* and compared to *RaNS*, *LES* and *DNS*. From Choi and Moin [17] we extract the Reynolds dependent grid size for *RaNS* and *LES-wm*:

$$N_{RaNS|wm} = 54.7 \frac{L_3}{L_1} n_1 n_2 n_3 Re_{L_1}^{2/7} \left[\left(\frac{Re_{L_1}}{Re_{x_0}} \right)^{5/7} - 1 \right], \tag{117}$$

for a *LES-wr*:

$$N_{wr} = 0.021 \frac{L_3}{L_1} \frac{n_{2,laminar}}{\Delta x_{1,w}^{+} \Delta x_{3,w}^{+}} Re_{L_1}^{13/7} \left[1 - \left(\frac{Re_{x_0}}{Re_{L_1}} \right)^{6/7} \right], \tag{118}$$

and for *DNS*:

$$N_{DNS} = 0.000153 \frac{L_3}{L_1} Re_{L_1}^{37/14} \left[1 - \left(\frac{Re_{x_0}}{Re_{L_1}} \right)^{23/14} \right]. \tag{119}$$

Here $n_1 n_2 n_3$ is the number of grid points within the cube $\delta \times \delta \times \delta$, $n_{2,laminar}$ is the number of wall-normal grid points within the laminar sublayer, and $x_{k,w}^{+}$ is the *LES* cell size in wall units.

Following Chapman [13] *RaNS* typically resolves the cube $\delta \times \delta \times \delta$ using $n_1 n_2 n_3 \approx 1 \times 20 \times 0.5 = 10$ cells, while for wall-modeled *LES* Choi and Moin [17] report typical grid resolutions $n_1 n_2 n_3 \approx [1200, 33000]$. In wall-resolved *LES* Choi and Moin [17] find typical resolution values $\frac{n_{2,laminar}}{\Delta x^+_{1,w} \Delta x^+_{3,w}} \approx [\frac{1}{390}, \frac{1}{25}]$. Here *LES* models represent turbulent scales down to the inertial range of the turbulent cascade. The *ODT* model, applied within *XLES*, potentially describes the full turbulent cascade within a 1D sub-domain, which leaves the 3D grid to capture non-turbulent effects (e.g. the domain or secondary instabilities). For the flat-plate airfoil even *ODT* stand-alone potentially leads to reasonable results (Lignell et al. [67] apply a *ODT* to a comparable turbulent case, but including buoyancy, by spatially advancing the *ODT* line). In consequence the (equidistant) *XLES* 3D resolution N_k in x_k-direction ($k = \{1, 2, 3\}$) is chosen independently of the Reynolds number for a flat-plate airfoil.

In the current *ODTLES* implementation the resolved small scales are represented by N_{RSS_k} equidistant cells in x_k-direction. Following Choi and Moin [17] for highly turbulent flows the number of grid points resolving the Kolmogorov length scale along a small distance dx_1 is $N_{RSS1} = 0.116 \frac{dx_1}{x_1} Re_x^{13/14}$. Equidistant *ODTLES* uses the smallest length scale globally in all 1D sub-domains, leading to

$$N_{ODTLES} = 0.116 K_{ODT} N_{LES2} N_{LES3} \frac{L_3}{L_1} Re_{L_1}^{13/14}. \tag{120}$$

A factor $K_{ODT} \approx 3 \times 6$ takes into account that 3 *XLES-grid*s are used (we assume that $N_{LES1} = N_{LES2} = N_{LES3}$) and equidistant *ODT* uses at least 6 cells to allow a turbulent event ('eddy') within the Kolmogorov length scale.

In principle *ODTLES* can be extended to non-equidistant grids within the 1D sub-domain, which is for example realized by the *aODT* implementation by Lignell et al. [67]. Although adaptive *ODT* is not used as a sub-grid model within a *XLES* approach yet, we investigate this interesting case as a worthwhile perspective and refer to it as *aODTLES*. For an adaptive grid we assume on average a resolution similar to *DNS* (in 1D) and integrate over the boundary layer thickness with $\frac{\delta}{x} = 0.16 Re_x^{-1/7}$ (see [17]) in the 1D sub-domain, leading to

$$N_{aODTLES} = 0.0103936 K_{aODT} N_{LES1} N_{LES3} \frac{L_3}{L_1} Re_{L_1}^{11/14} \left[1 - \left(\frac{Re_{x_0}}{Re_{L_1}} \right)^{25/14} \right]. \tag{121}$$

For adaptive *ODT* we assume $K_{aODT} = 3$ because 3 *XLES-grid*s are required (here we assume each *XLES-grid* uses the same *RSS* resolution and $N_{LES1} = N_{LES2} = N_{LES3}$). There is no additional assumption of a minimum number of cells representing the Kolmogorov length scale required for *aODT*.

We compare typical *RaNS* and *LES* resolutions (following [17] and [13]) with the *ODTLES* and *aODTLES* approach for different 3D resolutions in figure 9.

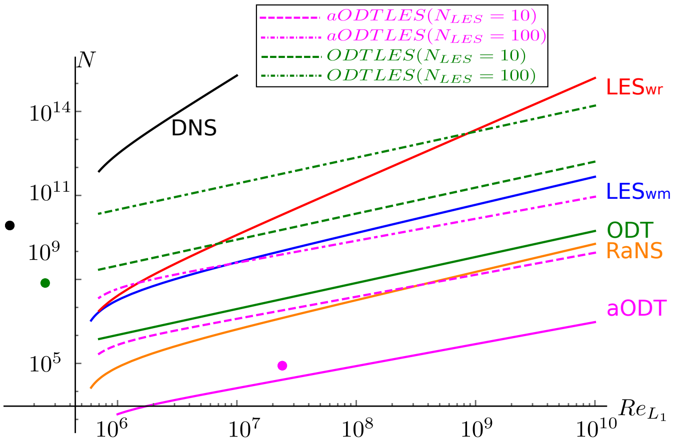

Figure 9: Number of grid points N required for the numerical simulations of a flow over a flat-plate airfoil with aspect ratio $L_3/L_1 = 4$ and a turbulent inflow with $Re_{x_0} = 5 \times 10^5$. *LES-wm* ($n_1 n_2 n_3 = 2500$) , wall-resolved *LES* ($n_{2,\text{laminar}}/\Delta x^+_{1,w} \Delta x^+_{2,w} = 1/200$), *RaNS* ($n_1 n_2 n_3 = 10$), *ODTLES* and *aODTLES* with $N_{\text{LES}1} = N_{\text{LES}3} = \{10, 100\}$ cells, and the *ODT* and *aODT* stand-alone model are shown. Additionally, actual simulations for a turbulent channel (assuming $Re_t \approx Re_{L_1}$) are shown for *DNS* ($Re_\tau = 5200$, black point), *ODTLES* ($Re_\tau = 10000$, green point), and *aODT* ($Re_\tau = 6 \times 10^5$, magenta point).

Additionally numerical computations for a turbulent channel are presented assuming a similarity of the turbulent Reynolds number in the channel and Re_{L_1}. Hereby the *DNS* by Lee and Moser [63] (we assume $N \approx 8.5 \times 10^9$, estimated for $L_3/L_1 = 4$), an *aODT* result by Meiselbach [71] ($N_{\text{aODT}} \approx [80000, 120000]$ (from Meiselbach [70])) and the *ODTLES* result with $Re_\tau = 10000$ in section 3.5.8 are used.

For weakly turbulent flows, *ODTLES* is subject to additional computational costs compared to standard *LES*. But *ODTLES* requires 3D resolutions independent of the turbulence intensity (except secondary effects), and thus highly turbulent flows in moderately complex domains are well described with low computational costs. In some flow regimes *ODTLES* is more efficient than *LES-wm* and although it represents advective and diffusive effects down to the Kolmogorov length scale. Incorporating *aODT* into a *XLES* framework seems to be an especially promising alternative to *LES-wm* and even *RaNS* simulations for highly turbulent flows in simple domains (requiring low 3D resolutions). Note that the *aODTLES* model for a low 3D resolution (e. g. N_{LES}= 10 cells per direction) is even more efficient than an equidistant *ODT* approach stand-alone.

Additionally incorporating the EMC-*SGM* into *ODT* or *aODT* can further decrease the computational costs of *ODTLES* (cf. [89]) and *aODTLES*.

Note that in the presented estimation the costs of the computation within one discrete cell is neglected, because the different modeling strategies typically vary by a low factor ($\lesssim 2$), which is not strongly affecting the estimation in figure 9.

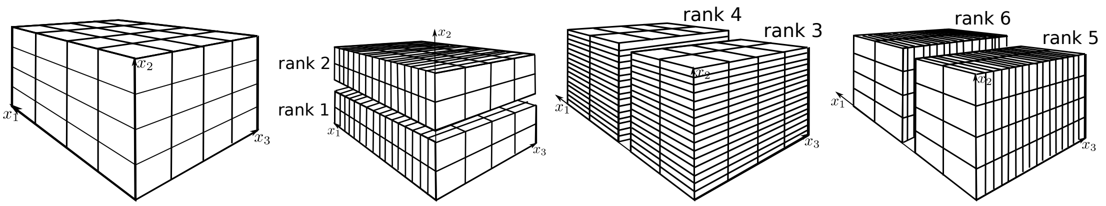

(a) *LES* grid (b) *XLES-grid* 1 (c) *XLES-grid* 2 (d) *XLES-grid* 3

Figure 10: Illustrative *ODTLES* domain decomposition for *XLES-grid*s in 10b – 10d for 6 *CPU*s (here declared ranks) and $N_{LES}= 4$ in each direction. The Poisson problem is solved serial on the 3D large scale grid illustrated in 10a.

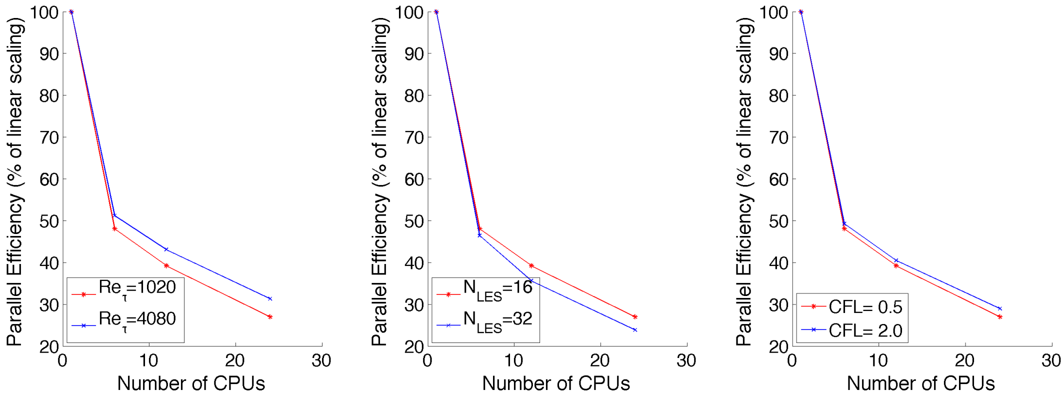

(a) Varying Re_τ. (b) Varying N_{LES}. (c) Varying $CFL = CFL_{RSS}$.

Figure 11: Strong parallel scaling for an *ODTLES* turbulent channel flow. As not stated otherwise the scaling for $Re_\tau = 1020$, $N_{LES} = 16$, $N_{RSS} = 2048$ ($N_{RSS} = 8192$ for $Re_\tau = 4080$), and $CFL = CFL_{RSS} = 0.5$ is shown in 11a–11c.

3.5.8 *ODTLES: Parallelization*

The scope of this work does not include the development of a highly parallel algorithm. Nevertheless the *CPU*-time and memory required to compute highly turbulent flows call for a sufficiently parallel algorithm. Especially to handle the *ODTLES* memory requirements, a shared memory parallelization using a message passing interface (*MPI*) is advantageous.

Figures 10b–10d illustrate the domain decomposition of the *XLES-grid*s. Within each of these *XLES-grid*s the predictor-step implementation is identical to standard approaches includes ghost cells. The Poisson problem is limiting parallel performance in many *DNS* implementations. This term can be treated in *ODTLES* with relative low effort, because the corrector step is performed only on the 3D large scale grid (see figure 10a). In the present implementation the Poisson problem is solved serial and in most cases limiting the parallel performance. The current *ODTLES* implementation is sufficient to perform computations using up to $\mathcal{O}(100)$ *CPU*s with reasonable parallel efficiency.

We conduct a strong parallel scaling study for a turbulent channel, whereby the identical problem is computed with different numbers of *CPU*s $\{1, 6, 12, 24\}$.

E. g. with 6 *CPU*s a parallel efficiency of $\approx 50\%$ means a speedup factor ≈ 3 compared to a single *CPU* computation. All parallel results show a linearly decreasing parallel efficiency.

Very specific in *ODTLES* is the fact that the advancement is dominated by *ODT* triplet maps without parallel communication requirements which leads to advantageous parallel properties: It has a positive effect for the parallelization efficiency with increasing Re_τ (figure 11a), increasing *XLES* resolution ratio (K_N) (figure 11), and increasing *CFL*-number (figure 11c).

The *ODTLES* approach is highly parallelizable for highly turbulent flows in simple domains, because especially for these flows high *XLES* resolution ratios (K_N) and the high *ODT* activity further increase the parallel efficiency with increasing turbulence intensity.

3.6 NUMERICAL PROPERTIES OF THE XLES IMPLEMENTATION

There are *XLES* and *ODTLES* specific terms, which cannot be adapted from standard *LES* approaches. In particular the coupling terms include a deconvolution. In this section a possible numerical approximation of the deconvolution l_k^{-1} in x_k-direction is introduced (section 3.6.1) and the numerical properties of the coupled advection scheme are investigated in section 3.6.2 and 3.6.3.

3.6.1 *Deconvolution Algorithm*

In sections 3.4.2.2 and 3.4.2.3 coupling terms between the *XLES-grid*s are introduced. A discrete interpretation of the coupling matrix $(\underline{\underline{C}}\, \underline{\underline{l}}^{2D}) \approx \underline{\underline{l}}^{\dagger} * \underline{\underline{C}}\, \underline{\underline{l}}^{2D}$ is required to numerically represent these coupling terms. Within the matrix $\underline{\underline{l}}^{\dagger}$ (see Eq. (73)) a deconvolution operator $[l_k^{-1}]$ has to be interpreted numerically. Note that exact continuous definition of a deconvolution operator is not available within implicit filtered equations.

In general the fields $\phi = \{u, \theta\}$ (indices are skipped in this section) cannot be reconstructed exactly ($[l^{-1}l] \neq 1$), because by averaging (e.g. $\phi^{LES} = [l^{d}]\phi$) information gets lost. This is not reconstructible, unless only large scale information is present in the full spectrum, which is fortunately the case in *XLES*, as shown by an example in Eq. (74). A possible interpretation of a convolution includes, that the convolved property can be numerically approximated within the same spatial grid, but contains no small scale properties. By applying the discrete box filter in Eq. (56) the convolved quantity is represented on a large scale grid which corresponds to the filter size. The discrete deconvolution $[l^{-1}{}_{d}]$ interprets a large scale property which is represented on a large scale grid within a highly resolved grid, of course still containing only large scale informations. In this sense the discrete operators $[l^{-1}{}_{d}\, l^{d}]$ correspond to the above mentioned interpretation of a convolution .

In principle the deconvolution approach is not restricted to one particular filter definition (e.g. spectral filter, box filter, Gaussian filter), but the mass conservation is greatly simplified if the discrete box filter in Eq. (56) is used, as shown in appendix (A.2).

The deconvolution within *XLES* is not intended to construct small-scale features, but rather, to modify the low-wavenumber content of an existing fully resolved property.

The deconvolution is related to the reconstruction within a *FVM* and this for the term reconstruction has been used in [89] and [69]. McDermott [69] and authors therein investigate several possible reconstruction algorithms suitable for 3D approaches incorporating *ODT*. This modification must meet several requirements:

- Integral constraints are imposed to satisfy conservation laws at the level of the individual 3D coarse-grained cells. This means the averaged large scale field needs to be preserved by the deconvolution, e.g. to enable the consistency preservation of the 3D velocity field, which is required for the mass conservation and the coupling terms, as well as for the 'LES limit' of the *XLES* model (in section 3.4.7):

$$[l^{d}][l^{-1_{d}}] = 1. \tag{122}$$

- The deconvolution must in some sense modify the large scale structure along the resolved direction and simultaneously preserve the small-scale structure. In this sense this deconvolution is a reconstruction of existing structures rather than a construction of something that does not otherwise exist.

- The reconstruction method is required to be high-order accurate to avoid noticeable discontinuities.

In this section we introduce a discrete approximation of the deconvolution operator $[l^{-1}]$ for the purpose of computing highly resolved fields $\phi^{d} \approx [l^{-1_{d}}]\phi^{\mathrm{LES}_{d}}$ by discretely interpreting $[l^{-1_{d}}]$ from a box filtered field $\phi^{\mathrm{LES}_{d}} = [l^{d}]\phi$.

Schmidt et al. [89] introduces a multilevel Fromm reconstruction algorithm (here called Schmidt's scheme), which fulfills the requirements: The recursive algorithm approximates $\phi^{d} \approx [l^{-1_{d}}]\phi^{\mathrm{LES}_{d}}$ exhibiting the smoothness of a 8th order interpolation without changing the box filtered field ($[l^{d}]\phi^{d} = \phi^{\mathrm{LES}_{d}} \equiv [l^{d}]\phi$). The algorithm is computational fast, stable, well-behaved, and uses only a 3-point stencil in each recursive step n_r to achieve its high accuracy.

The continuous deconvolution problem $\phi^{d} = [l^{-1_{d}}]\phi^{\mathrm{LES}_{d}}$ with a known discrete box-filtered field $\phi^{d,\mathrm{LES}}$ exactly satisfies the relation

$$\phi^{d,\mathrm{LES}}(x_j) = \frac{1}{K_N} \sum_{i=(j-1)K+1}^{jK} \phi^{d}(x_i) \tag{123}$$

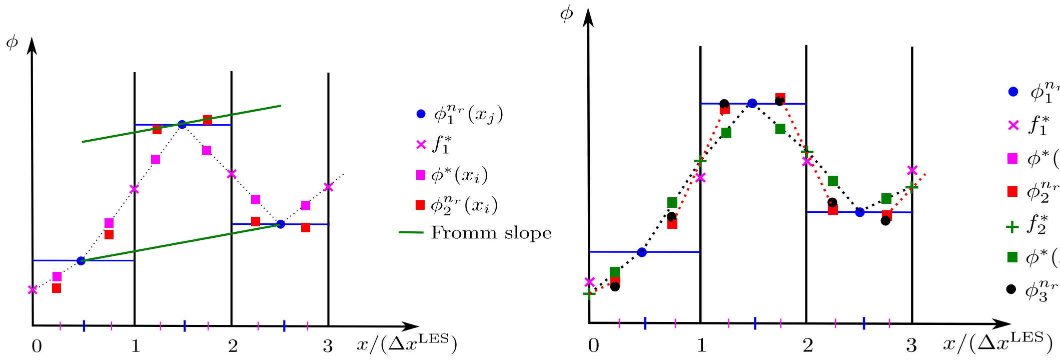

(a) First iteration. (b) Second iteration.

Figure 12: Multilevel Fromm reconstruction. First and second iterations are shown in 12a and 12b. Further iterations follow the steps of the second iteration.

for a smooth set of $N^{\mathrm{RSS}} = K_N\, N^{\mathrm{LES}}$ (where $K_N = N_{\mathrm{RSS}}/N_{\mathrm{LES}} = 2^{n_r}$) discrete values $\phi^d(x_i)$ at uniformly spaced locations x_i. Note that Eq. (123) is the discrete form of the continuous box filter definition in Eq. (56).

Here Schmidt's algorithm is shown to compute a set of 2N reconstructed values $\phi^{n_r+1}(x_i)$ from the initial set of N original values $\phi^{n_r}(x_j)$. This process is recursively repeated $(n_r - 1)$ times for any resolution ratio $K_N = 2^{n_r}$. In the first recursive step we use $\phi^1(x_j) = \phi^{d,\mathrm{LES}}(x_j)$ and in the last recursive step the highly resolved values $\phi^d(x_i) = \phi^{\log_2(K_N)}(x_i)$ are computed.

For each recursive step n_r, an iterative multilevel Fromm schemes is applied (n_I counts the iterations; denoted like $\phi_{n_I}^{n_r}(x_j)$): Two 'starred' values $\phi^*(x_{i\pm})$ with x_{i-} and x_{i+} denote the first and second i-values located in cell j (see figure 12a) and are cell average preserving:

$$\phi^*(x_{i-}) = \frac{\phi_{n_I}^{n_r}(x_j) + f^*(x_j - (\Delta x^{n_r})/2)}{2} \tag{124}$$

$$\phi^*(x_{i+}) = \frac{\phi_{n_I}^{n_r}(x_j) + f^*(x_j + (\Delta x^{n_r})/2)}{2} \tag{125}$$

with the face values $f_{n_I}^*$ (see figure 12a) in the first iterative step $n_I = 1$:

$$f_1^*(x_j - (\Delta x^{n_r})/2) = \frac{\phi_1^{n_r}(x_j) + \phi_1^{n_r}(x_{j-1})}{2} \tag{126}$$

$$f_1^*(x_j + (\Delta x^{n_r})/2) = \frac{\phi_1^{n_r}(x_j) + \phi_1^{n_r}(x_{j+1})}{2}. \tag{127}$$

To guarantee a cell average preserving scheme the 'starred' values are corrected leading to the first iteration values

$$\phi_{n_I+1}^{n_r}(x_{i-}) = \phi^*(x_{i-}) + C_j \tag{128}$$

$$\phi_{n_I+1}^{n_r}(x_{i+}) = \phi^*(x_{i+}) + C_j \tag{129}$$

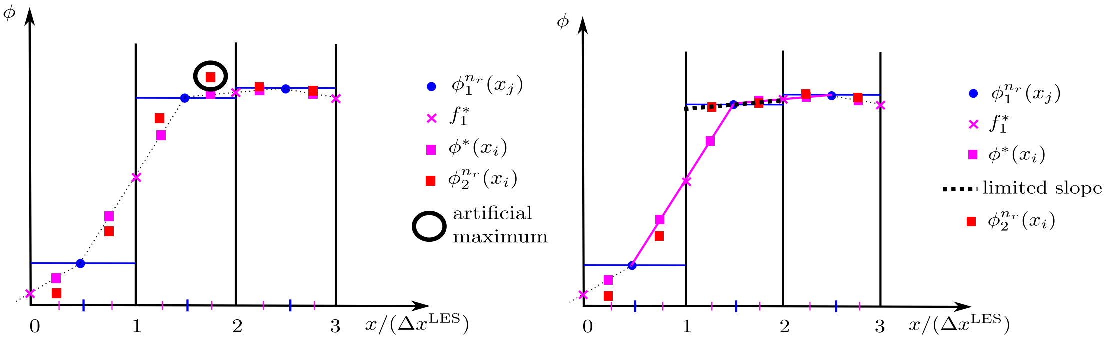

(a) Unlimited iteration

(b) Limited iteration

Figure 13: Limited multilevel Fromm reconstruction. The linear limiter undermines the iterative process, but is used in each recursive step. Thus a higher order approximation is possible.

with the correction in cell j

$$C_j = \Delta x^{n_r} + \frac{\phi^{n_r}_{n_I}(x_{i-}) + \phi^{n_r}_{n_I}(x_{i+})}{2}. \tag{130}$$

The slope between $\phi^{n_r+1}(x_{i-})$ and $\phi^{n_r+1}(x_{i+})$ corresponds to the Fromm slope (see e. g. [66])

$$\Delta_j^{\mathrm{Fromm}} = \frac{1}{2}\left(\phi^{n_r}(x_{j+1}) - \phi^{n_r}(x_{j-1})\right), \tag{131}$$

illustrated in figure 12a.

Further iterative steps increase the accuracy by recalculating the face values using

$$f^*_{>1}(x_j - (\Delta x^{n_r})/2) = \frac{\phi^{n_r}_{n_I+1}(x_{i-}) + \phi^{n_r}_{n_I+1}(x_{i--})}{2} \tag{132}$$

$$f^*_{>1}(x_j + (\Delta x^{n_r})/2) = \frac{\phi^{n_r}_{n_I+1}(x_{i+}) + \phi^{n_r}_{n_I+1}(x_{i++})}{2}. \tag{133}$$

based on the first iteration values $\phi^{n_r}_{n_I+1}(x_i)$, where $i++$ and $i--$ donate the value of $(i+)+1$ respective $(i-)-1$, as illustrated in figure 12b.

The method converges rapidly as the iterations n_I proceed. As Schmidt et al. [89] and Gonzalez-Juez et al. [33] report the algorithm lead to sufficient results using 4 iterations and thus one recursive level is finished:

$$\phi_1^{n_r+1}(x_i) = \phi_4^{n_r}(x_i). \tag{134}$$

As McDermott [69] shows, Schmidt's scheme does not preserve monotonicity for scalar shocks and therefore violate essentially non-oscillatory (*ENO*) properties: The algorithm produces artificial local extrema in areas of monotone large scale fields with large gradients, e.g. occurring near a wall.

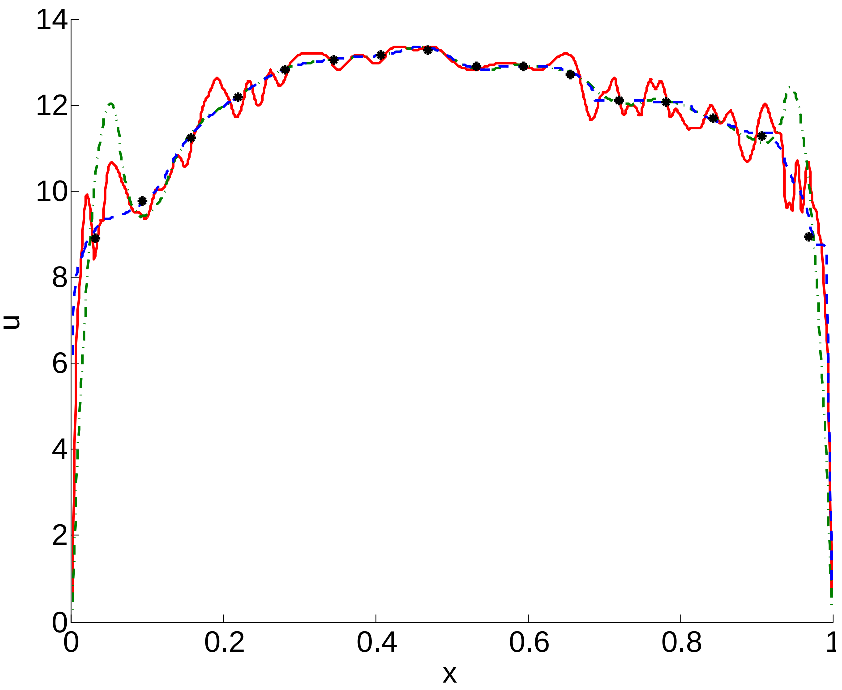

Figure 14: A representative instantaneous streamwise velocity profile u (solid) for a turbulent channel ($Re_\tau = 1020$) with $N_{LES} = 16$ and $N_{RSS} = 1024$ is shown. The large scale velocity $u^{LES_d} = [l^d]u$ is represented with points. The deconvolution $u^d \approx [l^{-1}{}_d]u^{LES_d}$ using Schmidt's algorithm is dashed-dotted and the limited algorithm is dashed. For both algorithms (limited and unlimited) the reconstructed field u^d preserves the box-filtered values $[l^d]u^d = u^{LES_d}$, but without the limiter unphysical overshoots occur near the walls.

Therefore Schmidt's scheme is expanded by applying a slope limiter adapted from Burbeau et al. [8] in each recursive level. Note that Burbeau et al. [8] shows the limiter to almost preserve the order of a high-order *DGM* by applying the limiter in each step of a *RK3* time scheme. Contrary to the original limiter by Burbeau et al. [8], we limit Schmidt's algorithm at an individual recursive level, only if an artificial extrema in a monotone region is directly identified, as figure 13a illustrates. Hereby monotonicity is defined locally for one cell j by including its neighbors $j-1$ and $j+1$.

Since the limiter is only applied in monotone areas its definition simplifies (here in a slope limiter notation):

$$\Delta_j = \min\left(\phi^{n_r}(x_{j+1}) - \phi^{n_r}(x_j), \phi^{n_r}(x_j) - \phi^{n_r}(x_{j-1})\right) \tag{135}$$

as figure 13b illustrates.

This procedure guarantees *ENO* properties, but suppresses the iterative character of the algorithm, which leads to a reduction of the approximation order. Nevertheless since the limiting process is decided for each individual recursive level, the resulting approximate order in limited regions is generally higher than linear.

The properties of the original algorithm and the limited one are demonstrated for a realistic instantaneous streamwise velocity profile u of a turbulent channel flow with high gradients at the walls, shown in Figure 14.

The numerical deconvolution algorithm error term ($\underline{\sigma}_{\dagger}^{\text{spatial}}$) can be written formally:

$$\underline{\sigma}_{\dagger}^{\text{spatial}} = (\underline{\underline{l}}^{\dagger} * \underline{\underline{C}} - \underline{\underline{l}}^{\dagger_d} * \underline{\underline{C}}) \left(\partial_{x_j} \left(\langle \underline{\hat{u}}_j \rangle * \underline{\hat{\phi}}_i - \langle \underline{\overline{u}}_j \rangle^{\text{LES}} * \underline{\overline{\phi}}_i^{\text{LES}} \right) + \underline{\underline{l}}^{2D} \underline{\mathcal{M}}_{\text{ODT}}^{\delta_i} \right) \tag{136}$$

for $\phi_i = \{u_i, \theta\}$.

There is no spectrally sharp way to implement this type of deconvolution. Various non-equivalent procedures are possible in principle. Schmidt et al. [89] describe a particular approach that is adopted here with a technical modification that improves its behavior near walls. To summarize, although the inverse operator $[l^{-1}]$ arises as a natural and necessary consequence of the *XLES* ansatz, the ansatz per se does not uniquely define its meaning nor guarantee that it can be specified in a way that is free of unintended artifacts.

In section 5.1.2 a specific situation is investigated where the deconvolution algorithm error term ($\underline{\sigma}_{\dagger}^{\text{spatial}}$) can be dominant for the scalar coupling.

3.6.2 *Coupled Linear Advection Scheme: Momentum Transport*

The characteristic shape of the *XLES-grid*s (figure 4b–4d) is considered when choosing the numerical schemes to be implemented, e.g. an implicit time discretization in the highly resolved direction is applied, while explicit time schemes are used to advect large scale properties (cf. section 2.1.2). Therefore different numerical advection schemes are mixed due to the *XLES* coupling terms, because the same property, represented by several *XLES-grid*s is simultaneously advanced by different numerical schemes. Additionally the coupling requires a deconvolution function, which interacts with these numerical schemes.

In this section we present the numerical properties of this coupled advection scheme. For simplicity the 3D large scale velocity fields $\underline{\overline{u}}_i^{\text{LES}}$ are resolved by N_{LES} cells in each direction. The *RSS* properties are discretized with N_{RSS} cells in all *XLES-grid*s.

The coupled momentum advection scheme numerically approximates the equation

$$0 = (\underline{\underline{\mathbb{1}}} - \underline{\underline{\delta_i}}) \left(\partial_t \underline{\hat{u}}_i + \sum_{j=1}^{3} \partial_{x_j} \langle \underline{\hat{u}} \rangle_j * \underline{\hat{u}}_i + \sum_{j=1}^{3} \left(\underline{\underline{l}}^{\dagger} * \underline{\underline{C}} \partial_{x_j} (\langle \underline{\hat{u}}_j \rangle * \underline{\hat{u}}_i - \langle \underline{\overline{u}}_j \rangle^{\text{LES}} * \underline{\overline{u}}_i^{\text{LES}}) \right) \right) \tag{137}$$

(according to Eq. (108); diffusive and *SGS* terms are not considered).

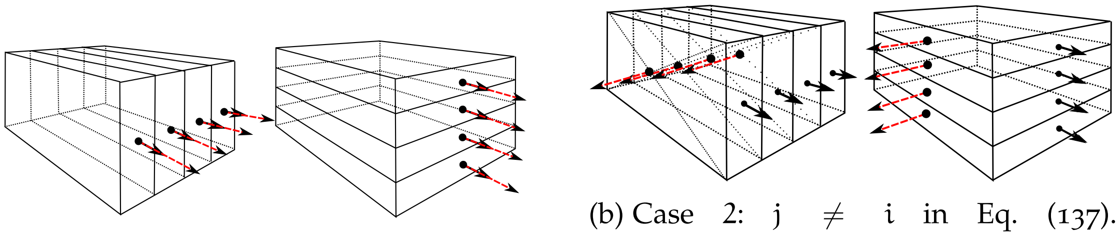

(a) Case 1: $j = i$ in Eq. (137). Coarsely resolved advection in *XLES-grid* 3 (left) and *XLES-grid* 2 (right).

(b) Case 2: $j \neq i$ in Eq. (137). Highly (coarsely) resolved advection in *XLES-grid* 3 (left) (*XLES-grid* 2 (right)).

Figure 15: *XLES* requires a coupled advection scheme. The advected velocity $\underline{\hat{u}}_i$ (bold arrows) is advected with the constant wave speed c_j (dashed arrows) and is resolved in two *XLES-grid*s. For the two relevant cases the discrete staggered grids within one 3D large scale cell (cf. figure 4) are shown in (a) and (b).

Fundamental properties of the coupled advection scheme, e.g. the numerical dissipation and dispersion, can be demonstrated by solving a one dimensional linear advection problem. Then a constant wave speed c_j replaces the advecting velocities in Eq. (137): $\underline{\hat{u}}_j = \underline{u}_j^{LES} = c_j \begin{pmatrix} 1 & 1 & 1 \end{pmatrix}^T$. In this section the linearized coupled advection scheme is investigated, while the full coupled non-linear advection scheme is studied in a convergence study of a turbulent channel flow (see section 4.1.4).

W.l.o.g. the advected velocity $\underline{u}_1$ is represented by the two staggered *XLES-grid* containing $\hat{u}_{2,1}$ and $\hat{u}_{3,1}$ respectively while $\hat{u}_{1,1}$ is evaluated using Eq. (106).

Two situations occur (see figure 15), as discussed here by a concrete example (generalization to other indices is trivial):

- Case 1: $j = i \overset{w.l.o.g.}{=} 1$ in Eq. (137): Advection into x_1-direction; In both *XLES-grid*s 2 and 3 the advection is coarsely resolved with N_{LES} grid cells.

- Case 2: $2 \overset{w.l.o.g.}{=} j \neq i \overset{w.l.o.g.}{=} 1$ in Eq. (137): Advection into direction x_2; In *XLES-grid* 2 the advection is resolved with N_{RSS} cells, respective with N_{LES} cells in *XLES-grid* 3.

To spatially discretize the advection terms, a central difference method (CDM) on a staggered grid is used (see section 2.1.1).

Two different advection schemes, *CN-CDM* and *RK3-CDM* are deployed within the coupled advection.

The properties of the *CN-CDM* and *RK3-CDM* schemes transfer to the coupled advection schemes (in Cases 1 and 2).

Based on the expressions *RK3-CDM* and *CN-CDM* the coupled advection scheme in Case 1 (Case 2) is called coupled scheme with *RK3* and *RK3* in time and spatial *CDM* (*RK3-RK3-CDM*) (coupled scheme with *CN* and *RK3* in time and spatial *CDM* (*CN-RK3-CDM*)).

To illustrate the coupling procedure *w.l.o.g.* for the *CN-RK3-CDM* scheme, and rewrite Eq. (137) in a semi-discrete form (in index notation). Hereby $\hat{u}_{3,1}$ is discretized in *XLES-grid* 3 in Eq. (138) and $\hat{u}_{2,1}$ in *XLES-grid* 2 in Eq. (139):

$$
\begin{aligned}
(\Delta t)\hat{u}_{3,1} = & \int_{\mathrm{RK3}} c_2 \partial_{x_2} \hat{u}_{3,1}\, dt \\
& + [l_3^{-1d}][l_2^{d}] \left(\int_{\mathrm{CN}} c_2 \partial_{x_2} \hat{u}_{2,1}\, dt - \int_{\mathrm{RK3}} c_2 \partial_{x_2} \overline{u}_{2,1}^{LES}\, dt \right)
\end{aligned} \tag{138}
$$

$$
\begin{aligned}
(\Delta t)\hat{u}_{2,1} = & \int_{\mathrm{CN}} c_2 \partial_{x_2} \hat{u}_{2,1}\, dt \\
& + [l_2^{-1d}][l_3^{d}] \left(\int_{\mathrm{RK3}} c_2 \partial_{x_2} \hat{u}_{3,1}\, dt - \int_{\mathrm{RK3}} c_2 \partial_{x_2} \overline{u}_{3,1}^{LES}\, dt \right) .
\end{aligned} \tag{139}
$$

Here the numerical time discretizations of the advection terms are indicated (*CN* and *RK3*). The discrete coupling operators $[l_k^d]$ and $[l_k^{-1d}]$ (see Eq. (56) and the algorithm described in section 3.4.2.1) are discretized by an *EE1* scheme in time. Also the non-linear advection part, which is not considered in the linear advection problem is discretized by an *EE1* scheme in time (see section 3.4.4).

The numerical properties of the underlying discrete advection schemes (*CN-CDM* and *RK3-CDM*), like stability and dissipative behavior, transfer to the fully discrete coupled linear advection schemes:

- The coupled advection scheme converges to the analytical solution for $N_{LES} \rightarrow \infty$ as illustrated in section 3.6.2.1 where the theoretical prediction e.g. shown in [105] is reproduced. This property is required to numerically realize the 'LES limit' and 'DNS limit' of *XLES* (section 3.4.7).

- The coupled advection scheme including the deconvolution (see section 3.6.1) maintain well defined large scale properties, even by simultaneously transporting small scale properties, as investigated in section 3.6.2.1.

The highly resolved *CN-CDM* scheme (using N_{RSS} cells) contributes to the coupled *CN-RK3-CDM* scheme (Case 2) and additionally increases the numerical accuracy of the coupled scheme. This is neither required for a well defined and converging *XLES* scheme nor the 'LES limit' (or 'DNS limit') of *XLES*. As investigated in section 3.6.2.1 the highly resolved advection terms increase the coupled numerical accuracy up to a *XLES* resolution ratio $K_N = N_{RSS}/N_{LES} \lesssim 10$. With $N_{RSS} \gtrsim 10 N_{LES}$ the overall numerical error is dominated by the coarsely resolved *RK3-CDM* scheme.

The coupled numerical schemes, simultaneously discretized by multiple *XLES-grids*, are found to be appropriate for linear advection.

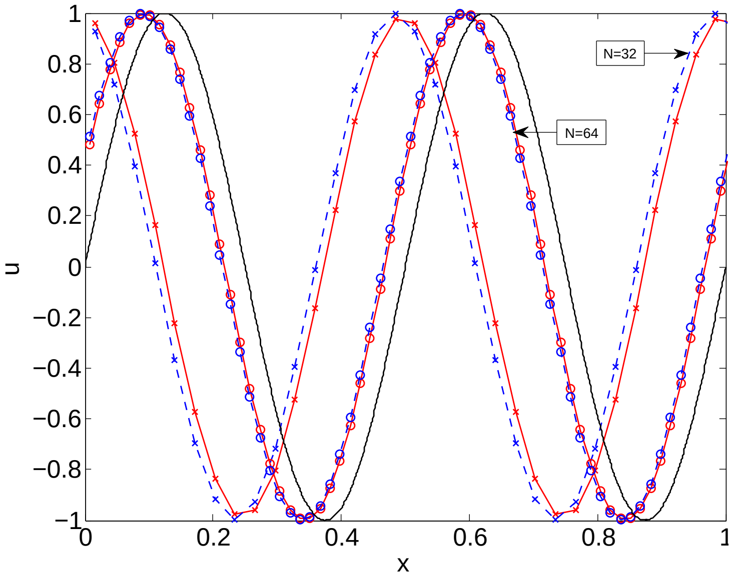

Figure 16: A linear wave is propagated with constant velocity $\underline{\hat{u}}_j = \underline{c}_j$ over 10 wavelengths. The coupled numerical schemes *CN-RK3-CDM* (dashed) and *RK3-RK3-CDM* (solid) with $N = N_{RSS} = N_{LES} = \{32, 64\}$ are shown. The black line is the analytical result.

3.6.2.1 *Coupled Linear Advection Scheme: Numerical Test*

The coupled advection scheme is investigated and verified by computing a linear wave propagation. The initial condition

$$u_1 = \sin(4\pi x_1) \tag{140}$$

and periodic boundary conditions are used. The number of cells for the resolved small scale fields N_{RSS} and the 3D large scale field N_{LES} are varied. The wave is propagated for 10 wavelengths ($t = 5\,L/c_j$; $L \equiv 1$; constant wave speed c_j).

We found the coupled advection schemes *RK3-RK3-CDM* (Case 1) and *CN-RK3-CDM* (Case 2) to be stable and slightly dispersive (see figure 16). Additionally *RK3-RK3-CDM* is little dissipative. The difference between *RK3-RK3-CDM* and *CN-RK3-CDM* is not significant. With increasing 3D resolution (N_{LES}) the dispersive behavior decreases (convergence).

Numerical convergence for the *XLES* coupled advection scheme is unconditionally obtained for increasing 3D resolution ($N_{LES} \to \infty$). This is valid for both coupled schemes: *RK3-RK3-CDM* and *CN-RK3-CDM*.

The convergence for the *CN-RK3-CDM* scheme with increasing small scale resolution ($N_{RSS} \to \infty$) and two choices of constant 3D resolution $N_{LES} = \{16, 64\}$ is additionally investigated. This kind of numerical convergence is not required to ensure a well defined and converging *XLES* approach.

A phase shift Φ describes the numerical dispersion and thus measures the numerical accuracy (see figure 17).

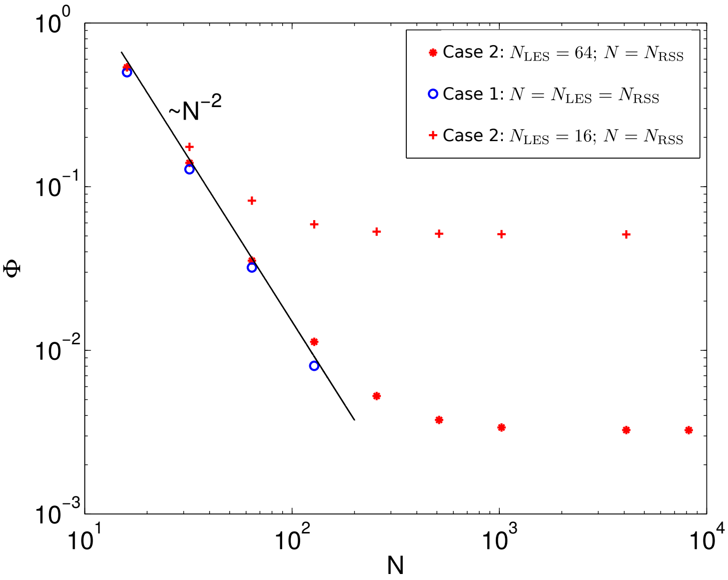

Figure 17: Φ is the phase difference between the analytical solution and the numerical result. Case 1: *RK3-RK3-CDM* scheme with $N = N_{\text{LES}} = N_{\text{RSS}}$. Case 2: *CN-RK3-CDM* scheme with $N = N_{\text{RSS}}$ and $N_{\text{LES}} = \{16, 64\}$. For a *CN-CDM* scheme Tsai et al. [105] analytically predict the behavior : $\Phi \sim N^{-2}$.

We find the numerical accuracy of the coupled advection scheme increasing up to a *XLES* resolution ratio $K_N \lesssim 10$. With higher K_N the numerical error of the coarse resolved scheme (RK3-CDM) dominates the coupled numerical error.

Thus the numerical accuracy is increased by increasing the resolved small scales within *XLES* up to some limit in addition to possibly resolving additional physical effects.

In this section the *CN-RK3-CDM* scheme demonstrates the preservation of (spectrally separated) large and small scale properties which are represented *w.l.o.g.* in *XLES-grid* 2.

A multi-scale wave with the initial condition

$$u_{2,1} = \sin(4\pi x_{2,1}) + 0.2\,\sin(128\pi x_{2,1}) \tag{141}$$

$$u_{3,1} = [l_3^{-1\,d}][l_2^{d}]u_{2,1} = \sin(4\pi x_{3,1}) \tag{142}$$

is propagated for 10 wavelengths using $N_{\text{LES}} = 64$ and $N_{\text{RSS}} = 4096$ cells in the x_2-direction (advanced by Eq. (139) and (138)).

Note that the higher mode $0.2\,\sin(128\pi x_{2,1})$ is only resolved within *XLES-grid* 2 while *XLES-grid* 3 only captures the lower mode.

The box filtered and small scale properties are preserved, but little dispersed due to numerical effects (see figure 18a).

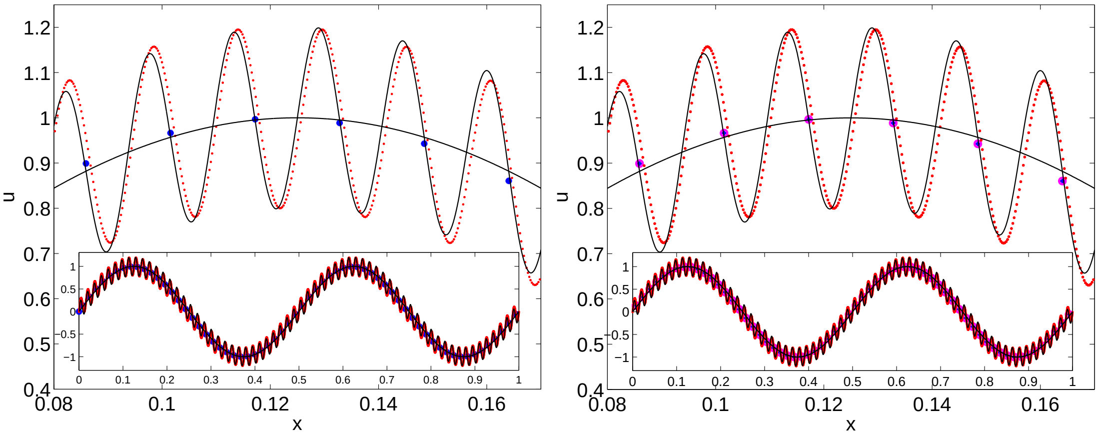

(a) Momentum transport.

(b) Scalar transport.

Figure 18: A multi-scale wave with the initial condition in Eq. (141) (black lines) propagates for 10 wavelengths. The full domain (small box) and one wave peak are shown. The big points in 18a corresponds to the 3D large scale velocity field ($N_{LES} = 64$ cells). For scalar advection (18b) large scale scalar fields ($N_{LES} = 64$ cells) are represented in 3 *XLES-grid*s, indicated by big points and open circles. The small points corresponds to the resolved small scales ($N_{RSS} = 4096$). There is not difference between linear momentum transport (advanced by 2 *XLES-grid*s) and scalar transport (advanced by 3 *XLES-grid*s). The black line corresponds to the analytical result.

3.6.3 *Coupled Linear Advection Scheme: Scalar Transport*

The scalar advection differs slightly from the momentum equation because the scalar field (θ) is defined in all *XLES-grid*s while each velocity component is advanced only in 2 *XLES-grid*s (due to reasoning in section 3.4.5). The coupled scalar advection scheme solves the equation (cf. Eq. (137)):

$$0 = \partial_t \underline{\hat{\theta}} + \sum_{j=1}^{3} \partial_{x_j} \langle \underline{\hat{u}}_j \rangle * \underline{\hat{\theta}} + \sum_{j=1}^{3} \left(\underline{\underline{l}}^{\dagger} * \underline{\underline{C}} \partial_{x_j} \left(\langle \underline{\hat{u}}_j \rangle * \underline{\hat{\theta}} - \langle \underline{\overline{u}}_j \rangle^{LES} * \underline{\overline{\theta}}^{LES} \right) \right) . \tag{143}$$

There is only one case to consider for the coupled scalar advection scheme, because θ is represented by 3 *XLES-grid*s:

- Case 1: $j \overset{w.l.o.g.}{=} 1$ in Eq. (143): In *XLES-grid* 1 the advection term is highly resolved while in *XLES-grid*s 2 and 3 it is coarsely resolved.

The scalar field (θ) is cell-centered while the velocities *w.l.o.g.* $\langle \underline{\hat{u}}_1 \rangle$ are face-centered on a staggered grid (see section 2.1.1.1).

The corresponding coupled scheme with *CN* and two times *RK3* in time and spatial *CDM* (*CN-RK3-RK3-CDM*) gives identical numerical results compared to *CN-RK3-CDM* for the linear momentum advection case, as figure 18 illustrates.

3.6.4 *Alternative Time Schemes*

There are other time schemes, which potentially can be adapted to the special requirements of the *ODTLES* time advancement (see section 3.5.5), e.g.:

- An implicit/explicit time scheme (*IMEX*) (see e.g. [12] and references cited therein) applied to *XLES* can in principle lead to a high-order time approximations for all terms (including non-linear advection and coupling). In these schemes an implicit scheme (e. g. *CN* or an implicit Runge-Kutta scheme, see e. g. [9]) is applied to selected terms in each stage of an explicit Runge-Kutta cycle. To apply this idea to *ODTLES* the coupling terms and *ODT* advancement have to be interpreted as explicit terms applied in each Runge-Kutta stage, which is especially counter-intuitive for the *ODT* advancement. For now we let this to be investigated in future studies.

- Adapting split-explicit schemes (see e.g. [29]) to the *XLES* coupled advection can especially decrease the dispersive effects that arise (numerical dispersion of the implemented coupled advection scheme is investigated in sections 3.6.2 and 3.6.3).

- Large time step wave propagation schemes based on the work by LeVeque [65] can perhaps improve the numerical properties by replacing the applied *CN* scheme within the *XLES* advection scheme.

Part II

APPLICATIONS

4

SHEAR DRIVEN TURBULENT PROBLEMS

Note that parts of this chapter, especially several figures are also presented in [2] and [3].

Shear driven turbulent flows occur in various engineering applications. Fundamental research in this area mostly simplifies the computational domain to purely investigate the influence of turbulence. Additionally turbulence models are often verified and parameters are determined by applying these models to fundamental turbulent flows. This chapter presents *ODT*, *XLES-U*, and *ODTLES* results for a turbulent channel (section 4.1) and a turbulent squared duct (section 4.2) to verify the model assumptions and numerical implementations and determine the model parameters. An *ODTLES#1* heated channel study was performed by the author in [1].

4.1 TURBULENT CHANNEL FLOW

The fully developed turbulent channel flow is one of the computationally most investigated flows in fundamental turbulence research. The simple domain (see figure 19) allows to investigate wall-bounded, incompressible flows including shear-driven turbulence without disturbing interactions by other physical effects and thus yields fundamental insights into statistical and structural characteristics of wall-bounded flows and turbulence per se.

The channel flow is bounded by 2 infinite parallel walls with a distance $2h$ (h is the channel half height) and can be investigated in terms of the incompressible Navier-Stokes equations (Eqs. 4 and 5 for *XLES*) by neglecting e. g. acoustic and gravitational effects. Within the Navier-Stokes equations, the flow is forced e. g. by a constant pressure gradient (F_i in Eq. (5)). Periodic boundary conditions in spanwise and wall-normal directions are applied. The maximum size of undisturbed simulated coherent structures is limited by the computational domain indicated in figure 19.

This flow regime is challenging in reference experiments: High spanwise to wall-normal aspect ratios in very long ducts are required to observe a statistically stationary flow.

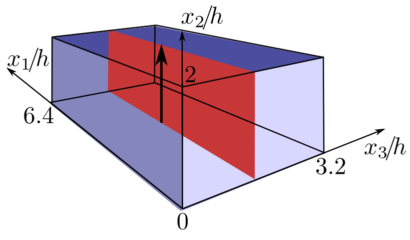

Figure 19: Coordinate system and computational domain of the turbulent channel investigated here. The bold arrow illustrates a possible 1D sub-domain.

In section 4.1.2 *ODT* turbulent channel flow results including high order statistics within a 1D sub-domain (see figure 19) are shown to be in good agreement with *DNS* simulations, whereby the symmetry properties of the channel are exploited. As discussed in section 3.5.2 a good agreement of *ODT* results with *DNS* implies an acceptable *ODT* momentum error term ($\sigma_{ODT_{ij}}$) and indicates the *ODT* model to be an appropriate *SGM* within *XLES*.

Additionally *LES-U*, *XLES-U*, and *ODTLES* approaches are compared within a convergence study in section 4.1.4. The presented results imply that suitable numerical schemes are applied and the *XLES-U* spatial momentum error term ($\underline{\sigma}^{\mathrm{spatial}}_{\mathrm{XLES-U_{ij}}}$) is reasonably low (cf. section 3.4.7).

The *ODTLES* model represents key flow features with unrivaled low 3D resolutions and pretty independent of the friction Reynolds number (Re_τ) as shown for highly turbulent channel flows in section 4.1.5.

In particular for a turbulent channel flow the 'ODT-limit' for $N_{\mathrm{LES}} = 1$ (section 3.5.2) and the 'DNS-limit' for $N_{\mathrm{LES}} = N_{\mathrm{DNS}}$ (section 3.4.7) of *ODTLES* implies both the representative quality and the computational costs to lie in between *ODT* and *DNS*, fully controlled by the chosen 3D resolution N_{LES}.

For a laminar flow through a channel a stationary solution is sufficiently described by the Stokes equation

$$0 = \nu \partial^2_{x_2} u_1 + F_1 \tag{144}$$

with the constant specific external forcing in x_1-direction $F_1 = 1\frac{m}{s^2}$ (e.g. a constant pressure gradient) and the velocity in streamwise direction u_1 (see figure 19). Eq. (144) can be solved analytically leading to $u_1(x_2) = \frac{F_1(hx_2 - x_2^2)}{2\nu}$. From this the wall shear stress ($\tau_W = \rho\nu\partial_{x_2} u_1|_{x_2=0}$) and the friction velocity ($u_\tau = \sqrt{\tau_W/\rho}$) are determined leading to the definition of the friction Reynolds number ($Re_\tau = \frac{u_\tau h}{\nu}$) for a laminar channel (we will refer to this as Re^{lc}_τ).

Re^{lc}_τ is fully determined by the forcing F_1 and the kinematic viscosity (ν) and corresponds to the mean Re_τ-value for a turbulent channel . Here a constant density $\rho = 1\frac{kg}{m^3}$ is assumed.

4.1.1 *ODT: Parameter Study*

To describe the channel flow by *ODT*, Eq. (44) is solved.

The *ODT* model contains 3 model parameters: C influences the overall eddy rate, Z the viscous damping, and the maximum eddy size ($l_{\max}$) is chosen $l_{\max} = h$ for a turbulent channel flow. Additionally $l_{\max}$ is an important parameter within the *ODTLES* model, because it describes the scale separation between the *XLES-U* and *ODT* sub-models.

Figure 20 shows illustrative tendencies of the *ODT* flow for model parameters deviating from the production parameters $C = 6.5$ and $Z = 300$. These productive parameters fairly match the parameters used by Meiselbach [71] ($C = 7$, $Z = 400$) for *aODT* and Gonzalez-Juez et al. [33], and [1] ($C = 6.35$, $Z = 392$) for *ODTLES#1*. The fact that the *ODT* model applied in this thesis contains 2 velocity components has no noticeable impact on the model parameters.

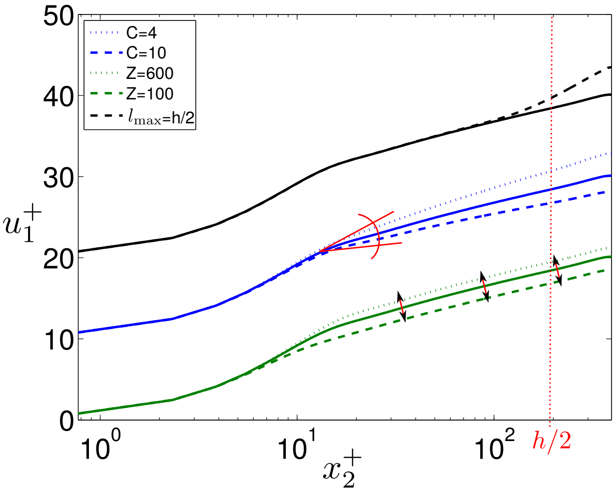

Figure 20: *ODT* parameter study for the law of the wall of a turbulent channel flow, mean streamwise velocity shown here. Results computed with production parameters $Z = 300$, $C = 6.5$, and $l_{\max} = h$ have a solid line. Influence of parameter deviations for Z (green), C (blue) and $l_{\max}$ (black) are shown. Profiles are shifted. The parameters Z influences the transition from the sublayer to the turbulent flow. The parameter C changes the slope within the law of the wall. With decreased $l_{\max}$ the logarithmic layer is restricted to the area near the wall ($y+ = x_2^+ \lesssim l_{\max}$).

4.1.2 *ODT: Turbulent Channel Flow*

As discussed in section 3.5.1, *ODT* momentum error terms ($\sigma_{\mathrm{ODT}_{ij}}$) can roughly be estimated by comparing *ODT* and *DNS* flow statistics for sufficient symmetric cases. The turbulent channel is an appropriate study case for *ODT* because of its distinct predominant direction. *ODT* results with friction Reynolds number $Re_\tau = 395$ are compared to the *DNS* by Kawamura et al. [49] (online available: [48])

The *ODT* model parameters are $C = 6.5$, $Z = 300$, and $l_{\max} = h$ following section 4.1.1. The *ODT* resolution is $N_{\mathrm{ODT}} = 1024$ (N_{ODT} corresponds to N_{RSS} in *XLES*). This corresponds to a equidistant *ODT* resolution in wall units $\Delta x^+_{2,\mathrm{ODT}} = 0.77$. Here the wall coordinates are: $x_2^+ = \frac{x_2 u_\tau}{\nu}$. To compute reliable *ODT* flow statistics a larger averaging period compared to *DNS* (or ensemble averaging) is required: the non-dimensional averaging time is $t_{ave} u_\tau^2/\nu = 5 \times 10^6$ non-dimensional time units after reaching a steady state, which is significantly larger than $t_{ave} u_\tau^2/\nu \geqslant 7900$ in *DNS*.

Figure 21 illustrates representative results for *ODT*: The averaged streamwise velocity profile (see figure 21a) and the overall turbulent kinetic energy (see figure 21c–21e) are described very well within the *ODT* model including the full spectrum of the turbulent cascade. The *ODT* specific determination of the turbulent kinetic energy budget terms is described by Meiselbach [71]. The similarity of *ODT* and *DNS* results implies a considerably small *ODT* momentum error term ($\sigma_{\mathrm{ODT}_{ij}}$). An exemplary *ODT* computing time is ≈ 9 CPU-seconds

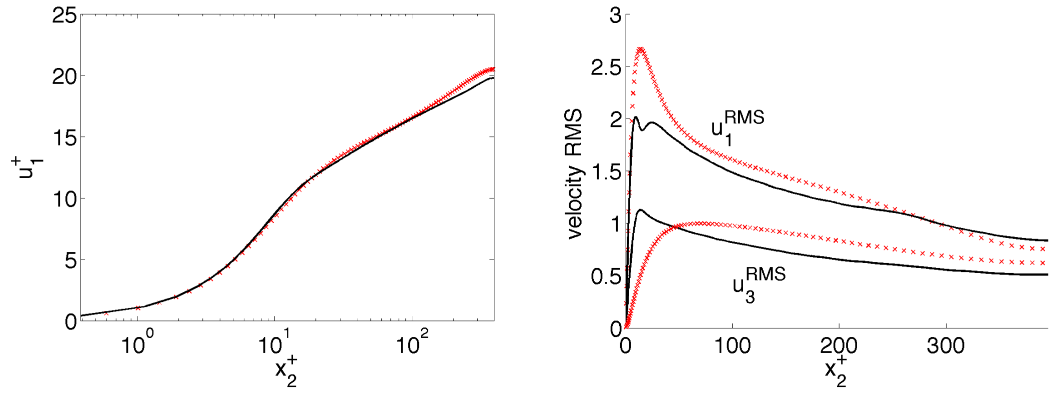

(a) *ODT*: law of the wall.

(b) Streamwise (u_{RMS}) and spanwise (w_{RMS}) velocity RMSs.

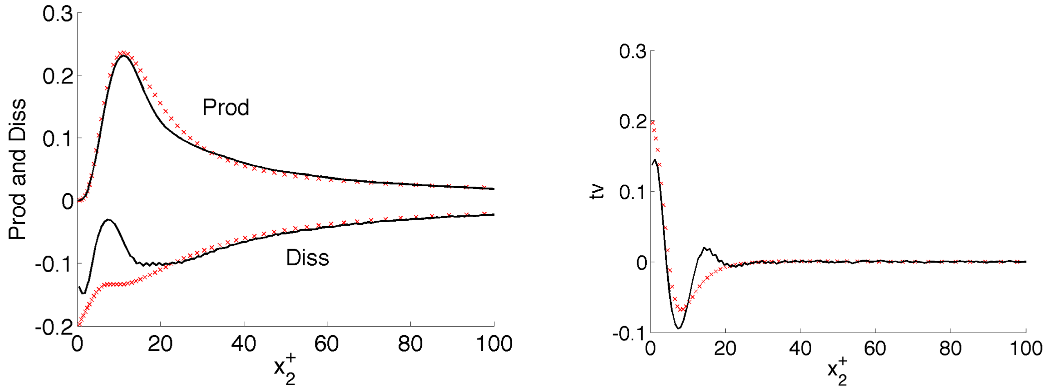

(c) Production (Prod) and Dissipation (Diss) of the turbulent kinetic energy.

(d) Viscous transport of the turbulent kinetic energy (tv).

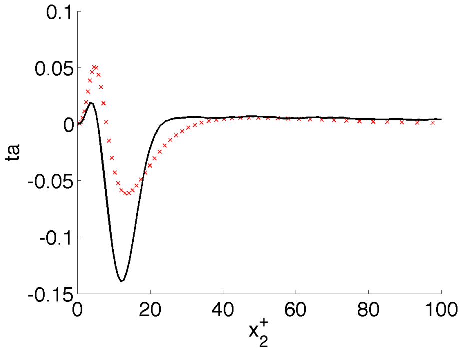

(e) Advective transport of the turbulent kinetic energy (ta).

Figure 21: Turbulent channel flow results ($Re_\tau = 395$) for *DNS* (small crosses) and *ODT* (solid) with $N_{ODT} = 1024$ cells.

to simulate for $t_{ave}u_\tau^2/\nu = 7900$ (the overall computing time is higher, because in the example the flow is averaged over $t_{ave}u_\tau^2/\nu = 5 \times 10^6$). Due to these low computational costs, *ODT* is a convenient sub-grid model. The *ODT-SGM* within *ODTLES* outperforms commonly used eddy viscosity models, because it computes a wide range of complex physical effects including realistic wall profiles for turbulent wall-bounded flows.

Further *ODT* results, including various physical small scale effects, are available in the literature (see e. g. [53], [88], [113], and [90]).

4.1.3 *XLES and ODTLES: Parameter Study*

The *ODTLES* model uses an *ODT* model to close the *XLES* equations. Since for a channel flow *ODT* is able to describe the flow stand alone (in section 4.1.2) it is reasonable to use the productive *ODT* parameters introduced in section 4.1.1 also for the full *ODTLES* model.

As mentioned in sections 4.1.1 and 3.5.1 the maximum eddy size (l_{max}) has a special role in *ODTLES*, because it controls the maximum turbulent scale, which is described by *ODT* and thus defines the spectral scale transition between the *ODT* and *XLES-U* sub-models. The ideal value for l_{max} depends on the numerical properties of the discretized *XLES* equations and has to be determined in numerical tests, as shown in figure 22.

Section 3.5 states $l_{max} = \Delta x^{LES}$ is a convenient choice. This is supported by figure 22 and the spectrum of the streamwise turbulent energy in figure 23. This choice also leads to a reasonable 'ODT limit'.

Figure 23 illustrates that *ODTLES* produces a reasonable spectrum for the specific turbulent kinetic energy independent of the 3D resolution. Contrary to *LES*, in *ODTLES* the spectrum includes high wave number content which is generated by the *ODT-SGM*. For $l_{max} = \Delta x^{LES}$ the transition from *XLES-U* to *ODT* represented turbulent energy is smooth and without artifacts in the estimated wave number region $k \approx N_{LES}$. Increasing l_{max} slightly decreases the agreement of the shown turbulent kinetic energy spectrum with the *DNS* results. In *LES* it seems especially challenging to simultaneously reproduce both a reasonable power spectrum and the right mean flow behavior for a turbulent channel (cf. [20]). In *ODTLES* both can be accomplished without changing properties of the *SGM* and additionally with little sensitivity to the 3D resolution.

In *ODTLES* the *CFL*-number controls the *ODTLES* momentum temporal error term ($\underline{\sigma}^{temporal}_{ODTLES_{ij}}$) (see section 3.4.4). On the one hand higher *CFL*-values increase the computational performance, on the other hand it leads to inaccuracies, as shown in figure 22 and thus choosing the *CFL*-number requires a cost-benefit estimation. For the turbulent channel, we use a *CFL*-number $CFL_{RSS} \leqslant 1$ corresponding to the highly resolved cell size (cf. Eq. (93)) to minimize $\underline{\sigma}^{temporal}_{ODTLES_{ij}}$.

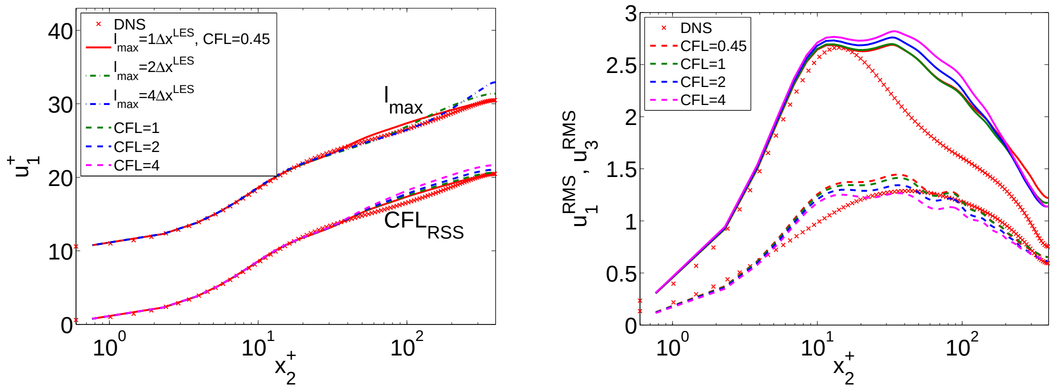

(a) *ODTLES*: Law of the wall parameter study for l_{max} and CFL_{RSS}.

(b) *ODTLES*: Velocity *RMS* parameter study for CFL_{RSS}.

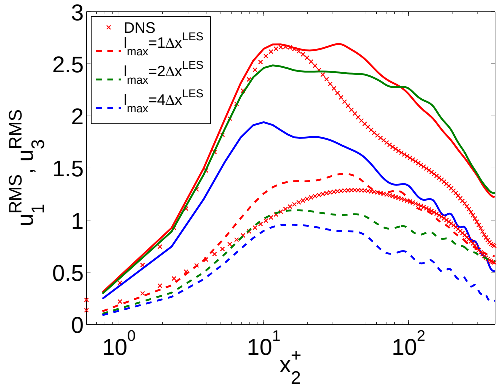

(c) *ODTLES*: Velocity *RMS* parameter study for l_{max}

Figure 22: Additionally to the *ODT* model parameters C (here $C = 6.5$) and Z (here $Z = 300$), *ODTLES* requires the maximum eddy size (l_{max}) and the *CFL*-number (here CFL_{RSS}). l_{max} determines the turbulent scale edge between *ODT* and *XLES-U* and *CFL* controls the *XLES* error term $\underline{\sigma}^{temporal}_{XLES-U_{ij}}$. Figure 22a shows the influence on the mean velocity, while 22b and 22c illustrate the influence on the velocity *RMS*s (u_1^{RMS}: solid; u_3^{RMS}: dashed).

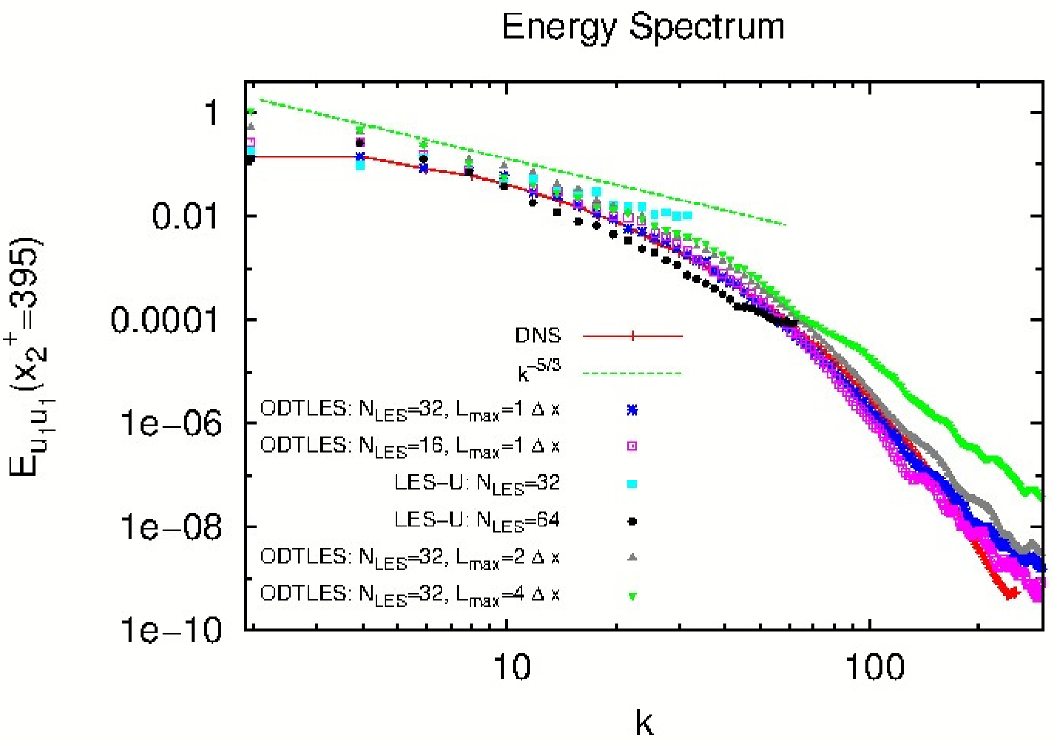

Figure 23: Spectrum of the streamwise turbulent kinetic energy in the channel center for $Re_\tau \approx 395$. The wave number k is oriented in the x_3-direction. *ODTLES* uses N_{RSS}= 1024 cells for the *RSS* and $N_{LES} = 16$ ($l_{max} = \Delta x^{LES}$ open magenta squares) respective $N_{LES} = 32$ 3D cells ($l_{max} = \Delta x^{LES}$ blue stars, $l_{max} = 2\Delta x^{LES}$ gray triangles, and $l_{max} = 4\Delta x^{LES}$ green triangles). Additionally unclosed *LES* with $N_{LES} = 32$ (cyan squares) and $N_{LES} = 64$ (black circles) cells are shown. For comparison a *DNS* result (red line with pluses, by Lee and Moser [63]) and the $k^{-5/3}$ power law (dashed green line) are shown.

Table 7: Channel flow resolution in wall coordinates for $N_{RSS} = 1024$ in each direction using the domain in figure 19 and equidistant cells.

Re_τ	N_{LES}	$\Delta x^+_{RSS_1}$	$\Delta x^+_{RSS_2}$	$\Delta x^+_{RSS_3}$	$\Delta x^+_{LES_1}$	$\Delta x^+_{LES_2}$	$\Delta x^+_{LES_3}$
395	16	2.46	0.77	1.23	156.0	49.4	79.0
395	32	2.46	0.77	1.23	78.0	24.7	39.0
395	64	2.46	0.77	1.23	39.0	12.3	19.5

4.1.4 *XLES and ODTLES: Convergence Study*

The *ODTLES* model includes some temporal and spatial model error terms $\sigma_{ODT_{ij}}$ and $\underline{\sigma}^{spatial}_{XLES-U_{ij}}$. $\sigma_{ODT_{ij}}$ is shown to be small following section 4.1.2. The temporal error term $\underline{\sigma}^{temporal}_{ODTLES_{ij}}$ vanishes for *CFL*-numbers based on the *RSS* cell size (Δx^{RSS}).

Additionally numerical errors can lead to inaccuracies which includes especially the error term due to the reconstruction $\underline{\sigma}^{spatial}_{\dagger}$.

4.1.4.1 *Compare XLES-U and LES-U*

To verify that the spatial *XLES-U* error terms $\underline{\sigma}^{spatial}_{XLES-U_{ij}}$ and numerical errors are acceptable, a convergence study of *XLES-U* compared to *LES-U* and *DNS* results is convenient, as suggested in section 3.4.7.

The convergence study is performed for a fully developed turbulent flow, including the full diversity of non-linear advective effects: A turbulent channel flow with a friction Reynolds number $Re_\tau = 395$ is computed and compared to *DNS* results by Kawamura et al. [49] (online available: [48]). This case also corresponds to the *ODT* results in figure 21.

The *DNS* is resolved with $N_{DNS} = 192$ non-equidistant cells in the horizontal direction (between the walls). For the spatial discretization a *CDM* is used. The time is discretized using a *CN* scheme for the wall-normal non-linear terms and a second order Adams-Bashforth scheme for other terms (results for higher resolutions and higher order schemes are also available online). This numerical scheme is comparable to the *XLES-U* numerical scheme (see sections 2 and 3.6).

For the *XLES-U* convergence study, the number of equidistant 3D large scale cells N_{LES} for all directions is increased using the values $N_{LES} = \{16, 32, 64\}$ while $N_{RSS} = 1024$ is kept constant.

Using the domain in figure 19 and equidistant cells lead to the resolutions in wall coordinates shown in table 7. As stated in section 3.5.1 *ODT* 'eddies' mainly occur in the wall-normal direction x_2 in a channel flow. Thus the *RSS* resolution in the other directions is not required to be sufficient to allow *ODT* triplet maps, nevertheless the cell size is still in the range of the Kolmogorov length scale (η_K).

The time step size is limited by Eq. (96) with $\mathrm{CFL}_{\mathrm{RSS}} = 0.45$ corresponding to the small spatial cells Δx^{RSS}.

To produce statistically significant results, the flow is averaged for $t_{ave} u_\tau^2/\nu \geqslant 9875$ non-dimensional time units (compared to $t_{ave} u_\tau^2/\nu = 7900$ for DNS) after reaching a statistically steady state.

Additionally equidistant discretized *LES-U* channel flow results (solving Eqs. (101) and (105) with $N_{\mathrm{RSS}} = N_{\mathrm{LES}}$, see section 3.4.7) are compared to *XLES-U*. The latter resolves additional advective and diffusive small scale effects. Those can be identified by comparing the *XLES-U* and *LES-U* channel flow results. The error term $\underline{\sigma}^{\mathrm{spatial}}_{\mathrm{XLES-U}_{ij}}$ does not occur in *LES-U*.

Figure 24 illustrates the results: The mean velocity profiles computed by *XLES-U* (see figure 24b) and *LES-U* (see figure 24a) are compared to *DNS*.

Additionally the streamwise and spanwise velocity *RMS*s (see figure 24c) and the budget terms of the turbulent kinetic energy (see figure 24d- 24f) are shown for *XLES-U*, *LES-U*, and *DNS*.

Both *XLES-U* and *LES-U* show convergence towards the *DNS* results with increasing 3D resolution. Following arguments in section 3.4.7 this implies the *XLES* error term $\underline{\sigma}^{\mathrm{spatial}}_{\mathrm{XLES-U}_{u_i}}$ to be small. Additionally the non-linear terms for *XLES-U* and *LES-U* are sufficiently represented and converging, even if the under-resolved velocity profile (figure 24a and 24b) indicates noticeable numerical dissipation. This behavior is very similar to comparable *LES* studies, e. g. by Denaro [20].

XLES-U is able to accurately represent diffusive effects, e.g. the laminar sublayer near the walls, independent of the 3D large scale resolution and reproduces basic advective effects including turbulence with $N_{\mathrm{LES}} \gtrsim 32$ cells for $Re_\tau = 395$. Additionally the turbulence statistics profit from the additional small scale effects represented by *XLES* compared to *LES-U* even with low 3D resolutions.

4.1.4.2 *Comparison of ODTLES and XLES-U*

To show the significant effect of *ODT* as a *SGM*, the *ODTLES* model is investigated in a similar convergence study Additionally the *DNS* results by Kawamura [48] are presented for comparison reasons.

For this convergence study illustrated in figure 25 both, *XLES-U* and *ODTLES*, are using $N_{\mathrm{LES}} = \{16, 32, 64\}$ (equidistant) 3D large scale cells and $N_{\mathrm{RSS}} = 1024$ cells resolving the small scale. The resolutions in wall coordinates equal those in table 7.

The XLES time step size is again limited by Eq. (96) with $\mathrm{CFL}_{\mathrm{RSS}} = 0.45$ to minimize $\underline{\sigma}^{\mathrm{temporal}}_{\mathrm{ODTLES}_{ij}}$. The *ODT* advancement is only indirectly influenced by this *CFL*-number.

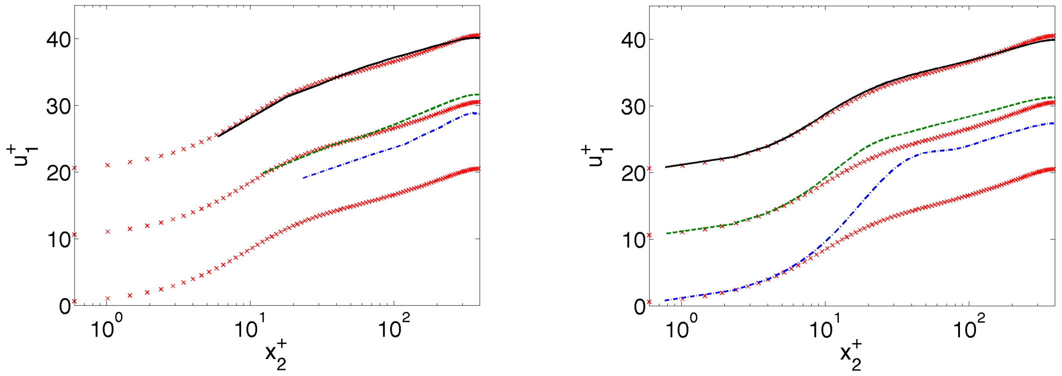

(a) LES: law of the wall ($\overline{u}_1^{LES}$). Profiles shifted with increasing N_{LES}.

(b) XLES: law of the wall ($\hat{u}_{2,1}$). Profiles shifted with increasing N_{LES}.

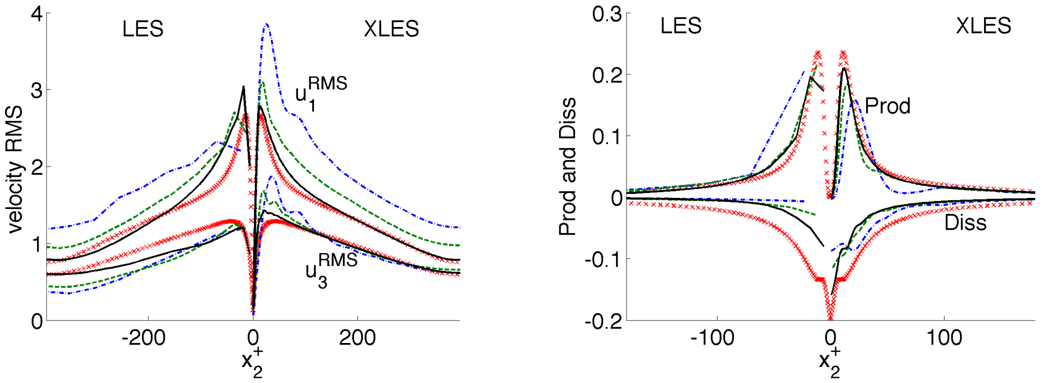

(c) Streamwise (u_1^{RMS}) and spanwise (u_3^{RMS}) velocity RMS.

(d) Production (Prod) and Dissipation (Diss) of the turbulent kinetic energy.

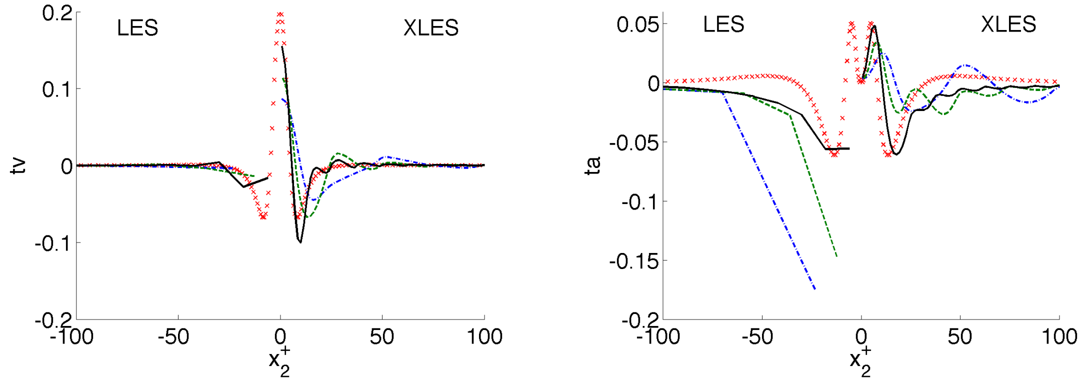

(e) Viscous transport of the turbulent kinetic energy (tv).

(f) Advective transport of the turbulent kinetic energy (ta).

Figure 24: Turbulent channel flow results for DNS (small crosses), *LES-U*, and *XLES-U* with $N_{LES} = 16$ (dash-dotted), $N_{LES} = 32$ (dashed), and $N_{LES} = 64$ (solid). The *XLES-U* small scales are resolved using $N_{RSS} = 1024$ cells. *XLES-U* mean and statistical flow properties are based on the velocity field perpendicular to the channel walls $\hat{u}_{2,i}$ (in the LES limit: $\hat{u}_{2,i} = \overline{u}_i^{LES}$).

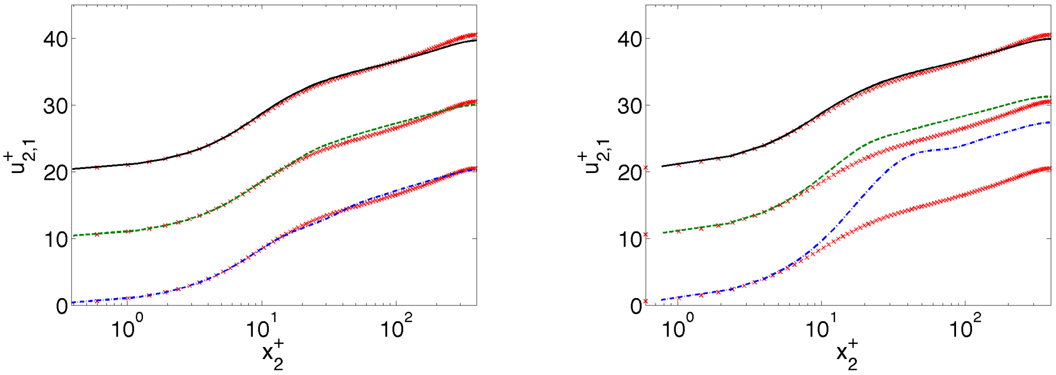

(a) ODTLES: law of the wall ($\hat{u}_{2,1}$). Profiles shifted with increasing N_{LES}.

(b) XLES : law of the wall ($\hat{u}_{2,1}$). Profiles shifted with increasing N_{LES}.

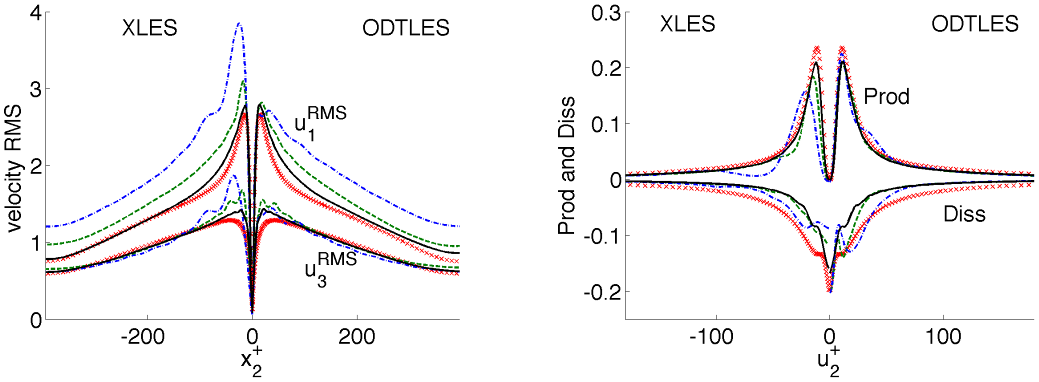

(c) Streamwise (u_1^{RMS}) and spanwise (u_3^{RMS}) velocity RMS

(d) Production (Prod) and Dissipation (Diss) of the turbulent kinetic energy

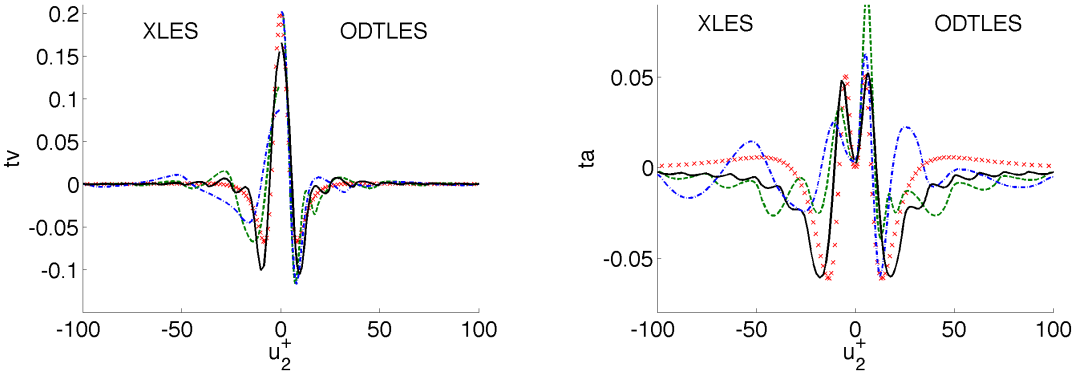

(e) Turbulent diffusion of the turbulent kinetic energy (tv)

(f) Molecular diffusion of the turbulent kinetic energy (ta)

Figure 25: Turbulent channel flow results for *DNS* (small crosses), *ODTLES*, and *XLES-U* with $N_{LES} = 16$ (dash-dotted), $N_{LES} = 32$ (dashed), $N_{LES} = 64$ (solid). The small scales are resolved using $N_{RSS} = 1024$ cells. The flow statistics are based on the velocity field $\hat{u}_{2,i}$.

The *ODT* model parameters are $C = 6.5$ and $Z = 300$ according to section 4.1.1. The maximum eddy length l_{max} in XLES-grid k equals the 3D large scale cell size Δx_k^{LES} (following section 4.1.3).

To produce statistically significant results, the flow is averaged for $t_{ave}u_\tau^2/\nu \geqslant 9875$ non-dimensional time units similar to the *XLES* results.

The mean velocity profiles computed by *ODTLES* (see figure 25a) and *XLES* (see figure 25b) are compared to *DNS*.

Additionally the streamwise and spanwise velocity RMS (see figure 25c) and the budget terms of the turbulent kinetic energy (see figure 25d–25f) are shown.

ODTLES and *XLES-U* show convergence towards the *DNS* results with increasing 3D resolution. *ODTLES* is able to represent the flow field and turbulent statistics even with the very low 3D resolution $N_{LES} = 16$, including the laminar sublayer near the walls and the budget terms of the turbulent kinetic energy.

Heated Channel flow studies using *ODTLES#1* were presented in Glawe et al. [1]. Thereby the scalar property was represented only by *XLES-grid* 2.

4.1.5 *ODTLES: High Reynolds Number Flow*

ODTLES combines the ability of the *ODT* model to describe all scales of highly turbulent flows within a 1D sub-domain of the full 3D domain with a coarse grained *XLES* approach representing the geometry of the 3D domain for a turbulent channel and introducing additional 3D effects compared to *ODT* standalone.

As shown in a convergence study in section 4.1.4 low Reynolds numbers are well described by *ODTLES* with only $N_{LES} = 16$ cells. To demonstrate the *ODTLES* ability to describe highly turbulent flows within a simple domain, we conduct turbulent channel flow computations with $N_{LES} = 32$ cells (in 3D) and up to $N_{RSS} = 16384$ cells to represent additional small scale effects, which allows Reynolds numbers $Re_\tau \leqslant 10000$.

The *RSS* and 3D resolutions are summarized in table 8. The *CFL*-number is chosen following Eq. (96) with $CFL \leqslant 1$ and *ODT* parameters are: $C = 6.5$, $Z = 300$, and $l_{max_k} = \Delta x_k^{LES}$.

The mean velocity profiles for several friction Reynolds numbers are illustrated in figure 26a and compared to *DNS* by Kawamura et al. [49] and Lee and Moser [62] (online available: [48] and [63]). The *ODTLES* computation with $Re_\tau = 10000$ is in good agreement with the laminar solution near the wall and the law of the wall. This corresponds to a logarithmic function $u_2^+ = u_2/u_\tau = \frac{1}{\kappa}\ln(x_2^+) + C^+$ with the von Kármán constant $\kappa = 0.384$ and an additional constant $C^+ = 4.15$ (obtained by Lee and Moser [62] for a turbulent channel with $Re_\tau = 5200$).

The streamwise and spanwise velocity *RMS* (see figure 26b) are in good agreement with the available *DNS* in the laminar region near the wall and beyond the first 3D cell. Within the first 3D cell, *ODT* typically has some issues

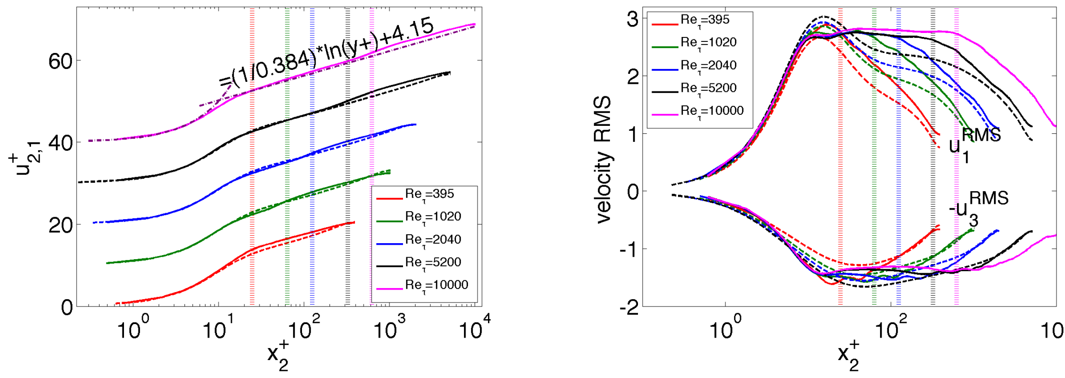

(a) Law of the wall. Profiles shifted with increasing Re_τ.

(b) Streamwise (u_{RMS}) and spanwise ($-w_{RMS}$) velocity RMS.

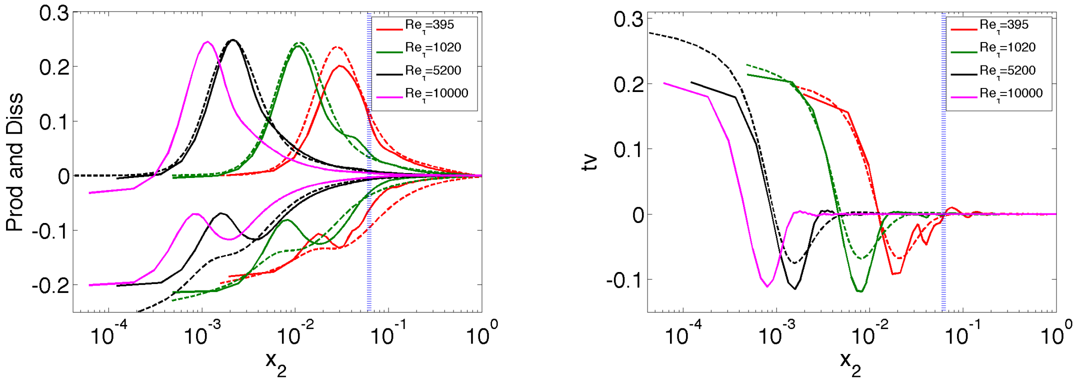

(c) Production (Prod) and Dissipation (Diss) of the turbulent kinetic energy.

(d) Viscous transport of the turbulent kinetic energy (tv).

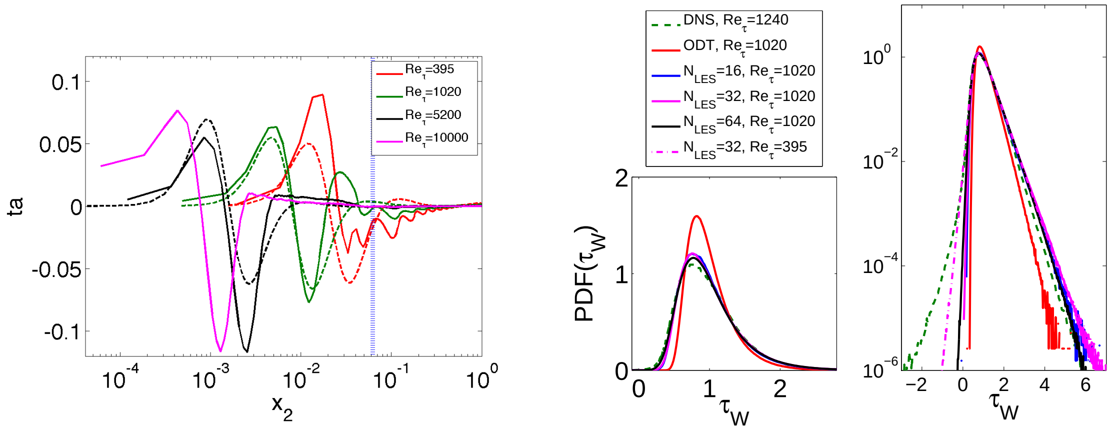

(e) Advective transport of the turbulent kinetic energy (ta).

(f) Wall shear stress τ_W: linear (left) and logarithmic (right).

Figure 26: Turbulent channel flow results for ODTLES (solid) and available DNS (dashed) for $N_{LES} = 32$ (if not indicated otherwise). The resolution in wall coordinates is presented in table 8. The size of the first 3D cell is illustrated by vertical lines for the different Re_τ values. Figure 26f compares the ODT and ODTLES wall shear stress ($Re_\tau = \{395, 1020\}$) for various N_{LES} to DNS ($Re_\tau = 1240$). For $Re_\tau = 10000$ no *DNS* result is available.

Table 8: Channel flow resolution in wall coordinates for $N_{LES} = 32$ in each direction using the domain in figure 19 and equidistant cells. All *DNS* results are produced using a non-equidistant grid.

Re_τ	N_{RSS}	$\Delta x^+_{RSS_1}$	$\Delta x^+_{RSS_2}$	$\Delta x^+_{RSS_3}$	$\Delta x^+_{LES_1}$	$\Delta x^+_{LES_2}$	$\Delta x^+_{LES_3}$	$\Delta x^+_{DNS_2}$
395	1024	2.46	0.77	1.23	78.8	24.7	39.4	>0.44
1020	2048	3.20	1.00	1.61	204.2	63.8	102.0	>0.15
2040	4096	3.20	1.00	1.61	408.4	127.6	204.2	>0.43
5200	8192	4.02	1.26	2.00	1040.0	325.0	520.0	> 0.07
10000	16484	3.89	1.22	1.96	2000.0	625.0	1000.0	–

in representing the velocity *RMS* (this also applies for the budget terms of the kinetic energy).

In figure 26c–26e the budget terms of the turbulent kinetic energy are shown to be in good agreement with the *DNS* results, especially for highly turbulent flows.

The convergence of *ODTLES* with increasing 3D resolution can be observed within statistical properties including 3D effects not represented by *ODT*: The *PDF* of τ_W shows e. g. convergence with increasing 3D resolution, while within other statistical informations, e. g. the velocity *RMS* the *ODT* specific effects are represented in decreasing strengths with increasing N_{LES}.

ODT and *ODTLES* wall shear stress statistics for $Re_\tau = 1020$, illustrated in figure 26f, are compared to *DNS* results by Schlatter and Örlü [87] for $Re_\tau = 1240$. The *ODT* wall shear statistics are in rather good agreement with the DNS (see figure 26f left), which indicates *ODT* to be an accurate near-wall model, yet by including additional 3D resolution $N_{LES} > 1$ within *ODTLES* the *PDF* is significantly improved. A more detailed investigation (see figure 26f right) shows that *ODTLES* underestimates rare backflow events. The reason could be that the responsible 3D structures near the wall are not represented due to the coarse 3D resolution, because the 3D cell size in wall units is $\Delta x^+_{LES_2} \approx 31.9$ for the highest considered 3D resolution $N_{LES} = 64$ (with $Re_\tau = 1020$). The result with lower Reynolds number ($Re_\tau = 395$) with 3D cell size in wall units $\Delta x^+_{LES_2} \approx 24.7$ supports this hypothesis. With increasing 3D resolution *ODT* specific issues in the near-wall statistics decreases in *ODTLES*. Here we assume a low Reynolds number sensitivity of the wall shear stress statistics, as Schlatter and Örlü [87] report, to qualitatively compare τ_W-statistics with different Re_τ.

In summary *ODTLES* is able to capture the mean flow and turbulence statistics of highly turbulent flows up to $Re_\tau = 10000$ within a simple domain. The computational costs are significant lower compared to *DNS*: Lee et al. [61] report to use about 260×10^6 CPU hours on 786×10^3 cores for the *DNS* with

$Re_\tau = 5200$, while the corresponding *ODTLES* simulation takes ≈ 15000 CPU hours on 24 cores.

A detailed investigation of the expected computational costs relative to *RaNS*, *LES* and *DNS* in section 3.5.7 shows *ODTLES* to be convenient to describe highly turbulent flows in domains of moderate complexity.

4.2 SQUARE DUCT FLOW

Sections 4.1.4 and 4.1.5 show turbulent channel flow results for the *ODTLES* model to be in good agreement with *DNS*. With increasing 3D resolution a convergence to *DNS* is observed, but even within an 'ODT-limit' (corresponding to a single 3D cell) the *ODT* model reproduces key flow features stand-alone (see 4.1.2).

The squared duct flow combines a simple geometry (see figure 28a) and a complex flow behavior including secondary instabilities (secondary flow of Prandtl's second kind) and turbulent fluctuations. In the turbulent duct flow, a turbulence induced flow structure transitions, these secondary instabilities occur, which are not captured by *ODT*.

Since the *ODT* model cannot describe secondary instabilities within a duct flow, a proper 'ODT-limit' cannot be expected. Thus key secondary features are required to be resolved in 3D, leading to the enhanced Reynolds dependency of N_{LES} compared to the channel flow.

For low Reynolds numbers (near the value for sustained turbulence) the size of the secondary flow structures in cross-stream direction corresponds to the half duct height (h). This flow regime in a squared duct is investigated by Uhlmann et al. [107] using *DNS*. Even for higher turbulent Reynolds numbers the cross-stream extension of the secondary instabilities is rather large scale compared to turbulent fluctuations occurring e.g. near the wall. Nevertheless these small scale fluctuations play an important role for the duct flow because they generate secondary instabilities. The *ODT* model was shown to accurately describe small scale fluctuations and the secondary instabilities correspond to a rather large scale 3D flow feature which can be described by the *XLES* framework. Thus *ODTLES* is a promising model to describe the duct flow, as shown in *ODTLES#1* (see [33] and [1]) and *ODTLES* studies (see [3]).

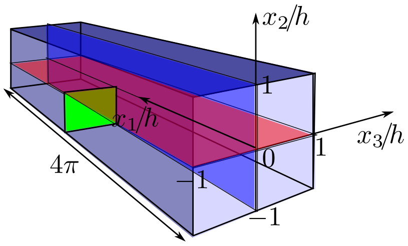

Figure 27: Coordinate system and computational domain (Ω) of the squared duct investigated here.

A 1D solution equivalent to the laminar channel flow in section 4.1 is not possible for a laminar duct flow. Nevertheless the friction Reynolds number

(Re_τ) can be computed at each lateral position (e. g. $-1 < x_3 < 1; x_2 = -1$ in figure 27). Influenced by the side walls the friction Reynolds number (Re_τ) is smaller in each lateral position than the corresponding Re_τ for a laminar channel (called Re_τ^{lc} in this section) with identical forcing F_1 and kinematic viscosity. The spanwise averaged friction Reynolds number is $\mathrm{Re}_{\tau_{ave}} = \frac{1}{|\partial\Omega|}\int_{\partial\Omega} \frac{u_\tau(x)\,h}{\nu}\,dx_1\ dx_{2|3}$ and characterizes the global interplay between the flow and the walls.

The squared duct flow is often characterized by its bulk Reynolds number (Re_B) with ($\mathrm{Re}_B = \frac{u_B\,h}{\nu}$). Hereby the bulk velocity (u_B) is the volume averaged streamwise velocity $u_B = \frac{1}{|\Omega|}\int_\Omega u_1\,dx_1\,dx_2\,dx_3$.

ODTLES duct flow results are computed by solving Eqs. (101) and (105) identically to the channel flow, but for the computational domain shown in figure 27. Thus both $\mathrm{Re}_{\tau_{ave}}$ and Re_B are derived from computed *ODTLES* results.

4.2.1 *ODTLES: Square Duct Flow*

The *CFL*-number is chosen following Eq. (96) with $\mathrm{CFL}_{\mathrm{RSS}} \leqslant 1$. The *ODT* model parameters are $C = 6.5$, $Z = 300$, and $l_{\max_k} = \Delta x_k^{\mathrm{LES}}$, which is identical to the channel flow setup in section 4.1.5.

The flow is averaged for $t_{ave}u_B/h \geqslant 2800$ non-dimensional time units after reaching a steady state which is assumed to be sufficient to investigate the secondary instabilities. This is supported by a study of vortex structures by Uhlmann et al. [107] where nearly symmetric 8-vortex structures are observed for lower averaging times at bulk Reynolds number $\mathrm{Re}_B \geqslant 2600$. Additionally the *ODTLES* results are averaged over the 4 quadrants. Note that the *DNS* by Pinelli et al. [81] uses $t_{ave}u_B/h \geqslant 7000$ to produce meaningful high order statistics.

Figure 28 compares the secondary flow computed by *ODTLES* for a moderate bulk Reynolds number $\mathrm{Re}_B \approx 2600$ with the *DNS* by Pinelli et al. [81] (online available: [106]). Hereby *ODTLES* uses $N_{\mathrm{LES}} = \{16, 32\}$ large scale cells per direction and the XLES specific small scale properties are resolved by $N_{\mathrm{RSS}} = 1024$ cells. The corresponding *RSS* and 3D resolutions are summarized in table 9.

Table 9: Duct flow resolution in wall coordinates in each direction using the domain in figure 28a and equidistant cells. The wall coordinates are based on Re_τ^{lc} for the laminar channel which is an upper limit for maximum local friction Reynolds number within the duct.

Re_τ^{lc}	Re_B	$\mathrm{Re}_{\tau_{ave}}$	N_{RSS}	N_{LES}	$\Delta x^+_{\mathrm{RSS}_1}$	$\Delta x^+_{\mathrm{RSS}_2}$	$\Delta x^+_{\mathrm{RSS}_3}$	$\Delta x^+_{\mathrm{LES}_1}$	$\Delta x^+_{\mathrm{LES}_2}$	$\Delta x^+_{\mathrm{LES}_3}$
250	2667	174	512	16	6.14	0.98	0.98	196.2	31.3	31.3
250	2514	174	512	32	6.14	0.98	0.98	98.2	15.6	15.6
322	3485	226	1024	32	3.94	0.62	0.62	126.4	20.2	20.2

666	8446	464	2048	32	4.08	0.66	0.66	261.4	41.6	41.6
1250	17338	870	2048	32	7.66	1.22	1.22	490.6	78.1	78.1
2500	38387	1758	4096	32	7.66	1.22	1.22	981.3	156.3	156.3
5000	83457	3486	8192	32	7.66	1.22	1.22	1962.4	312.5	312.5

The primary flow and key features of the secondary flow shown in figure 28 are in good agreement with the *DNS* results even with the very low 3D resolution of $N_{LES} = 16$ cells. Furthermore the *ODTLES* results indicate a convergence towards the *DNS* results with increasing 3D resolution.

The secondary mean velocity field alters with increasing Reynolds number, as investigated in figure 29. In particular each secondary vortex structure tends towards a triangular shape for increasing Reynolds number. The vorticity approaches the duct corner with increasing Reynolds number, indicating fast changes of the secondary flow directions in this area.

In the present formulation, both Re_B and $Re_{\tau_{ave}}$ are simulated results. Nevertheless their correlation states the relation of near-wall flow phenomena with global flow structures. Especially *ODTLES* results with a 3D resolution $N_{LES} = \{16, 32, 64\}$ are consistent with the empirical correlation by Jones [43][1] even for high bulk Reynolds numbers, as illustrated in figure 30. This indicates a good *ODTLES* representation of the global flow structures and a well represented near-wall flow (laterally averaged) for highly turbulent flows with low 3D resolutions. In particular this means that in the investigated regime the friction velocity grows almost linearly with the bulk velocity. Also figure 30 suggests, that at least $N_{LES} = 16$ 3D cells per direction are required to resolve 3D flow structures corresponding to the secondary flow. The *XLES-U* results in figure 30 tend towards the laminar solution, which implies that the *ODT-SGM* is required for high bulk Reynolds numbers.

ODTLES results with low 3D resolutions show a tertiary instability above some N_{LES}-dependent threshold Reynolds number (between 8446 and 17338 for $N_{LES} = 32$) in the corner region (see figure 31).

The 3D tertiary structure in the corner region is of similar size as the corresponding 3D computational cell. Its influence on the flow is primarily local. The insufficient 3D resolution leads to an under-resolved pressure gradient which could prevent an adequate change of a fluid parcel's direction (blue arrows within figure 31).

In particular highly 3D resolved result in figure 31c suggest that the insufficient 3D resolution causes the tertiary instabilities. Nevertheless even with low 3D resolutions the cross-stream flow is adequately resolved in the wall-normal direction (green arrows within figure 31). An equivalent interpretation is that the local symmetry properties required by the *ODT-SGM* are not valid in the

---

[1] Correlation: $f^{-1/2} = 2\log_{10}(2.25 Re_B f^{1/2}) - 0.8$, with the friction factor $f = 8u_\tau^2/u_B^2$

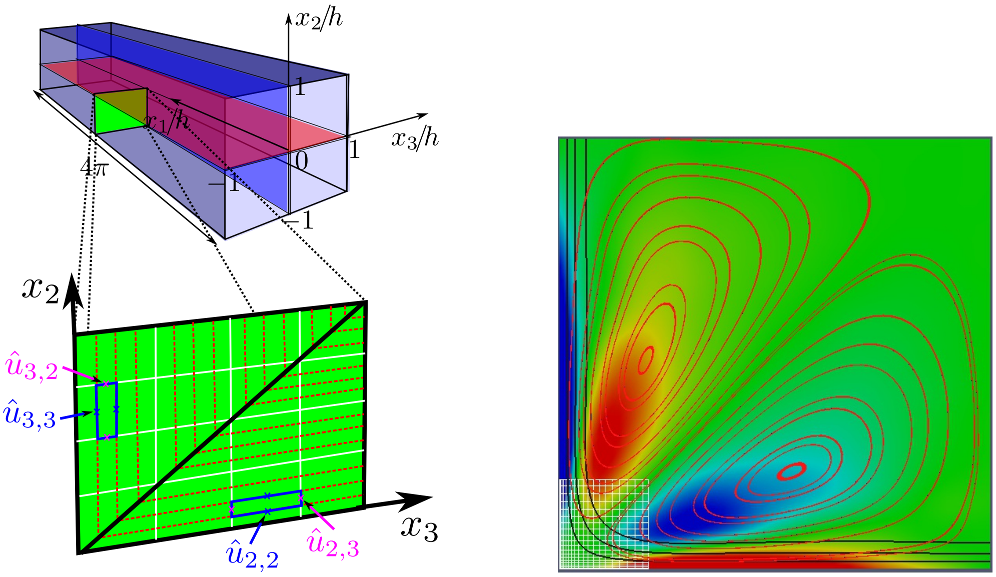

(a) Geometry and illustrated *XLES-grid*s.
(b) *DNS*: $\mathrm{Re_B} = 2600$.

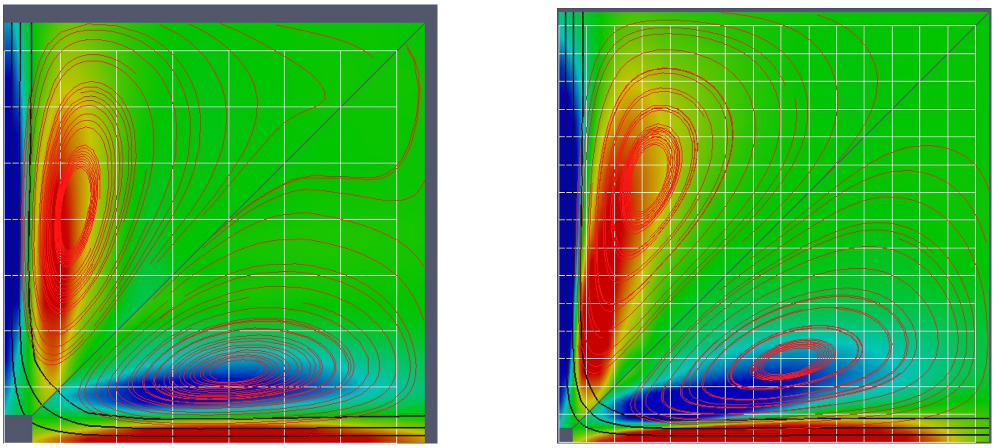

(c) *ODTLES*: $N_{\mathrm{LES}} = 16$, $\mathrm{Re_B} = 2667$.
(d) *ODTLES*: $N_{\mathrm{LES}} = 32$, $\mathrm{Re_B} = 2514$.

Figure 28: All results are averaged in time and streamwise direction. One quadrant of the duct is shown (see 28a). The 3D grid is indicated by white lines (for the *DNS* only in the corner region). *ODTLES* properties are illustrated like cell centered and show additional small scale features (resolved by $N_{\mathrm{RSS}} = 1024$ cells) using the *XLES-grid* highly resolved in vertically x_2-direction (horizontally x_3-direction) in the lower right (upper left) triangular region, as illustrated in 28a. Only dynamical variables are plotted for *ODTLES* (no boundary conditions), which leads to the gap in the flow field at the corner. Contour lines of the primary mean flow (black) for $u_1 = \{0.2, 0.4, 0.6\} \max(u_1)$, streamlines of the secondary mean flow (u_2, u_3) in red and the 2D vorticity $\omega_{2D} = \partial_{x_2} u_3 - \partial_{x_3} u_2$ (RGB color coded) are shown.

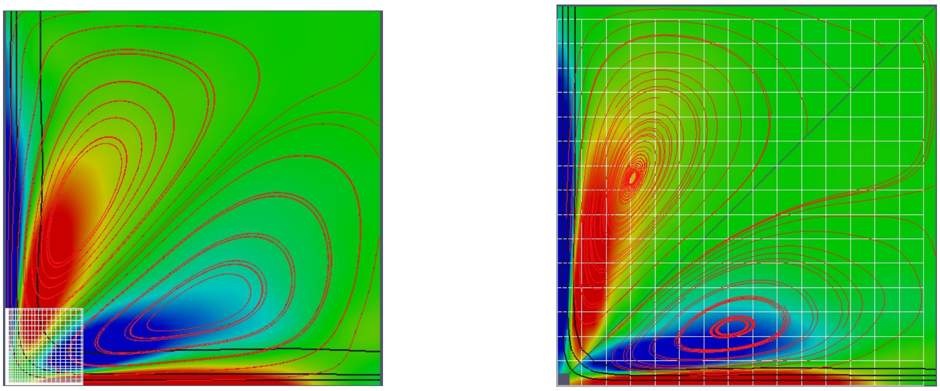

(a) *DNS*: $Re_B = 3500$.

(b) *ODTLES*: $Re_B = 3485$, $N_{RSS} = 1024$.

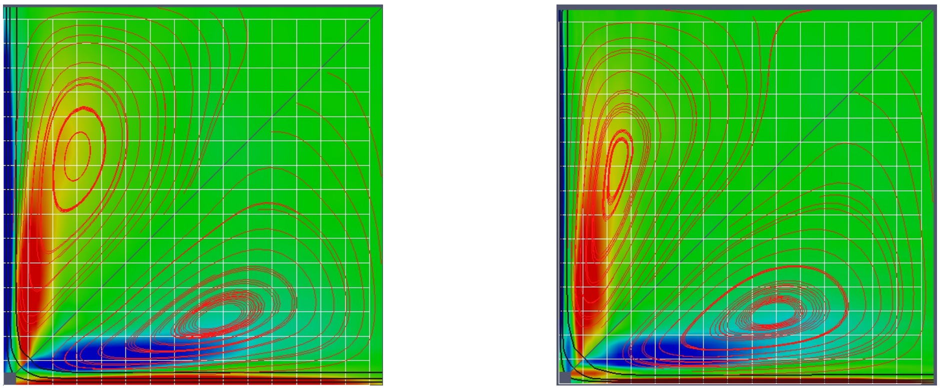

(c) *ODTLES*: $Re_B = 8446$, $N_{RSS} = 2048$.

(d) *ODTLES*: $Re_B = 17338$, $N_{RSS} = 2048$.

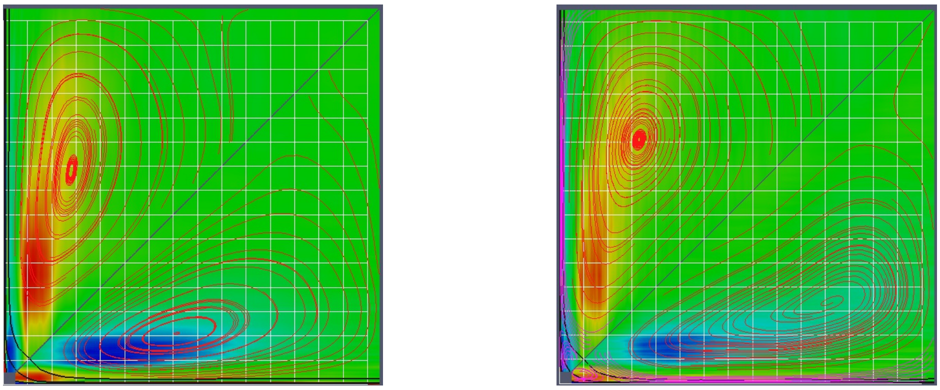

(e) *ODTLES*: $Re_B = 38387$, $N_{RSS} = 4096$.

(f) *ODTLES*: $Re_B = 83457$, $N_{RSS} = 8192$.

Figure 29: *ODTLES* and *DNS* squared duct results with $N_{LES} = 32$ for different bulk Reynolds numbers (Re_B). Primary and secondary streamlines and vorticity are illustrated similar to figure 28.

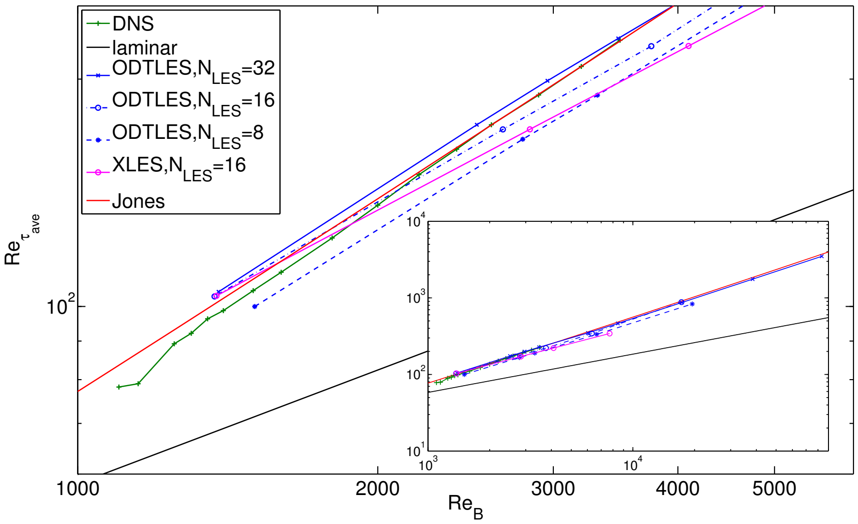

Figure 30: The correlation between $Re_{\tau_{ave}}$ and Re_B in the turbulent regime is empirically described by Jones [43] (red line) and confirmed by *DNS* (e. g. [106]; green line). *ODTLES* with $N_{LES} = 32$ (blue line) and even with $N_{LES} = 16$ (blue dashed-dotted line) corresponds to the empirical prediction up to a highly turbulent regime. *ODTLES* results with $N_{LES} = 8$ (blue dashed line) and *XLES-U* results (magenta line) slightly tends towards the laminar solution (black line). This indicates that the 3D resolution is not sufficient (for $N_{LES} = 8$) and the *ODT* model is required.

duct corner. More reliable and conclusive results might be possible through future *DNS* studies.

Nevertheless the tertiary structure is very local and not preventing the *ODTLES* model from describing the global key flow features of the primary and secondary flow, as figure 30 suggests.

Figure 32 illustrates *ODTLES* streamwise mean velocities and their *RMS*s with $N_{LES} = 32$ at several lateral positions $x_3/h = \{0, 0.25, 0.75\}$. For moderate Re_B the *ODTLES* results are in good agreement with *DNS* results (see [106]). For high Re_B (where no *DNS* is available) a logarithmic behavior is observed for the positions near the duct center ($x_3/h = \{0.0, 0.25\}$) This corresponds to the law of the wall for turbulent channel flows, obtained by Lee and Moser [62] for a turbulent channel with $Re_\tau = 5200$. The velocity *RMS*s behave similar to the *RMS*s of the turbulent channel flow: Within the first 3D cell, as indicated by vertical lines, the velocity *RMS* deviates from the *DNS* results, which is an effect caused by the *ODT-SGM* (cf. figure 26).

Mean spanwise velocities and their *RMS*s are illustrated in figure 33.

The averaged spanwise velocity in the vicinity of the duct corner ($x_3/h = 0.75$) is of higher magnitude and well represented by *ODTLES*. The spanwise velocity *RMS*s are in good agreement with existing *DNS* results, but show the *ODT* specific behavior within the first 3D cell. A low correlation between *ODTLES* and *DNS* is observed in the spanwise velocity in the duct center which

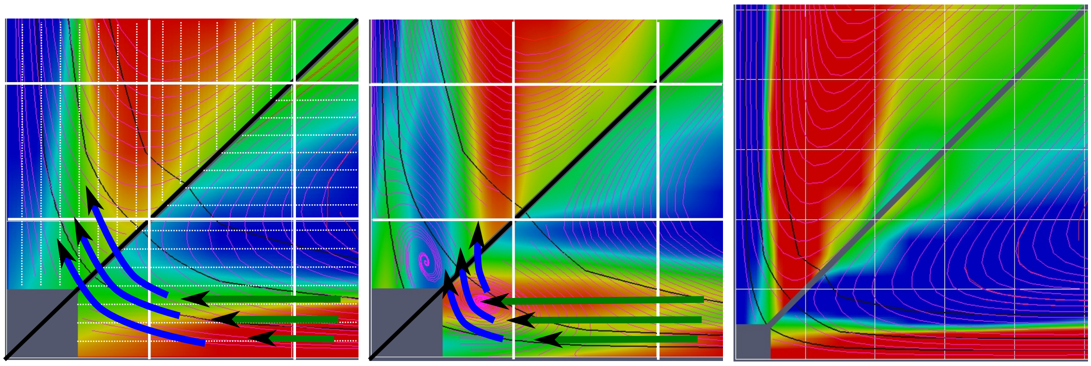

(a) $Re_B = 3485$, $N_{RSS} = 1024$, $N_{LES} = 32$, cf. figure 29b

(b) $Re_B = 17338$, $N_{RSS} = 2048$, $N_{LES} = 32$, cf. figure 29d

(c) $Re_B = 17338$, $N_{RSS} = 2048$, $N_{LES} = 64$.

Figure 31: Zoom into the corner region of the squared duct flow. Primary and secondary streamlines and the vorticity are illustrated similar to figure 28. Figure 31a additionally shows the small scale resolution (illustrative with $N_{RSS} = 256$ instead of simulated $N_{RSS} = 1024$). An exemplary cross-stream flow approaches the corner parallel to the horizontal wall (green arrows) with wall-normal velocity gradients highly resolved only in the *XLES-grid* 2 (cf. figure 28a). Near the corner the vertical wall forces a flow stagnation and an associated pressure gradient drives the flow in the horizontal direction (blue arrows) which is highly resolved only in *XLES-grid* 3. For high Reynolds number duct flows (31b) both effects occur within one 3D cell, which is not well represented by *ODTLES* because the coupling procedure only communicates small scale effects affecting the large scale. This could lead to unphysical flow behavior within the 3D cell containing the corner. With increased 3D resolution the effect disappears (figure 31c).

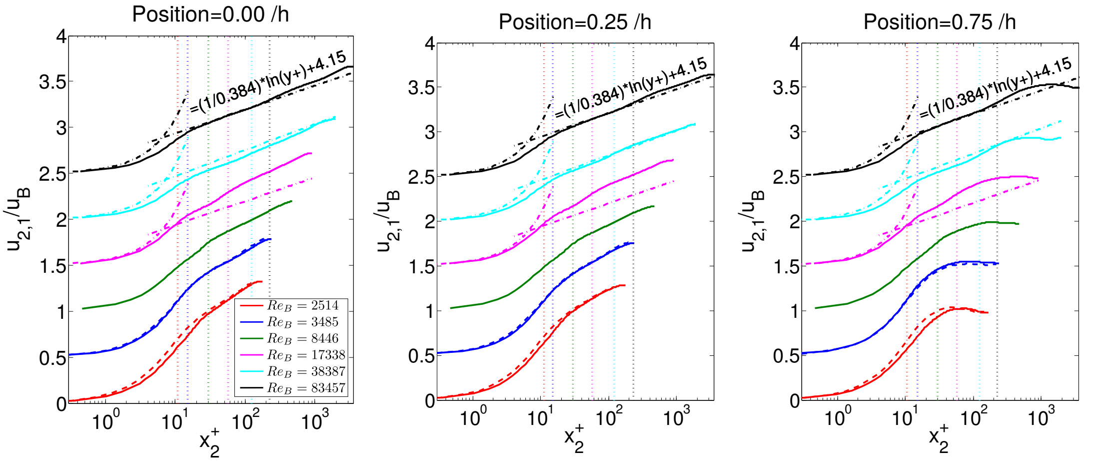

(a) Streamwise velocity at $x_3 = 0$.

(b) Streamwise velocity at $x_3 = 0.25/h$.

(c) Streamwise velocity at $x_3 = 0.75/h$.

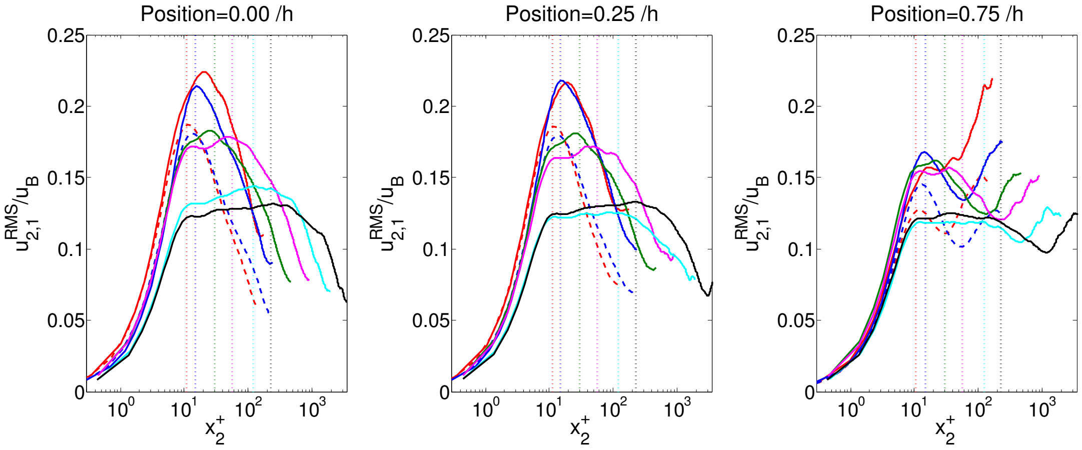

(d) Streamwise velocity *RMS* at $x_3 = 0$.

(e) Streamwise velocity *RMS* at $x_3 = 0.25/h$.

(f) Streamwise velocity *RMS* at $x_3 = 0.75/h$.

Figure 32: The *ODTLES* streamwise mean velocity (corresponding to the law of the wall) and the streamwise velocity *RMS*s are shown at different lateral locations for $2514 < Re_B < 83457$ (see legend in 32a). All *ODTLES* computations use $N_{LES} = 32$ large scale cells. The profiles are not averaged over the 4 quadrants. The dashed lines correspond to available *DNS* data or the logarithmic law obtained for a turbulent channel with $Re_\tau = 5200$ by Lee and Moser [63]. The vertical and dotted lines indicate the size of the first 3D cell.

is of low magnitude (similar to the turbulent channel flow, where the averaged spanwise velocities vanish). Possibly this flow properties depends stronger on the averaging period t_{ave}.

In summary *ODTLES* demonstrates its ability to describe and predict non-trivial flow behavior including secondary instabilities within a squared duct. Qualitative and quantitative properties are in good agreement with *DNS* results and behave reasonably also for bulk Reynolds numbers not reached by *DNS* yet. The correlation of $Re_{\tau_{ave}}$ to Re_B behaves according to an empirical correlation by Jones [43] for *ODTLES* with at least $N_{LES} = 16$ cells per direction.

We suspect that the flow transition leading to tertiary instability is a model artifact, which is supported by results with higher 3D resolution, although a physical cause cannot be ruled out until definitive evidence such as a *DNS* result becomes available. Nevertheless the tertiary structure is very local and not preventing the *ODTLES* model from describing the key flow features of the primary and secondary flow.

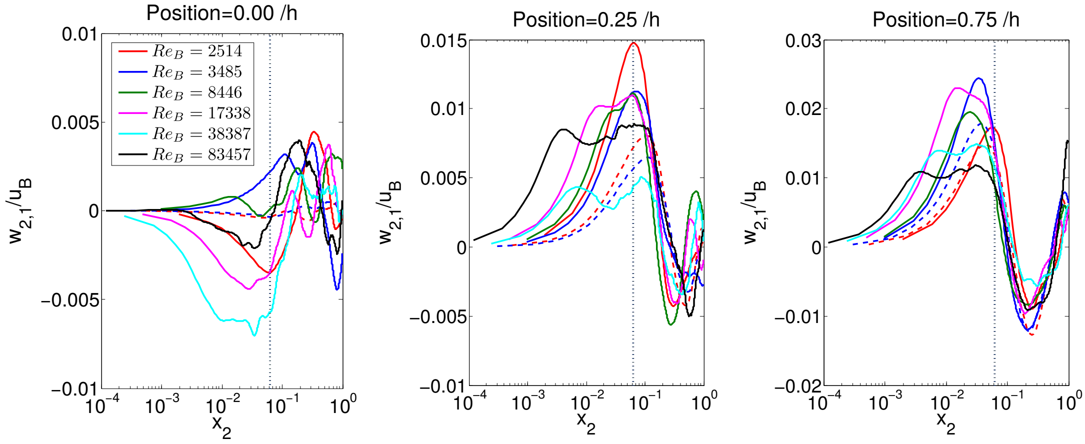

(a) Spanwise velocity at $x_3 = 0$. (b) Spanwise velocity at $x_3 = 0.25/h$. (c) Spanwise velocity at $x_3 = 0.75/h$.

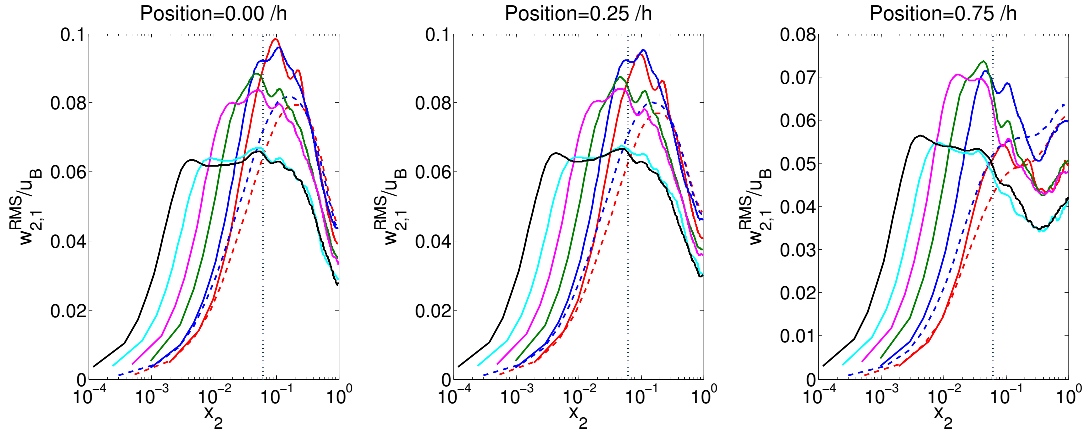

(d) Spanwise velocity *RMS* at $x_3 = 0$. (e) Spanwise velocity *RMS* at $x_3 = 0.25/h$. (f) Spanwise velocity *RMS* at $x_3 = 0.75/h$.

Figure 33: The *ODTLES* spanwise mean velocity (corresponding to the law of the wall) and the spanwise velocity *RMS*s are shown at different lateral locations for $2514 < Re_B < 83457$ (see legend in 33a). All *ODTLES* computations use $N_{LES} = 32$ large scale cells. The profiles are not averaged over the 4 quadrants. The dashed lines corresponds to available *DNS* data. The vertical dotted lines indicate the size of the first 3D cell.

5

BUOYANCY DRIVEN TURBULENT PROBLEMS

Buoyancy driven turbulent flows occur in various engineering and meteorological applications. To investigate convective transport this chapter present *ODT* and *ODTLES* results including determination of model parameters for Rayleigh-Bénard flows, which are one of the most fundamental buoyancy driven flows.

5.1 RAYLEIGH-BÉNARD FLOW

The domain is very similar to the channel domain, but with different aspect ratios (Γ) (see figure 34). The infinite walls are heated from the bottom and cooled down at the top of the Rayleigh-Bénard cell, which leads to an unstable stratification and convective Rayleigh-Bénard motion. The *XLES* Oberbeck-Boussinesq equations (101), (102), and (105) are solved.

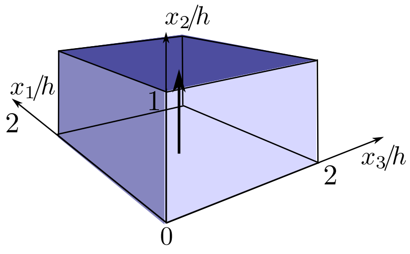

Figure 34: Coordinate system and computational domain for the Rayleigh-Bénard cell investigated here: with $\Gamma = 2$ and periodic boundary conditions in the horizontal directions. The bold arrow illustrates a possible 1D subdomain.

The Rayleigh number ($Ra = \frac{g(\Delta\theta)}{\nu\kappa} L^3$) corresponds to the ratio of typical convective and diffusive effects (cf. section 1.1).

Upon a critical Rayleigh number (Ra_c) convective transport occurs. The overall transport phenomena include a large scale circulation (*LSC*) in the bulk region and transport through thermal and kinematic boundary layer regions near the walls. The *LSC* includes plumes, as obtained in many geophysical flows, e. g. for the Earth's core mantle convection (recently studied e. g. by Mulyukova et al. [76]).

Due to convection the net heat transport, expressed by the Nusselt number ($Nu = \frac{\alpha L}{\kappa}$), is significantly enhanced ($Nu = 1$ corresponds to pure diffusive transport). Thus in particular the behavior of the Nusselt number with respect to Ra and Pr are of interest to prescribe the global properties of a Rayleigh-Bénard cell and the influence of convective transport per se. Section 5.1.4 investigates the Nusselt number correlation with *ODT* and *ODTLES*.

Grossmann and Lohse [35] establish a qualitative understanding of convective phenomena and corresponding boundary layer effects (see also [101] for updated prefactors). Universal scaling properties of pure convection, even considering side walls, are developed. Grossmann and Lohse [35] introduce 4 regimes to describe $Nu(Ra, Pr)$ and $Re_t(Ra, Pr)$ depending on whether the boundary layer or the *LSC* dominates the global thermal respective kinetic energy dissipation. Subregimes additionally describe whether the thermal or the

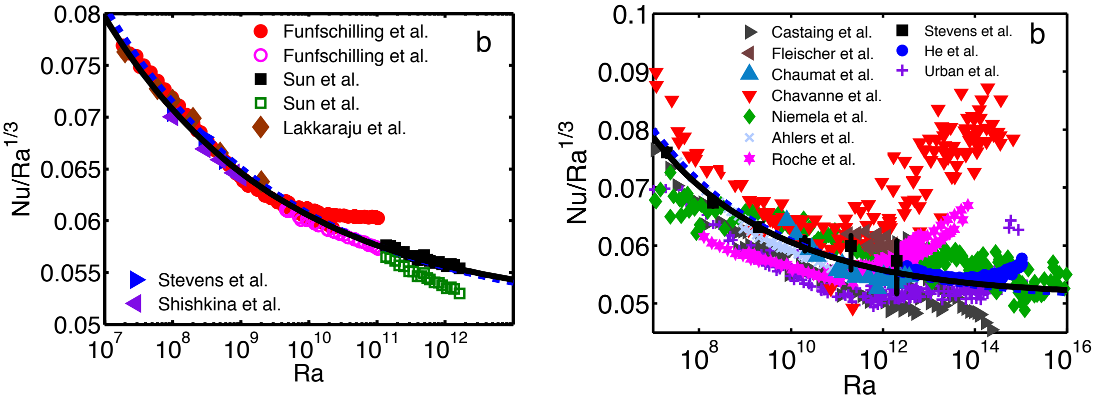

(a) $\Gamma = 1$, in [27, 103, 100, 92] (with $\mathrm{Pr} = 4.38$) and [59] (with $\mathrm{Pr} = 5.4$).

(b) $\Gamma = 0.5$, different Pr, in [11, 26, 14, 15, 77, 5, 84, 99, 102, 38, 108].

Figure 35: Nusselt number scaling for various Pr ($0.7 \lesssim \mathrm{Pr} \lesssim 10^2$) and aspect ratios $\Gamma = \{0.5, 1\}$. The solid (black) lines indicates the theory by Grossmann and Lohse [35] and the dashed blue lines include the corrected factors by Stevens et al. [101]. In 35a open symbols indicate the uncorrected data and solid symbols the data after correction for the finite plate conductivity. The figures were published by Stevens et al. [101]
[Reproduced with permission from R.J.A.M. Stevens and D. Lohse: The unifying theory of scaling in thermal convection: the updated prefactors, Journal of Fluid Mechanics 730:295–308, 2013. ©2013 Cambridge University Press].

viscous boundary layer is thicker. For Pr$=1$, as investigated in this thesis, two regimes occur:

1. For $\mathrm{Ra} \lesssim 1.66 \times 10^{10}$ the thermal and kinetic dissipation rates (ϵ_θ and ϵ_ν) are boundary layer dominated.

2. For $\mathrm{Ra} \gtrsim 1.66 \times 10^{10}$ the thermal and kinetic dissipation rates are bulk dominated (by the *LSC*.)

In figure 35 these scaling laws are compared to various experiments and *DNS* for $\Gamma = \frac{1}{2}$ and $\Gamma = 1$ and for various Prandtl numbers.

Kraichnan [58] predicts another regime transition, towards the often called 'ultimate regime', at very high $\mathrm{Ra} \gtrsim \mathrm{Ra}_u$ (with the critical Rayleigh number (Ra_u)). Upon Ra_u the laminar shear boundary layer is speculated to break down through nonlinear transition to turbulence and a scaling $\mathrm{Nu} \sim \mathrm{Ra}^{1/2}$ is expected. The transition towards this 'ultimate regime' at Ra_u depends on Pr and the aspect ratio (Γ). Chillà and Schumacher [16] e. g. state that roughly $\mathrm{Ra}_u \sim \Gamma^{-2.5}$ holds. As figure 35b suggests experiments found a sudden change in the Nusselt number behavior for $\Gamma = \frac{1}{2}$, but these experiments are extremely challenging and controversially discussed (cf. [36]). Highly resolved numerical simulations are not reaching this second Ra_u yet.

In experiments and most *DNS* circular and rectangular geometries with sidewalls are used. The application of *ODT* is more meaningful for the more idealized Rayleigh-Bénard flow without side walls (periodic boundary conditions),

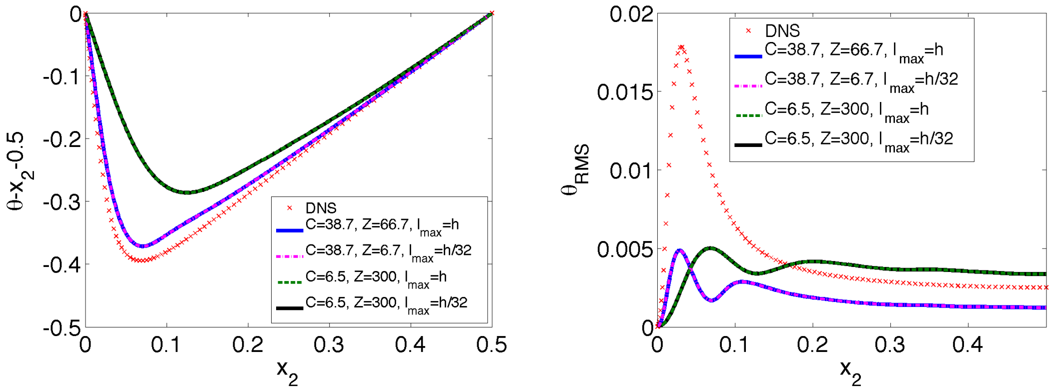

(a) ODT: scalar field (θ)

(b) ODT: *RMS* of θ

Figure 36: Rayleigh-Bénard flow computed by *ODT* for Ra= 5×10^6, Pr= 1, $N_{ODT} = 1024$, and $t_{ave} = t\sqrt{g * (\Delta\theta) * \Gamma}/h \geqslant 5400$: 36a shows the mean scalar field (shifted), 36b its *RMS*. θ fairly agrees using an increased eddy rate ($C = 38.7$, $Z = 66.7$). The *RMS* does not reproduce the *DNS* in the near-wall region for any parameter set. The l_{max} parameter does not influence the computed results.

because due to the symmetry a 1D sub-domain (see arrow in figure 34) is more reasonable.

DNS results with periodic boundary conditions are provided by Petschel et al. [79, 80] and compared to *ODT* in section 5.1.1 and *ODTLES* in sections 5.1.2 and 5.1.3.

5.1.1 *ODT: Parameter Study*

Wunsch and Kerstein [113] presents Rayleigh-Bénard studies and *ODT* Nusselt number scaling for varying Pr and Ra numbers. Especially *PDF*s of small scale fluctuations and global Nu scalings agree well with available experiments. In their study Wunsch and Kerstein [113] determine *ODT* parameters C and Z for Rayleigh-Bénard flows, which differ from those in shear-driven flows. They present 3 possible parameter sets, that maintain scaling properties within *ODT*. We will use the parameters $C = 38.7$ and $Z = 66.7$, which lead to a good agreement of the mean scalar field (θ) with existing *DNS* results. Additionally the productive parameters $C = 6.5$ and $Z = 300$ for the turbulent channel flow are applied to the Rayleigh-Bénard case. The occurring discrepancy between computed *ODT* results helps to understand the underlying physical mechanisms. According to their role in Eq. (51), the parameters $C = 38.7$ and $Z = 66.7$ increase the eddy rate distribution and therefore the *ODT* turbulent transport compared to the channel parameters $C = 6.5$ and $Z = 300$.

As illustrated in figure 36a the parameters $C = 38.7$ and $Z = 66.7$ better agree with the *DNS* by Petschel et al. [79, 80] for $Ra = 5 \times 10^6$ and $Pr = 1$.

Nevertheless *ODT* higher order statistics differ significantly from the *DNS*, as shown in figure 36b.

Figure 36 also demonstrates, that the parameter l_{max} does not influence the *ODT* results, but experiments and 3D simulations conclude that a significant amount of heat transport is due to *LSC*. This implies that the *ODT* model compensates the inability to describe 3D large scale convective transport by an increased amount of small scale transport, which explains the better θ-agreement with $C = 38.7$ and $Z = 66.7$. This indicates that the *ODT* results with these parameters can be associated with the bulk-dominated regime (cf. section 5.1.4), but to some extent the good agreement in the θ-profile in figure 36a does not mean that *ODT* represents the right physical mechanisms.

5.1.2 *ODTLES: Parameter Study*

All presented cases use aspect ratio $\Gamma = 2$ and periodic boundary conditions in the horizontal directions. In each direction $N_{\text{LES}} = 32$ (if not mentioned otherwise) equidistant 3D cells are used. Due to the aspect ratio this leads to a 2 times higher 3D resolution in the wall-normal direction.

ODTLES is able to describe the *LSC* and thus the *ODT* compensation for *LSC* due to small scale transport is not necessary, as the parameter study in figure 37 demonstrates. *ODTLES* yields reasonable results, even with $C = 6.5$ and $Z = 300$, the parameters used for shear-driven flow, as investigated in figure 37.

From a conceptual point of view applying these *ODTLES* parameters also to buoyancy driven flows maintains a universality of the parameters, but the outcome has to be reasonable. Even if slightly varying the parameters might enhance the computed results, we prefer to use the same parameters as in shear driven flows (cf. figure 37), because they lead to a satisfactory outcome.

Additionally the similarity of scalar results by *XLES-U* and *ODTLES* implies that the essential scales for the chosen Rayleigh number are sufficiently described even without the *ODT-SGM*. Nevertheless the velocity statistics differs noticeably and *ODT* small scale advection becomes more relevant for more highly turbulent cases (presented in section 5.1.3).

The *CFL*-number only has a small influence to the flow results, as shown in figure 37, which implies that the temporal error terms $\underline{\sigma}^{\text{temporal}}_{\text{ODTLES}_{ij}}$ and $\underline{\sigma}^{\text{temporal}}_{\text{ODTLES}_{\theta j}}$ are rather small in the investigated flow configuration. This allows to increase of *CFL*-number in computations for performance reasons with acceptable model errors.

The influence of the 3D resolution N_{LES} is investigated in figure 38. Hereby we find, that very coarse 3D resolutions with fully coupled scalar fields ($\underline{\theta}$) lead to an artifact: An additional unphysical inflection point in the θ mean profile occurs whose spatial extent is related to the 3D large scale cell size (Δx^{LES}) and vanishes with a certain Ra-dependent 3D resolution. For $Ra = 5 \times 10^6$ and

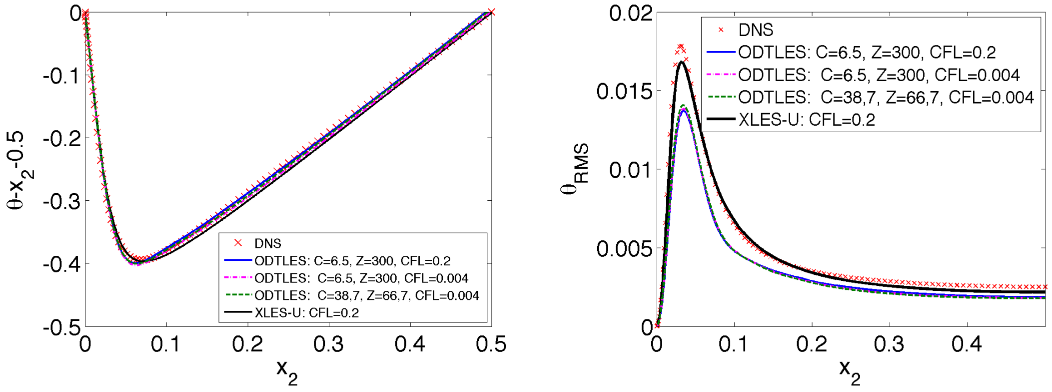

(a) *ODTLES*: θ.

(b) *ODTLES*: *RMS* of θ.

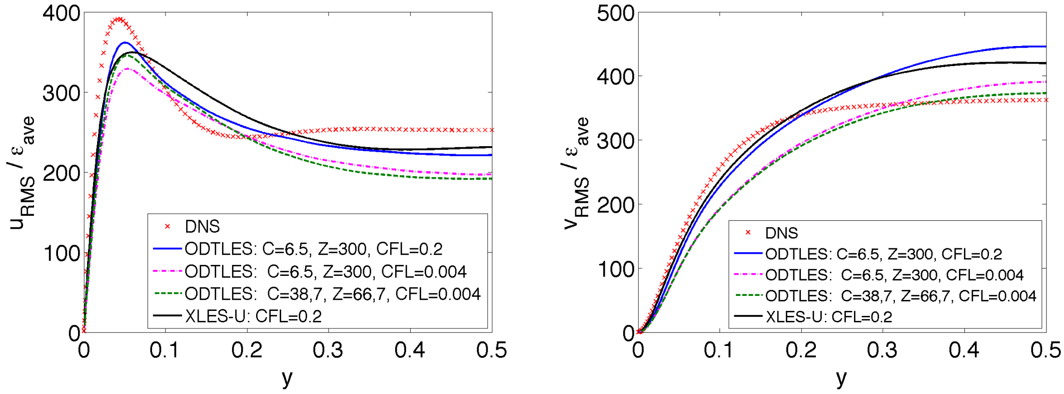

(c) *ODTLES*: horizontal velocity *RMS*.

(d) *ODTLES*: vertical velocity *RMS*.

Figure 37: *ODTLES* Rayleigh-Bénard flow with $Ra = 5 \times 10^6$, $Pr = 1$, $N_{LES} = 32$, $N_{RSS} = 1024$, and $t_{ave} = t\sqrt{g * (\Delta\theta) * \Gamma / h} \geqslant 135$. Compared to the *ODT* results (cf. figure 36) *ODTLES* only weakly depends on the *ODT* parameters C and Z. Good agreement of *XLES* and *DNS* results indicate relative weak influence of *ODT* turbulent events. A weak influence of the *CFL*-number indicates that $\underline{\sigma}^{\text{temporal}}_{\text{ODTLES}_{ij}}$ and $\underline{\sigma}^{\text{temporal}}_{\text{ODTLES}_{\theta j}}$ are small.

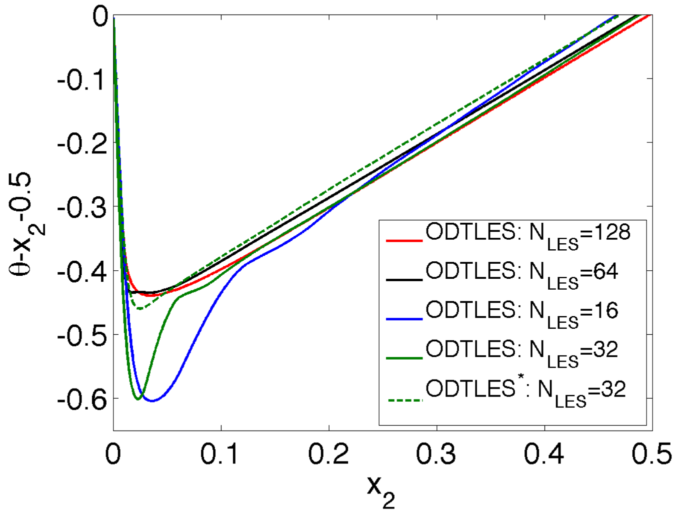

Figure 38: *ODTLES*: Mean scalar field (θ) for $\mathrm{Ra}= 5 \times 10^8$. *ODTLES* results converge for increasing 3D resolution , but require a Ra-dependent threshold 3D resolution ($N_{\mathrm{LES}} \approx 64$ for $\mathrm{Ra}= 5 \times 10^8$) to prevent unphysical inflection points from occurring in the mean θ-profile. The unphysical behavior is related to *XLES* scalar coupling terms. Neglect of these terms (called ODTLES* here) improves the results.

$N_{\mathrm{LES}} = 32$ no artifacts are found but by increasing the Rayleigh number to $\mathrm{Ra} = 5 \times 10^8$ a higher 3D resolution is required to prevent additional inflection points. We find this slow convergence to physical behavior to be related to the *XLES* scalar coupling terms

$$\underline{\mathcal{X}}_{\theta j} \approx \underline{\underline{l}}^{\dagger} * \partial_{x_j} \underline{\underline{C}} \left(\left\langle \underline{\hat{u}}_j \right\rangle * \underline{\hat{\theta}} - \left\langle \underline{\overline{u}}_j \right\rangle^{\mathrm{LES}} * \underline{\overline{\theta}}^{\mathrm{LES}} \right) \tag{145}$$

(see (p 3) in table 5), because neglecting the term in Eq. (145) prevent the reported unphysical behavior. We will call the *ODTLES* model with neglected *XLES* scalar coupling terms ODTLES* in this section. Note that the scalar *ODT* advancement including molecular diffusion terms are still coupled between different *XLES-grid*s. For ODTLES* the 'LES-limit' still holds and for high N_{LES} a convergence towards *DNS* can be observed.

To investigate specific *XLES* scalar coupling terms in detail a turbulent scalar flux in *XLES-grid* 2 for different 3D resolutions is shown in figure 39. This flux corresponds to an averaged coupling term within the *XLES* scalar coupling term ($\underline{\mathcal{X}}_{\theta j}^{\mathrm{XLES}}$). The shown flux properties induce a strong N_{LES} and Ra dependency of $\underline{\sigma}_{\dagger}^{\mathrm{spatial}}$ due to the reconstruction of the scalar. This means high Rayleigh number results by *ODTLES* require a considerably higher 3D resolution, but ODTLES* results still agree well with existing *DNS* and are performed for high Ra (see section 5.1.3).

This behavior for highly under-resolved scalar flows is rather a limitation of the reconstruction algorithm for challenging near-wall profiles (the flux in fig-

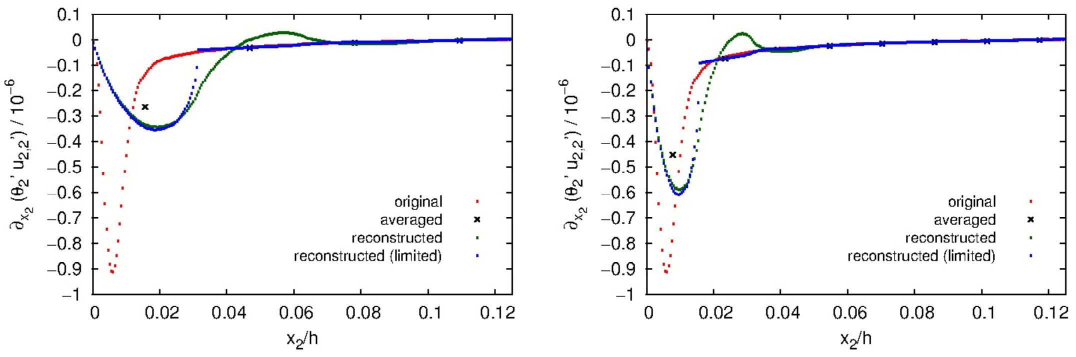

(a) $N_{LES} = 16$

(b) $N_{LES} = 32$

Figure 39: The ability of the reconstruction algorithm is limited as shown for one scalar coupling flux term for very coarse 3D resolution with $N_{LES} = 16$ (39a) and $N_{LES} = 32$ (39b). This scalar coupling flux is an statistical average of the *XLES* scalar coupling terms in Eq. (145) (with $i = 2$ and *XLES-grid* 2). The 'original' flux $\partial_{x_2}(\hat{\theta}_2' \hat{u}_{2,2}')$ (red dots) is computed using $N_{LES} = 128$ cells ($t_{ave} = t\sqrt{g * (\Delta\theta) * \Gamma}/h \approx 15$). The spatial averaged flux (black crosses) is computed by $[l_2^d]\partial_{x_2}(\hat{\theta}_2' \hat{u}_{2,2}')$ using the corresponding 3D resolution and the reconstructed flux (green dots) corresponds to $[l_2^{-1^d} l_2^d]\partial_{x_2}(\hat{\theta}_2' \hat{u}_{2,2}')$. Here $[l_2^{-1^d}]$ is computed by Schmidt's algorithm. An additional limiter (blue dots) prevent an artificial overshoot, but locally reduces the approximation order. The limiter does not influence the occurrence of unphysical inflection points (cf. figure 38).

ure 38) than a fundamental problem within the coupling terms per se. The approximation and especially reconstruction of these challenging near-wall profiles requires an increased 3D resolution in *ODTLES*. One possible interpretation is that the deconvolution algorithm error term ($\underline{\sigma}_{\dagger}^{\text{spatial}}$) locally exceeds the magnitude of the *XLES* scalar coupling term itself for very coarse 3D resolutions.

Here further investigations of the interplay of *XLES* coupling terms and reconstruction algorithms are advisable to decrease the Ra-dependency of the *ODTLES* 3D resolution due to challenging coupling flux profiles. Note that for this coupling flux, the limiter applied to the reconstruction algorithm (cf. . section 3.6.1) locally leads to a linear reconstructed profile, which is not the case in investigated reconstructed profiles in shear-driven flows.

No evidence was found that similar artifacts caused by the reconstruction algorithm for very coarse 3D resolutions occur for the shear-driven flows investigated in chapter 4.

5.1.3 *ODTLES: Rayleigh-Bénard Flow*

The *ODT* model parameters for *ODTLES* Rayleigh-Bénard flows are $C = 6.5$, $Z = 300$, and $l_{\max_k} = \Delta x_k^{\text{LES}}$, which is identical to the channel and square duct flow setup in chapter 4. The *CFL*-number is chosen following Eq. (93) with $\text{CFL}_{\text{LES}} \leqslant 0.2$.

The flow is averaged for $t_{ave} = t\sqrt{g * (\Delta\theta) * \Gamma / h} \geqslant 135$ non-dimensional time units after reaching a steady state compared to e. g. $t_{ave} = 110$ in the *DNS* by Kaczorowski and Wagner [47].

We compare *ODTLES* results for Ra$= 5 \times 10^6$ and Pr$= 1$ with *DNS* by Petschel et al. [79, 80]. This *DNS* is appropriate for comparison, because periodic boundary conditions are used for the horizontal flow. Contrary to the *DNS* which mainly investigate the influence of Prandtl numbers on the boundary layers, here the influence of the Rayleigh number on the overall flow is investigated. In particular the Nusselt number behavior is investigated in section 5.1.4.

About the required resolution to represent all boundary layer effects, Shishkina et al. [91] states for $\text{Pr} = 1$: "one is on the safe side if"

$$\Delta x_{\text{DNS}} \lesssim 2^{-3/2} a^{-1} \text{Nu}^{-3/2} h \tag{146}$$

with the $a \approx 0.482$ (measured for a cylindrical cell with $\Gamma = 1$). We estimate the Nusselt number a priori (see Eq. (147).

Figure 40 illustrates the influence of the Rayleigh numbers (Ra$\leqslant 5 \times 10^{10}$) to the scalar and velocity fields. The computational domain (Ω) is illustrated in figure 34 with $\Gamma = 2$. Following arguments in section 5.1.2, for high Rayleigh numbers the scalar *XLES-U* coupling terms in Eq. (145) are omitted, leading to a slightly modified ODTLES* model. Computations are conducted using

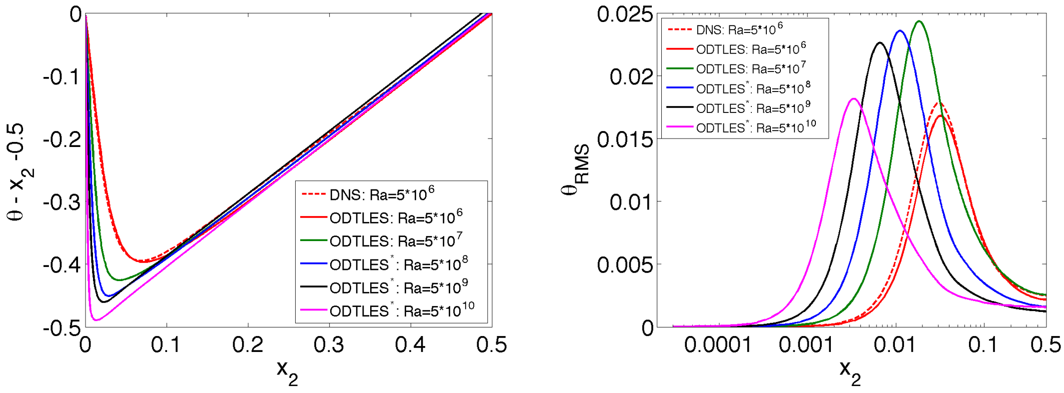

(a) *ODTLES*: θ.

(b) *ODTLES*: *RMS* of θ.

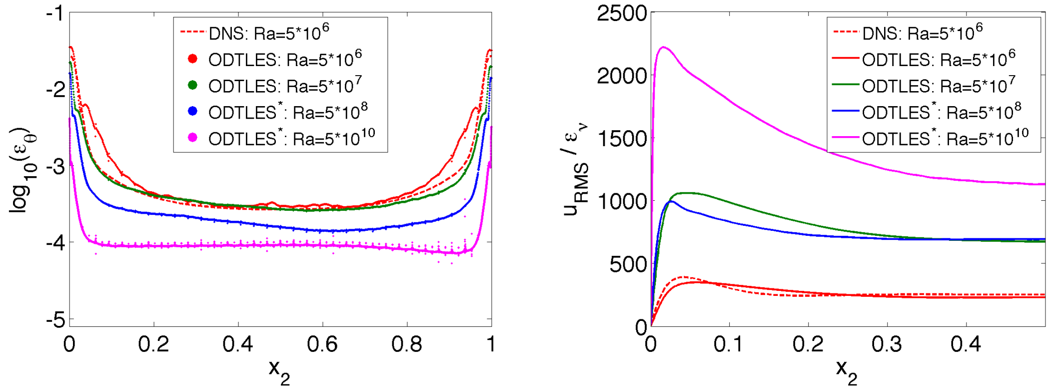

(c) *ODTLES*: Scalar Dissipation.

(d) *ODTLES*: horizontal velocity *RMS*.

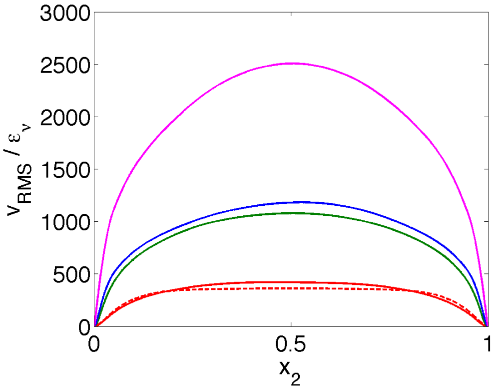

(e) *ODTLES*: vertical velocity *RMS*.

Figure 40: ODTLES and ODTLES* high-Ra flow in a Rayleigh-Bénard cell with N_{LES}= 32 cells for all cases. Following arguments in section 5.1.2, *XLES-U* coupling terms are neglected for high Ra (leading to the ODTLES* model). Following Petschel et al. [80], velocity *RMS*s are normalized by the volume-averaged viscous dissipation rate.

Table 10: The required resolution to fully resolve the boundary layer (Δx_{DNS}) is estimated for Pr= 1 in [91] and compared to the *RSS* resolution in *ODTLES* in wall-normal (Δx_2^{RSS}) and horizontal direction ($\Delta x_1^{RSS} = \Delta x_3^{RSS}$ for Γ= 2).

Ra	N_{RSS}	Δx_{DNS}	Δx_2^{RSS}	Δx_1^{RSS}
5×10^6	1024	8.674×10^{-3}	9.77×10^{-4}	1.195×10^{-3}
5×10^7	2048	3.299×10^{-3}	4.88×10^{-4}	9.77×10^{-4}
5×10^8	4096	1.238×10^{-3}	2.44×10^{-4}	4.88×10^{-4}
5×10^9	8192	4.59×10^{-4}	1.22×10^{-4}	2.44×10^{-4}
5×10^{10}	16384	1.68×10^{-4}	6.10×10^{-5}	1.22×10^{-4}
5×10^{11}	32768	6.0×10^{-5}	3.05×10^{-5}	6.10×10^{-5}

N_{LES}= 32 cells per direction to represent the 3D *LSC*. The *RSS* resolutions are summarized in table 10. Figures 40a–40c show *ODTLES* scalar field statistics to be in good agreement with the *DNS* (cf. [79, 80]) for Ra= 5×10^6 and Pr= 1. Figures 40d and 40e also show the horizontal and vertical velocity *RMS* to be in good agreement with available *DNS* data.

ODTLES results for higher Rayleigh numbers behave reasonably in their scalar and kinematic statistics. Note that higher Rayleigh number *DNS* results for periodic boundary conditions are currently not available for comparison. Nevertheless the *ODTLES* and ODTLES* results show similar behavior for increasing Rayleigh number as *DNS* results with side walls.

5.1.4 *ODT and ODTLES: Nusselt Number Scaling*

Typical experiments and numerical results for the Nusselt number scaling obtain $Nu = C_{Nu}\, Ra^{\gamma_{eff}}$ with a Nusselt scaling prefactor (C_{Nu}) and the effective Nusselt scaling exponent (γ_{eff}).

For the Rayleigh-Bénard convection with $Pr = 1$, Grossmann and Lohse [35] suggest a Nusselt number scaling over a wide range of Ra including several regimes (cf. previously in section 5.1) with

$$Nu = 0.27 \cdot Ra^{1/4} + 0.038 \cdot Ra^{1/3} \tag{147}$$

which is in agreement with experimental results for $Pr \approx 1$ (prefactors are derived using experimental data). This scaling law is almost indistinguishable from the scaling $Nu = 0.22 \cdot Ra^{0.289}$ for $10^6 < Ra < 10^{14}$ (cf. figure 41). Following Ahlers et al. [4] the influence of Γ (investigated for $\Gamma = \frac{1}{2}$ and Γ= 1) to γ_{eff} is small, but C_{Nu} varies noticeable (also compare figures 35b with 35a). Note that $Ra_u \sim \Gamma^{-2.5}$ which influences the transition towards the 'ultimate regime'

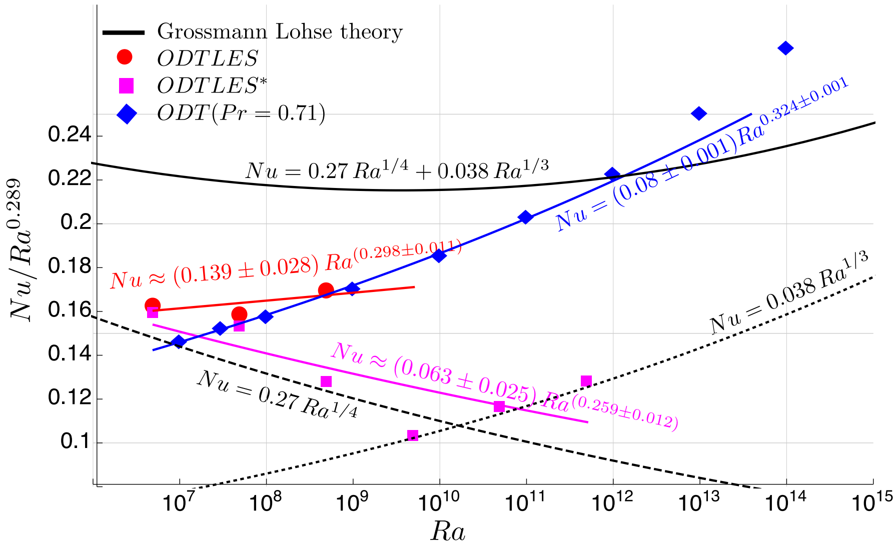

Figure 41: The *ODTLES* and ODTLES* Nusselt number behavior is compared to the theory by Grossmann and Lohse [35] for Pr= 1 (black solid line). Following this theory there are two regimes additively affecting the Nusselt number behavior: the boundary layer dominated (black dashed line) and the bulk dominated (black dotted line) regime. Additionally *ODT* results for Pr= 0.71 with $C = 38.7$ and $Z = 66.7$ are presented. The 3D resolution in ODTLES* and *ODTLES* ($\mathrm{Ra} \leqslant 5 \times 10^7$) is $N_{\mathrm{LES}} = 32$ and $N_{\mathrm{LES}} = 64$ for *ODTLES* with $\mathrm{Ra} = 5 \times 10^8$. *ODTLES* results show a scaling behavior comparable to theory for the computed Ra. ODTLES* results seem to include the regime transition, but the additive character is missing.

with $\mathrm{Nu} \sim \mathrm{Ra}^{1/2}$ introduces a strong correlation between the Nusselt number and the aspect ratio.

Figure 41 shows the Nu scaling by Grossmann and Lohse [35] with *ODTLES* and *ODT* results.

ODT results use the parameters $C = 38.7$, $Z = 66.7$, and $l_{\mathrm{max}} = h$ and up to $N_{\mathrm{ODT}} = 262144$ cells for a slightly decreased Prandtl number $\mathrm{Pr} = 0.71$. As discussed in section 5.1.1 the chosen parameters describe a bulk dominated regime (corresponding to $\gamma_{\mathrm{eff}} = 1/3$), but *ODT* eddy events replace the *LSC*. *ODTLES* results are computed for $\mathrm{Ra} \leqslant 5 \times 10^8$ using $N_{\mathrm{LES}} = 32$ cells for $\mathrm{Ra} < 5 \times 10^8$ and $N_{\mathrm{LES}} = 64$ cells for $\mathrm{Ra} = 5 \times 10^8$, as shown in figure 41. For *ODTLES* simulations with higher Rayleigh numbers a higher 3D resolution (cf. section 5.1.2) is required due to the necessary reconstruction of challenging coupling flux terms near the walls. To avoid this Ra-dependency of the 3D resolution a possible approach is to neglect the *XLES* scalar coupling terms. This is done by the ODTLES* model which is even able to describe the transition between the boundary layer dominated and the bulk dominated regime, but their additive character is missing. Possibly this effect can be explained by the neglected *XLES-U* scalar coupling or temporal error terms $\underline{\sigma}^{\mathrm{temporal}}_{\mathrm{XLES-U_{ij}}}$ and $\underline{\sigma}^{\mathrm{temporal}}_{\mathrm{XLES-U_{\theta j}}}$ caused by the increased *CFL*-number. Of course the application of the ODTLES* model is rather a quick fix than a well-founded modeling strategy and further investigations especially of these challenging coupling fluxes and alternative reconstruction strategies are required. Maybe deconvolution strategies developed in the field of image processing can lead to further improvements of the *XLES* and especially *ODTLES* models. Nevertheless we can learn something about the *ODTLES* model behavior and the underlying physics even from the ODTLES* model results. The Nusselt number behavior in both the boundary layer and the bulk dominated regimes are well represented by the ODTLES* model. Especially the regime transition seems to further depend on the neglected coupling flux terms. A possible interpretation is that this regime transition especially requires transfer between the *RSS* represented near wall boundary layer behavior and 3D resolved bulk flow properties. This transfer is partly represented by the *XLES* scalar coupling terms neglected in ODTLES*.

ODTLES shows its fundamental ability to reproduce scaling law properties for buoyancy driven flows including regime transitions between boundary layer dominated and bulk dominated flows. Compared to the turbulent channel flow in section 4.1 where an increasing 3D resolution can be used to smoothly adjust the outcome from the *ODT* stand alone result (for one 3D cell) towards the *DNS* result for very high 3D resolutions, in the Rayleigh-Bénard flow a certain 3D resolution is required to approximate certain *XLES* scalar coupling fluxes. Considering the *ODT* stand alone result for Rayleigh-Bénard flow, which requires an adjustment of the *ODT* parameters C and Z, this is not surprising. Neglecting certain *XLES* scalar coupling terms within the ODTLES* model helps to avoid the introduction of additional inflection points within θ-profile. This indicates that the *XLES* scalar coupling plays a major role by creating these behaviors. Further investigations of the *XLES* scalar coupling and especially the reconstruction of challenging near-wall flux profiles is required to use the *ODTLES* model in high Rayleigh number flows.

The transition towards the 'ultimate regime' is assumed to be caused by enhanced turbulence due to increasing *LSC* kinetic energy. The *ODTLES* representation of such an effect strongly depends on the chosen values for the parameters C and Z. Thus *ODTLES* is less appropriate to investigate the transition in detail. Nevertheless an investigation of the properties of the 'ultimate regime' itself seems to be a worthwhile topic for future *ODTLES* or *aODTLES* studies.

Part III

CONCLUSION AND OUTLOOK

6

CONCLUSION

In this work an extended *LES* (*XLES*) approach is introduced. This approach is intended as a basis for a new class of turbulence models, tailored to describe a (*XLES* specific) macrostructure of highly turbulent flows including highly resolved 1D or 2D effects (e. g. molecular diffusion or cloud convection) in domains of moderate complexity.

The *ODTLES* model is one special approach in the *XLES* family of models, where the one-dimensional turbulence (*ODT*) model closes the *XLES* equations (as a sub-grid model). Contrary to *LES* and *RaNS*, the *ODT* model exploits domain specific symmetry properties and is not based on eddy viscosity or self similarity assumptions of turbulence scales. *ODT* describes all turbulent scales, including small scale effects like molecular diffusion, but *ODT* stand alone requires a certain global domain symmetry. Thus the *XLES* filter approach can be interpreted to rather separate physical effects than physical 3D scales (like *LES*), but notwithstanding unclosed *XLES* (*XLES-U*) and *ODTLES* collapse to *DNS* and unclosed *LES* within distinguished limits.

The *ODTLES* model can be interpreted as a compromise between *LES* and *ODT*, which only requires local symmetry properties. This is valid for flows in rather simple domains. In particular the *XLES* 3D resolution can be chosen independent of the turbulence intensity, unless turbulent Reynolds number changes cause a global flow structure transition, e.g. due to secondary instabilities (see section 4.2.1). In principle this allows the computation of highly turbulent flows, e. g. over a flat-plate airfoil, including the full range of physical scales, but with computational costs comparable to wall-modeled *LES*, or even *RaNS*.

Especially in fundamental research including atmospheric flows and combustion, crucial small scale effects in domains of moderate complexity frequently occur. These additional physical effects, described by chemical mechanisms and additional scalar fields, are well tested for *ODT* and can be adapted to *ODTLES*. Scalar coupling terms between different *XLES-grid*s can be formulated using the *XLES* coupling introduced in this thesis and the *XLES* framework is the first approach which consistently couples scalar properties as well as velocities between *XLES-grid*s (in previous *ODTLES* version only velocities were coupled). Especially the *XLES* scalar coupling terms and the incorporated reconstruction require further investigation to allow very low 3D resolutions. Alternatively the application of the less rigorous ODTLES* model, which neglects *XLES* scalar coupling terms, can be used. An alternative scalar coupling is provided by the LEM3D model (cf. [74]).

Especially to demonstrate the *ODTLES* ability to describe statistical properties occurring in geophysical flows *ODTLES* is applied to the Rayleigh-Bénard flow, which uses the coupling of scalar properties represented by different *XLES-grid*s.

The unclosed *XLES* equations and its numerical representation are verified:

- By analyzing the coupled (linear) advection scheme occurring in *XLES*.
- By performing a convergence study: The turbulent channel flow with $Re_\tau = 395$ is compared to *DNS* and *LES-U*. Thereby *XLES-U* requires relatively low 3D resolutions (compared to *LES-U*) to reproduce fundamental flow statistics, especially in the near wall region. E.g. the laminar sublayer is fully represented independently of the 3D resolution.

ODTLES results are demonstrated to be in good agreement with *DNS* and possess predictive capabilities:

- By performing a convergence study: The turbulent channel flow with $Re_\tau = 395$ is compared to *DNS* and *XLES-U*. Even for very low 3D resolutions *ODTLES* represents the channel flow very well.
- *ODTLES* accurately describes a turbulent channel flow up to friction Reynolds number $Re_\tau \leqslant 10000$ with high accuracy and relatively low computational costs, even using very coarse 3D resolutions (e.g. $N_{LES} = 16$ cells per direction).
- *ODTLES* is able to reproduce the primary and secondary flow in a square duct with coarse 3D resolution and considerable high bulk Reynolds numbers $Re_B \leqslant 83457$.
- *ODTLES* (and $ODTLES^*$) incorporate buoyancy effects and model Rayleigh-Benárd flows realistically including large scale circulations for considerably high Rayleigh numbers $Ra \leqslant 5 \times 10^{11}$.

These cases are important examples for fundamental, highly turbulent flows in rather simple domains that are of interest in fundamental turbulence research, meteorology, and other associated fields of application. Thus *ODTLES* and other future *XLES* models are promising and highly parallelizable approaches for fundamental and applied turbulent flows.

7

OUTLOOK

The focus of this work is to introduce the mathematical framework necessary to derive the *XLES* approach, which is a consistent way to incorporate *ODT* into 3D simulations. The present *ODTLES* implementation uses a simple, equidistant *ODT* model resulting in a relative high number of grid cells (*#DoFs*) compared to adaptive *ODT*.

There are several ways to improve the present *ODTLES* formulation.

Any improvement leading to a gain in efficiency and reduced *#DoFs* can be used either to increase the reachable turbulence intensity (increasing N_{RSS}) or to increase the treatable complexity of the computational domain (increasing N_{LES}).

Suggestions by the author include:

1. Improve *ODT*:
   a) *aODT* by Lignell et al. [67] outperforms the turbulence intensity reachable by equidistant *ODT*, as Meiselbach [71] recently showed in *aODT* simulations up to $Re_\tau \leqslant 6 \times 10^5$, but *aODT* introduces additional interpolation effects.
   b) The ensemble mean closure (EMC) model further decrease the required *#DoFs* by introducing another layer of modeling.
2. Improve *XLES-U*:
   a) Non-equidistant *XLES-grid*s would distribute the necessary 3D resolution more efficiently.
   b) The *XLES* formulation in function spaces can be used to derive a *XLES* formulation e. g. for unstructured grids (see appendix A.3). This would require research especially to close the filtered equations, since the current *ODT* model formulations might not be applicable.
   c) Numerical improvements are possible and suggested within the corresponding sections. E. g. *IMEX* schemes might decrease numerical inaccuracies. Several alternative advection schemes potentially outperform the numerical properties of the implemented *CN-RK3-CDM* and *CN-RK3-RK3-CDM* schemes (see section 3.6.4).
3. Improve algorithm:
   a) The parallelization can be significantly improved. Especially due to the high computational time spend within the *ODT* advancement and the Poisson problem solved on the 3D large scale, a potential

high parallelization is possible, which even gets more efficient for increasing turbulence intensities (cf. section 3.5.8).

b) From an algorithmic point of view a well-structured (object-oriented) *CFD*-codes can be expanded to *XLES-U* with moderate coding effort by reusing existing mesh-structures to define *XLES-grid*s. This could also include 3 velocity components within each *XLES-grid*.

It is the authors opinion that especially combining available state-of-the-art *CFD*-codes (point (3.b)) with the *aODT* model (point (1.a)) can automatically include points (2.a), (2.c), and (3.a) with manageable effort and potentially leads to a powerful tool in fundamental turbulent research and supplement the scope of *RaNS* and *LES* applications by problems with essential small-scale features.

Another long term goal could be to develop an unstructured *XLES* model (point (2.b)) which could supplement *RaNS* simulations in engineering applications.

Recently Jozefik et al. [45] present a compressible *aODT* model and its application to combustion problems. This *aODT* model in principle allows to close a compressible *XLES* framework to be developed. Especially the *XLES* formulation within function spaces can be extended to use a *DGM* numerical scheme, which is appropriate to solve compressible *XLES* filtered equations. In this context the autonomous microstructure evolution (*AME*) model introduced by Kerstein [52] has to be mentioned. *AME* solves pseudo-compressible equations using a *XLES*-related framework.

The *XLES* filter concept can help to reduce issues within current superparameterization approaches, e. g. the *CRCP* approach. Therefore *XLES-CRCP* involves two (or three) coupled 1D filtered grids. Thus future investigations of superparameterizations in *XLES*-like formulations might improve meteorological or climatological models or even build the basis for new models.

A

APPENDIX

A.1 XLES: VECTOR NOTATION

We introduce an alternative to the vector notation in section 3.4 by writing the XLES solution field in index notation. The XLES vector $\underline{\hat{\phi}}_i$ includes the XLES vector elements $\hat{\phi}_{k,i}$ represented in XLES-grids k, $k = \{1, 2, 3\}$.

In index notation the resolved small scale (RSS) terms $s_1l_2l_3$, $l_1s_2l_3$, and $l_1l_2s_3$ can be expressed by one term: $s_kl_{k\oplus1}l_{l\oplus2}$, where $\{k, k \oplus 1, k \oplus 2\}$ is a positive permutation of $\{1, 2, 3\}$ (the 1D filter operators are commutative). The operator $\oplus$ denotes the positive permutation:

$$q \oplus x = ((q + x - 1) \mod 3) + 1 \tag{148}$$

for $q = \{1, 2, 3\}$ and $x = \{1, 2\}$ (valid in three dimensions).

The XLES resolved *XLES* solution fields (Eq. (61)) are written in index notation (using the operator $\oplus$):

$$\begin{aligned}
\overline{\phi}_i &= [l_1l_2l_3 + s_1l_2l_3 + l_1s_2l_3 + l_1l_2s_3]\,\phi_i \\
&= \left[l_1l_2l_3 + \sum_{q=1}^{3} s_ql_{q\oplus1}l_{q\oplus2}\right]\phi_i \\
&= \left[\sum_{q=1}^{3}\left(l_ql_{q\oplus1}l_{q\oplus2} + s_ql_{q\oplus1}l_{q\oplus2}\right) - 2l_1l_2l_3\right]\phi_i.
\end{aligned} \tag{149}$$

The 3D large scale operator $[l_1l_2l_3]$ in the last row of Eq. (149) can be expressed in terms of $[l_ql_{q\oplus1}l_{q\oplus2} + s_ql_{q\oplus1}l_{q\oplus2}]$:

$$\begin{aligned}
-2l_1l_2l_3 &= -\sum_{q=1}^{3}(1 - \delta_{qk})(l_ql_{q\oplus1}l_{q\oplus2}) \\
&= -\sum_{q=1}^{3}(1 - \delta_{qk})((l_ql_q + l_q - l_ql_q)l_{q\oplus1}l_{q\oplus2}) \\
&= -\sum_{q=1}^{3}(1 - \delta_{qk})l_q(l_ql_{q\oplus1}l_{q\oplus2} + \underbrace{(1 - l_q)}_{=s_q}l_{q\oplus1}l_{q\oplus2})
\end{aligned} \tag{150}$$

with the Dirac Delta operator defined in Eq. (107).

Here an additional arbitrary index $k = \{1, 2, 3\}$ is introduced. Eq. (150) is satisfied for $k = 1$, $k = 2$, and $k = 3$. This index k spans the XLES vector.

Insertion of the 3D large scale operator (Eq. (150)) into the XLES resolved scales (Eq. (149)) leads to:

$$\overline{\phi}_{k,i} = \left[\sum_{q=1}^{3} (1-(l_q - l_q\delta_{qk}))\left(l_q l_{q\oplus1} l_{q\oplus2} + s_q l_{q\oplus1} l_{q\oplus2}\right)\right]\phi_i,\ k=\{1,2,3\}. \tag{151}$$

This XLES resolved solution field $\overline{\phi}_{k,i}$ reproduces exactly the XLES resolved scales in Eq. (61) including the XLES coupling $\underline{\underline{C}}\,\underline{\underline{s}}^{1D}\underline{\underline{l}}^{2D}$. XLES is interpreted as approach filtering the governing equations by applying the operator $[l_1 l_2 l_3 + s_1 l_2 l_3 + l_1 s_2 l_3 + l_1 l_2 s_3]$ compared to $[l_1 l_2 l_3]$ in LES (cf. table 4).

A.2 XLES: MASS CONSERVATION: RESOLVED SMALL SCALES

Divergence-free XLES velocity fields $\underline{\hat{u}}_i^d$ are guaranteed, if the 3D large scale velocity field $\underline{\overline{u}}_i^{LES_d} = [l_k^d]\hat{u}_{k,i}$ fulfills three conditions (see section 3.4.5):

- Con.1: $\overline{u}_{k,i}^{LES_d}$ is consistent ($\overline{u}_i^{LES_d} = \overline{u}_{k,i}^{LES_d}$)
- Con.2: $\overline{u}_i^{LES_d}$ is divergence free (enforced by a 3D standard approach)
- Con.3: $[l_k^d]$ is a discrete 1D box filter (defined in Eq. (32)) in x_k-direction.

The XLES velocity fields $\underline{\hat{u}}_i$ are divergence free as proved within one 3D large scale cell of the size Δx_k in x_k-direction (operator $\oplus$ is defined in Eq. (148), superscript d skipped):

$$\begin{aligned}
0 &= \int_{-\frac{\Delta x_k}{2}}^{\frac{\Delta x_k}{2}} \sum_{j=1}^{3} \partial_{x_j}(\overline{u}_{k,j}^{LES} + \check{u}_{k,j})\, dx_k = \int_{-\frac{\Delta x_k}{2}}^{\frac{\Delta x_k}{2}} \sum_{j=1}^{3} \partial_{x_j}\hat{u}_{k,j}\, dx_k \qquad (152)\\
&= \int_{-\frac{\Delta x_k}{2}}^{\frac{\Delta x_k}{2}} \partial_{x_k}\hat{u}_{k,k}\, dx_k + \int_{-\frac{\Delta x_k}{2}}^{\frac{\Delta x_k}{2}} \partial_{x_{k\oplus1}}\hat{u}_{k,k\oplus1}\, dx_k + \int_{-\frac{\Delta x_k}{2}}^{\frac{\Delta x_k}{2}} \partial_{x_{k\oplus2}}\hat{u}_{k,k\oplus2}\, dx_k\\
&= \hat{u}_{k,k}\left(\frac{\Delta x_k}{2}\right) - \hat{u}_{k,k}\left(-\frac{\Delta x_k}{2}\right) + \partial_{x_{k\oplus1}}\int_{-\frac{\Delta x_k}{2}}^{\frac{\Delta x_k}{2}} \hat{u}_{k,k\oplus1}\, dx_k + \partial_{x_{k\oplus2}}\int_{-\frac{\Delta x_k}{2}}^{\frac{\Delta x_k}{2}} \hat{u}_{k,k\oplus2}\, dx_k\\
&\overset{\text{Con.3}}{=} \overline{u}_{k,k}^{LES}\left(\frac{\Delta x_k}{2}\right) - \overline{u}_{k,k}^{LES}\left(-\frac{\Delta x_k}{2}\right) + \partial_{x_{k\oplus1}}\overline{u}_{k,k\oplus1}^{LES} + \partial_{x_{k\oplus2}}\overline{u}_{k,k\oplus2}^{LES}\\
&= \int_{-\frac{\Delta x_k}{2}}^{\frac{\Delta x_k}{2}} \sum_{j=1}^{3} \partial_{x_j}\overline{u}_{k,j}^{LES}\, dx_k \overset{\text{Con.1}}{=} \int_{-\frac{\Delta x_k}{2}}^{\frac{\Delta x_k}{2}} \sum_{j=1}^{3} \partial_{x_j}\overline{u}_{j}^{LES}\, dx_k \overset{\text{Con.2}}{=} 0.
\end{aligned}$$

for each XLES-grid $k = \{1,2,3\}$. Here a staggered grid is used, leading to $\hat{u}_{k,k}^d\left(\frac{\Delta x_k}{2}\right) = \overline{u}_{k,k}^{LES_d}\left(\frac{\Delta x_k}{2}\right)$ (without additional interpolation).

This in particular means the resolved small scale (RSS) velocity fields $\underline{\check{u}}_j^d$ are divergence free by construction.

A.3 ALTERNATIVE XLES INTERPRETATION: CONVOLUTION FUNCTION SPACE

Variational formulations of the governing equations lead to the well-known finite element methods and discontinuous Galerkin methods. In this section the mathematical techniques known from variational formulations are applied to describe different filter strategies.

Thereby the aim is to connect the idea to describe the governing equation in a test function space ($\mathcal{F}_T$) and the dynamic variables (e. g. u_i) within an ansatz function space ($\mathcal{F}_A$), whereby for *XLES*-like approaches $\mathcal{F}_T$ and $\mathcal{F}_A$ are related to tensor products of 1D convolution functions similar to the ansatz in section 3.4.2.1. A rigorous derivation especially of the properties of the functional convolution spaces $\mathcal{F}_T$ and $\mathcal{F}_A$ is out of the scope of this section and only indicated. To some extent this concept is related to *LES*-filtering: The decomposition e. g. of the *XLES* Leonard stress ($\underline{\mathcal{L}}_{ij}^{2D}$) includes an ansatz and a test filter. In this case the corresponding ansatz and test spaces are one-dimensional.

This section is not required to understand the *XLES* and especially *ODTLES* models and can be interpreted as an outlook section. Nevertheless the presented alternative interpretation of filter strategies provides a mathematical framework that can be extended for specific requirements (e. g. unstructured grids, cf. section A.3.3).

As an example section A.3.2 introduces the *XLES-U* approach for a simplified governing equations in this formulation. Thereby the focus is to reproduce the *XLES-U* system of equation derived in section 3.4.

The notation in this section is related to the *XLES* vector notation. Slight differences are stated explicitly.

A.3.1 *General Formulation*

The simplified equation (without pressure term) describes advective transport of the velocity $\mathbf{u} = \begin{pmatrix} u_1 & u_2 & u_3 \end{pmatrix}^T$ in an integral form:

$$0 = \int_\Omega \partial_t \mathbf{u} \, d\mathbf{x} + \int_\Omega \nabla \cdot \mathbf{F} \, d\mathbf{x} \tag{153}$$

with the spatial coordinates in vector notation $\mathbf{x} = \begin{pmatrix} x_1 & x_2 & x_3 \end{pmatrix}^T$ and the advective fluxes $\mathbf{F} = \mathbf{u} \otimes \mathbf{u}$ ($\otimes$ is an outer product). In this section a standard vector notation for coordinates and variables (bold fonts) is used additionally to the variational vector formulation (indicated by an underbar).

Similar to the variational formulations, the variables $\mathbf{u}$ and $\mathbf{F}$ are approximated using an ansatz function, e. g. :

$$\mathbf{u}(\mathbf{x},t) \approx \sum_{l=1}^{A} \Psi_l(\mathbf{x})\mathbf{u}_l(t) = \underline{\Psi}^T(\mathbf{x})\underline{\mathbf{u}}^A(t) \text{ with } \underline{\mathbf{u}}^A = \begin{pmatrix} \mathbf{u}_1 & \dots & \mathbf{u}_A \end{pmatrix}^T, \tag{154}$$

$$\mathbf{F}(\mathbf{x},t) \approx \sum_{l=1}^{A} \Psi_l(\mathbf{x})\mathbf{F}_l(t) = \underline{\Psi}^T(\mathbf{x})\underline{\mathbf{F}}^A(t) \tag{155}$$

where a A-dimensional ansatz function space ($\mathcal{F}_A$) and a T-dimensional test function space ($\mathcal{F}_T$) are used. Here $\underline{\mathbf{u}}^A$ and $\underline{\mathbf{F}}^A$ are vectors of coefficient corresponding to the filtered fields for a *XLES*-like approach.

The governing equation (153) is multiplied by the test functions $\underline{\varphi}$ within a T-dimensional test function space leading to

$$0 = \int_\Omega \underline{\varphi}\partial_t \underline{\Psi}^T \underline{\mathbf{u}}^A + \sum_{j=1}^{3} \underline{\varphi}\nabla \cdot \underline{\Psi}^T \underline{\mathbf{F}}^A. \tag{156}$$

Note that the size of the test function space not necessarily equals the size of the ansatz function space.

So far this formulation corresponds to a standard variational formulation. If the test function space equals the ansatz function space the resulting scheme is called a Galerkin scheme.

A.3.2 *XLES-U Interpretation*

The scope of this section is to introduce an unclosed *XLES* equivalent approach using the idea of functional convolution spaces.

For test functions that are stationary we can state:

$$0 = \int_\Omega \partial_t \underline{\varphi}\, \underline{\Psi}^T \underline{\mathbf{u}}^A \, d\mathbf{x} + \int_\Omega \underline{\varphi}\nabla\, \underline{\Psi}^T \underline{\mathbf{F}}^A \, d\mathbf{x}. \tag{157}$$

In standard variational formulations $\underline{\varphi}\nabla$ is expressed in a weak sense, where the derivative of the test functions is used. For a *XLES*-like formulation the nabla-operator interchanges with φ, because the partial derivatives are still well defined within each *XLES-grid* corresponding to the each test function (cf. Eq. (159)).

To follow an *XLES-U* like approach we use the ansatz

$$\underline{\Psi}^T = \begin{pmatrix} l_1 l_2 l_3 & s_1 l_2 l_3 & l_1 s_2 l_3 & l_1 l_2 s_3 \end{pmatrix} \tag{158}$$

with the 1D filter operator in x_k-direction $[l_k]$ (cf. to the *XLES* resolved scales in table 4). This ansatz contains all scales which are represented by *XLES*.

The *XLES-U* ansatz (158) neglects the *XLES* unresolved terms $[l_1 s_2 s_3 + s_1 l_2 s_3 + s_1 s_2 l_3 + s_1 s_2 s_3]$, which are not further considered here.

The test function leading to an *XLES* formulation is

$$\underline{\varphi} = \begin{pmatrix} l_2 l_3 \\ l_1 l_3 \\ l_1 l_2 \end{pmatrix} . \tag{159}$$

This choice automatically allows a discrete representation of the governing equation (157) within the *XLES-grid*s illustrated in figures 4b–4d.

Note that only the *XLES-U* equation is derived and numerical approximation errors are not investigated. Additionally the filter operators themselves do not allow a statement e. g. about the effective implicit filter length.

The ansatz and test function spaces are connected due to a $\mathcal{F}_T$-$\mathcal{F}_A$-transformation matrix $\underline{\underline{V}}$:

$$\underline{\Psi} = \underline{\underline{V}}^T \, \underline{\varphi} \tag{160}$$

with

$$\underline{\underline{V}} = \begin{pmatrix} l_1/3 & \mathbb{1} - l_1 & 0 & 0 \\ l_2/3 & 0 & \mathbb{1} - l_2 & 0 \\ l_3/3 & 0 & 0 & \mathbb{1} - l_3 \end{pmatrix} . \tag{161}$$

This transformation matrix takes the role of the so called Vandermonde matrix in certain variational formulations but is not unique for the *XLES-U* formulation. An alternative transformation matrix is e. g. :

$$\underline{\underline{V}}' = \begin{pmatrix} l_1 & \mathbb{1} - l_1 & 0 & 0 \\ 0 & 0 & \mathbb{1} - l_2 & 0 \\ 0 & 0 & 0 & \mathbb{1} - l_3 \end{pmatrix} \tag{162}$$

and leads to an identical behavior (inserted in Eq. (160)). This reflects the 3D large scale consistency condition $l_1(l_2 l_3) = l_2(l_1 l_3) = l_3(l_1 l_2) = \frac{1}{3}(l_1(l_2 l_3) + l_2(l_1 l_3) + l_3(l_1 l_2))$.

Using the transformation matrix $\underline{\underline{V}}$ we can further investigate the governing equation (157):

- to compute the linear term $\partial_t \underline{\varphi} \, \underline{\Psi}^T \underline{u}_i^A$ the mass matrix equivalent $\underline{\varphi} \, \underline{\Psi}^T$ has to be investigated. By assuming e. g. a spectral filter we can use

$l_k^2 = l_k,\ k = \{1,2,3\}$ in the linear term (in standard *LES* only one filter application is required for linear terms) leading to:

$$\underline{\varphi}\,\underline{\Psi}^{\mathrm{T}} = \underline{\varphi}\,\underline{\varphi}^{\mathrm{T}}\underline{\underline{V}} \begin{pmatrix} l_1 l_2 l_3 & l_2 l_3 - l_1 l_2 l_3 & 0 & 0 \\ l_1 l_2 l_3 & 0 & l_1 l_3 - l_1 l_2 l_3 & 0 \\ l_1 l_2 l_3 & 0 & 0 & l_1 l_2 - l_1 l_2 l_3 \end{pmatrix} \tag{163}$$

The resulting velocity scales are discretely represented by the *XLES-grid*s and the 3D large scale grid illustrated in figure 4.

- the non-linear terms $\nabla\underline{\varphi}\,\underline{\Psi}^{\mathrm{T}}\underline{F}_{ij}^{A}$ require a representation of the advective fluxes within the *XLES-grid*s (cf. figures 4b–4d) corresponding to the test function space ($\mathcal{F}_{\mathrm{T}}$).

The advective flux can be interpreted using Eq. (160):

$$\nabla\underline{\varphi}\,(\underline{\underline{V}}^{\mathrm{T}}\,\underline{\varphi})^{\mathrm{T}}\underline{\mathbf{F}}^{A} = \nabla\underline{\varphi}\,\underline{\varphi}^{\mathrm{T}}\underline{\underline{V}}\,\underline{\mathbf{F}}^{A}, \tag{164}$$

where the matrix $\underline{\varphi}\,\underline{\varphi}^{\mathrm{T}}\underline{\underline{V}}$ has to be interpreted. To derive an *XLES* framework similar to section 3.4, we also have to identify e. g. the $\underline{\mathcal{L}}_{ij}^{2D}$ ($\mathbf{L}^{2D}$, which is the matrix form of $\underline{\mathcal{L}}_{ij}^{2D}$) in this variational-like ansatz: the *XLES* Leonard stress can be interpreted by rearranging the test function:

$$\underline{\varphi}\,\underline{\underline{V}}\,\underline{\mathbf{F}}^{A} = (\underline{\mathbb{1}} + \underline{\varphi} - \underline{\mathbb{1}})\underline{\underline{V}}\,\underline{\mathbf{F}}^{A} = \left((\underline{\varphi}^{-1}) * \underline{\varphi} + \underline{\varphi} - \underline{\mathbb{1}}\right)\underline{\underline{V}}\,\underline{\mathbf{F}}^{A} \tag{165}$$

where $\mathbf{L}^{2D} = (\underline{\varphi} - \underline{\mathbb{1}})\underline{\varphi}^{\mathrm{T}}\underline{\underline{V}}\,\underline{\mathbf{F}}^{A}$, the element-wise Hademard multiplication ($*$), and $\underline{\varphi}^{-1} = \begin{pmatrix} l_2^{-1} l_3^{-1} & l_1^{-1} l_3^{-1} & l_1^{-1} l_2^{-1} \end{pmatrix}^{\mathrm{T}}$.

The resulting advection terms are

$$\partial_{x_j}\underline{\varphi}\,\underline{\varphi}^{\mathrm{T}}\underline{\underline{V}}\,\underline{\mathbf{F}}^{A} = \partial_{x_j}(\underline{\varphi}^{-1} * \underline{\varphi})\underline{\varphi}^{\mathrm{T}}\underline{\underline{V}}\,\underline{\mathbf{F}}^{A} + \mathbf{L}^{2D}. \tag{166}$$

Note that both the *XLES* Leonard stresses and the resulting advective fluxes ($(\underline{\varphi}^{-1}) * \underline{\varphi}\,\underline{\varphi}^{\mathrm{T}}\underline{\underline{V}}\,\underline{\mathbf{F}}^{A}$) are defined within the test function space.

The full convolution matrix within the non-linear *XLES* terms is

$$(\underline{\varphi}^{-1} * \underline{\varphi})\,\underline{\varphi}^{\mathrm{T}}\underline{\underline{V}} = \begin{pmatrix} l_2 l_3 & l_2 l_3 - l_1 l_2 l_3 & l_1 l_3 - l_1 l_2 l_3 & l_1 l_2 - l_1 l_2 l_3 \\ l_1 l_3 & l_2 l_3 - l_1 l_2 l_3 & l_1 l_3 - l_1 l_2 l_3 & l_1 l_2 - l_1 l_2 l_3 \\ l_1 l_2 & l_2 l_3 - l_1 l_2 l_3 & l_1 l_3 - l_1 l_2 l_3 & l_1 l_2 - l_1 l_2 l_3 \end{pmatrix}. \tag{167}$$

Following arguments in section 3.4.2.2 the matrix

$$(\underline{\underline{l}}^{\dagger} * \underline{\mathbb{1}})\underline{\varphi}^{\mathsf{T}}\underline{\underline{V}} = \underline{\varphi}\,(\underline{\varphi}^{-1} * \underline{\varphi})^{\mathsf{T}}\underline{\underline{V}} \tag{168}$$
$$= \begin{pmatrix} l_2 l_3 & l_2 l_3 - l_1 l_2 l_3 & l_2 l_1^{-1}(l_1 l_3 - l_1 l_2 l_3) & l_3 l_1^{-1}(l_1 l_2 - l_1 l_2 l_3) \\ l_1 l_3 & l_1 l_2^{-1}(l_2 l_3 - l_1 l_2 l_3) & l_1 l_3 - l_1 l_2 l_3 & l_3 l_2^{-1}(l_1 l_2 - l_1 l_2 l_3) \\ l_1 l_2 & l_1 l_3^{-1}(l_2 l_3 - l_1 l_2 l_3) & l_2 l_3^{-1}(l_1 l_3 - l_1 l_2 l_3) & l_1 l_2 - l_1 l_2 l_3 \end{pmatrix}$$

can be numerically interpreted within the test function space which corresponds to the *XLES-grid*s.

Eq. (168) shows an alternative argumentation to introduce $\underline{\underline{l}}^{\dagger}$: Instead of $(\underline{\underline{l}}^{\dagger} * \underline{\mathbb{1}})$ the *XLES* Leonard stress can be build using the transposed $(\underline{\underline{l}}^{\dagger} * \underline{\mathbb{1}})^{\mathsf{T}}$ within the convolution matrix $\underline{\varphi}\,\underline{\varphi}^{\mathsf{T}}\underline{\underline{V}}$, which leads to the required form (168). This can be interpreted as a modified *XLES* Leonard stress $\mathbf{L}^{2D} = \underline{\varphi}(\underline{\varphi} - \underline{\mathbb{1}}))^{\mathsf{T}}\underline{\underline{V}}\,\underline{\mathbf{F}}^{A}$ which is rather based on the ansatz-filter than the test-filter.

The advective flux $\mathbf{F} = \mathbf{u} \otimes \mathbf{u}$ is linearized in section 3.4.2.2. In the variational-like formulation this means that the full matrix in Eq. (168) is applied to both the advecting velocities and the advected velocities. Thereby terms of the form $[l_1 l_2]\mathbf{u} \otimes [l_2 l_3]\mathbf{u}$ are neglected (cf. Eq. (76)).

Note within Eq. (168) the submatrix

$$\begin{pmatrix} l_2 l_3 - l_1 l_2 l_3 & l_2 l_1^{-1}(l_1 l_3 - l_1 l_2 l_3) & l_3 l_1^{-1}(l_1 l_2 - l_1 l_2 l_3) \\ l_1 l_2^{-1}(l_2 l_3 - l_1 l_2 l_3) & l_1 l_3 - l_1 l_2 l_3 & l_3 l_2^{-1}(l_1 l_2 - l_1 l_2 l_3) \\ l_1 l_3^{-1}(l_2 l_3 - l_1 l_2 l_3) & l_2 l_3^{-1}(l_1 l_3 - l_1 l_2 l_3) & l_1 l_2 - l_1 l_2 l_3 \end{pmatrix} \tag{169}$$

applied to $\underline{\mathbf{F}}^{\mathsf{T}}$ $(\in \mathcal{F}_{\mathsf{T}})$ equals the *XLES-U* coupling $\underline{\underline{l}}^{\dagger} * \underline{\underline{C}}\,(\underline{\hat{u}}_j * \underline{\hat{u}}_i - \underline{\overline{u}}_j^{\mathrm{LES}} * \underline{\overline{u}}_i^{\mathrm{LES}})$ as described in section 3.4.2.2.

In summary we can state that the ansatz and test functions in Eqs. (158 and 159) can be used to derive the *XLES-U* equations if the same approximations as in section 3.4.2.2 are used.

The *XLES-U* equation can also be derived for a Galerkin equivalent ansatz function space by using $\underline{\varphi} = \underline{\Psi} = \begin{pmatrix} l_2 l_3 \\ l_1 l_3 \\ l_1 l_2 \end{pmatrix}$ which is not shown in detail here.

A.3.3 *Towards Unstructured XLES*

In *XLES-U* the test functions are local (in the *XLES* example box filters), so Eq. (157) is valid for each individual computational 3D grid cell (Ω_n) (corresponding to the 3D large scale grid cell in figure 4a). The same concept is also used in discontinuous Galerkin methods.

For an unstructured grid, the 'filter separation' can be performed on a cubic reference cell, even if each cell in the physical space is e. g. a tetrahedron. The transformation between the physical coordinates (e. g. tetrahedrons) defined by the coordinates $\mathbf{x} = \begin{pmatrix} x_1 & x_2 & x_3 \end{pmatrix}^T$ into the cubic reference cell with $\mathbf{a} = \begin{pmatrix} a_1 & a_2 & a_3 \end{pmatrix}^T$ can be described by a spatial transformation matrix $\mathbf{T}$ such that

$$\mathbf{x} = \mathbf{T}\mathbf{a}. \tag{170}$$

The specific appearance of $\mathbf{T}$ depends on the unstructured discretization in the physical space and is not further investigated here. For several choices, e. g. tetrahedrons, the transformation matrices are known and routinely applied in *DGM* (cf. [39]).

The corresponding Jacobi matrix $\mathbf{J}$ in 3D is defined by

$$\mathbf{J} = \begin{pmatrix} \partial_{a_1} x_1 & \partial_{a_2} x_1 & \partial_{a_3} x_1 \\ \partial_{a_1} x_2 & \partial_{a_2} x_2 & \partial_{a_3} x_2 \\ \partial_{a_1} x_3 & \partial_{a_2} x_3 & \partial_{a_3} x_3 \end{pmatrix} \tag{171}$$

and fulfills $d\mathbf{x} = \mathbf{J}\, d\mathbf{a}$.

Thus the ∇-operator in physical space is:

$$\nabla_{\mathbf{x}} = (\mathbf{J})^{-1} \nabla_{\mathbf{a}} = \frac{1}{\det(\mathbf{J})} \mathbf{T}\, \nabla_{\mathbf{a}}. \tag{172}$$

In the integral formulation of Eq. (157) for one individual computational 3D grid cell (Ω_n) we find

$$\begin{aligned} 0 &= \int_{\Omega_n} \underline{\varphi} \partial_t \mathbf{u}\, d\mathbf{x} + \int_{\Omega_n} \underline{\varphi} \nabla_{\mathbf{x}}^T \mathbf{F}\, d\mathbf{x} \\ &= \int_{\Omega_n} \underline{\varphi} \partial_t \mathbf{u} \det(\mathbf{J})\, d\mathbf{a} + \int_{\Omega_n} \underline{\varphi} \left(\frac{(\mathbf{T}\nabla_{\mathbf{a}})^T}{\det(\mathbf{J})} \right) \mathbf{F} \det(\mathbf{J})\, d\mathbf{a} \\ &= \int_{\Omega_n} \underline{\varphi} \partial_t \mathbf{u} \det(\mathbf{J})\, d\mathbf{a} + \int_{\Omega_n} \underline{\varphi} \nabla_{\mathbf{a}}^T \mathbf{F}(\mathbf{a})\, d\mathbf{a}, \end{aligned} \tag{173}$$

where the dynamic variables $\underline{\mathbf{u}}$ can be interpreted in both coordinate systems, e. g. :

$$\mathbf{u} \approx \underline{\Psi}^T(\mathbf{x}) \underline{\mathbf{u}}^A(\mathbf{x}) = \underline{\Psi}^T(\mathbf{a}) \underline{\mathbf{u}}^A(\mathbf{a}). \tag{174}$$

and the advective flux is

$$\mathbf{T}^T \mathbf{F} = \mathbf{F}(\mathbf{a}) \approx \underline{\Psi}^T(\mathbf{a}) \underline{\mathbf{F}}^A(\mathbf{a}) \tag{175}$$

Thus all computations are possible within the reference cell. For *XLES*-like approaches this means the filter operations (including the ansatz functions $\underline{\Psi}^{\mathrm{T}}(\mathbf{a})$) are defined in this reference cell. E. g. for a tetrahedral physical cell, the Jacobi determinant only depends on the physical cell volume.

This concept is a basis for a possible unstructured *XLES* formulation. In principle similar transformations can be defined for the *XLES* formulation in section 3.4. Details are in the scope of future investigations. Its uncertain if *ODT* can perform reasonably within a system of reference cells or if other models can close the unstructured *XLES* equations.

A.3.4 *Further Potentially Related Approaches*

In section A.3.2 the 2D filtered *XLES-U* apprach is briefly investigated in a variational-like formulation. In principle all *XLES*-related filter approaches, e. g. as summarized in table 4, can be interpreted within this variational-like formulation. The corresponding ansatz and test functions are shown in table 11.

The standard discontinuous Galerkin method uses basis functions ϕ in the variational formulation. Hesthaven and Warburton [39] summarized possible choices for ϕ. A possible concept is to connect the convolution ansatz and test functions and the *DGM* basis functions as orthogonal subspaces within higher-level ansatz and test function spaces. In this way the *XLES* filter concept and the variational *DGM*-formulation do not interfere. At the end each *XLES-grid* is discretized using a *DGM* formulation.

For further theoretical and applied investigations of the XLES-vector space or related spaces defined by 'filter separations', especially its relation to functional spaces, it might be useful to take further advantage of the techniques developed for *FEM* and *DGM*. At this stage the XLES-vector space is interpreted more as a modeling concept than a mathematical product space. Nevertheless we hope that a variational-like filter formulation might help as a starting point to investigate the properties and applications of *XLES*-related models (e. g. in table 11) in future studies.

Table 11: Suggested test functions (φ) and ansatz functions (Ψ) lead to different potential *XLES*-related model approaches. The unresolved terms $\mathcal{S}$ have to be modeled, e. g. by *ODT* (in *ODTLES*) or an eddy viscosity model (in *LES*). For unstructured *XLES*, φ and Ψ are defined within reference 3D cells with known transformation rules (cf. section A.3.3). The functions ϕ refer to a possible *DGM* basis function system. Thus for *DG-XLES-U* the full function space can be defined using orthogonal subspaces for the *XLES*-filtering and the *DGM* basis functions.

Model	φ	Ψ
XLES-U	$(l_2l_3, l_1l_3, l_2l_3)^T$	$(l_1l_2l_3, s_1l_2l_3, l_1s_2l_3, l_1l_2s_3)^T$
XLES	$(l_2l_3, l_1l_3, l_2l_3)^T$	$(l_1l_2l_3, s_1l_2l_3, l_1s_2l_3, l_1l_2s_3, \mathcal{S})^T$
DG-XLES-U	$\phi \times (l_2l_3, l_1l_3, l_2l_3)^T$	$\phi \times (l_1l_2l_3, s_1l_2l_3, l_1s_2l_3, l_1l_2s_3)^T$
unstructured *XLES*	$(l_2l_3, l_1l_3, l_2l_3)^T$	$(l_1l_2l_3, s_1l_2l_3, l_1s_2l_3, l_1l_2s_3, \mathcal{S})^T$
LES-U	$(l_1l_2l_3)$	$(l_1l_2l_3)$
LES	$(l_1l_2l_3)$	$(l_1l_2l_3, \mathcal{S})^T$
DNS	$\mathbb{1}$	$\mathbb{1}$
DG-DNS	ϕ	ϕ

[4] Ahlers, G., Grossmann, S., Lohse, D., 2009. Heat transfer and large scale dynamics in turbulent rayleigh-bénard convection. Rev. Mod. Phys. 81, 503–537. (Cited on page 117.)

[5] Ahlers, G., He, X., Funfschilling, D., Bodenschatz, E., 2012. Heat transport by turbulent Rayleigh-Bénard convection for $\mathrm{Pr} = 0.8$ and $3 \times 10^{12} \leqslant \mathrm{Ra} \leqslant 10^{15}$: aspect ratio $\Gamma = 0.50$. New J. Phys. 14, 103012. (Cited on page 109.)

[6] Ashurst, W. T., Kerstein, A. R., 2005. One-dimensional turbulence: Variable-density formulation and application to mixing layers. Phys. Fluids 17, 025107. (Cited on page 28.)

[7] Boris, J. P., Grinstein, F. F., Oran, E. S., Kolbe, R. L., 1992. New insights into large eddy simulation. In: Fluid Dynamics Research. Vol. 10. North Holland, pp. 199–228. (Cited on page 27.)

[8] Burbeau, A., Sagaut, P., Bruneau, C.-H., 2001. A problem-independent limiter for high-order Runge-Kutta discontinuous Galerkin methods. J. Comput. Phys. 169, 111–150. (Cited on page 71.)

[9] Butcher, J. C., 1996. A history of Runge-Kutta methods. Appl. Numer. Math. 20, 247–260. (Cited on page 78.)

[10] Cao, S., Echekki, T., 2008. A low-dimensional stochastic closure model for combustion large-eddy simulation. J. Turbul. 9, 1–35. (Cited on page 6.)

[11] Castaing, B., Gunaratne, G., Heslot, F., Kadanoff, L., Libchaber, A., Thomae, S., Wu, X.-Z., Zaleski, S., Zanetti, G., 1989. Scaling of hard thermal turbulence in Rayleigh-Bénard convection. J. Fluid Mech. 204, 1–30. (Cited on page 109.)

[12] Cavaglieri, D., Bewley, T., 2015. Low-storage implicit/explicit Runge–Kutta schemes for the simulation of stiff high-dimensional ODE systems. J. Comput. Phys. 286, 172–193. (Cited on page 78.)

[13] Chapman, D. R., 1979. Computational aerodynamics development and outlook. Phys. Fluids 17, 1293–1313. (Cited on pages 63 and 64.)

[14] Chaumat, S., Castaing, B., Chilla, F., 2002. Rayleigh-Bénard cells: influence of plate properties. In: Castro, I. P., Hancock, P. E., Thomas, T. G. (Eds.), In Advances in Turbulence IX. International Center for Numerical Methods in Engineering, CIMNE. (Cited on page 109.)

[15] Chavanne, X., Chillà, F., Chabaud, B., Castaing, B., Hébral, B., 2001. Turbulent Rayleigh-Bénard convection in gaseous and liquid He. Phys. Fluids 13, 1300–1320. (Cited on page 109.)

[16] Chillà, F., Schumacher, J., 2012. New perspectives in turbulent Rayleigh-Bénard convection. Eur. Phys. E Soft Matter 35. (Cited on page 109.)

[17] Choi, H., Moin, P., 2012. Grid-point requirements for large eddy simulation: Chapman's estimates revisited. Phys. Fluids 24, 31–36. (Cited on pages 63 and 64.)

[18] Cline, D. A., 2015. A novel modeling approach for multiscale, multiphysics flow. Poster presented at SIAM CSE15, March 14–18, 2015, Salt Lake City, USA. (Cited on page 47.)

[19] Crank, J., Nicolson, P., 1996. A practical method for numerical evaluation of solutions of partial differential equations of the heat-conduction type. Adv. Comput. Math. 6, 207–226. (Cited on page 17.)

[20] Denaro, F. M., 2011. What does finite volume-based implicit filtering really resolve in large-eddy simulations? Journal of Computational Physics 230, 3849–3883. (Cited on pages 25, 86, and 90.)

[21] Dietze, E., Mellado, J., Stevens, B., Schmidt, H., 2013. Study of low-order numerical effects in the two-dimensional cloud-top mixing layer. Theor. Comp. Fluid Dyn. 27, 239–251. (Cited on page 28.)

[22] Dietze, E., Schmidt, H., Stevens, B., Mellado, J. P., 2015. Controlling entrainment in the smoke cloud using level set-based front. Meteorol. Z. 23, 661–674. (Cited on page 6.)

[23] Falgout, R. D., Yang, U. M., 2002. hypre: a library of high performance preconditioners. In: Preconditioners, Lecture Notes in Computer Science. pp. 632–641. (Cited on page 18.)

[24] Ferziger, J., Peric, M., 1999. Computational Methods for Fluid Dynamics. Springer. (Cited on pages 12, 13, 18, and 41.)

[25] Feynman, R., Leighton, R., Sands, M., 1963. The Feynman Lectures on Physics. Addison-Wesley, Boston. (Cited on page 4.)

[26] Fleischer, A. S., Goldstein, R. J., 2002. High-Rayleigh-number convection of pressurized gases in a horizontal enclosure. J. Fluid Mech. 469, 1–12. (Cited on page 109.)

[27] Funfschilling, D., Brown, E., Nikolaenko, A., Ahlers, G., 2005. Heat transport by turbulent Rayleigh-Bénard Convection in cylindrical samples with aspect ratio one and larger 536, 145–154. (Cited on page 109.)

[28] Fureby, C., 2008. Towards the use of large eddy simulation in engineering. Prog. Aerosp. Sci. 44, 381–396. (Cited on page 24.)

[29] Gadd, A. J., 1978. A split explicit integration scheme for numerical weather prediction. Q. J. Roy. Meteor. Soc. 104, 569–582. (Cited on page 78.)

[30] Gander, M., Halpern, L., 2013. Techniques for locally adaptive time stepping developed over the last two decades. In: Bank, R., Holst, M., Widlund, O., Xu, J. (Eds.), Domain Decomposition Methods in Science and Engineering XX. Vol. 91 of Lecture Notes in Computational Science and Engineering. Springer Berlin Heidelberg, pp. 377–385. (Cited on page 16.)

[31] Germano, M., 1986. A proposal for a redefinition of the turbulent stresses in the filtered Navier-Stokes equations. Phys. Fluids 29, 2323–2324. (Cited on pages 27 and 38.)

[32] Germano, M., Piomelli, U., Moin, P., Cabot, W. H., 1991. A dynamic subgrid-scale eddy viscosity model. Phys. Fluids A: Fluid Dynamics 3, 1760–1765. (Cited on page 27.)

[33] Gonzalez-Juez, E. D., Schmidt, R. C., Kerstein, A. R., 2011. ODTLES simulation of wall-bounded turbulent flows. Phys. Fluids 23, 125102. (Cited on pages 61, 62, 70, 83, and 96.)

[34] Grabowski, W. W., Smolarkiewicz, P. K., 1999. CRCP: a Cloud Resolving Convection Parameterization for modeling the tropical convecting atmosphere. Physica D: Nonlinear Phenomena 133, 171–178. (Cited on pages 7, 32, and 33.)

[35] Grossmann, S., Lohse, D., 2000. Scaling in thermal convection: a unifying theory. J. Fluid Mech. 407, 27–56. (Cited on pages 108, 109, 117, and 118.)

[36] Grossmann, S., Lohse, D., 2011. Multiple scaling in the ultimate regime of thermal convection. Phys. Fluids 23. (Cited on page 109.)

[37] Gustafsson, B., Kreiss, H.-O., Oliger, J., 1995. Time-Dependent Problems and Difference Methods. John Wiley & Sons, Inc., Hoboken, NJ, USA. (Cited on page 12.)

[38] He, X., Funfschilling, D., Nobach, H., Bodenschatz, E., Ahlers, G., 2012. Transition to the ultimate state of turbulent Rayleigh-Bénard convection. Phys. Rev. Lett. 108, 024502. (Cited on page 109.)

[39] Hesthaven, J. S., Warburton, T., 2007. Nodal Discontinuous Galerkin Methods: Algorithms, Analysis, and Applications. Springer Publishing Company, Incorporated. (Cited on pages 12, 135, and 136.)

[40] Horenko, I., 2010. On clustering of non-stationary meteorological time series. Dynam. Atmos. Oceans 49, 164–187. (Cited on page 53.)

[41] Ivanov, M. S., Gimelshein, S. F., 1998. Computational hypersonic rarefied flows. Annu. Rev. Fluid Mech. 30, 469–505. (Cited on page 9.)

[42] Jiménez, J., Moser, R. D., 2000. Large-eddy simulations: Where are we and what can we expect? AIAA Journal 38, 605–612. (Cited on page 28.)

[43] Jones, Jr., D. C., 1976. An improvement in the calculation of turbulent friction in rectangular ducts. J. Fluids Eng. ASME 98, 173–180. (Cited on pages 98, 101, and 104.)

[44] Jones, W., Launder, B., 1972. The prediction of laminarization with a two-equation model of turbulence. Int. J. Heat Mass Transfer 15, 301–314. (Cited on page 24.)

[45] Jozefik, Z., Kerstein, A. R., Schmidt, H., 2015. Simulation of shock-turbulence interaction in non-reactive flow and in turbulent deflagration and detonation regimes using one-dimensional turbulence. submitted to Combust. Flame. (Cited on page 126.)

[46] Jung, J.-H., Arakawa, A., 2010. Development of a quasi-3d multiscale modeling framework: Motivation, basic algorithm and preliminary results. J. Adv. Model Earth Sy. 2. (Cited on pages 7 and 32.)

[47] Kaczorowski, M., Wagner, C., 2009. Analysis of the thermal plumes in turbulent Rayleigh-Bénard convection based on well-resolved numerical simulations. J. Fluid Mech. 618, 89–112. (Cited on page 115.)

[48] Kawamura, H., Dec. 2014. DNS database. `http://murasun.me.noda.tus.ac.jp/turbulence/index.html`, [Online; accessed Dec 2014]. (Cited on pages vii, 84, 89, 90, and 93.)

[49] Kawamura, H., Abe, H., Matsuo, Y., 1999. DNS of turbulent heat transfer in channel flow with respect to Reynolds and Prandtl number effects. Int. J. Heat Fluid Fl. 20, 196–207. (Cited on pages 84, 89, and 93.)

[50] Kerstein, A. R., 1999. One-dimensional turbulence: Model formulation and application to homogeneous turbulence, shear flows, and buoyant stratified flows. J. Fluid Mech. 392, 277–334. (Cited on page 28.)

[51] Kerstein, A. R., 2007. Documentation of basicodt, a simple odt code: Version 1. 2007. `https://sites.google.com/site/odtresearch/home`. (Cited on page 28.)

[52] Kerstein, A. R., 2008. Autonomous microstructure evolution. In: Hillebrandt, W., Kupka, F. (Eds.), Interdisciplinary aspects of turbulence. Lecture Notes in Physics. Springer, Berlin. (Cited on page 126.)

[53] Kerstein, A. R., Ashurst, W. T., Wunsch, S., Nilsen, V., 2001. One-dimensional turbulence: Vector formulation and application to free shear flows. J. Fluid Mech. 447, 85–109. (Cited on pages 28, 30, and 86.)

[54] Klein, R., 1995. Semi-implicit extension of a godunov-type scheme based on low mach number asymptotics i: One-dimensional flow. J. Comput. Phys. 121, 213–237. (Cited on page 10.)

[55] Klein, R., 2005. Multiple spatial scales in engineering and atmospheric low mach number flows. ESAIM: M2AN 39, 537–559. (Cited on page 9.)

[56] Klein, R., 2009. Asymptotics, structure, and integration of sound-proof atmospheric flow equations. Theor. Comp. Fluid Dyn. 23, 161–195. (Cited on page 9.)

[57] Klein, R., 2010. Scale-dependent models for atmospheric flows. Annu. Rev. Fluid Mech. 42, 249–274. (Cited on page 9.)

[58] Kraichnan, R. H., 1962. Turbulent thermal convection at arbitrary Prandtl number. Phys. Fluids 5, 1374–1389. (Cited on page 109.)

[59] Lakkaraju, R., Stevens, R. J. A. M., Verzicco, R., Grossmann, S., Prosperetti, A., Sun, C., Lohse, D., 2012. Spatial distribution of heat flux and fluctuations in turbulent Rayleigh-Bénard convection. Phys. Rev. E 86. (Cited on page 109.)

[60] Launder, B., Sharma, B., 1974. Application of the energy-dissipation model of turbulence to the calculation of flow near a spinning disc. Letters in Heat and Mass Transfer 1, 131–137. (Cited on page 24.)

[61] Lee, M., Malaya, N., Moser, R. D., 2013. Petascale direct numerical simulation of turbulent channel flow on up to 786k cores. In: Proceedings of SC13: International Conference on High Performance Computing, Networking, Storage and Analysis. ACM, pp. 1–11. (Cited on page 95.)

[62] Lee, M., Moser, R. D., 2015. Direct numerical simulation of turbulent channel flow up to $Re_\tau = 5200$. J. Fluid Mech. 774, 395–415. (Cited on pages 5, 93, and 101.)

[63] Lee, M., Moser, R. D., Feb. 2015. DNS database. `http://turbulence.ices.utexas.edu`, [Online; accessed Feb 2015]. (Cited on pages vii, 65, 88, 93, and 103.)

[64] Leonard, A., 1975. Energy cascade in large-eddy simulations of turbulent fluid flows. Adv. Geophys. 18, 237–248. (Cited on pages 27, 28, 37, and 38.)

[65] LeVeque, R. J., 1985. A large time step generalization of Godunov's method for systems of conservation laws. SIAM J. Numer. Anal. 22, 1051–1073. (Cited on page 78.)

[66] LeVeque, R. J., 2002. Finite-Volume Methods for Hyperbolic Problems. Cambridge University Press. (Cited on page 70.)

[67] Lignell, D., Kerstein, A., Sun, G., Monson, E. I., 2013. Mesh adaption for efficient multiscale implementation of one-dimensional turbulence. Theor. Comput. Fluid Dyn. 27, 273–295. (Cited on pages 6, 64, and 125.)

[68] Lilly, D. K., 1967. The representation of small scale turbulence in numerical simulation experiments. In: IBM Scientific Computing Symposium on environmental sciences. Yorktown heights, pp. 195–210. (Cited on page 26.)

[69] McDermott, R. J., 2005. Toward one-dimensional turbulence subgrid closure for large-eddy simulation. Ph.D. thesis, University of Utah. (Cited on pages 7, 62, 68, and 70.)

[70] Meiselbach, F. T., Apr 2015. private communication. (Cited on page 65.)

[71] Meiselbach, F. T., 2015. Application of ODT to turbulent flow problems. Ph.D. thesis, BTU Cottbus-Senftenberg. (Cited on pages 6, 31, 65, 83, 84, and 125.)

[72] Meister, A., 1999. Numerik linearer Gleichungssysteme, Eine Einfuehrung in moderne Verfahren. Vieweg Verlag, Braunschweig, Wiesbaden. (Cited on page 17.)

[73] Mellado, J., Ansorge, C., 2012. Factorization of the fourier transform of the pressure-Poisson equation using finite differences in colocated grids. ZAMM Z. Angew. Math. Mech. 92, 380–392. (Cited on page 12.)

[74] Menon, S., Kerstein, A., 2011. The linear-eddy model. In: Echekki, T., Mastorakos, E. (Eds.), Turbulent Combustion Modeling: Advances, New Trends and Perspectives. Springer, pp. 221–247. (Cited on pages 6 and 123.)

[75] Moin, P., Kim, J., 1982. Numerical investigation of turbulent channel flow. J. Fluid Mech. 118, 341–377. (Cited on page 27.)

[76] Mulyukova, E., Steinberger, B., Dabrowski, M., Sobolev, S. V., 2015. Survival of LLSVPs for billions of years in a vigorously convecting mantle: Replenishment and destruction of chemical anomaly. J. Geophys. Res-Sol. Ea. 120, 3824–3847. (Cited on page 108.)

[77] Niemela, J. J., Skrbek, L., Sreenivasan, K. R., Donnelly, R. J., 2000. Turbulent convection at very high Rayleigh numbers. Nature 404, 837–840. (Cited on page 109.)

[78] Ostilla-Mónico, R., Verzicco, R., Lohse, D., 2015. Effects of the computational domain size on direct numerical simulations of Taylor-Couette turbulence with stationary outer cylinder. Phys. Fluids 27. (Cited on page 13.)

[79] Petschel, K., Stellmach, S., Wilczek, M., Lülff, J., Hansen, U., 2013. Dissipation layers in Rayleigh-Bénard convection: A unifying view. Phys. Rev. Lett. 110, 114502. (Cited on pages vii, 110, 115, and 117.)

[80] Petschel, K., Stellmach, S., Wilczek, M., Lülff, J., Hansen, U., 2015. Kinetic energy transport in Rayleigh-Bénard convection. J. Fluid Mech. 773, 395–417. (Cited on pages vii, 110, 115, 116, and 117.)

[81] Pinelli, A., Uhlmann, M., Sekimoto, A., Kawahara, G., 2010. Reynolds number dependence of mean flow structure in square duct turbulence. J. Fluid Mech. 644, 107–122. (Cited on page 97.)

[82] Pope, S., 2000. Turbulent Flows. Cambridge University Press. (Cited on pages 7, 23, and 26.)

[83] Rai, M. M., Moin, P., 1991. Direct simulations of turbulent flow using finite-difference schemes. J. Comput. Phys. 96, 15–53. (Cited on page 13.)

[84] Roche, P. E., Gauthier, F., Kaiser, R., Salort, J., 2010. On the triggering of the Ultimate Regime of convection. New J. Phys. 12. (Cited on page 109.)

[85] Sagaut, P., 2006. Large Eddy Simulation for Incompressible Flows: An Introduction. Springer Verlag. (Cited on page 43.)

[86] Sannan, S., Weydahl, T., Kerstein, A. R., 2013. Stochastic simulation of scalar mixing capturing unsteadiness and small-scale structure based on mean-flow properties. Flow Turbul. Combust. 90, 189–216. (Cited on pages 6 and 43.)

[87] Schlatter, P., Örlü, R., 2010. Assessment of direct numerical simulation data of turbulent boundary layers. J. Fluid Mech. 659, 116–126. (Cited on pages vii and 95.)

[88] Schmidt, H., Kerstein, A. R., Wunsch, S., Nédélec, R., Sayler, B. J., 2013. Analysis and numerical simulation of a laboratory analog of radiatively induced cloud-top entrainment. Theor. Comp. Fluid Dyn. 27, 377–395. (Cited on page 86.)

[89] Schmidt, R. C., Kerstein, A. R., McDermott, R., 2008. ODTLES: A multi-scale model for 3D turbulent flow based on one-dimensional turbulence modeling. Comput. Methods Appl. Mech. Engrg. 199, 865–880. (Cited on pages 6, 7, 32, 61, 62, 65, 68, 70, and 72.)

[90] Schulz, F., Glawe, C., Schmidt, H., Kerstein, A., 2013. Toward modeling of CO2 multi-phase flow patterns using a stochastic multi-scale approach. Environ. Earth Sci. 70, 3739–3748. (Cited on page 86.)

[91] Shishkina, O., Stevens, R. J., Grossmann, S., Lohse, D., 2010. Boundary layer structure in turbulent thermal convection and its consequences for the required numerical resolution. New J. Phys. 12, 075022. (Cited on pages 115 and 117.)

[92] Shishkina, O., Thess, A., 2009. Mean temperature profiles in turbulent Rayleigh-Bénard convection of water. J. Fluid Mech. 633, 449. (Cited on page 109.)

[93] Smagorinsky, J., 1963. General circulation experiments with the primitive equations. Mon. Weather Rev. 91, 99–164. (Cited on pages 24 and 26.)

[94] Smits, A. J., Marusic, I., 2013. Wall-bounded turbulence. Phys. Today 66, 25–30. (Cited on page 5.)

[95] Spalart, P., 2000. Strategies for turbulence modelling and simulations. Int. J. Heat Fluid Fl. 21, 252–263. (Cited on pages 8 and 23.)

[96] Spalart, P., Allmaras, S., 1992. A one-equation turbulence model for aerodynamic flows. In: 30th Aerospace Sciences Meeting and Exhibit. American Institute of Aeronautics and Astronautics. (Cited on page 23.)

[97] Spalart, P. R., 2009. Detached-eddy simulation. Annu. Rev. Fluid Mech. 41, 181–202. (Cited on page 6.)

[98] Spiteri, R. J., Ruuth, S. J., 2002. A new class of optimal high-order strong-stability-preserving time discretization methods. SIAM J. Numer. Anal. 40, 469–491. (Cited on page 17.)

[99] Stevens, R. J., Lohse, D., Verzicco, R., 2011. Prandtl and Rayleigh number dependence of heat transport in high Rayleigh number thermal convection. J. Fluid Mech. 688, 31–43. (Cited on page 109.)

[100] Stevens, R. J. A. M., Overkamp, J., Lohse, D., Clercx, H. J. H., 2011. Effect of aspect ratio on vortex distribution and heat transfer in rotating Rayleigh-Bénard convection. Phys. Rev. E 84, 056313. (Cited on page 109.)

[101] Stevens, R. J. A. M., van der Poel, E. P., Grossmann, S., Lohse, D., 2013. The unifying theory of scaling in thermal convection: the updated prefactors. J. Fluid Mech. 730, 295–308. (Cited on pages vii, 108, and 109.)

[102] Stevens, R. J. A. M., Verzicco, R., Lohse, D., 2010. Radial boundary layer structure and Nusselt number in Rayleigh-Bénard convection. J. Fluid Mech. 643, 495–507. (Cited on page 109.)

[103] Sun, C., Xia, K.-Q., 2005. Scaling of the Reynolds number in turbulent thermal convection. Phys. Rev. E 72, 067302. (Cited on page 109.)

[104] Toro, E. F., 1999. Riemann Solvers and Numerical Methods for Fluid Dynamics: A Practical Introduction, 2nd Edition. Springer, Berlin. (Cited on pages 12 and 16.)

[105] Tsai, T., Yang, J., Huang, L., 2002. Hybrid finite-difference scheme for solving the dispersion equation. J. Hydraul. Eng. 128, 78–86. (Cited on pages 74 and 76.)

[106] Uhlmann, M., Jan. 2013. DNS database. `www.ifh.kit.edu/dns_data`, [Online; accessed Feb 2013]. (Cited on pages vii, 97, and 101.)

[107] Uhlmann, M., Pinelli, A., Kawahara, G., Sekimoto, A., 2007. Marginally turbulent flow in a square duct. J. Fluid Mech. 588, 153–162. (Cited on pages 96 and 97.)

[108] Urban, P., Hanzelka, P., Kralik, T., Musilova, V., Srnka, A., Skrbek, L., 2012. Effect of boundary layers asymmetry on heat transfer efficiency in turbulent Rayleigh-Bénard convection at very high Rayleigh numbers. Phys. Rev. Lett. 109, 154301. (Cited on page 109.)

[109] Vincenti, W. G., Kruger, C. H., 1975. Introduction to physical gas dynamics. Huntington, N.Y. : Krieger, reprint of the 1967 ed. published by Wiley, New York. (Cited on pages 4 and 9.)

[110] von Larcher, T., Beck, A., Klein, R., Horenko, I., Metzner, P., Waidmann, M., Igdalov, D., Gassner, G., Munz, C.-D., 2015. Towards a framework for the stochastic modelling of subgrid scale fluxes for large eddy simulation. Meteorol. Z, 313–342. (Cited on pages 53, 54, and 55.)

[111] Vreman, B., Geurts, B., Kuerten, H., 1997. Large-eddy simulation of the turbulent mixing layer. J. Fluid Mech. 339, 357–390. (Cited on page 27.)

[112] Wilcox, D. C., 1993. Turbulence modelling for CFD. DCW Industries, La Cañada. (Cited on pages 23 and 24.)

[113] Wunsch, S., Kerstein, A. R., 2005. A stochastic model for high-Rayleigh-number convection. J. Fluid Mech. 528, 173–205. (Cited on pages 86 and 110.)

[114] Zienkiewicz, O. C., Taylor, R. L., Nithiarasu, P., 2006. The finite element method for fluid dynamics, 6th Edition. Butterworth-Heinemann. (Cited on page 12.)

COLOPHON

This document was typeset using the typographical look-and-feel `classicthesis` developed by André Miede. The style was inspired by Robert Bringhurst's seminal book on typography *"The Elements of Typographic Style"*. `classicthesis` is available for both LaTeX and LyX:

`http://code.google.com/p/classicthesis/`

Happy users of `classicthesis` usually send a real postcard to the author, a collection of postcards received so far is featured here:

`http://postcards.miede.de/`

Final Version as of April 11, 2016 (`classicthesis` version 4.1).

DECLARATION

I hereby certify that this thesis has been composed by me and is based on my own work, unless stated otherwise. No other person's work has been used without due acknowledgment in this thesis. All references and verbatim extracts have been quoted, and all sources of information, including graphs and data sets, have been specifically acknowledged.

Hiermit erkläre ich an Eides Statt, dass ich die vorliegende Arbeit selbstständig und nur unter Zuhilfenahme der ausgewiesenen Hilfsmittel angefertigt habe. Sämtliche Stellen der Arbeit, die im Wortlaut oder dem Sinn nach anderen gedruckten oder im Internet verfügbaren Werken entnommen sind, habe ich durch genaue Quellenangaben kenntlich gemacht. Die Arbeit wurde nicht an anderer Stelle eingereicht.

Berlin, August 2015

Christoph Glawe